The University of Manitoba

THE DISSOLUTION OF MAGNETITE FILMS FROM CARBON STEEL SURFACES

by

DAVID S. MANCEY

A Thesis submitted to the Faculty of Graduate Studies in partial fulfillment of the requirements for the Degree of Master of Science through the Department of Chemistry.

The research work was conducted at the Research Chemistry Branch, Whiteshell Nuclear Research Establishment, Pinawa, Manitoba ROE 1LO

Winnipeg, Manitoba, 1985

THE DISSOLUTION OF MAGNETITE FILMS FROM CARBON STEEL SURFACES

BY

DAVID S. MANCEY

A thesis submitted to the Faculty of Graduate Studies of
the University of Manitoba in partial fulfillment of the requirements
of the degree of

MASTER OF SCIENCE

CONTENTS

ABSTRACT

This study was performed to assist in the development of a dilute chemical decontamination reagent for use in the primary coolant circuits of CANDU reactors.

The dissolution of magnetite films grown on carbon steel electrodes in high temperature autoclaves was investigated in acidic aqueous solutions of complexing agents. Film dissolution was studied by monitoring both the release of dissolution products to solution and the open-circuit potential of the electrode. Also, pre-dissolution and post-dissolution study of the electrode surface was performed by scanning electron microscope.

All film dissolutions featured a rapid solution penetration to the substrate steel, involving little oxide dissolution, initiating metal dissolution. This anodic process initially couples to the reductive dissolution of magnetite in a process called autoreduction. As autoreduction proceeds, pore-oxide dissolution causes the area of metal exposed to increase, causing the mixed potential of the film to drift cathodically. Autoreduction persists until proton reduction is thermodynamically feasible, at which point proton reduction appears to rapidly replace magnetite reduction as the principal cathodic half-reaction. Thus, active corrosion commences. No significant oxide dissolution process other than autoreduction appears to operate prior to the onset of active corrosion.

In the systems studied, autoreduction is normally rate controlled by oxide dissolution. Autoreductive oxide dissolution in acidic EDTA solutions at room temperature is inefficient, being confined almost exclusively within pores in the oxide film. Thermal or chemical acceleration of autoreduction causes the pore oxide dissolution process to become transport limited. Further acceleration of the reaction causes magnetite dissolution to occur generally over the entire film surface, increasing the efficiency of oxide dissolution by autoreduction.

The oxide dissolution process appears to be rate controlled by the dissolution of surface cation-chelate species. The dissolution rate dependencies upon pH, anion identity and anion concentration are consistent with the adsorption and dissolution model proposed by Matijević et al. [16,17,36,78]. The abilities of sulphate, EDTA and oxalate to promote the autoreductive dissolution of magnetite appear to be comparable.

ACKNOWLEDGEMENTS

The author expresses his gratitude to Dr. D.W. Shoesmith for his guidance and encouragement throughout the course of this work.

A special thanks is extended to Diane Doern for her skilled operation of the Scanning Electron Microscope and production of the micrographs. Diane must also be thanked for her able assistance in the laboratory.

The author also expresses his appreciation and gratitude to Grant Bailey for much helpful advice.

The author also expresses his thanks for the iron analyses that were performed by Mike Lau and Ken Wazney.

A special thanks is extended to Marg McDowall and Pat McCooeye for their skill and patience in typing this thesis.

CHAPTER 1

INTRODUCTION

1.1 REASONS FOR STUDYING OXIDE DISSOLUTION

The primary coolant circuits of commercial nuclear power reactors are constructed principally from either carbon steel, stainless steel or inconel (a nickel-based alloy). Most primary coolant circuits contain components made from each of these materials. During routine operation corrosion of these metals releases a variety of transition metal ions into the water coolant. These ions are carried with the coolant flow through the nuclear reactor core where they are subject to high neutron fluxes. A proportion of the ions become radioactive as a consequence of neutron absorption. The radioactive metal ions are carried around the primary coolant circuit, eventually precipitating as mobile solids, or undergoing incorporation into adherent oxide films by ion exchange and film growth mechanisms. The oxides formed are frequently mixed-transition metal spinel oxides, the composition of which varies as a function of substrate, location within the circuit, time and coolant water chemistry. These radioactive oxides accumulate over periods of years, their presence in regions of the primary coolant circuit remote from the reactor core adding significantly to the radiation exposures of maintenance personnel. To facilitate maintenance operations it is desirable to remove the radioactive oxide films. The design of a nuclear reactor primary coolant circuit means that

dissolution of the radioactive oxides using solution reagents is the favoured method of decontamination.

To perform chemical decontaminations it is necessary to shut down the nuclear reactor. A number of constraints are placed upon chemical decontaminations by reason of safety, efficiency and cost. Primary coolant circuit pressurization is undesirable, hence the maximum decontamination temperature is $\sim$ 100°C. The volume of reagent required should be minimized, and the radioactive transition metal ions should be recoverable from the spent decontaminant using ion-exchange resins in order to alleviate waste handling problems. The reagents used must not cause unacceptable corrosion, particularly localized corrosion such as pitting. Also, the reagents must either be easy to purge from the circuit following decontamination, or must degrade to innocouous species on reactor startup.

Besides decontamination of nuclear reactors, many other motives for studying oxide dissolution processes exist. Oxide dissolution is a necessary part of many processes of commercial significance, e.g., the extraction of metals from ores, surface preparation of metals, production of microelectronic components, recycling of nuclear fuel, initiation of local corrosion processes, stress corrosion cracking, general breakdown of materials passivity and degradation of photoelectrochemical devices.

A survey of the literature on oxide dissolution indicated that studies have most frequently been performed on oxides in isolation, even in those instances where the purpose of the research was the investigation of oxide film dissolution. In some systems the impact of the substrate is negligible, for instance when the oxide film is impervious or if the substrate is inert. Frequently this is not the case, and when both the oxide and substrate are exposed to solution both can undergo dissolution. In such situations the metal can impose a potential on the oxide different from the rest potential of the free oxide, changing the nature of the oxide dissolution process.

The study of oxide film dissolution is often more difficult than the study of discrete oxide particles due to additional complexities such as variation in oxide stoichiometry as a function of depth, complex morphology, and local rather than general dissolution processes. Oxide powders are often commercially available, or can be produced in the laboratory by relatively simple preparative methods. Preparative techniques capable of producing oxide films of predictable stoichiometry, structure and morphology are not so well developed. Thus, many investigations have been performed using monodispersed oxide particles uniform in composition, morphology and dimension.

1.2 CLASSIFICATION OF OXIDE DISSOLUTION PROCESSES

Oxide dissolution processes can be divided into three basic categories by virtue of the overall reactions (A) direct, (B) reductive,

and (C) oxidative [1]. For reactions in each of these categories the nature of the rate-determining reaction can be: chemical, transport, and additionally for the redox categories (B) and (C) electronic-charge transfer (electrochemical). Immediately, one class of dissolution processes involving anion redox reactions can be disregarded for oxides. The thermodynamic stability of the oxide ion means that both oxidation and reduction of this ion is energetically unfavourable. However, it should be noted that for other anions such as sulphide this is not the case.

For oxides of metals that exhibit multiple valence the oxide dissolution processes outlined in Table 1.1 are possible. It should be noted that for both the reductive (B) and oxidative (C) oxide dissolution process there must be a second accompanying redox reaction. Overall rate control can be exerted either by the oxide dissolution half-reaction or this second redox half-reaction. For reductive oxide dissolution processes the accompanying oxidation reaction can be the anodic dissolution of the underlying metal (autoreduction) or electron transfer from a solution species (solute induced reductive dissolution (SIRD)). A subgroup of the latter reaction type, involving reduction by a solution metal complex, is often distinguished, this process being commonly called ligand-bridge assisted dissolution (LBAD).

1.3 OXIDE DISSOLUTION PROCESSES

Table 1.1 defines 14 classes of oxide dissolution processes according to the nature of the rate-determining reaction step. For redox oxide dissolution processes, rate control can also be exerted by the accompanying half-reaction. In the following brief review of oxide dissolution studies, the processes are only divided into the three broad reaction categories.

The dissolution of beryllium oxide in sulphuric acid, investigated by Koch [2], is an example of a direct dissolution reaction.

$$>Be(II)O + 2H^{+}(aq) \rightarrow Be(II)(aq) + H_2O \qquad (1.1)$$

(where (>) indicates a solid state species)

Other direct dissolution processes have been identified and studied by Devuyst and Warren [3], Warren et al. [4-8], Pryor and Evans [9], Azuma and Kametani [10], Bradbury [11], Gorichev [12,13], Bruyere and Blesa [14], Matijević et al. [15-17] and Gilbert and Ouellet [18].

The dissolution of cobalt(III) oxide in chromium(II) chloride solutions proceeds by a reductive pathway:

$$>Co(III)_2O_3 + 6H^{+}(aq) + 2Cr(II)(aq) \rightarrow 2Co(II)(aq) + 2Cr(III)(aq) + 3H_2O \qquad (1.2)$$

Reductive dissolution has been studied on a number of occasions, e.g., Zabin and Taube [19], Koch [20], Devuyst and Warren [3,8], Segal and Sellers [21-23] and Baumgartner et al. [24]. Detailed kinetic studies have been performed on a number of systems, allowing the elucidation of reaction mechanisms. Although considerable progress has been made, many details of reaction mechanism remain unresolved.

The study of oxidative dissolution processes has been generally less comprehensive than reductive dissolution. There are, however, a few such processes that have been studied in detail, e.g., the anodic dissolution of spinel oxide electrodes, Kishi et al. [25,26] and Kawashima et al. [27]. Certain spinel oxides are considered good candidates as anode materials for water electrolyzers, and the anodic dissolution of these oxides has often been addressed during these studies, e.g., Tarasevich et al. [28], Tseung et al. [29] and Haenen et al. [30]. Additionally, many studies have been performed on the oxidative dissolution of uranium dioxide,

$$>U(IV)O_2 \rightarrow (U(VI)O_2)^{2+}_{(aq)} + 2e^- \qquad (1.3)$$

e.g., Hiskey [31], Nicol and Needes [32], Sunder et al. [33]. A number of oxidative dissolution processes are of commercial significance. For instance, permanganate-based reagents are used to dissolve chromium-rich oxides from boiler circuits

$$>Cr(III) + MnO_4^-(aq) + 2H_2O \rightarrow CrO_4^{2-}(aq) + MnO_2 + 4H^+(aq) \qquad (1.4)$$

Also, the ferric ion oxidation of sulphides is an anion oxidative dissolution process that is exploited for the processing of mineral ores

$$>Pb(II)S + 2Fe(III)(aq) \rightarrow Pb(II)(aq) + 2Fe(II)(aq) + S \qquad (1.5)$$

1.4. IRON OXIDE FILM DISSOLUTION PROCESSES

The principal aim of this research is to develop a decontamination reagent suitable for use in CANDU reactors. The primary coolant used in these reactors is heavy water (D_2O), the circuit being constructed principally from carbon steel. The concentration of dissolved deuterium in primary coolant is maintained at a high level to control water radiolysis products, and as a consequence magnetite, not Fe(III) oxide film growth occurs. The magnetite is not pure, but contains varying concentrations of substituent transition metal cations, principally Ni, Cr, and Co.

To develop a decontamination reagent suitable for use in CANDU reactors it is therefore necessary to study the dissolution of magnetite from carbon steel surfaces. The reagents currently in use are basically a mixture of chelating agents (EDTA, oxalate, citrate) plus a number of proprietary additives. Investigations of related dissolution processes are discussed in detail in the following chapters. It is apparent from these studies that the dissolution of magnetite film from a carbon steel surface will proceed by one of the following mechanisms:

(i) Direct Dissolution

$$>Fe_3O_4 + 8H^+(aq) \rightarrow 2Fe(III)(aq) + Fe(II)(aq) + 4H_2O \quad (1.6)$$

Shoesmith et al. [34] claimed that this mechanism was occurring when magnetite films on iron were dissolving in solutions containing oxalate ions. Oxalate was envisaged as accelerating direct dissolution by absorbing at Fe(III) sites in the magnetite lattice, thereby facilitating proton attack of the oxide ions in the lattice. Baumgartner et al. [24] proposed that this reaction occurs during the initial stages of magnetite dissolution in oxalic acid. Although few detailed studies of magnetite dissolution in EDTA have been performed, the dissolution studies in EDTA solutions by Matijević et al. [16,35,36] with β-FeOOH, hematite and nickel ferrite, and Gilbert et al. [18] with magnetite strongly suggest a direct dissolution process.

(ii) Solute Induced Reductive Dissolution

These reactions involve the reduction of Fe(III) ions in the oxide lattice to Fe(II) ions, via an electron transfer from a solution species. If the solution species is a metal complex the reaction is commonly called a ligand-bridge assisted dissolution (LBAD) process. Reductive dissolution via this pathway is fast for iron oxide and nickel ferrite dissolution, Figure 1, and can be brought about by a number of. Cr(II) and V(II) reagents [21,23]. Both the oxalate and EDTA complexes

of Fe(II) have been observed to promote LBAD [24,37]. For ferrous oxalate, $Fe(II)(C_2O_4)$, the reduction can be written:

$$>Fe(III) + Fe(II)C_2O_4(aq) \rightarrow >Fe(II) + (Fe(III)C_2O_4)^+(aq) \quad (1.7)$$

$$>Fe(II) + H_n(C_2O_4)^{n-2}(aq) \rightarrow Fe(II)(C_2O_4)(aq) + nH^+ \quad (1.8)$$

A subset of such reductive dissolution processes is reactions in which oxalic acid at elevated temperatures [38] or thioglycolic acid [39] directly reduce the solid state cations. Such reagents can also operate indirectly by producing low oxidation state solution metal complexes that subsequently reduce the solid state ions.

(iii) Autoreduction

In this mechanism the oxide film is dissolved by reaction with the underlying metal:

$$>Fe(II)Fe(III)_2O_4 + 8H^+(aq) + >Fe(0) \rightarrow 4Fe(II)(aq) + 4H_2O \quad (1.9)$$

Shoesmith et al. [34,40] demonstrated that this mechanism occurs during the dissolution of magnetite films on iron in the presence of citrate, EDTA and oxalate. Although these studies did not determine which oxide dissolution reaction was dominant, both autoreduction and direct dissolution were thought to contribute significantly to oxide dissolution in oxalate solutions.

TABLE 1.1

OXIDE DISSOLUTION REACTIONS

OVERALL REACTION	ION SPECIES	TYPES OF RATE DETERMINING PROCESS
A. DIRECT $\blacktriangleright M^{II}O + H_2L \rightarrow M^{II}L(aq) + H_2O$	CATION $\blacktriangleright M^{II} + L^{2-} \rightarrow$ $\rightarrow M^{II}L(aq)$	CHEMICAL $\blacktriangleright M^{II} + L^{2-}(ADSORBED) \rightarrow M^{II}L\ (ADSORBED)$
		TRANSPORT $M^{II}L(SURFACE) \rightarrow M^{II}L(aq)$
	ANION $\blacktriangleright O^{2-} + 2H^{+} \rightarrow H_2O$	CHEMICAL $OH^{-}(ADSORBED) \rightarrow OH^{-}(SURFACE)$
		TRANSPORT $H^{+}(aq) \rightarrow H^{+}(SURFACE)$

(continued)

TABLE 1.1 (continued)

OXIDE DISSOLUTION REACTIONS

OVERALL REACTION	ION SPECIES	TYPES OF RATE DETERMINING PROCESS
B. REDUCTIVE $\blacktriangleright M^{II}O + H_2L + e^- \rightarrow (M^{I}L)^-(aq) + H_2O$	CATION $\blacktriangleright M^{II} + L^{2-} + e^- \rightarrow (M^{I}L)^-(aq)$	ELECTROCHEMICAL $\blacktriangleright M^{II} + e^- \rightarrow \blacktriangleright M^{I}$
		CHEMICAL $(M^{I}L)^-(ADSORBED) \rightarrow (M^{I}L)^-(aq)$
		TRANSPORT $L^{2-}(aq) \rightarrow L^{2-}(SURFACE)$
	ANION $\blacktriangleright O^{2-} + 2H^+ \rightarrow H_2O$	CHEMICAL $\blacktriangleright O^{2-} + H^+ \rightarrow \blacktriangleright OH^-$
		TRANSPORT $H^+(aq) \rightarrow H^+(SURFACE)$

(continued)

TABLE 1.1 (continued)

OXIDE DISSOLUTION REACTIONS

OVERALL REACTION	ION SPECIES	TYPES OF RATE DETERMINING PROCESS
C. OXIDATIVE $\blacktriangleright M^{II}O + H_2L \rightarrow (M^{III}L)^+(aq) + H_2O + e^-$	CATION $\blacktriangleright M^{II} + L^{2-} \rightarrow (M^{III}L)^+(aq) + e^-$	ELECTROCHEMICAL $\blacktriangleright M^{II} \rightarrow \blacktriangleright M^{III} + e^-$
		CHEMICAL $\blacktriangleright M^{III} + L^{2-} \rightarrow (M^{III}L)^+(ADSORBED)$
		TRANSPORT $(M^{III}L)^+(SURFACE) \rightarrow (M^{III}L)^+(aq)$
	ANION $\blacktriangleright O^{-2} + 2H^+ \rightarrow H_2O$	CHEMICAL $OH^-(ADSORBED) + H^+ \rightarrow H_2O(ADSORBED)$
		TRANSPORT $H^+(aq) \rightarrow H^+(SURFACE)$

(continued)

TABLE 1.1 (concluded)

OXIDE DISSOLUTION REACTIONS

NOTES

▶( ) - indicates a solid-state species.

( )(aq) - indicates a solvated species in the solution bulk.

( )(SURFACE) - indicates a solvated species in very close proximity to the solid-solution interface.

( )(ADSORBED) - indicates a species adsorbed on the oxide surface.

CHAPTER 2

ELECTROCHEMISTRY AT METAL-OXIDE-SOLUTION INTERFACES

2.1 INTRODUCTION

The potential distribution across an oxide solution interface affects both interfacial ion and electron transfer processes. The interfacial potential that controls such processes often differs from the net potential difference that exists between the solution bulk and the oxide bulk. To determine the potential available at the interface it is necessary to know how the potential drop is distributed through both the oxide and solution phases. For metals it is commonly assumed that, by virtue of the high concentration of charge carriers, the potential within the solid is constant from the bulk to the interface, the result being that the entire potential change exists on the solution side of the interface. This assumption is often invalid for semiconductors. For oxide dissolution processes the potential distribution on both the oxide and solution side of the interface must be considered. This requires a general appreciation of the behaviour of semiconductors, and for the purposes of this study, specific knowledge of the semiconducting properties of magnetite. Further, it is necessary to determine whether the potential distributions in the oxide and solution are subject to change as a consequence of changes in composition, structure, charge carrier concentration or other variables.

2.2 SEMICONDUCTING OXIDES

Conduction in intrinsic semiconductors is by means of an equal number of oppositely charged mobile charge carriers. A pair of charge carriers is formed in intrinsic semiconductors as an excited electron jumps across the energy gap between the valence and conduction bands. This event leaves a hole in the previously full valence band, which can be considered effectively as a point of positive charge. Both the electron present in the conduction band and hole present in the valence band contribute to the conductivity of the substance. The magnitude of the energy gap between valence and conduction bands influences the concentration of charge carriers and hence the substance's conduction properties.

The concentration of charge carriers in a typical semiconductor at room temperature is in the range 10^{13}-10^{16} cm^{-3}, metals having values in the region of 10^{22} cm^{-3}. The electrical conductivity of a semiconductor is given by the sum of the conductivities of the positive and negative charge carriers.

$$k = e(C_e U_e + C_h U_h) \qquad (2.1)$$

where

k = electrical conductivity

e = absolute value of the electronic charge

C_e = concentration of electrons

U_e = effective mobility of electrons

C_h = concentration of holes

U_h = effective mobility of holes.

The electrons and holes, besides having opposite charges, may have different effective mobilities. Also, semiconductors may feature different concentrations of positive and negative charge carriers. As a consequence of these differences, the significance of the two charge carriers can differ, and the carrier that contributes most to the total conductivity is referred to as the majority carrier. Semiconductors that have negatively charged majority carriers are n-type. When the majority carriers are positively charged, the semiconductor is p-type.

A potential difference applied across a semiconductor acts upon the mobile charge carriers causing charge to accumulate at both semiconductor interfaces. One interface will gain a net positive charge, the other a net negative charge, as dictated by the potential gradient. The distribution of potential, and hence the distribution of charge, within the semiconducting film is influenced by (i) the net potential charge across the film, (ii) the concentration of charge carriers, and (iii) the thickness of the film.

The zones of excess charge that form at the semiconductor interface are termed space-charge regions. The thickness of this region, termed the Debye length, increases as the concentration of charge carriers decreases, achieving thicknesses as great as 10,000 Å. This space-charge region in the semiconductor can be considered

analogous to the Guoy-Chapman diffuse layer in the electrolyte, the identity of charge carriers being electronic rather than ionic. The potential distribution, and hence the charge transfer characteristics, of a semiconducting film is strongly influenced by film thickness. For films < 30 Å thick, quantum-mechanical tunneling means that the film is essentially transparent to the passage of electrons. More substantial films with a thickness less than the Debye length have charge transfer characteristics influenced by the metal, the oxide, and both the semiconductor-electrolyte and semiconductor-metal interfaces. For films considerably thicker than the Debye length, the charge transfer behaviour will not be influenced by the substrate metal, only the semiconductor-electrolyte interface and the semiconductor properties being of significance. Butler [41] has proposed simple models for the distribution of potential across both thick and thin semiconducting films. A linear potential distribution exists in semiconducting films that are considerably thinner than the material's Debye length, Figure 2. For films much thicker than the Debye length, an S-shaped potential distribution is observed, Figure 2.

The magnetite films used for the experimental studies reported in this thesis are unquestionably much thicker than the Debye length for magnetite. Therefore, the impact of the metal-oxide interface can be disregarded for solution-oxide interfacial charge transfer reactions. The proposed model of semiconductor films requires that the charge carriers exhibit unrestricted mobility. However, some semiconductors feature charge carriers that are trapped on the surface, in what are

commonly called surface states. These surface states are unable to move in a direction normal to the interface. It is thought that these charge carriers are trapped by virture of having energies within the band gap between valence and conduction bands. The presence of these trapped holes or electrons causes a reduction in the potential drop across the space charge region. At high surface state densities the potential drop across this region approaches zero and metal-like behaviour ensues.

Undoubtedly magnetite features surface states that arise from surface defects and adsorbed species. The impact of these surface states on the dissolution processes investigated is unknown. However, an awareness that this phenomenon could occur is necessary when studying such systems.

A study of how the semiconducting properties of iron oxide films influence electrochemical behaviour was undertaken by Stimming and Schultze [42,43]. Their studies were restricted to a very thin passive film on iron, and the behaviour observed was complex. The conduction characteristics of the maghemite (γ-Fe_2O_3) component in the film varied as a function of potential, behaving as a n-type semiconductor, insulator and p-type semiconductor. The impact of potential on electrochemical behaviour is reinforced by the claim that electron transfer reactions occur via the conduction band at low potentials and via the valence band at high potentials. Previously unexplained experimentally observed characteristics of electron transfer reactions on passive iron

were rationalized using this model. The study strongly indicates that the semiconducting properties of oxide films have a significant effect on electrochemical behaviour.

2.3 STRUCTURE OF THE ELECTRICAL DOUBLE LAYER IN THE SOLUTION

The commonly accepted model for the solution side of an electrode-electrolyte interface is the Helmholtz electrical double layer, Figure 3.

The inner Helmholtz layer lies adjacent to the electrode and constitutes a region where unsolvated charges may be specifically adsorbed. The outer Helmholtz layer is defined as existing at the plane of closest approach for solvated ions. Beyond this layer is the Gouy-Chapman region of diffuse charge. In the absence of specific adsorption, electrostatic considerations determine the identity of the ions drawn to the surface, opposite charges tending to accumulate on the electrode and solution sides of the interface.

The occurrence of specific adsorption can significantly change the potential distribution in solution, Figure 4. Specific adsorption can occur even when the electrostatic interactions are unfavourable. Thus, specific anion adsorption can occur on a negatively charged surface if the bond formation is sufficiently favourable thermodynamically. Thus, depending on the circumstances, specific adsorption can both inhibit and enhance dissolution processes. Further, due to the

strength of the chemical bonds between a specifically adsorbed species and the surface, changes in the potential at the electrolyte surface will not necessarily have a major impact on the identity or concentration of specifically adsorbed ions.

Specific adsorption on metal and oxide surfaces has been studied frequently. Of particular interest to this study of oxide dissolution in solutions containing chelating agents is the work of Yoneyama et al. [44] on the effects of potential on oxalate adsorption on nickel oxide.

Semiconducting properties can be induced in nickel oxide by lithium doping, and such electrodes exhibit ideal polarizability over a specific potential range. Within this range, a change in the electrode potential varies the charge accumulated in the interfacial region without allowing charge transfer across the interface.

Single crystal electrodes were used to ensure that uncontrollable surface characteristics were reduced to a minimum. The experiments involved immersion of the electrode in perchloric acid solutions with and without oxalic acid present. The quantity of oxalic acid adsorbed on the surface of the electrode was determined for potentials from -0.2 to +0.6 V (vs SCE) using galvanostatic methods. The flat band potential was estimated to be +0.85 V (vs SCE) so that at all potentials within the range studied the electrode carried a negative charge.

Variations in adsorption times between 5 and 40 minutes had no impact on the quantity of absorbate present on the electrode, indicating a fast adsorption process. The quantity of oxalate adsorbed showed a relatively weak dependence upon potential. At any given pH the adsorbed oxalate concentration varied by only a factor of 3 as a function of potential. The potential of maximum adsorption shifted in the cathodic direction as the pH was increased, from +0.3 V (vs SCE) at pH $\backsim$ 1 to +0.0 V (vs SCE) at pH $\backsim$ 6. Very little adsorption was observed in highly acidic solutions, pH = -0.92.

The quantity of oxalate adsorbed increased approximately linearly with oxalate concentration from 0 to 1×10^{-3} mol$\cdot$dm^{-3}. Further increases in oxalate concentration produced only minor changes in the adsorbate surface concentration. The maximum surface adsorbate concentration rose as the pH decreased in the range 1 to 6. The major adsorbed species appeared to be oxalate anions, with $C_2O_4^{2-}$ adsorbing more strongly than $HC_2O_4^-$.

The behaviour of malonic acid ($CH_2(COOH)_2$) and succinic acid ($HO_2C(CH_2)_2CO_2H$) was similar to that observed for oxalic acid. When the solution compositions of the three acids were adjusted to give equivalent concentrations of anions, the surface concentrations were found to be:

oxalate > malonate > succinate .

A comparison between the number of cationic sites theoretically available with the maximum surface concentration of oxalate observed suggested that 0.5 of theoretical coverage was achieved, assuming that one oxalate anion was associated with two cationic sites.

The quantity of adsorption was found to increase significantly as the charge carrier concentration of the nickel oxide increased. This was thought to arise because electrodes with high carrier concentrations maintained a higher surface concentration of positive sites when polarized below the flat-band potential. This higher concentration of positive sites promoted a higher surface concentration of specifically adsorbed anions. It was also observed that the surface adsorbate concentration was unaffected by the identity of the crystal plane exposed.

The results obtained in this study are consistent with the adsorption model proposed by Matijević [17], and demonstrate that both solution and oxide properties significantly affect the surface adsorbate concentration. The solution parameters identified as important are (i) the nature of the adsorbate, (ii) adsorbate concentration, and (iii) the pH. Additionally, the charge carrier concentration of the oxide was found to strongly influence the surface adsorbate concentration. In contrast, surface potential variations within the range investigated had relatively little impact on the surface concentration of these specifically adsorbed dicarboxylic acids.

2.4 INTERFACIAL CHARGE TRANSFER REACTIONS

Once an appreciation is gained of the potential distribution across the interface, the implications for ion and electron transfer processes can be considered. For an electron transfer process occurring between a solution species and the electrode, the potential available to drive the reaction is influenced by the locations of the participating centres. Such processes usually involve electron transfer between a species in the outer Helmholtz plane and a surface atom or ion in the solid. Therefore, the potential that determines the rate of this electron transfer process is that between the surface of the electrode and the outer Helmholtz plane. Clearly, the activation energy of such a process would be significantly changed if specific adsorption occurred and interposed a monolayer of charged ions. Also, as may be the case for reductive oxide dissolution, the particular atomic species reduced may not be located at the surface, but may be several atom layers distant from the interface. Thus, the potential gradient within the thin oxide layer becomes important, and the overall activation energy for the process may be significantly changed. Although this discussion has been restricted to electron transfer reactions at the interface, ion transfer reactions are expected to be similarly affected.

2.5 DISSOLUTION OF IONIC COMPOUNDS

All dissolution processes involve the transfer of ions across the solid-solution interface. Therefore, it is essential to understand

the factors affecting such processes. Vermilyea [45] proposed a theory to explain the direct dissolution of ionic solids in aqueous media. This theory represents a development of the ideas originally proposed by Engell [46]. An ionic substance immersed in aqueous solution develops a potential difference at the interface due to ion exchange. The potential is determined, in part, by the steady-state concentration of certain exchangeable ions referred to as "potential-determining ions". For oxides and hydroxides the dominant potential-determining ions are metal ions, protons and hydroxide ions.

The double layer potential (ψ) is given by:

$$\psi = \frac{RT}{zF} \ln a/a_o \qquad (2.2)$$

where z = Charge of the potential-determining ion

a = Activity of the potential-determining ion

a_o = Activity of the potential-determining ion in the isoelectric solution

R = Gas constant

T = Absolute temperature

F = Faraday constant.

where the isoelectric solution is the solution that produces a double layer potential (ψ) of zero, i.e., an uncharged particle.

In the development of this model, Vermilyea makes the simplifying assumption that the space charge layer in the solid is negligible, so

that the interfacial potential exists entirely within the solution. Also, the potential in the solution, the electrical double layer potential, exists only across the Helmholtz layer. It is recognized that this may not be true for semiconducting oxides, or for solutions with a low ionic strength.

For a charged surface the rate of ion removal (r_r) is given by:

$$r_r = nK_r \exp\left(\frac{\alpha z F \psi}{RT}\right) \tag{2.3}$$

and the deposition rate (r_a) by:

$$r_a = CK_a \exp -\left(\frac{(1-\alpha) z F \psi}{RT}\right) \tag{2.4}$$

where C = ion concentration in solution

n = number of ions per unit surface area of the solid

α = transfer coefficient

K_r = rate constant for ion removal

K_a = rate constant for ion addition.

Expressions of the form given above can be written for both cations and anions. The net rate of ion removal (r) is given by

$$r = r_r - r_a \ . \tag{2.5}$$

To maintain charge neutrality the net rate of anion removal must equal the net rate of cation removal. Hence,

$$r = r_r^+ - r_a^+ = r_r^- - r_a^- \quad . \tag{2.6}$$

This approach leads to a number of qualitative results:

(i) For the same driving force the greatest dissolution rate and potential change are obtained if the solution is undersaturated with respect to the ion having the greatest exchange rate.

(ii) The addition of species that complex with the potential-determining ions can greatly increase the rate of dissolution. It is recognized that this effect can arise in part from the reduced solution activity of the potential-determining ion, and also from a reduced activation energy for the rate-determining process.

For the dissolution of a hydroxide in acid solutions, assuming negligible back reaction, the reaction rate equals the rate of cation removal and is given by:

$$r = r_r^+ = n_+ K_r^+ \exp\left(\frac{\alpha_+ z_+ F\psi}{RT} \right) \quad . \tag{2.7}$$

Assuming that the hydroxide ions are removed exclusively as water following protonation, then

$$r = r_r^- = n_- K_r^- . [H^+] . \exp\left(\frac{\alpha_- z_- F\psi}{RT} \right) \quad . \tag{2.8}$$

Solving for ψ yields

$$r = n_+ K_r^+ \left[\frac{n_- K_r^- [H^+]}{n_+ K_r^+} \right]^{\left[\frac{\alpha_+ z_+}{\alpha_+ z_+ - \alpha_- z_-} \right]} . \tag{2.9}$$

Assuming $\alpha_+ = \alpha_-$

$$r = n_+ K_r^+ \left[\frac{n_- K_r^- [H^+]}{n_+ K_r^+} \right]^{\left[\frac{z_+}{z_+ - z_-} \right]} . \tag{2.10}$$

Consider an oxide dissolution process in which the oxide ions are singly protonated and dissolve as hydroxide ions, i.e., $z_- = -2$. Assuming that n_+, n_-, K_r^+ and K_r^- are constant, then, for $z_- = -2$:

$$\text{If } Z_+ = 1 \qquad \text{Rate proportional to } [H^+]^{1/3} \tag{2.11}$$

$$\text{If } Z_+ = 2 \qquad \text{Rate proportional to } [H^+]^{1/2} \tag{2.12}$$

$$\text{If } Z_+ = 3 \qquad \text{Rate proportional to } [H^+]^{3/5} \quad . \tag{2.13}$$

In this way it can be seen that fractional rate dependencies upon the hydrogen ion concentration are predicted. The work of Koch [2] on beryllium oxide dissolution demonstrated that rate orders of approximately 1/2 were found with a variety of acids.

Vermilyea [45] considers the impact of an applied potential on the dissolution process. The results indicate that small changes from the equilibrium potential theoretically should produce enormous changes in surface concentration. The changes are so large that they almost certainly do not actually arise, although profound effects on the surface composition will occur. A corollary of this large change of surface composition with potential is that the surface of the crystal will possess a very large capacitance. Consequently, it will usually not be possible to change the double layer potential appreciably by the application of external potentials. This approach indicates that applied potentials can yield no more than a twofold increase in dissolution rate above that observed for a freely dissolving crystal. Increasing already large overpotentials causes a decrease in reaction rate. It is implicitly assumed in the development of this theory that faradaic processes, leading to changes in oxidation state, do not occur.

This theory explains the origin of the fractional rate dependencies upon hydrogen ion concentration observed in many oxide dissolution studies. The form of the dependence is seen to arise from the charges carried by the reacting ions.

It is demonstrated that the rate of ion dissolution observed for freely dissolving crystals cannot be accelerated by more than a factor of 2 by the application of potentials to the crystal-solution interface. Thus, if during magnetite dissolution a significant rate dependence upon potential is observed, the clear implication would be

that an electrochemical rather than purely chemical process must be occurring.

2.6 MIXED POTENTIALS

During the experiments performed in this work the potential measured is a mixed potential, commonly called the corrosion potential. A mixed potential is observed because more than one half-reaction is occurring on the electrode surface. In its simplest form a mixed potential arises from the contributions of one anodic and one cathodic half-reaction. However, the situation need not be this simple, as more than one anodic or cathodic process can occur simultaneously.

In order to be able to interpret the experimentally observed corrosion potential-time behaviour, it is necessary to know how this potential relates to both the anodic and cathodic equilibrium half-reaction potentials, which are related to the thermodynamics of the particular half-reaction.

Consider a clean metal disk corroding in an electrolyte. In its simplest form, such a corrosion reaction involves only two coupled half-reactions, both the anodic and cathodic reactions occurring simultaneously on the metal surface. At equilibrium no net current is produced, the currents associated with the two half-reactions being equal in magnitude but opposite in sign. The value of the anodic and

cathodic currents is referred to as the corrosion current, and is a direct measure of the rate of corrosion.

If a reference electrode immersed in the same electrolyte is connected through a high impedence voltmeter to the corroding metal electrode a mixed potential is recorded, commonly called a corrosion potential.

If each half-reaction is considered as a reversible process with a finite forward and reverse reaction rate, then the net half-reaction current arises from the difference between forward and reverse currents.

Anodic Reaction

$$M \underset{I_a^r}{\overset{I_a^f}{\rightleftharpoons}} M^{n+} + ne^- \qquad (2.14)$$

The net anodic current (I_a)* is given by:

$$I_a = I_a^r - I_a^f \qquad (2.15)$$

---

*The nomenclature used is defined at the end of this section.

Cathodic Reaction

$$nH^+ + ne^- \underset{I_c^r}{\overset{I_c^f}{\rightleftharpoons}} nH \qquad (2.16)$$

The net cathodic current (I_c) is given by:

$$I_c = I_c^f - I_c^r \qquad (2.17)$$

At the corrosion potential

$$I_{corr} = I_a = -I_c \qquad (2.18)$$

Rather than measuring currents it is more appropriate to consider current densities and thereby remove the dependence on the area of the electrode. This is particularly significant when contemplating mixed potentials when the areas available to each half-reaction need not be equal.

Every half-reaction is characterized by an equilibrium exchange current density (i_o). When a given half-reaction is at equilibrium the forward and reverse currents are finite, but equal and opposite. Thus, even though no net current is produced a finite current density exists on the electrode surface. This current density is referred to as the equilibrium exchange-current density (i_o). This

parameter reflects the kinetic properties of a given half-reaction under a particular set of interfacial conditions. Thus, for a metal dissolution reaction

$$M \rightleftharpoons M(n) + ne^- \tag{2.19}$$

varying the identity of the crystallographic plane of the metal exposed, the temperature, pH and solution speciation can all cause the value of i_o to change. The values of equilibrium exchange-current densities (i_o) vary greatly between systems as shown for a single reaction in Table 2.1.

Table 2.1

Exchange Current Densities (i_o) at 25°C

Metal	System	Medium	log i_o, A cm^{-2}
Platinum	H^+/H_2	H_2SO_4	-3.1
Mercury	H^+/H_2	H_2SO_4	-12.1
Nickel	H^+/H_2	H_2SO_4	-5.2
Lead	H^+/H_2	H_2SO_4	-11.3

Table taken from J. O'M. Bockris and A.K.N. Reddy [47].

The relationship between the equilibrium exchange current density and the exchange current is given by the following relationship:

For the anodic half-reaction: $I_a = A_a \cdot i_{o,a}$ (2.20)

For the cathodic half-reaction: $I_c = A_c \cdot i_{o,c}$ (2.21)

For simple systems in which only two half-reactions are coupled, and neither half-reaction is controlled by transport processes, the Butler-Volmer equation applies. This relationship permits the forward and reverse half-reaction currents to be expressed in terms of the half-reaction overpotential and the half-reaction equilibrium exchange currents

$$I_a^f = A_a \cdot i_{o,a} \cdot \exp(-\frac{\vec{\alpha}_a F}{RT} \eta_a) \quad (2.22)$$

$$I_a^r = A_a \cdot i_{o,a} \cdot \exp(\frac{\overleftarrow{\alpha}_a F}{RT} \eta_a) \quad (2.23)$$

Substituting equations (2.22) and (2.23) into (2.15) yields

$$I_a = A_a \cdot i_{o,a} \cdot \left[\exp(\frac{\overleftarrow{\alpha}_a F}{RT} \eta_a) - \exp(-\frac{\vec{\alpha}_a F}{RT} \eta_a)\right] \quad (2.24)$$

The overpotential, or driving force, for each half-reaction is a measure of how far the half-reaction has departed from equilibrium. For the simple system discussed the overpotential for each half-reaction is the difference between the corrosion potential and the half-reaction equilibrium potential.

By definition, the potential imposed on both half-reactions is E_{corr}. Thus, the overpotential can be expressed as:

Anodic half-reaction: $$\eta_a = E_{corr} - E_a^e \quad (2.25)$$

Cathodic half-reaction: $$\eta_c = E_{corr} - E_c^e \quad (2.26)$$

A simplifying assumption is made that all the transfer coefficients are equal to 0.5.

$$\overleftarrow{\alpha}_c = \overrightarrow{\alpha}_c = \overleftarrow{\alpha}_a = \overrightarrow{\alpha}_a = 0.5 \quad (2.27)$$

Combining equations (2.24), (2.25) and (2.27) gives:

$$I_a = A_a \cdot i_{o,a} \left[\exp\left(\frac{F}{2RT}(E_{corr} - E_a^e)\right) - \exp\left(\frac{F}{2RT}(E_a^e - E_{corr})\right)\right] \quad (2.28)$$

Combining equation (2.28) with the equivalent equation for the cathodic half-reaction in equation (2.18) gives:

$$E_{corr} = \frac{RT}{F} \cdot \ln\left[\frac{A_a \cdot i_{o,a} \cdot \exp\left(\frac{FE_a^e}{2RT}\right) + A_c \cdot i_{o,c} \cdot \exp\left(\frac{FE_c^e}{2RT}\right)}{A_a \cdot i_{o,a} \cdot \exp\left(-\frac{FE_a^e}{2RT}\right) + A_c \cdot i_{o,c} \cdot \exp\left(-\frac{FE_c^e}{2RT}\right)}\right] \quad (2.29)$$

Consider

$$A_a \cdot i_{o,a} \gg A_c \cdot i_{o,c} \quad (2.30)$$

Evaluating equation (2.29) for this condition reveals that:

$$E_{corr} \backsim E_a^e \tag{2.31}$$

Similarly, when

$$A_c \cdot i_{o,c} >> A_a \cdot i_{o,a} \tag{2.32}$$

$$E_{corr} \backsim E_c^e \tag{2.33}$$

It can be seen that the relative magnitudes of the anodic and cathodic equilibrium exchange currents determine whether the corrosion potential adopts a value closer to the anodic or cathodic half-reaction equilibrium potential. Throughout the course of a dissolution process the values of A_a and A_c can change, thereby causing the corrosion potential to change. During the autoreductive dissolution of a magnetite film

Anodic Half-reaction: $Fe(0) \rightleftharpoons Fe(II) + 2e^-$ (2.34)

Cathodic Half-reaction: $Fe_3O_4 + 8H^+ + 2e^- \rightleftharpoons 3Fe(II) + 4H_2O$ (2.35)

The area of oxide available for dissolution will progressively diminish and that of the metal will rise as the oxide is dissolved. In this way, it can be seen that initially $A_c >> A_a$ and $E_{corr} \backsim E_c^e$; however, when near complete oxide dissolution has occurred $A_a >> A_c$ and therefore

$E_{corr} \backsim E_a^e$. These statements only remain true as long as no alternative half-reactions commence.

NOMENCLATURE

I_c	Net current for the cathodic half-reaction	(A)
I_a	Net current for the anodic half-reaction	(A)
I_c^f	Forward current cathodic half-reaction	(A)
I_c^r	Reverse current cathodic half-reaction	(A)
I_a^f	Forward current anodic half-reaction	(A)
I_a^r	Reverse current anodic half-reaction	(A)
I_{corr}	Corrosion current	(A)
A_c	Area available to cathodic half-reaction	(m^2)
A_a	Area available to anodic half-reaction	(m^2)
$i_{o,c}$	Equilibrium exchange-current density cathodic half-reaction	($A \cdot m^{-2}$)
$i_{o,a}$	Equilibrium exchange-current density anodic half-reaction	($A \cdot m^{-2}$)
$I_{o,c}$	Equilibrium exchange-current of cathodic half-reaction	(A)
$I_{o,a}$	Equilibrium exchange-current of anodic half-reaction	(A)
$\vec{\alpha}_c$	Forward transfer coefficient of cathodic half-reaction	(Dimensionless)
$\overleftarrow{\alpha}_c$	Reverse transfer coefficient of cathodic half-reaction	(Dimensionless)
$\vec{\alpha}_a$	Forward transfer coefficient of anodic half-reaction	(Dimensionless)

$\overleftarrow{\alpha}_a$	Reverse transfer coefficient of anodic half-reaction	(Dimensionless)
η_c	Overpotential for the cathodic half-reaction	(V)
η_a	Overpotential for the anodic half-reaction	(V)
E_{corr}	Corrosion potential	(V)
R	Gas constant	$(J \cdot mol^{-1} \cdot K^{-1})$
T	Absolute temperature	(K)
F	Faraday constant	$(C \cdot mol^{-1})$

2.7 THERMODYNAMICS

The Nernst equation is derived from basic thermodynamic principals, and expresses, in electrochemical terms, the relationship between equilibrium reactant activities and the reaction electromotive force (emf). Commonly, concentrations are substituted for activities. Therefore, for the reaction

$$Fe(III) + e^- \rightleftharpoons Fe(II) \qquad (2.36)$$

The Nernst relationship is

$$E = E^o + \frac{RT}{nF} \ln\left[\frac{[Fe(III)]}{[Fe(II)]}\right] \qquad (2.37)$$

Similarly, for the reaction

$$Fe_3O_4 + 8H^+ + 2e^- \rightleftharpoons 3Fe(II) + 4H_2O \qquad (2.38)$$

the Nernst relationship is (assuming that the activity of solids is unity)

$$E = E^{o} + \frac{RT}{nF} \ln \left[\frac{[H^{+}]^{8}}{[Fe(II)]^{3}} \right] \qquad (2.39)$$

$$E = E^{o} - \frac{3RT}{nF} \cdot \ln[Fe(II)] - \frac{8RT}{nF} \cdot (2.303) \cdot (pH) \qquad (2.40)$$

where

E	= Measured half-reaction equilibrium potential
E^{o}	= Standard half-reaction equilibrium potential
R	= Gas constant
T	= Absolute temperature
n	= electrons per molecule oxidized or reduced
F	= Faraday constant
$[Fe(III)]$	= Ferric ion concentration
$[Fe(II)]$	= Ferrous ion concentration
$[H^{+}]$	= Hydrogen ion concentration

It is important to emphasize that the Nernst relationship is only applicable to equilibrated systems.

Pourbaix diagrams are a convenient vehicle for expressing thermodynamic data in electrochemical terms. These diagrams have a pH and a potential axes, and for a given system in graphical fashion present solubility, stability and redox equilibrium data.

Figure 5 is taken from "Atlas of Electrochemical Equilibria in Aqueous Solutions", by M. Pourbaix [48].

It should be noted that unless specific solution species concentrations are given on the figure, concentrations are assumed to be 1×10^{-6} mol·dm^{-3}. The addition of a strong complexing agent to such a system would unquestionably influence equilibria involving solution species. In the presence of $EDTA^{4-}$ the ferric ion complex is thermodynamically favoured by comparison to the ferrous complex. Hence, the solution equilibrium potential for the Fe(II)/Fe(III) redox pair, equation 4', would be shifted significantly in the cathodic or negative direction.

Inspection of Figure 5 indicates that the stability regions for magnetite and aqueous ferric ion do not adjoin. To proceed from one zone to the other necessitates movement through either the region of stability for Fe_2O_3 or solution ferrous ion. This strongly suggests that there is no facile reaction pathway from magnetite to solution ferric ion species. On the basis of the thermodynamic data, it appears that dissolution of magnetite as ferrous ion appears to offer the most facile mechanism, necessitating reductive dissolution.

CHAPTER 3

PHYSICAL AND STRUCTURAL PROPERTIES OF OXIDES

3.1 INTRODUCTION

Both the chemical and structural properties of oxides determine their dissolution behaviour. This chapter outlines some of the important structural characteristics of magnetite and related oxides.

Both electron and ion mobilities within oxides can significantly affect their chemical and physical properties. Magnetite has long been recognized as a near-metallic semiconductor, and studies of iron oxides suggest that the cationic mobility within cubic close-packed iron oxides is also considerable.

The principal oxide found on the steel surfaces within CANDU primary coolant circuits is magnetite. A significant part of the radioactivity associated with these films originates from radioactive transition metal cations that substitutionally displace iron cations within the magnetite lattice. Low levels of substituent transition metal cations in magnetite cause significant changes in the oxide's electrophysical properties. The manner in which the physical and electrophysical properties of magnetite, and related oxides, affect dissolution behaviour is discussed in the following chapter.

The evidence presented in this chapter outlines how some of the physical and electrophysical properties of iron and spinel type oxides arise from structural characteristics. Also, it appears that many of the apparent inconsistencies in oxide behaviour are attributable to uncontrolled structural variations introduced during oxide preparation. The preparative process that seems to be of primary importance in determining oxide characteristics is annealing, the major variations in behaviour occurring between annealed and nonannealed oxides.

3.2 GENERAL OXIDE PROPERTIES

FeO, Fe_3O_4 (magnetite) and γ-Fe_2O_3 (maghemite) all exhibit cubic close-packing of oxide ions. Only hematite (α-Fe_2O_3) differs, possessing a hexagonal close-packed structure. A magnetite unit cell consists of 32 oxide anions, containing a total of 64 tetrahedral and 32 octahedral holes. However, the number of equivalent octahedral and equivalent tetrahedral sites are 8 and 16, respectively. In stoichiometric magnetite, the 8 equivalent tetrahedral holes and 8 equivalent octahedral holes are occupied by ferric ions, while the ferrous ions occupy the remaining 8 equivalent octahedral holes.

The close structural relationship between magnetite and maghemite is demonstrated by the observed ease of interconversion, Sidhu et al. [49] and Wells [50]. This relationship is further demonstrated by studies with FeO. This oxide is normally nonstoichiometric, the

compound displaying a temperature dependent iron deficiency. This permits FeO samples of various stoichiometries to be produced. X-ray diffraction studies reveal that an approximately straight-line relationship exists between the unit cell dimension and the composition expressed as the Fe:O ratio. Extrapolation of this relationship to the compositions of Fe_3O_4 and γ-Fe_2O_3 provides values for the unit cell dimension of these compounds that is in good agreement with the experimentally determined values.

This relationship can be given physical significance using the following model. The crystallographic anion unit cell of magnetite has a total of 32 octahedral sites. When all of these sites are filled with ferrous ions stoichiometric FeO is obtained. Replacement of a small fraction (n) of the Fe(II) ions with 0.67n Fe(III) ions would retain charge neutrality and yield nonstoichiometric FeO. Further replacement of the Fe(II) ions by Fe(III) ions would yield Fe_3O_4 when 24 Fe ions are present, and γ-Fe_2O_3 when 21.33 Fe ions are distributed randomly throughout the octahedral and tetrahedral sites.

This model of an anion lattice in which iron cations exhibit valence exchange and considerable mobility has been used to explain features of iron oxide chemistry. Wells [50] proposes that FeO oxidation occurs by the extension of the cubic close-packed lattice of oxygen atoms. As oxygen atoms are added to the oxide surface Fe ions from the bulk of the oxide migrate to the surface. This leads to a diminished iron concentration in the bulk of the oxide, Fe(II)

oxidations in the bulk oxide and subsequent electron migration to the surface maintaining overall charge neutrality throughout the structure. The work of Sidhu et al. [49] provides strong experimental evidence that such a mechanism is active during the oxidation of magnetite (Fe_3O_4) to maghemite (γ-Fe_2O_3) at 190°C.

3.3 PROPERTIES OF MIXED-VALENCE COMPOUNDS

Magnetite (Fe_3O_4) is a mixed-valence compound according to the definition of Robin and Day [51]. Such compounds contain ions of the same element in two different formal oxidation states. Robin and Day divided mixed-valence compounds into four classes on the basis of physical properties, demonstrating that the extent of electron delocalization between the metal ions was the principal source of the behavioural differences.

The barrier to electron transfer between different metal ions in a mixed valence compound will be large if (i) the two ions are of different elements, (ii) the coordination geometry of the two sites differ, or (iii) the ligands at the two sites differ. When the energy barrier to electron exchange is low, the electron can freely move between ions. On this basis rapid electron exchange between the octahedrally coordinated ferrous and ferric ions in magnetite would be anticipated. Mössbauer studies, Bauminger et al. [52] and Evans et al. [53] reveal that the octahedral ions formally designated as Fe(II) and Fe(III) ions are indistinguishable at 300 K, indicating that valence

oscillation occurs at a rate $> 10^8\ s^{-1}$. Although the exact mechanism of conduction in magnetite remains unresolved [54], the valence exchange process contributes very significantly to the conductivity at ambient temperatures.

Although the normal spinel Fe_3O_4 has never been prepared it is valuable to consider the properties such a compound would possess. All the ferric ions in such a compound would be octahedrally coordinated and all the ferrous ions tetrahedrally coordinated. Thus, a considerable barrier would exist to electron transfer between ferric and ferrous ions by virtue of their different coordination environments. The compound would exhibit trapped valences, and would have physical properties significantly different from magnetite.

3.4 STRUCTURE OF SPINELS

A crystallographic unit cell of a spinel, dimension ~ 8.6 Å, contains 32 approximately cubic close-packed oxygen ions. Two types of cation sites are available, 8 equivalent tetrahedrally coordinated and 16 equivalent octahedrally coordinated sites.

The nature of a spinel, AB_2O_4, can be described by the parameter Ω, the fraction of B atoms in tetrahedral holes, Table 3.1.

Table 3.1

Cation Distributions in Spinels $[A(II)B(III)_2O_4]$

Spinel	Ω	Octahedral Sites	Tetrahedral Sites
Normal	0	All B ions	All A ions
Inverse	1/2	1/2 B ions and all A ions	1/2 B ions
Random	1/3	2/3 B ions and 2/3 A ions	1/3 B ions and 1/3 A ions

The normal spinel arrangement is energetically favoured due to the fact that the more highly charged trivalent cations are octahedrally coordinated, while the lower charged divalent cations occupy the tetrahedral sites. The difference in energy between the normal and inverse type structures is not great, crystal field effects being sufficient to cause changes in the preferred structure.

The prediction of whether a particular spinel will adopt the normal or inverse structure is one of the successes of the Crystal Field Theory, Huheey [55] and Blasse [56]. For each of the two metal ions comprising the spinel, the CFT can predict in semi-quantitative fashion the relative stabilities of that ion in tetrahedral and octahedral sites. Thus, for each ion an Octahedral Site Stabilization Energy (OSSE) can be estimated. The values for each ion, when combined, give a quite reliable method of predicting the spinel's structure.

The anions in a spinel oxide provide a weak crystal field. Hence, ions such as Ni(II)(d^8) and Fe(III)(d^5) adopt high spin configurations. Therefore, the Fe(III)(d^5) ion provides no crystal field stabilization energy (CFSE) in either tetrahedral or octahedral sites. The OSSE is zero. The Fe(II)(d^6) ion exhibits a small OSSE, which appears to be sufficient in the case of Fe_3O_4 to allow the adoption of an inverse rather than normal structure.

For nickel ferrite ($NiFe_2O_4$) the OSSE energy of the high spin Ni(II)(d^8) ion dictates that the inverse structure is adopted. All chromites (MCr_2O_4) have a normal structure by virtue of the large positive OSSE displayed by the high spin Cr(III)(d^3) ion.

3.5 STRUCTURE OF FERRITES

One subclass of spinels is the ferrites that have the empirical formula MFe_2O_4, where M is commonly a transition metal cation. The majority of ferrites have the inverse spinel structure, which in part is due to Fe(III) ions having zero stabilization energy for the octahedral sites. The only normal, or approximately normal, ferrites are those of Zn(II) and Mn(II). Both of these ions also exhibit zero octahedral site stabilization energy.

There are a number of orderly superstructures that spinels can adopt, such that for example 8A+8B ions or 4A+12B ions consistently occupy the octahedral sites. Large differences in the ionic charge

favour the ordering of cations. A similar ordering is observed for cation vacancies. Increases in temperature tend to promote crystallographic disorder. Thus, as magnetite or other spinels are heated, a number of distinct transition temperatures are observed at which various levels of order are lost. For example, in Fe_3O_4 ordering of the octahedrally located Fe(II) and Fe(III) ions occurs below 120 K, while above this temperature a random arrangement exists. With this adoption of a random arrangement comes much greater electron mobility, as demonstrated by a dramatic rise in conductivity at this temperature. This is known as the Verwey transition, Verwey and Haaymann [57].

Waltz and Rivas [58] performed detailed studies of the crystallographic changes caused by a variation of temperature for manganese ferrites. Following the magnetic properties of the ferrite through the temperature range 80 to 530 K indicated that five relaxations occurred. Neutron diffraction studies [59,60] of manganese ferrites indicate that such compounds contain a significant number of cation vacancies. Electrophysical properties in particular are sensitive to the cation vacancy concentration. These studies clearly suggest that spinel composition is more truthfully represented by the empirical formula of the form:

$$\square_{\Delta}M_xFe_{3-x-\Delta}O_4 \qquad (3.1)$$

where M is a substituent cation, and $\square$ is a cation vacancy. These studies indicate that, as the value of x for manganese ferrites is

raised from 0 to 3, the spinel undergoes a gradual change from an inverse to a normal structure. Thus, at any intermediate value of x the following empirical formula describes the distribution of ions and vacancies:

$$(\square_{\Gamma}Mn(II)_{y-\Gamma}Fe(III)_{1-y})\ [\square_{\theta}Fe(II)_{1-y-t-\theta}Fe(III)_{1+y-s}Mn(III)_{s}Mn(II)_{t}]O_4 \qquad (3.2)$$

Tetrahedrally Coordinated Octahedrally Coordinated

where

Γ = cation vacancy concentration tetrahedral sites

θ = cation vacancy concentration octahedral sites.

In this spinel, electron exchange can occur between octahedrally coordinated iron and manganese ions.

$$Mn(II)Fe(III) \rightleftharpoons Mn(III)Fe(II) \quad . \qquad (3.3)$$

Unlike magnetite, and as a consequence of the pair being composed of ions of different elements, one of these pairs is energetically favoured. The Mn(III)-Fe(II) pair is more stable than the Mn(II)-Fe(III) pair due to the operation of Jahn-Teller effects. The five relaxations observed for this spinel are due to the formation of tightly bound Mn(III)-Fe(II) octahedral pairs and by the long range diffusion of Mn(II) ions via octahedral-site vacancies, this latter effect growing in significance as the vacancy concentration rises.

Marshall et al. [61] studied the distribution of ferric and ferrous ions with the quaternary Fe(II)-Fe(III)-Zn(II)-Cr(III) spinel solid solution series. It was found that octahedral site ferrous-ferric charge hopping may be the most important phenomenon stabilizing the inverse ion distribution.

The distribution of cations in a spinel can be influenced by thermal history. For instance, $NiMn_2O_4$ when slowly cooled from high temperatures gives $\Omega = 0.47$, but when quenched $\Omega = 0.37$.

3.6 ELECTRONIC CONDUCTIVITY

The electronic conduction mechanism and electrical properties of ferrites are incompletely understood [62]. Many parameters influence ferrite conductivity, including chemical components, component concentrations, preparation, thermal history, temperature, and cation vacancy concentrations.

The conductivities of various oxides are given in Table 3.2, with the generally recognized conductivity ranges for metals, semiconductors and insulators. It can be seen that magnetite is a highly conductive semiconductor.

Table 3.2

Oxide Conductivities at Room Temperature

Substance	Conductivity ($\Omega^{-1}cm^{-1}$)	Reference
Magnetite Fe_3O_4	$10-10^2$	62,63
Nickel Ferrite $NiFe_2O_4$	1-10	62,63
Cobaltites MCo_2O_4	$10^{-4}-10^{-2}$	28
Simple Oxides MnO, NiO, Co_2O_3	$10^{-6}-10^{-4}$	28
Typical Metals Cu, Fe	10^4-10^6	47
Semiconductors Si, Ge	$10^{-9}-10^2$	47
Insulators	$10^{-22}-10^{-10}$	47

Rivas et al. [63] prepared a series of ferrites using a preparative method that yielded ferrites possessing consistent cation vacancy concentrations and morphologies. Consequently, the results listed in Table 3.3 indicate the effect of chemical composition upon ferrite conductivity.

Table 3.3

Ferrite Conductivity as a Function of Composition [63]

Spinel	Conductivity at Room Temperature ($\Omega^{-1}cm^{-1}$)
Fe_3O_4	3.6
$Mn_{0.6}Fe_{2.4}O_4$	1.4
$Ni_{0.8}Fe_{2.2}O_4$	0.4
$Co_{0.6}Fe_{2.4}O_4$	0.05

The results clearly indicate that the chemical composition of otherwise similar ferrites significantly influences electrophysical behaviour.

Whall et al. [62] measured the conductivities of a series of nickel ferrites and magnetite single crystals. The conductivity of magnetite remained constant at $\sim$ 300 $\Omega^{-1}cm^{-1}$ in the temperature range 300 to 1150 K. The ferrite conductivity progressively declined as the nickel concentration increased. At 300 K the conductivity of $Ni_{0.9}Fe_{2.1}O_4$ was 0.2 $\Omega^{-1}cm^{-1}$, the conductivity increasing as the temperature increased achieving a value of 10 $\Omega^{-1}cm^{-1}$ at 1000 K.

The method of spinel preparation significantly influences conductivity. While the results of Whall et al. [62] and Rivas et al. [63] are in good agreement for nickel ferrite, the conductivities reported for magnetite are two orders of magnitude apart.

The work of Street [64] also demonstrated that both oxide morphology and oxide thermal history significantly influence physical properties.

Kovtun et al. [54] proposed that the electrons exchanging between octahedral ferrous and ferric ions are pair-localized, and are not free to migrate from one ion to another throughout the whole crystal. This exchange pair model provides an explanation for the observed n-type semiconductivity of magnetite. Crystal field theory indicates that the high spin Fe(II)(d^6) ion has a larger CFSE than the

Fe(III)(d^5) ion when octahedrally coordinated. As the Fe(III)(d^5) ion is stabilized with respect to the Fe(II)(d^6) ion, the ion pair should behave as a negative charge carrier.

Kovtun et al. [54] used the exchange pair model to explain why $Co_{1-\partial}(Fe_{2+\partial})O_4$ displays n-type semiconductivity when $\partial > 0$ and p-type semiconductivity when $\partial < 0$. When $\partial < 0$ exchange pairs of Co(II)(d^7) and Co(III)(d^6) ions are present in octahedral sites. The Co(II)(d^7) ion has the higher CFSE in octahedral environments, and hence the exchange pair carries a positive charge and the spinel displays p-type semiconductivity. When $\partial > 0$ exchange pairs of Fe(II)(d^6) and Fe(III)(d^5) ions are present in octahedral sites, and therefore n-type semiconductivity is displayed. At $\partial = 0$ no exchange pairs are present, and on this basis the conductivity should display a minimum at $\partial = 0$. This is confirmed by the work of Jonker [65].

These studies indicate that small changes in chemical composition can produce disproportionally large changes in the electrophysical properties of spinel oxides. The identity of the substituent cation is clearly important in determining oxide electrophysical properties. It appears that one of the most significant characteristics of the substituent cation is the ion's ability to establish a valence exchange pair with iron cations. To do so the substituent cation must exhibit at least two relatively stable oxidation states within a cubic close-packed oxide lattice.

3.7 VACANCY CONCENTRATION AND IONIC MOBILITY

Ionic motion by hopping between empty lattice sites was first proposed by Verwey [66] following work with the spinel, γ-alumina. This model indicates that increased cation mobility would be anticipated within magnetite, as this compound departs from stoichiometry as a consequence of an increasing cation vacancy concentration.

Tarasevich and Efremov [28] state that the electrical conductivity of semiconductors depends upon the concentrations of free electrons and holes or vacancies. In hole-type or p-type semiconductors the band theory indicates that the electrical conductivity of a substance should increase with the increasing stoichiometric excess of oxygen. Such behaviour is observed for the p-type semiconductor spinel Co_3O_4, Shub et al. [67]. Therefore, most metal oxides exhibit minimum conductivity when stoichiometric, Rosencwaig [68]. However, Verwey and Haaymann [57] found that magnetite displays maximum conductivity at stoichiometry. It appears that adding defects to the magnetite structure only serves to trap valences locally, thereby increasing the barrier to electron transfer and hence decreasing electrical conductivity.

It appears that magnetite is unusual in that the introduction of cation vacancies causes the iron ion mobility to increase and the electronic conductivity to decrease. Consequently, the electrophysical

and electrochemical behaviour of stoichiometric and nonstoichiometric magnetite could differ significantly for this reason.

Sidhu et al. [66] determined the diffusion coefficient for iron in magnetite at 190°C. The value obtained, $\sim 2 \times 10^{-15}$ $cm^2 s^{-1}$, is twelve orders of magnitude less than that reported by Gallagher et al. [69]. Part of this large disparity appears to originate from the non-stoichiometry of the magnetite used. The Fe(II):Fe(III) ion ratio in the magnetites produced by Gallagher et al. and Sidhu et al. were 0.33 and $\sim$ 0.44, respectively, the value for stoichiometric magnetite being 0.5. In both instances, the structure was confirmed by X-ray diffraction. The greater the departure from stoichiometry the larger the concentration of cation vacancies and, therefore, the greater the cation mobility. Thus, the correlation between stoichiometry and ion mobility is as anticipated, only the magnitude of the difference being surprising.

The cation vacancy concentration in spinel oxides can be varied in a well-defined manner by adjusting the partial pressure of oxygen present during high temperature sintering, Kronmüller et al. [70]. It is possible that variations in the conductivities reported for magnetite arise, at least in part, from uncontrolled variations in cation vacancy concentrations caused during oxide preparation.

3.8 PREPARATIVE METHODS

Studies of oxide properties have been performed on materials produced by a considerable variety of techniques. Oxide properties are strongly influenced by the method of preparation. The following techniques have been applied to the formation of iron oxides and mixed metal spinel oxides. All the techniques used fall into two general categories; (i) high temperature sintering/calcining processes, and (ii) low temperature precipitation processes. The principal difference between the techniques is the maximum temperature achieved during preparation, being > 800°C and < 105°C, respectively.

3.8.1 High Temperature Oxide Preparations

Ceramic techniques are commonly used in which the metal components of the desired mixed metal spinel are combined as oxides in quantities corresponding to the desired stoichiometry. The mixture of oxides is normally milled for extended periods to promote homogenity and then subjected to prolonged high-temperature calcination, normally at temperatures in the range 1000 to 1400°C. A modification of this technique involves the coprecipitation of hydroxides or oxalates from solutions containing the appropriate mixture of metal salts. This process has the advantage that homogeneous mixed precipitates are obtained. This initial step is followed by drying and sintering as outlined above.

High temperature sintering processes yield oxides with low specific areas. The nickel ferrites produced by Segal and Sellers [21,38] had surface areas of < 0.04-1.2 $m^2 g^{-1}$, for particles < 50 to > 300 μm in size. For oxides produced at temperatures of 1400°C, the surface areas determined by nitrogen absorption techniques are only slightly greater than the calculated geometric values. It was observed that decreasing the calcining temperature to 1000°C caused a 10-fold increase in surface area.

Jones et al. [71] performed a detailed investigation of the impact of calcining temperature upon oxide surface area using nickel oxide. The oxide was prepared initially by a low temperature precipitation process to yield a product of high surface area, 99 $m^2 g^{-1}$. The surface area was reduced by an order of magnitude by sintering at 550°C, by a further order of magnitude at 900°C, and finally a surface area of 0.4 $m^2 g^{-1}$ was achieved following sintering at 1450°C. Similar results were obtained by Kametani et al. [72] for hematite. The dried, uncalcined oxide from an aqueous precipitation process had a surface area of 10 $m^2 g^{-1}$. This was reduced three orders of magnitude by sintering at 800°C.

3.8.2 Low Temperature Oxide Preparations

The hematite hydrosols used by Matijević et al. [16,17,73,74] were produced by aging dilute and aqueous solutions of ferric chloride at 100-105°C for 24-28 h. The hydrosols were repeatedly washed to

remove chloride and ferric ions. The average diameter of the particles produced was 0.09-0.10 μm. The particles themselves were composed of much smaller uniform, defect free, crystallites. The surface area of the hematite produced varied considerably between runs, ranging from 11.9-30 $m^2 g^{-1}$.

Matijević et al. [35] produced colloidal dispersions of β-FeOOH by the method described previously, with the modification that the ferric chloride solution was more concentrated. The β-FeOOH particles were rod-like, with a length of 1 μm and a surface area of 10.4 $m^2 g^{-1}$.

Regazzoni and Matijević [36] produced nickel ferrites by a process similar to that described above. Mixed nickel and ferrous hydroxides were precipitated by the addition of sodium hydroxide to an acid solution containing ferrous and nickel salts in a molar ratio of 2:1. Aging of this gel at 99°C for 4 hours yielded spherical ferrite particles with a modal diameter of 0.1±0.02 μm, and composition $Ni_{0.53}Fe_{2.47}O_4$.

Sidhu et al. [75] prepared a number of substituted magnetites using a coprecipitation process developed by David and Welch [76] and similar to that used by Matijević et al. [77,78]. The magnetite crystal growth process being followed by X-ray diffraction, no product other than magnetite was detected at any point in the crystal growth process. The crystal diameters were in the range 0.03-0.04 μm, with a surface

area varying between 9-21 $m^2 g^{-1}$. It is interesting to note that the magnetite produced by this method had an iron content lower than for stoichiometric magnetite. This was attributed to strongly adsorbed water. Also, the Fe(II):Fe(III) ratio, determined by solution analysis, was consistently less than the theoretical value of 0.5, typically having a value of 0.44. Dissolution of magnetite containing other transition metals at trace levels indicated that, for Co, Ni and Zn, the dopants were distributed homogeneously throughout the spinel, whereas for Cu, Mn and Cd the dopants were concentrated at the surface of the particles.

Baumgartner et al. [24,39], Blesa et al. [79,80] and Bruyère et al. [14], using a slight modification of Matijević's method, produced magnetite particles with an average diameter of $\sim$ 0.2 μm and a specific surface area $\sim$ 10 $m^2 g^{-1}$. In each case Mossbauer, X-ray diffraction and scanning electron microscope studies indicated the formation of high purity, highly crystalline particles that were either stoichiometric or nearly-stoichiometric.

Buxton and Rhodes [37,81] used Matijević's method to produce hematite and magnetite with the modification that the aging process was extended to two weeks. The average particle diameter was 0.8 μm for magnetite and 0.45-1.5 μm for hematite. Particle clustering was observed for hematite.

The two types of preparative method produce oxides that possess significantly different physical and chemical properties. Studies have indicated differences in the following characteristics: specific surface area, morphology, particle size, defect concentration, vacancy concentration, stoichiometry, homogenity, ionic conductivity and electronic conductivity. Such variations most probably account for major disparities between several studies of nickel ferrite dissolution behaviour.

CHAPTER 4

THE INTERDEPENDENCE OF OXIDE PROPERTIES AND DISSOLUTION BEHAVIOUR

4.1 INTRODUCTION

This chapter examines how the chemical, structural, physical and electrophysical properties of oxides effect dissolution behaviour. Additionally, consideration is given to the manner in which all these properties are changed by dissolution due to the operation of processes such as: incongruent dissolution, anisotropic dissolution, particle fragmentation and ion exchange processes.

This complex interdependence of oxide properties and dissolution behaviour makes the investigation of dissolution processes difficult. In particular, complex mixed-metal spinel oxides can display many forms of incongruency during dissolution, causing the oxide to change significantly throughout the dissolution process.

Work from a variety of scientific fields contribute to the understanding of oxide dissolution processes including: colloidal and interfacial science, surface science, electrochemistry, solid state chemistry and solution chemistry. Insights into the dependence of oxide dissolution behaviour on oxide properties comes principally from two areas of study. Kinetic studies of oxide dissolution processes involving the dissolution of discrete oxide particles in aqueous

suspension, and various electrochemical investigations of oxide and oxide film electrodes that include relatively infrequent study of dissolution behaviour.

4.2 MORPHOLOGY

4.2.1 Introduction

Many aspects of oxide morphology affect dissolution processes including: (i) specific surface area; (ii) grain size and structure; (iii) dislocation density; (iv) anisotropic reactivity; and (v) oxide topography.

Oxide films can be composed of multiple layers, each layer possessing different properties. The morphology of oxide films can be influenced by the structure and morphology of the substrate metal.

4.2.2 Specific Surface Area

Unless transport processes are rate controlling, the rate of a dissolution process should be proportional to the instantaneous surface area of the solid. For the simple case of uniform spherical particles undergoing dissolution, the form of the iron release rate dependence on time is readily calculable. This simple shrinking core model has been

used successfully to interpret oxide dissolution kinetics, Segal and Sellers [21], and Baumgartner et al. [39]. Such a model predicts a progressively declining reaction rate with time.

The specific surface area of an oxide was shown to be strongly dependent upon preparative method, principally the annealing temperature. The range of specific surface areas observed for spinel oxides was from < 0.04 to 20 $m^2 g^{-1}$, approximately three orders of magnitude variation. For example, Bradbury [11], when investigating the dissolution of hematite in oxalic acid, found that the rate of dissolution of uncalcined hematite was 100 times greater than for calcined hematite. The principal cause appeared to be changes in specific surface area.

4.2.3 Grain Size and Structure

Hematite (α-Fe_2O_3) dissolution was studied by Azuma and Kametani [10], and they observed a progressively rising reaction rate throughout the dissolution process that was attributed to particle fragmentation.

Eisenlauer and Matijević [73] studied the dissolution of hematite (α-Fe_2O_3) sols with an average particle diameter of 94 nm. X-ray diffraction studies revealed that these particles were paracrystalline, consisting of much smaller uniform, defect-free globular crystallites.

It is probable that both the grain structure and intergranular adhesion within individual crystallites influences dissolution behaviour. Additionally, crystallite size and intercrystallite adhesion also appear significant, particularly in dissolution processes involving particle fragmentation.

4.2.4 Dislocation Density

Within the confines of single grains, crystallographic imperfections called dislocations occur, two common types being screw and edge dislocations. When dislocations emerge on the surface of a crystal, sites of enhanced reactivity are often created. The number of such dislocations can often be determined by surface examination following etching. For metals the density of dislocations ranges from $10\ cm^{-2}$ to $10^{12}\ cm^{-2}$. The significance of dislocations during oxide dissolution process has not been examined in depth. However, the study of magnetite dissolution in tris-(picolinato) vanadium(II) by Allen, Sellers and Tucker [82] revealed that regular pits were produced by attack at screw dislocations.

4.2.5 Anisotropic Dissolution

Warren et al. [4] observed anisotropic dissolution of hematite (α-Fe_2O_3) in hydrochloric acid. The dissolution rates of five different crystal planes were studied. The iron release rate in each case was constant, but different for different faces, varying by over an order of

magnitude. Following partial dissolution, single crystals featured well defined facets characteristic of anisotropic dissolution.

Warren et al. [4,7] found that the degree of anisotropy exhibited during the dissolution of hematite (α-Fe_2O_3) was related to the anion present. Anisotropic dissolution occurred in HCl, but in $HClO_4$ a much slower and isotropic dissolution process was observed. Warren and Roach [5] proposed that anisotropic dissolution can lead to the fragmentation of oxide particles. This break-up of oxide particles is proposed as an explanation for oxide dissolutions that exhibit progressively rising rates.

The development of crystal facets during a dissolution process is an indication that a chemical dissolution step is rate controlling. In this situation the dissolution process for each crystal face proceeds at its chemically determined limit. Thus, differences in crystal plane reactivities are reflected in the relative rates, causing the development of facets due to anisotropic dissolution. When a transport process is rate controlling dissolution from all crystal planes is retarded to a common rate, and no development of facets occurs.

4.2.6 Oxide Topography

The pitting of metals has been extensively studied by Vetter and Strehblow [83]. It has been proposed that the nucleation of pits can occur at grain boundaries, surface scratches and inclusions. Little

work has been done to study such local dissolution processes during oxide dissolutions. However, the study of magnetite dissolution in tris-(picolinato) vanadium(II) by Allen et al. [82] observed the formation of deep fissures that appeared to commence at crystal discontinuities or scratches.

The topography of both oxides and oxide films has a significant impact on dissolution behaviour. For porous oxide films the solution composition within the oxide pores can depart significantly from that of the bulk solution. The confined geometry of the pore severely restricts transport between the pore solution and the solution bulk, so that frequently reaction rates within a pore are transport limited. These local chemistry changes can produce both locally enhanced and retarded dissolution processes.

The impact of film morphology on dissolution processes has been studied in detail using alumina films on aluminum. It is generally recognized, Diggle [1], that porous alumina films formed on aluminum contain two morphological forms of alumina. There exists a thin, barrier-type oxide film adjacent to the metal, over which lies a much thicker porous oxide film.

The pore structure can be approximated to that of a cylinder. Therefore, two distinct sites exist within a pore; the pore walls and pore base. The pore terminates at the barrier-type oxide. Since the barrier layer contains the electrostatic field, the dissolution rates

from the pore base and walls will differ. The dissolution rate from the pore base is described by Diggle [1] as interface potential assisted, while that from the pore walls is termed open-circuit.

The relative areas of pore bases and walls typically differ by more than three orders of magnitude. Studies have indicated that for alumina films the dissolution rates of pore base and pore wall are identical for open-circuit dissolution. In the presence of applied fields the barrier layer dissolution is interface potential assisted, while the pore-wall dissolution is similar to that observed under open-circuit conditions. According to Diggle [1], the time required for the complete dissolution of porous alumina films in sulphuric acid is independent of film thickness. The explanation proposed is that concurrent pore widening and pore shortening occurs, although uncertainty exists as to the exact mechanism of the pore dissolution processes.

4.3 SPINEL OXIDE COMPOSITION

The comparison of oxide dissolution rate data obtained by different workers is frequently of little value. The parameters influencing oxide properties are often inadequately defined. However, for spinel oxides within a single study, a consistent method of oxide preparation gives a reasonable assurance that the observed changes in behaviour can be attributed principally to changes in composition.

Sellers et al. [38] investigated the impact upon dissolution behaviour of changing the identity of the divalent cation in ferrites. Four ferrites, (MFe_2O_4) where M = Co, Fe, Mn and Ni were prepared using an identical method. The dissolution behaviour was investigated in oxalic acid at 140°C. The rates of dissolution displayed a strong dependence upon the identity of the divalent ion. The order of reactivity was found to be Fe > Mn > Co > Ni, the relative rates being 35:9:4:1. The observation that magnetite dissolution occurs more rapidly than other ferrites is consistent with other studies.

It was proposed that, in oxalic acid, the dissolution rate is inversely proportional to the stability of the $M(II)-(C_2O_4)^{2-}$ complex, stable complexes inhibiting dissolution. It was further proposed that the relative solubilities of the $M(II)-(C_2O_4)^{2-}$ complexes also influence the dissolution rate. The former proposal is inconsistent with the frequently observed proportionality between dissolution rate and complexing ability. The dissolution rate dependence on ferrite composition is not completely understood.

Sellers et al. [38] reported that the ferrite dissolution rate dependence on composition observed in oxalic acid was not observed in tris-(picolinato) vanadium(II). Using identical ferrites the rate only varied by a factor of two.

Sellers and Williams [38] investigated the dissolution of a series of nickel chromium ferrites ($Ni_{0.6}Cr_xFe_{2.4-x}O_4$) in oxalic acid at

140°C. The rate of dissolution was found to depend strongly upon chemical composition. As the value of x increased from 0.3 to 1.5, the rate of dissolution decreased by a factor > 10. When the value of x was raised to 2, the rate of dissolution further diminished, insignificant dissolution occurring in 4 hours. The dissolution mechanism occurring was not clearly identified, and it appeared that either direct dissolution or reductive dissolution by oxalic acid could be occurring. Incongruent dissolution was observed, specific leaching of iron and nickel leaving a chromium enriched surface. It was proposed that Cr(III) ions dissolve only after neighbouring ions have been removed by an undercutting mechanism. A similar mechanism was proposed by Segal and Sellers [21] to explain the dissolution behaviour of nickel ferrites.

Sellers and Williams [38] state that unpublished work by Sellers shows that spinel oxide dissolution rates in bis(histidinato) vanadium(II) and tris-(picolinato) vanadium(II) show similar sensitivities to oxide chromium content. Since this dependence is seen for several different reaction mechanisms it is thought that some physical rather than chemical surface characteristic is involved. It is proposed that preferential dissolution of iron leads to an increasing surface concentration of chromium. The high energy sites at which dissolution most readily occurs eventually become blocked by chromium ions, and hence the dissolution process slows.

These studies clearly show that the dissolution behaviour of spinel oxides is significantly effected by chemical composition, and

that the identity of both the divalent and trivalent cations are important. Further, the dissolution rate sensitivity to composition varies as the dissolution mechanism changes.

4.4 CONGRUENCY OF SPINEL OXIDE DISSOLUTION

Congruent dissolution in this context is taken to mean that the dissolution of each cation within a complex oxide proceeds such that the relative rates are in proportion to the stoichiometry of the oxide.

The congruency of dissolution processes can be studied either by following the release of cations to solution or by surface analysis of the oxide following partial dissolution. Determining the relative reactivities of cations of different elemental origin is relatively simple. However, magnetite, and most ferrites, contain both Fe(II) and Fe(III) ions and determining the relative reactivities of these ions is more difficult. The major problem is the ease of Fe(II) oxidation, so that either the post dissolution solution rates or the post dissolution surface composition is distorted prior to analysis. A further complexity introduced by spinel oxide chemistry is that a substance can feature a common cation, Fe(III) ions in magnetite, in crystallographically distinct sites. The study of the relative reactivities of these sites is a demanding task.

The studies discussed initially are concerned with the congruency of mixed metal spinel oxides, principally nickel ferrite.

These studies indicate that incongruent dissolution between the different cations is observed, and that the form of this incongruency varies as both solution and oxide characteristics change. The latter part of this discussion is concerned with attempts to determine the relative reactivities of the cations in magnetite. These studies demonstrate the difficulty of performing such investigations both experimentally and in the interpretation of the results.

The dissolution of nickel ferrite in tris-(picolinato) vanadium(II) was studied by Segal and Sellers [21]. The work revealed an initially incongruent dissolution process. The solution iron:nickel ratio initially greatly exceeded the shoichiometric value of 2, indicating that in the early stages of dissolution preferential dissolution of iron occurred. This effect was short-lived, the solution metal ratio rapidly returning to a value of 2. The nickel ferrite used for these studies was stoichiometric ($NiFe_2O_4$) produced by a high temperature calcination of coprecipitated metal hydroxides.

In contrast to the behaviour observed by Segal and Sellers [21], a study of nickel ferrite dissolution by Regazzoni and Matijević [36] detected an incongruency of markedly different form. They studied the dissolution of a non-stoichiometric nickel ferrite ($Ni_{0.53}Fe_{2.47}O_4$) produced by a low temperature precipitation process. The dissolutions were performed in mildly acidic EDTA solutions at 80°C. Both the iron and nickel release rates were observed to rise throughout the dissolution process. The dissolution was incongruent, the rate of nickel

release being proportionally greater than that for iron throughout the first half of the dissolution process. Approximately 30% of the iron remained as a solid when all the nickel had dissolved. This incongruent dissolution was displayed throughout the pH range 4-10.

It is suggested that the observed incongruent dissolution arises from inhomogeneities in the ferrite, which is composed of a nickel-rich outer layer and a nickel-depleted core.

Kishi, Shimizu and Nagai [25] investigated the dissolution of a nickel ferrite ($Ni_{0.64}Fe_{2.36}O_4$) in acidic sulphate and chloride solutions using electrochemical techniques. The dissolution process was investigated under both open circuit and anodic polarization conditions.

The behaviour observed was complex, distinct differences in behaviour being found between ferrite in the as-made condition and ferrite that had undergone partial dissolution.

When anodic potentials were applied to the as-made ferrite the extent of dissolution observed in 2 hours increased with increasing solution concentrations of both chloride and sulphate. This suggests that under these circumstances the dissolution rate is controlled by a chemical dissolution process that exhibits a rate dependence on the anion concentration. Anodic dissolution of as-made ferrite electrodes. exhibited congruent release of metal to solution at all anion concentrations studied. This behaviour is not observed if this procedure is

preceded by a period of open circuit dissolution, under these circumstances incongruent dissolution is observed. The solution iron:nickel ratio is less than that in the spinel. This disparity in the iron:nickel ion ratios observed in the solid and solution increased as the solution anion concentration increased.

During open circuit dissolution of as-made ferrite electrodes in solutions containing $< 1 \times 10^{-2}$ mol·dm^{-3} sulphate concentrations, the solution cation ratio following 2 hours of dissolution was equal to that in the spinel. Congruent dissolution was not observed when the sulphate concentration was increased, the release of iron remaining approximately constant while the release of nickel increased significantly. At high sulphate concentrations the release of nickel actually exceeded that of iron.

The behaviour of the ferrite in the as-made condition differs significantly from the ferrite following partial dissolution. This could arise either from inhomogeneities present in the as-made ferrite or because the surface composition is charged as a consequence of incongruent dissolution. Anodic polarization appears to inhibit the dissolution of iron relative to nickel. This preferential dissolution of nickel is accentuated by increased solution concentrations of both sulphate and chloride.

Allen et al. [82] studied the surface composition and morphology of spinel oxides following partial dissolution in a variety

of reagents. Following careful preparation of naturally occurring magnetite (Fe_3O_4) and franklinite ($ZnFe_2O_4$) crystals, dissolution of the <111> plane was investigated. X-ray photoelectron spectroscopy (XPS) and scanning electron microscopy (SEM) were used to characterize the spinel surface prior to and following dissolution. Care was taken at all stages to avoid aerobic oxidation.

The surface of the magnetite following treatment with potassium permanganate appeared to contain very little Fe(II). This was attributed to the oxidation of the surface Fe(II) giving rise to the formation of a surface layer of hematite (α-Fe_2O_3). As little Fe(II) was detectable in the XPS spectra, the workers suggested that the depth to which the oxidation had occurred is > 5 nm, the penetration depth of this technique.

It should be noted that the workers did not consider the possibility of the replacement of Fe(II) in the lattice by Mn(II) from solution. Thus Fe(II) could have been exchanged and not oxidized. This could give rise to an outer film of the spinel $MnFe_2O_4$ and not hematite as the workers suggest. It is unclear whether surface examination for manganese was performed.

A magnetite crystal following treatment with hydrochloric acid featured a surface Fe(II):Fe(III) ion ratio equal to that of the bulk oxide indicating that congruent dissolution occurred.

The surface of a magnetite crystal after treatment with tris-(picolinato) vanadium(II) appeared to be enriched with Fe(II) ions. This reagent has been shown to cause magnetite dissolution through a reductive process, involving a very rapid electron transfer specifically to Fe(III) ions in the magnetite lattice.

Segal and Sellers [21,23] claimed that during the reductive dissolution of spinel oxides, Fe(II) ions formed by reduction dissolve rapidly in a process that is not rate limiting. However, Allen et al. [82] showed that magnetite featured an enhanced surface concentration of Fe(II) ions following partial reductive dissolution. To explain these results, Segal and Sellers [21,23] proposed that reduced Fe(III) ions dissolve prior to the Fe(II) originally present in magnetite. This explanation appears unsatisfactory, as it requires significantly different dissolution rates for two apparently identical octahedral ions, the original Fe(II) and the reduced Fe(III).

During studies with magnetite it was not possible to determine whether the surface Fe(II) ions found were originally Fe(III) ions that had undergone reduction or residual octahedral Fe(II) ions. In an attempt to distinguish between these possibilities, similar experiments were performed with hematite (α-Fe_2O_3) and franklinite ($ZnFe_2O_4$), both of which are initially free of Fe(II) ions. Following partial reductive dissolution no ferrous ion was detected at the oxide surface, and it was concluded that reduction and dissolution occurred concurrently.

There are a number of unsatisfactory features in this work. The choice of franklinite as an Fe(II) ion-free spinel is unfortunate. This ferrite is a normal spinel [61]. Therefore, in addition to removing Fe(II) ions from the ferrite the distribution of Fe(III) ions is changed, a factor that may well significantly affect the dissolution behaviour. Mössbauer spectroscopy was used in an attempt to distinguish between the susceptibility of octahedral and tetrahedral Fe(III) ions in magnetite to reduction [119]. It is claimed that a diminution in the octahedral site component occurs after partial reductive dissolution. Also, in unpublished work Sellers observed that the reductive dissolution of $MnFe_2O_4$ (normal spinel) proceeds at approximately twice the rate of $NiFe_2O_4$ (inverse spinel) and $CoFe_2O_4$ (inverse spinel) under otherwise identical conditions, suggesting that the rate of reaction varies as a function of the concentration of octahedrally coordinated Fe(III). The authors note that such small increases in rate could well be attributable to uncontrolled variation of other oxide characteristics.

Buxton, Rhodes and Sellers [37] demonstrated that the dissolution of hematite (α-Fe_2O_3) and magnetite (Fe_3O_4) in EDTA solution proceeds by a SIRD process involving the Fe(II)-EDTA complex. In this study, the authors attempted to determine the relative reactivities of the Fe(III) and Fe(II) ions in magnetite. They followed the solution concentrations of Fe(II) and Fe(III) species throughout the course of the dissolution process. They claimed that the increases in the solution concentrations of Fe(III) and Fe(II) match the release of reduced Fe(III) and Fe(II) from the magnetite lattice. The experimental

results obtained indicated that the quantity of Fe(III) released to solution was greater than twice the quantity of Fe(II). This was taken as strong evidence that lattice Fe(II) is dissolved at a slower rate than reduced Fe(III). This disparity in the Fe(II) and Fe(III) ion release rates persisted for > 100 minutes. The reasoning of Buxton et al. requires that Fe(III) ion release remains proportionally greater than Fe(II) following apparently significant Fe(III) ion depletion in the oxide. The results obtained are those anticipated if a slow post-dissolution oxidation of Fe(II) to Fe(III) occurred following congruent dissolution.

The reasoning used by Buxton et al. assumes that complete reduction of Fe(III) ions in the solid state occurs prior to dissolution. The ferric ions within magnetite are equally divided between two different crystallographic sites as shown in equation (4.1). It is not known whether one or both types of ferric ions, or indeed what fraction of these solid state ions, have to undergo solid state reduction to cause dissolution.

Taking into account the distribution of species between the different crystal sites, the dissolution reaction can be written

$$[Fe(II)][Fe(III)](Fe(III))O_4 + (x+y)Fe(II)_{(Adsorbed)}$$
$$\rightarrow [Fe(II)]_{1+x}(Fe(II))_y[Fe(III)]_{1-x}(Fe(III))_{1-y}O_4$$
$$+ (x+y)Fe(III)_{(Adsorbed)} \qquad (4.1)$$

where:

[ ] indicates octahedrally coordinated ions

( ) indicates tetrahedrally coordinated ions

When: $x = 1$ and $y = 0$; Reaction confined to complete reduction of octahedral ferric ions

$y = 1$ and $x = 0$; Reaction confined to complete reduction of tetrahedral ferric ions

$x = 1$ and $y = 1$; complete reduction of all ferric ions.

Thus, the statement by Buxton et al. that the increases in the solution concentration of Fe(III) and Fe(II) match the release of reduced Fe(III) and Fe(II) from the magnetite lattice is only true if $(x+y) = 2$. Under such circumstances all solid phase ferric ions are reduced prior to dissolution and hence the increase in solution Fe(III) ion concentration equals the release of reduced Fe(III) ions. When $(x+y) < 2$, ferric ions from the oxide dissolve unreduced and hence the increase in solution Fe(III) concentration no longer equals the release of reduced Fe(III).

The studies demonstrate that incongruent dissolution does occur, and that variations in surface composition thoughout a dissolution process can cause a significant decrease in dissolution rate. Further, the form of the incongruency during direct dissolution was shown to be dependent upon the complexing species present. The form of the incongruency observed for a given spinel is also dependent upon the dissolution mechanism.

The relative reactivities of the octahedral and tetrahedral sites have not been conclusively determined. The identity of cations in both crystallographic sites has been shown to strongly influence the rates of dissolution. Therefore, dissolution of cations from one type of site does not appear to be rate controlling for all spinels.

It is possible that, close to the solution interface, the structure of the spinels departs significantly from that in the bulk, MacKrodt and Tasker [84]. For this reason the coordination of former octahedral and tetrahedral ions may change so as to lessen the difference between them. Distinguishing between the reactivities of such ions may not be possible.

4.5 CATION EXCHANGE BY MAGNETITE

Benton and Horsfall [85] observed that magnetite, when introduced into acid solutions, releases ferrous ions in exchange for protons. Tronc et al. [86] performed a detailed study of the process using colloidal magnetite produced by a method similar to that of Matijević [16,17,73,74,78]. The cationic sol at pH 2-3 contained approximately spherical particles with diameters of about 100 Å. Analysis of the colloidal particles revealed an Fe(III) to total Fe ratio in the range 0.80-0.90, the value expected for stoichiometric magnetite being 0.67.

Immediately upon introduction of the cationic sol to distilled water Fe(II) ion release commenced. After a period of one week the Fe(III) to total Fe ratio had achieved a value in the range 0.95-0.98, i.e., almost total depletion of Fe(II) ions.

The controlled addition of base to an Fe(II) ion depleted colloid suspended in a weakly acid solution of Fe(II) chloride was studied. Immediate precipitation of Fe(II) hydroxide did not occur. Precipitation did not commence until the Fe(II) ion to total Fe ratio in the colloid had risen from its former value in the range 0.02-0.05 to 0.33 (the value expected for stoichiometric magnetite). These results are consistent with a readily reversible exchange of Fe(II) ions in the colloidal magnetite with solution protons.

When Co(II) ions are substituted for Fe(II) ions in the experiment described previously, similar results were obtained. Co(II) uptake was described as being three times less than Fe(II) when precipitation of Co(II) hydroxide commenced. This is assumed to mean that the Co(II) ion to total Fe ratio in the colloid had reached a value of 0.11. This quantity of cobalt was readily desorbed by reacidification of the suspension.

The adsorption of Ni(II) was also investigated, little or no ion exchange being detectable. Precipitation of Ni(II) hydroxide occurred immediately upon addition of base.

The desorption kinetics of these colloids were studied for the case of Fe(II) ions only. The results suggest that release of 70% of the Fe(II) ions occurred very rapidly, the desorption of the remaining Fe(II) ions occurring over a long period of time. Approximately 10 to 15% of the Fe(II) ions remained after 17 hours.

X-ray diffraction studies of the colloids prior to and following depletion of Fe(II) ion revealed only spinel-type lines, no variation in the unit-cell parameter being observed. The Fe(II):total Fe ratios measured by chemical methods were confirmed by X-ray diffraction.

Tronc et al. [86] proposed that the Fe(II) ion uptake by the Fe(II) depleted colloid occurred by the adsorption of hydrolyzed Fe(II) ion species, producing an outer shell of magnetite. The electrons liberated upon partial oxidation of the absorbed Fe(II) ion species migrated into the particle causing reduction of Fe(III) ions. This process continued until the core concentrations of octahedral Fe(III) and octahedral Fe(II) ions were equal. It was proposed that electron migration and hence, ferrous ion absorption, ended once equipopulation of octahedral sites by Fe(II) and Fe(III) ions was achieved. To counter the charge imbalance caused by electron migration to the particle core, it was proposed that proton migration occurred. The X-ray diffraction studies indicated that iron diffusion into the core was not significant.

The different behaviour of Co(II) and Ni(II) was attributed to the inability of these ions to undergo oxidation upon adsorption. It was suggested that the adsorption of ions was effectively governed by the Co(II)/Fe(III) or Ni(II)/Fe(III) redox couple.

The results suggested that the rapid and reversible exchange of Fe(II) for protons observed for magnetite was governed by the ability of magnetite to conduct electrons, and the ease of Fe(II) ion Fe(III) ion interconversion both at the oxide interface and in octahedral sites within the cubically close packed oxygen lattice.

The magnetite particles used during this study had a diameter of only 100 Å. A unit cell of magnetite contains 32 oxide ions and has a dimension of $\sim$ 8.6 Å. Thus, the particles used contain approximately 2×10^4 oxide ions. The behaviour of such a small particle will differ significantly from larger magnetite crystals, and the significance of these ion exchange properties is expected to diminish as the particle size increases. This work does, however, pose some interesting questions concerning the nature of the magnetite-solution interface during dissolution. It is possible that rapid processes such as this produce an interfacial oxide layer depleted in Fe(II) ions. This clearly has implications for investigations of the relative reactivities of octahedral and tetrahedral sites.

Insufficient information is available to determine whether these effects observed in non-complexing solution will be of

significance in solutions containing strong complexing reagents. Also, such effects may be insignificant for freely dissolving magnetite.

4.6 THE SITE OF REDUCTION DURING REDUCTIVE DISSOLUTION

Reductive dissolution of an oxide film on metal can be caused either by the migration of an electron from the substrate metal into the oxide or by the transfer of an electron across the oxide solution interface. Two types of reductive dissolution process can be envisaged: (i) the reduction being confined to a very thin surface layer of oxide that rapidly dissolves following reduction; or (ii) considerable reduction of the bulk oxide preceding dissolution.

For reductive dissolution only involving cation reduction at sites close to the solution interface, the bulk oxide conductivity will have little effect on the rate of heterogeneous electron transfer. Such a reaction delivers the electron to the oxide in very close proximity to the favoured reduction site. The rate of electron transfer for this type of process will be controlled by the potential gradients and structure of the interface. However, if the electron is supplied from the base metal, electron migration must occur through the entire thickness of the oxide film. The rate of electron transfer in such situations will be influenced by the electrophysical properties of the oxide bulk.

If reductive dissolution necessitates bulk oxide reduction prior to dissolution, the electrons delivered either from the base metal or the solution would have to migrate considerable distances within the oxide. In this way, the electrophysical properties of the oxide are likely to influence both types of reductive dissolution. Further, the electrophysical properties of the reduced oxide will become important as well as those of the original oxide.

Little work has been done to determine whether substantial reduction precedes dissolution or whether reduction is confined to a surface layer that has a strained crystallographic structure. Riley and Sykes [87] studied the reduction of thin passive films grown electrochemically on low alloy steel. Galvanostatic reduction experiments indicated that approximately complete oxide reduction was observed before significant dissolution, a large and sudden release of iron being observed as the oxide reduction process reached completion. Shoesmith et al. [88] performed galvanostatic reductions on mixed hematite-magnetite films, and observed an initial charge retention by the oxide prior to the initiation of iron release at a rate equivalent to the supplied current. This suggests that a significant oxide reduction occurs prior to the initiation of dissolution.

Both the work of Riley and Sykes [87] and Shoesmith [88] were electrochemical experiments in which the charge was driven through a Fe(III) oxide from the substrate metal. Such oxides are relatively poor conductors. Therefore, it is quite possible that a reduction wave

travels through the oxide to the solution interface, at which time dissolution commences. Similar behaviour would not necessarily be observed for magnetite since it possesses a much greater conductivity.

Although concerned with oxidation processes in nickel ferrite films, the work of Kishi, Himizu and Nagi [25] provides some interesting clues as to the nature of the redox reaction with spinel oxides. Kishi, Shimizu and Nagi [25] investigated the dissolution of a nickel ferrite ($Ni_{0.64}Fe_{2.36}O_4$) in acidic sulphate and chloride solutions. Anodic polarization experiments were performed which identified an anodic process that was attributed to the oxidation of octahedrally coordinated ferrous ions. The electrochemical measurements revealed that this oxidation process was unaffected by both the identity and concentration of surface adsorbed species. This result clearly suggests that the ferrous ion oxidation is taking place at a site that is unperturbed by surface adsorbed species. Also, the results indicate that the oxidation was confined to a very thin surface region.

Few studies have addressed the problem of whether bulk oxide reduction precedes dissolution. Those discussed above provide interesting results, but do not resolve the problem. Electrochemical investigations have identified systems in which apparently complete oxide reduction precedes dissolution, and other systems in which oxide redox reactions are confined to thin interfacial regions.

4.7 OXIDE CONDUCTIVITY

Only one study has been identified which attempted a systematic investigation of the dependence of oxide dissolution behaviour on oxide conductivity. The results of this study are generally inconclusive.

Devuyst and Warren [8] investigated the dissolution behaviour of hematite (α-Fe_2O_3) using a series of samples of different electrical conductivity. The conductivity of the hematite was adjusted by titanium doping up to a maximum concentration of 3 wt%.

Hematite dissolutions were performed in oxalic acid. Devuyst and Warren, and Baumgartner et al. [24], had conclusively determined that a SIRD reaction involving a Fe(II)-oxalate complex was the dominant dissolution process.

It was feared that changes in dopant concentration might cause changes in oxide morphology and thus mask the true dissolution rate dependence upon conductivity. In order to avoid this problem, the ratio of dissolution rates in oxalic acid and hydrochloric acid were determined. Thus, the rate ratio was determined as a function of dopant concentration. The rate ratio initially increased rapidly with dopant concentration, and reached a maximum at 0.8 wt% titanium and declined slowly thereafter to 3 wt% titanium. The rate ratio increased by a factor of 6 as the titanium concentration rose from 0 to 0.8 wt%. This

compositional change causes the conductivity to rise by more than ten orders of magnitude. Devuyst and Warren proposed that these results were due to the adsorption of ferrous oxalate complexes at the oxide surface, which enhanced the surface conductivity of the undoped oxides by the formation of ferrous sites.

Although not stated, it seems implicit that the rate ratio method was adopted on the assumption that dissolution in oxalate would proceed by a reductive dissolution process and that direct dissolution would occur in hydrochloric acid. However, other studies [19,22,89] have indicated that the chloride ion can promote heterogeneous electron transfer reactions. Therefore, this rate ratio might not truly reflect the rate acceleration caused by changes in oxide conductivity. Unfortunately, the basic rate data for the dissolutions in each acid were not presented [8].

The results of this study are generally inconclusive. Further study is required to determine whether oxide conductivity affects the rate of heterogeneous electron transfer processes during SIRD.

4.8 ION-VACANCY CONCENTRATION

The impact of ion-vacancy concentrations on oxide dissolution processes have not been comprehensively studied, although such effects have been proposed on a number of occasions as possible explanations for aspects of dissolution behaviour.

The study performed by Jones et al. [71] serves to illustrate the complexity of the relationship between dissolution behaviour and ion-vacancy concentrations.

Jones et al. [71] performed a detailed study to determine the effect prior annealing temperature has on the rate of nickel oxide dissolution in nitric acid. Nickel oxide was selected because it possesses a simple crystal structure, p-type semiconductivity and exhibits relatively small departures from stoichiometry.

Dissolutions were performed at 60°C in nitric acid to minimize complications due to complexation. At all annealing temperatures used highly perfect crystals were formed, the size of the crystals rising with annealing temperature.

The dissolution rate per unit surface area falls significantly with increasing prior annealing temperature. Following compensation for changes in surface area, there was an order of magnitude decrease in dissolution rate as the annealing temperature was increased from 700 to 1450°C. All dissolutions featured a modest progressive increase in dissolution rate per unit surface area during the dissolution process.

Study of partially dissolved crystals indicated that a general, and principally isotropic, dissolution occurred. Conductivity measurements, and other studies, indicate that nickel oxides prepared at temperatures below 700°C have a high cation vacancy concentration.

Thermodynamics indicates that the equilibrium cation vacancy concentration rises as the annealing temperature increases. On this basis it would be anticipated that if the dissolution rate were proportional to the cation-vacancy concentration then the dissolution rate would increase with increasing prior annealing temperature. Experimentally, the opposite is observed.

The parameter that appears to be of greatest significance is not the absolute cation vacancy concentration, but the excess concentration over and above the equilibrium concentration for the annealing temperature employed. The cation vacancy concentration of the oxide prior to annealing is considerably greater than the equilibrium concentration at 60°C. This large excess cation vacancy concentration is trapped in the oxide at temperatures below 700°C as a consequence of the restricted ionic mobilities.

If the nickel oxide is annealed at a temperature > 900°C, the defect concentration achieves the equilibrium value, and although this defect concentration is greater than that prior to annealing, the excess concentration is lower and consequently the dissolution rate is lower. It appears that at an annealing temperature > 900°C, the structure of the oxide is free to change to accommodate the high equilibrium vacancy concentrations so that the thermodynamically favoured state is achieved. Following preparation, the oxide contains a lower absolute cation vacancy concentration, but as a consequence of the preparation and the immobility of the ions, has a non-equilibrium structure. It appears

that as the oxide departs from the equilibrium structure, dissolution is facilitated.

The above mechanism cannot account for the differences in dissolution rates observed between different annealing temperatures above 900°C, as all such samples should have zero excess cation vacancy concentrations. The origin of these effects has not been identified. The concentration of kink sites and changes in particle size are possibly involved.

The increase in dissolution rate with extent of dissolution has not been satisfactorily explained. The influence of particle size, changes in the availability of high energy surface sites, and interference from solution species present prior to dissolution and released during dissolution have all been proposed as possible explanations.

This study clearly indicates the significance of annealing during oxide preparation. Much of the variability observed during oxide dissolution studies can be attributed to different annealing procedures. Although the principal effects seem to arise from changes of specific surface area, changes in the cation vacancy concentration could also play a significant part.

CHAPTER 5

DIRECT DISSOLUTION

5.1 INTRODUCTION

A substance is said to be dissolving by a direct process when no redox reactions occur, both the anions and cations within the solid transferring from the solid to solution state without a change in valence; e.g., for magnetite

$$>Fe_3O_4 + 8H^+(aq) \rightarrow 2Fe^{3+}(aq) + Fe^{2+}(aq) + 4H_2O \quad .$$

For oxides of metals that exhibit only one accessible oxidation state dissolution, by necessity, must proceed by a direct pathway, since oxide ion oxidation can normally be disregarded. The rates of direct dissolution processes vary considerably. For instance, nickel ferrite dissolution by this mechanism is so slow in acid that the substance is considered insoluble [90], whereas many oxides, MgO, ZnO and CuO, dissolve readily in dilute acids by direct dissolution pathways.

For convenience, this chapter will be divided into direct dissolution processes occurring in inorganic acids and those occurring in acidic solution of strong complexing agents. The discussion deals

principally with iron oxides and ferrites since these oxides are the focus of the experimental study reported in this thesis.

5.2 DIRECT DISSOLUTION IN INORGANIC ACIDS

The dissolution of magnetite (Fe_3O_4), hematite (α-Fe_2O_3) and ferrites by inorganic acids is slow. Bradbury [11] observed less than 1% dissolution of powdered hematite following 24 hours exposure to 1 $mol \cdot dm^{-3}$ hydrochloric acid at 80°C.

Oxide dissolution studies performed in inorganic acids reveal diverse dissolution behaviour, even under apparently comparable conditions. This appears to be attributable to (i) chemical differences between oxides, (ii) the identity of the acid anion, (iii) differences in experimental method, and (iv) oxide preparation.

Several investigations of hematite dissolution behaviour have been performed. Following an initial surge of dissolution, Pryor and Evans [9] observed progressively diminishing rates consistent with the shrinking core model of dissolution. They rationalized the initially rapid dissolution as a consequence of high surface defect concentration. The studies typically involved < 1% dissolution so that the results obtained are probably not representative of bulk oxide behaviour.

The study by Azuma and Kametani [10] followed hematite (α-Fe_2O_3) dissolution processes to completion, and observed complex iron

release behaviour. Up to 0.5% dissolution the rate diminished with time, and following this the rate increased until approximately 30% dissolution. This increase in dissolution rate was attributed to the fragmentation of the oxide particles. The third and final phase of dissolution featured a progressively decreasing rate.

These studies indicate the difficulties of performing kinetic studies of oxide dissolution processes, and such studies have been few in number. Both Gorichev et al. [13] and Bruyère and Blesa [14] studied the dissolution of magnetite in sulphuric acid. The study by the latter workers observed behaviour consistent with the shrinking core model of dissolution. This was not the case in the former study, the rate having been observed to rise progressively up to 25% dissolution. Subsequently the iron release rate remained constant to 60% dissolution, and finally declined to completion. This behaviour was thought to be a consequence of anisotropic dissolution. The most plausible explanation for these apparent discrepancies is that the different methods of magnetite preparation used produced samples with substantially different structures, and that these structural features significantly affect the dissolution behaviour.

Warren et al. [4] studied the dissolution of single hematite (α-Fe_2O_3) crystals and found that the identity of the acid anion had a major impact on the nature of the dissolution process. Five days of exposure to hot concentrated $HClO_4$ produced only a modest general attack. Ten minutes in hot concentrated HCl dissolved an equal amount

of oxide and produced severe pitting. Thus, the identity of the acid used influences not only the overall rate of dissolution, but also the degree of anisotropy exhibited during dissolution.

Warren and Monhemius [6,91] investigated the dissolution of hematite (α-Fe_2O_3) and goethite (α-FeOOH) in various acids. A comparison of the dissolution rates observed for both substances consistently indicates the following order of reactivity:

$$HClO_4 < H_2SO_4 < HCl \quad .$$

The approximate relative rates were:

$$1:20:30 \quad .$$

This study suggests that the rate-determining process is the desorption of a surface complex. The order of acid reactivity suggests that the rate is proportional to the complexing ability of the anion for Fe(III) ions. Azuma and Kametani [10] observed a similar correlation during a study of hematite (α-Fe_2O_3) dissolution. It appears generally true that oxide dissolution rates in strong acids exhibit a strong dependence upon the identity of the anion present, and that the rates are approximately proportional to the solution complexing ability for the oxide cation. This claim is supported by a number of oxide dissolution studies involving nonferrous oxides [3], aluminum [3], copper [92] and beryllium [2].

A number of significant observations arise from these studies of direct oxide dissolution in inorganic acids.

(1) The preparation of the oxide greatly affects the form and rate of the dissolution process. Variations in crystal defect concentrations, fragmentation of oxide particles, and changes in oxide morphology have all been observed during oxide dissolution processes. The consequence of these changes is that oxide dissolution processes frequently do not display the progressively diminishing rate predicted by simple models.

(2) The degree of anisotropy observed during dissolution and the overall dissolution rate are strongly dependent on the identity of the solution anionic species. There appears to be some measure of correlation between the rate of oxide dissolution observed and the complexing ability of the anion present.

(3) The dependence of oxide dissolution rate upon pH appears to vary as the identity of the oxide and acid change, and also as the acid concentration varies. A direct proportionality between acid concentration and oxide dissolution rate has been observed for the dissolution of goethite (α-FeOOH) in $HClO_4$ and H_2SO_4 [7], and hematite (α-Fe_2O_3) in concentrated HCl [4]. However, the dissolution rate of hematite in dilute HCl is found to vary as the square of the acid concentration [5,10]. For cuprite [92] and beryllium oxide [2] the rate of oxide dissolution has been found to display a

progressively declining sensitivity to the acid concentration as the concentration increases.

The theory of the dissolution of ionic compounds in aqueous media proposed by Vermilyea [45] predicts fractional oxide dissolution rate dependencies upon pH. The exact form of the dependence is affected by the charge of the potential-determining ions. In this way some of the apparently inconsistent dissolution rate dependencies upon pH can be explained. The identity of the anion significantly influences dissolution behaviour. Clearly such effects have hindered investigation of dissolution rate dependence on pH. Systematic studies that have separated the pH effect and the anion effect are scarce.

5.3 DIRECT DISSOLUTION IN STRONG COMPLEXING AGENTS

Matijević et al [16] suggests that chelating agents can promote oxide dissolution in one of two ways: (i) the complexing agent can reduce the solution concentration of the free metal ion, thereby shifting the solubility equilibrium and promoting dissolution, or (ii) the complexing agent can chemisorb on the oxide and assist dissolution by accelerating the desorption of a surface cation complex.

Matijević et al performed a series of studies to investigate dissolution and absorption processes occurring in solutions of various chelates with β-FeOOH [35], hematite (α-Fe_2O_3) [16,73,74], nickel ferrite ($Ni_{0.53}Fe_{2.47}O_4$) [36] and magnetite (Fe_3O_4) [78].

The connection between a reagent's ability to promote oxide dissolution and its solution complexing strength has been proposed, section 5.2. For this reason, many dissolution studies have been performed with EDTA (ethylenediaminetetra-acetic acid). EDTA is a powerful and widely used complexing agent, the stability constants for ferric and ferrous ions being $\sim 10^{25}$ and $\sim 10^{14}$, respectively [93].

Matijević et al. investigated the dissolution of hematite hydrosols in oxalic and citric acids [15] and EDTA solution [36] as a function of solute, solute concentration, pH and temperature. The sensitivity of the dissolution process to the anionic species present was clearly demonstrated. No dissolution of the sols occurred as a consequence of prolonged exposure to hot concentrated nitric acid. However, under similar conditions significant dissolution occurred in citric acid, oxalic acid and EDTA solutions. Electrophoretic mobility studies demonstrated that solute adsorption on the oxide occurs, the extent of adsorption increasing as the temperature and solute concentration rise. The adsorption is strongly pH dependent, the surface concentration of oxalate, citrate and EDTA complexes rising significantly as the pH decreases in the pH range 3 to 10. This dependence is rationalized in terms of a model that considers the electrostatic contribution to the free energy [17]. The coadsorption of protons onto the oxide surface serves to reduce the electrostatic repulsion between adsorbed anions. The surface proton concentration is increased as the bulk solution proton activity increases, thereby raising the equilibrium surface anion concentration. Additionally, the

pH also affects the surface complex concentration as a consequence of changing the solution speciation.

These studies identified the adsorbate species. In oxalic acid solutions only the $C_2O_4^{2-}$ ion is adsorbed, whereas for citric acid both the trivalent and divalent ions are adsorbed. The evidence suggests that bonding to the oxide surface occurs through two carboxylate groups, consistent with the observation that only anions carrying a charge of two or greater adsorb. This is in agreement with the infrared studies of Parfitt and Russell [94-96] on anion adsorption on oxides and hydrous oxides of iron. Their work indicates that oxalate is strongly adsorbed, achieving high surface concentrations. The oxalate species appears capable of bonding to the surface either as a mononuclear or binuclear complex.

For each complex considered a series of adsorption isotherms at different pH values was determined. These isotherms relate the equilibrium surface complex concentration to the equilibrium solution chelate concentration. Based on the assumption that the maximum surface complex concentration observed represented complete surface coverage the surface area occupied by each complex was calculated. At pH=2.7 an EDTA molecule apparently occupies 96 $Å^2$, whereas at the isoelectric point, pH $\sim$ 7, the corresponding area is 170 $Å^2$. This suggests that as the pH is varied the conformation of the EDTA complex undergoes changes. A surface adsorbed oxalate species appears to occupy 8.3 $Å^2$ and a citrate species 33 $Å^2$ per molecule. No indication was given as to the

sensitivity of these coverage areas to pH. The relative magnitudes of these areas correspond well to adsorbate size, and are in good agreement with values obtained using radioactive tracer studies [97].

A number of multidentate ligands in addition to EDTA were studied, significant differences in adsorption behaviour being observed between the chelating agents. This suggests that the chelate charge, size and conformation all influence the surface adsorption characteristics of these molecules.

These studies by Matijević et al. indicate that the rate of oxide dissolution in citric and oxalic acids is directly proportional to the surface concentration of the adsorbate, and that proton concentration affects the rate of oxide dissolution only as a consequence of the changes induced in the adsorbate surface concentration. While the dissolution of hematite in citrate and oxalate solutions appears to proceed by a common mechanism involving the desorption of a surface complex at all pH values from 3 to 10, this does not appear to be the case for EDTA. At 26°C, the maximum hematite dissolution rate in EDTA is achieved at pH $\curvearrowleft$ 10, the adsorption density of EDTA rising as the pH decreases in the pH range 11 to 3. Clearly, under these conditions, the dissolution rate is not directly proportional to the surface complex concentration.

Chang and Matijević [16] performed a detailed study of the dissolution kinetics of hematite in EDTA and other related multidentate

ligand solutions. During the dissolution of hematite in dilute EDTA solutions, the iron release rate displays a complex dependence upon the extent of oxide dissolution. The iron release rate dependence upon pH changes as the dissolution proceeds and also varies with temperature.

At a temperature of 26°C the iron release rate increases significantly as the pH is increased in the range 3 to 7. However, at 100°C, the pH dependence is opposite to that seen at 26°C. The marked differences in behaviour at the two temperatures studied strongly suggest that different dissolution mechanisms predominate.

It is proposed that the dissolution of hematite in EDTA at 26°C involves the loss of ferric ions that are not complexed with EDTA, complexation subsequently taking place in solution. At 100°C the dissolution involves the desorption of ferric ion-EDTA surface complexes.

This model rationalizes the opposite pH dependencies exhibited at 26°C and 100°C. At both temperatures, decreasing pH in the range 2 to 9 causes increased EDTA adsorption, increasing the surface concentration of the Fe(III)-EDTA complex. At 26°C this serves to block the dissolution occurring from the EDTA free surface sites, while at 100°C this change increases the surface concentration of Fe(III)-EDTA participating in the rate-determining desorption process. The dependence of the iron release rate upon extent of oxide dissolution is not satisfactorily explained. This effect is very significant at 100°C, the iron

release rate decreasing progressively throughout the dissolution. The effect becomes more marked as the pH increases from 3.5 to 9.0, such that at pH=9 the dissolution process terminates after a period of 1 hour following only fractional hematite dissolution. It is suggested that this effect may be caused by the progressive development of an insoluble surface film, although the nature of this film is not specified.

Matijević et al. suggested that at 26°C EDTA promotes the dissolution of hematite by reducing the free-ferrous ion concentration in solution. If this process is occurring, the rate of oxide dissolution would be expected to show a dependence upon the complexing ability of EDTA, which is strongly influenced by pH. Decreasing the pH causes protonation of EDTA, reducing the concentrations of the strongly complexing $EDTA^{4-}$ and $EDTAH^{3-}$ ions and thereby reducing the complexing power of EDTA solutions. At a pH of 4 the unprotonated and singly protonated forms of EDTA only represent 4×10^{-7}% and 0.6%, respectively, of the total EDTA solution concentration. The observations of Devuyst and Warren that no hematite or goethite dissolution occurs in EDTA solutions at a pH $\sim$ 4 [3] and that the optimum pH for the dissolution of oxidized copper ores is pH 8.5-10 [98] support the mechanism proposed by Matijević.

Gilbert and Ouellet [18] studied the adsorption of EDTA on, and subsequent dissolution of, small monodispersed magnetite particles. Similar experiments were performed with β-FeOOH and hematite, the results obtained being consistent with comparable studies performed on

these substances by Rubio and Matijević [35] and Chang, Healy and Matijević [74], respectively. Unfortunately, the kinetics of the dissolution process were not followed, the extent of dissolution being measured only at the conclusion of experiments lasting 20-24 h. This is surprising in light of the complex dissolution behaviour reported by Matijević and their own preliminary investigations, which indicated that the contact time significantly changes the extent of Fe_3O_4 dissolution. To further illustrate the complex form of the dissolution processes, changes in the contact time altered the apparent dependence of the iron release upon pH. As a consequence of the approach taken, the results provide little insight into the iron release rate during dissolution. The study indicated that variations in EDTA concentration in the range 7×10^{-4} to 1×10^{-1} mol·dm^{-3} have little effect on the release of iron during dissolution.

Gorichev et al. [12] investigated the dissolution of magnetite in EDTA solutions as a function of pH at 60°C. All the iron release versus time plots had a characteristic s-shape. An initially low iron release rate is observed, increasing progressively to about 10% dissolution, and thereafter remaining constant to ~ 80% dissolution. Finally, the rate slows upon approaching complete dissolution. The iron release rate during the linear portion of the iron release profile reaches a maximum, and the initial induction period achieves a minimum at pH=2.16. The rate of reaction was found to be independent of EDTA concentration in the range 0.01-0.2 mol·dm^{-3}. The relatively simple dissolution behaviour observed during this study appears to be attributable to the

type of oxide used. The oxide used was purchased commercially, and therefore was most probably produced by a high temperature method.

Although direct comparison between the dissolution rates observed by Gorichev et al. and Gilbert et al. is difficult due to the different experimental conditions employed, a crude comparison is possible. Gorichev et al. observed that in a 1×10^{-2} mol·dm^{-3} EDTA solution, pH $\sim$ 4.5 at 65°C, 80-100 μm magnetite crystals were half dissolved after 150 min. Under approximately comparable conditions, Gilbert et al. had observed $\sim$ 10% dissolution of 0.4 μm magnetite particles after 7 days. Comparison of these oxide dissolution studies emphasizes the major impact oxide preparation has upon dissolution behaviour. The work of Matijević et al. clearly demonstrates the advantage of adopting a preparative method capable of yielding a consistent product. These studies permit comparisons to be made between the dissolution behaviour of different oxides and the performance of various reagents. Meaningful comparison between studies performed in different laboratories is difficult at best.

As was observed for dissolutions in inorganic acids, the form of the iron release during dissolution is complex and variable. The iron release rates observed under apparently similar conditions varied enormously.

The dissolution mechanism proposed by Matijević appears to successfully account for many of the major experimental observations.

CHAPTER 6

REDUCTIVE DISSOLUTION

6.1 INTRODUCTION

The reductive dissolution of magnetite

$$>Fe_3O_4 + 8H^+ + 2e^- \rightarrow 3Fe(III) + 4H_2O \qquad (6.1)$$

involves the reduction of solid state Fe(III) ions to Fe(II). Reductive dissolution reactions can proceed many orders of magnitude faster than direct dissolution processes, Figure 1.

The discussion of reductive dissolution processes is divided into three parts:

(i) Solute induced reductive dissolution (SIRD) involving complex reducing agents

$$>Fe(III) + V(II)(L)_n \rightarrow Fe(II)(aq) + V(III)(L)_n \quad . \qquad (6.2)$$

These reactions have been rather inappropriately called ligand-bridge assisted dissolution (LBAD) reactions. The use of this term implies an inner sphere heterogeneous electron transfer reaction, whereas generally the mechanistic distinction between an inner-sphere and outer-sphere

process has not been made. The discussion deals principally with complexes of Fe(II), V(II) and Cr(II).

(ii) Solute induced reductive dissolution (SIRD) reactions involving simple reducing agents, i.e., all reducing agents other than metal complexes. It does not appear that the direct reduction of solid state cations by simple reducing agents has been conclusively demonstrated, although it has been proposed as a possibility on several occasions. An example is the reduction of magnetite by oxalic acid at elevated temperatures:

$$>Fe_3O_4 + 8H^+ + C_2O_4^{2-} \rightarrow >3Fe(II) + 4H_2O + 2CO_2 \quad . \qquad (6.3)$$

The results of studies with oxalic acid and thioglycollic acid are presented and discussed.

(iii) Autoreduction can occur when magnetite and a ferrous metal in intimate contact are exposed to an electrolyte. This process involves the coupling of the anodic dissolution of the metal and reductive dissolution of magnetite:

$$>Fe(0) + >Fe_3O_4 + 8H^+ \rightarrow 4Fe(II) + 4H_2O \quad . \qquad (6.4)$$

Magnetite film growth on steel in aqueous environments often yields porous oxide films. The film porosity permits the electrolyte contact with both metal and oxide necessary for autoreduction.

6.2 SOLUTE INDUCED REDUCTIVE DISSOLUTION (SIRD) INVOLVING COMPLEX REDUCING AGENTS

One of the first studies of the reductive dissolution of oxides was performed by Zabin and Taube [19]. The reducing agent used throughout these studies was Cr(II)(aq), chosen because the substitution inertness of this complex is of considerable assistance in mechanistic studies. The work illustrated that significant differences in reaction mechanism are observed between heterogeneous electron transfer reactions and their homogeneous solution analogues. The difference arises, in part, because an electron transferred across a solution-solid interface to a solid need not be localized upon the recipient centre, electron migration within a solid permitting the electron to cause reduction at locations remote from the site of the electron transfer.

The concept of lattice disruption arising from the electron transfer to the solid was proposed. This was supported by the experimental observation that generally oxides containing metal ions that undergo a two electron reduction dissolved more rapidly than those cations restricted to one electron changes. It was suggested that steric effects may account for this observation, the increase in cation radius being greater for multiple, as opposed to single, electron reductions. The significance of the crystal structure disruption reflected the change in cation radius. It was also suggested that metal ion reductions can, in specific instances, cause significant crystal structure disruption as a consequence of changes in the preferred

crystal field geometry. For example, the reduction of Mn(III) to Mn(II) changes the preferred crystal field from an octahedral field possessing tetrahedral distortion to a symmetrical field.

Zabin and Taube investigated the dependence of oxide dissolution rates upon chloride ion concentration. The rate of reduction of every oxide studied increased with increasing chloride ion concentration. A single kinetic study was performed which demonstrated that the reaction rate displayed a direct dependence upon chloride concentration. This study did not permit the identification of the mechanism by which this effect arose. It is possible that the chloride ion acts as a bridging group. Segal and Sellers et al. [22,89] also report that chloride-mediated reactions have been observed in the reductive dissolution of α-Fe_2O_3, Fe_3O_4 and $NiFe_2O_4$ by Cr(II). The importance of the solution complexing species in such reactions is further demonstrated by the work of Koch [20] during a study of the Fe(II) induced reductive dissolution of MnO_2. The rate of reductive dissolution was found to be dependent upon the solution complexing species, dissolutions in sulphate proceeding faster than those in perchlorate.

It appears that participation of solution ferrous complexes in reductive dissolution processes was first recognized by Koch [20] in 1957 during an investigation of manganese dioxide dissolution. The reaction rate was found to be proportional to surface area and to ferrous ion concentration. This ferrous ion dependence was only observed

at low concentrations, $< 1x10^{-2}$ mol•dm^{-3}. The results clearly indicated the direct participation of ferrous species in the dissolution process.

Warren and Devuyst [3,8] identified participation by ferrous complexes in the reductive dissolution of hematite. The experimental studies performed were in 0.2 mol•dm^{-3} oxalic acid at 80°C. The oxide dissolution rate reported is very low in the pH range 1 to 4.5. This was interpreted as suggesting that neither $HC_2O_4^-$ or $C_2O_4^{2-}$ was strongly absorbed under these conditions. The subsequent work of Matijević et al. [15] and Parfitt et al. [96] indicated that this interpretation is incorrect. This discrepancy does not devalue principal conclusions of the study.

The addition of $1x10^{-4}$ mol•dm^{-3} ferrous oxalate to the hematite oxalate systems increased the dissolution rate by as much as 1000 times, the rate achieving a maximum at pH = 2.6-2.7. This rate acceleration was attributed to the adsorption of ferrous oxalate complexes at the oxide-electrolyte interface. It was proposed that the adsorbed ferrous oxalate complexes participate in an electron transfer reaction, donating an electron to an adjacent ferric ion in the oxide.

The dissolution rate of hematite in the presence of a fixed concentration of ferrous oxalate was determined as a function of pH. Calculations were performed to evaluate the changes in solution speciations caused by the pH changes. On the basis of these results, a rate equation of the following form was proposed:

$$\text{Dissolution rate} = k_1[Fe(II)(C_2O_4)_2^{2-}][H^+] + k_2[Fe(II)(C_2O_4)_3^{4-}][H^+] \quad (6.5)$$

where k_1 and k_2 are rate constants.

The rate equation gives a good fit to the experimental data. The form of the equation suggests that both $Fe(II)(C_2O_4)_2^{2-}$ and $Fe(II)(C_2O_4)_3^{4-}$ species are adsorbed on a protonated hematite. Experiments with malonic acid suggested that a similar mechanism was operative.

This work by Devuyst and Warren [3,8] was presented in 1972, but was unknown to Baumgartner et al. [24] when they performed an investigation into the dissolution of magnetite in oxalic acid solutions, which was published in 1983. Baumgartner et al. [24] studied the adsorption of oxalate species on magnetite as a function of pH using an electrokinetic mobility technique. The results strongly suggest adsorption of anionic oxalate species occurs.

No dissolution of magnetite was observed during 24 hours exposure to a 1×10^{-2} mol·dm^{-3} oxalic acid solution containing Fe(II) oxalate complexes, at pH = 7.6, temperature 30°C. However, when the pH was decreased to 4.1, complete dissolution required only ~ 100 minutes. Very little dissolution occurred in the initial 60 minutes, but after this induction period the reaction rate rose rapidly. When ferrous species are initially present in the oxalic acid solution, the

dissolution process was complete in 25 minutes, and the induction period was absent. The addition of ferric species to oxalic acid does not produce these effects.

The results clearly suggest the participation of ferrous oxalate species in the dissolution process, as previously observed by Warren and Devuyst [8]. On the basis of this study, the following mechanism was proposed for the dissolution of magnetite in oxalate solutions. The first step involves the replacement of surface-OH groups by oxalate anions

$$>Fe(III)\text{-}OH + HC_2O_4^- \rightleftharpoons >Fe(III)(C_2O_4) + H_2O \qquad (6.6)$$

$$>Fe(II)\text{-}OH + HC_2O_4^- \rightleftharpoons >Fe(II)(C_2O_4) + H_2O \quad . \qquad (6.7)$$

During the induction period the rate-determining dissolution process was assumed to be the desorption of a weakly bound surface ferrous-oxalate complex. This slow initial direct dissolution process gives rise to solution ferric and ferrous oxalate species in proportions governed by the magnetite stoichiometry,

$$>Fe(III)(C_2O_4) + (n\text{-}1)C_2O_4^{2-} \rightleftharpoons (Fe(III)(C_2O_4)_n)^{-(2n-3)} \qquad (6.8)$$

$$>Fe(II)(C_2O_4) + (n\text{-}1)C_2O_4^{2-} \rightleftharpoons (Fe(II)(C_2O_4)_n)^{-(2n-2)} \quad . \qquad (6.9)$$

The rapid acceleration in dissolution rate observed at the end of the induction period probably occurs as the solution concentration of ferrous ions reaches a value that establishes a critical surface concentration of the Fe(II)-oxalate complex. Once this condition is achieved an autocatalytic reductive dissolution process commences:

$$>Fe(III)(C_2O_4) + Fe(II)(C_2O_4)_{(Adsorbed)} \rightleftharpoons >Fe(II)(C_2O_4) + (Fe(III)(C_2O_4))^{+}_{(Adsorbed)} \qquad (6.10)$$

$$>Fe(II)(C_2O_4) \rightleftharpoons Fe(II)(C_2O_4)_{(Adsorbed)} \rightleftharpoons Fe(II)(C_2O_4)(aq) \quad . \qquad (6.11)$$

It is proposed that such reductive dissolution processes are promoted if the Fe(III) complex is stabilized with respect to the Fe(II) complex. This proposal is supported by unpublished work performed in systems containing cyanide (CN^-). Fe(II)-CN^- complexes are found to be ineffective in promoting dissolution. This is attributed to the greater stability of the Fe(II)-CN^- complexes than the analogous Fe(III) complexes.

It is suggested that oxalate plays a unique role among carboxylic chelating agents in that it initially promotes relatively fast direct dissolution and also facilitates electron transfer. Based on analogues with homogeneous solution electron transfer reactions involving carboxylic groups, it is suggested that the heterogeneous

reaction probably involves a bridging oxalate ligand, i.e., that the reaction proceeds by an inner-sphere electron transfer process.

Potentially, oxalate can act as a reducing reagent:

$$C_2O_4^{2-} \rightarrow 2CO_2 + 2e^- \qquad (6.12)$$

Sellers and Williams [38] studied the dissolution of oxides in aqueous oxalic acid at 140°C, such temperatures being achieved by using pressurized reaction vessels. The work indicated that at 140°C oxalic acid completely reduced solution ferric species to ferrous. It is therefore possible that at high temperatures oxalic acid acts directly as a reductive dissolution reagent, or promotes dissolution indirectly as a consequence of increasing the solution concentration of the Fe(II) species. At 30°C Baumgartner et al. [24] found that the addition of ferric ions had no impact on the duration of the induction period when light was rigorously excluded, suggesting clearly that oxalate was not acting as a solution chemical reducing agent. However, in the presence of light a photochemical reduction of ferric oxalate was observed.

The possibility remains that the initially slow dissolution of magnetite occurs as a consequence of a reductive process involving the oxalate species. However, it is more likely that this initial process is slow direct dissolution.

Both the study of Warren and Devuyst [3,8] and that of Baumgartner et al. [24] proposed that iron oxides dissolved in oxalic acid by a reductive dissolution process involving Fe(II)-oxalate complexes. In contrast, the study of nickel chromium ferrite dissolution in oxalic acid and nitrolotriacetic acid (NTA) by Sellers and Williams [38] indicated that such a process did not occur.

Sellers and Williams [38] studied the dissolution of the spinel oxide $Ni_{0.6}Cr_{0.6}Fe_{1.8}O_4$ in oxalic acid at 140°C. No evidence was found for the participation of Fe(II) oxalate species in a reductive dissolution process. The addition of ferrous ions to the oxalic acid at the commencement of a dissolution experiment produced only a slight increase in rate. At most, the SIRD reaction involving a Fe(II) oxalate complex could only be a minor contributor to the dissolution process, and this could be a consequence of the elevated temperature or the spinel oxide composition. The authors make no attempt to explain the absence of a significant reductive dissolution process involving Fe(II) oxalate.

Segal and Sellers [21] performed a detailed investigation of the kinetics of metal oxide dissolution. The studies used stoichiometric nickel ferrites produced by a two-step method involving precipitation, and calcination at 1000-1400°C in an argon atmosphere.

Dissolutions were performed in solutions of the strong reducing agent tris(picolinato)-vanadium(II). The rate of oxide

dissolution was found to be directly proportional to the instantaneous surface area, indicating that the rate-determining process occurred at the particle surface. Initially, the solution iron:nickel ratio greatly exceeded the stoichiometric value of 2, indicating that initially iron was preferentially released. The ratio rapidly returned to a value of $\sim$ 2, indicating congruent dissolution was quickly established.

The reaction rate was linearly dependent upon the concentration of $[V(II)(pic)_3^-]$. The authors state that this clearly established the rate-determining step as electron transfer at the oxide surface [115]. It was claimed that the relative substitution inertness of V(II) makes it virtually certain that the reaction proceeded by an outer-sphere electron transfer,

$$V(II)(pic)_3^- + >Fe(III) \rightarrow V(III)(pic)_3 + >Fe(II) \quad . \qquad (6.13)$$

The reaction rate increased significantly as the pH decreased; this pH dependence was attributed to a proton adsorption process at surface sites that followed a Langmuir adsorption isotherm.

On the basis of the experimental evidence the following reaction mechanism was proposed:

$$>S + (V(II)(pic)_3)^- \rightarrow >S^- + V(III)(pic)_3 \qquad (6.14)$$

$$>S + H^+ \rightleftharpoons >S{-}{-}H^+ \qquad (6.15)$$

$$>S - H^+ + (V(II)(pic)_3)^- \rightarrow >S{-}H + V(III)(pic)_3 \qquad (6.16)$$

$$>S + L \rightleftharpoons >S{-}L \qquad (6.17)$$

$$>S - L + (V(II)(pic)_3)^- \rightarrow >S{-}L^- + V(III)(pic)_3 \qquad (6.18)$$

where: L represents picolinate without regard to its state of protonation, and >S indicates a surface site.

Surface studies of partially dissolved crystals indicated that dissolution occurred preferentially at surface defects, suggesting that oxide morphology influenced the rate of oxide dissolution through the availability of high energy sites, such as kinks, ledges, or screw and edge dislocations.

The dissolution of the nickel component in the spinel is thought to occur by an under-cutting process, so that the nickel ions dissolve once the nearest iron neighbours have been removed. This mechanism is thought to explain the short-lived, but initially highly incongruent dissolution.

Inverse spinels such as nickel ferrite contain ferric ions in both octahedral and tetrahedral sites. It is considered probable that one of these sites is favoured as the recepient of the electron transferred in a reductive dissolution. However, on the basis of the

experiments performed by Segal and Sellers [21,22], it is not possible to distinguish between the reactivities of the two ferric ion types.

Segal and Sellers [22] note that crystal field theory predicts that ferric to ferrous ion reduction in an octahedral environment is energetically more favourable than at tetrahedral sites. Also, a ferric ion partially coordinated by water or hydroxide ions at the surface requires less ligand reorganization when the reduction involves an octahedrally coordinated ion. In work that remains unpublished, Sellers attempted to determine the relative susceptibility of octahedral and tetrahedral ferric ions to reduction by studying the dissolution of both inverse (Fe_3O_4, $NiFe_2O_4$, $CoFe_2O_4$) and normal ($MnFe_2O_4$) ferrites. These ferrites differ in their distribution of ferric ions between the two crystallographic sites. All Fe(III) ions in $MnFe_2O_4$ occupy octahedral sites, but in Fe_3O_4, $CoFe_2O_4$, and $NiFe_2O_4$ the Fe(III) ions are divided equally between octahedral and tetrahedral sites. Under otherwise identical conditions, $MnFe_2O_4$ is found to dissolve at twice the rate of $NiFe_2O_4$ or $CoFe_2O_4$, in proportion to the increased concentration of octahedrally located Fe(III) ions. This supports the crystal field theory prediction that reduction will occur preferentially at octahedrally situated Fe(III) ions, although the authors themselves state that such small changes in rate could be attributed to many other factors.

Particularly for the purposes of nuclear reactor decontamination, a radiation sustained reductive dissolution process has many merits. Buxton, Rhodes and Sellers [37] demonstrated that the reductive

dissolution of colloidal α-Fe_2O_3 and Fe_3O_4 in aqueous acids can be induced by radiation generated radicals. The strongly reducing radical $(CH_3)_2\dot{C}OH$, generated in situ, was used through these studies.

The results indicate that the dissolution of α-Fe_2O_3 and Fe_3O_4 is rate limited by the diffusion of radicals to the oxide particle. Radical-radical reactions and radical reactions with solution species mean that only a small fraction of the radicals generated react with the oxides. The addition of Fe(II)-Fe(III)-EDTA to such systems proved a very effective way of increasing the efficiency of the radical instigated reduction process,

$$(CH_3)_2\dot{C}OH + Fe(III)\text{-}EDTA \rightarrow Fe(II)\text{-}EDTA + (CH_3)_2CO + H^+ \qquad (6.19)$$

$$>Fe(III) + Fe(II)\text{-}EDTA \rightarrow >Fe(II) + Fe(III)\text{-}EDTA \qquad (6.20)$$

$$>Fe(II) \rightarrow Fe(II) \qquad (6.21)$$

$$Fe(II) + EDTA \rightarrow Fe(II)\text{-}EDTA \ . \qquad (6.22)$$

The radical causes the reduction of Fe(III)-EDTA species to Fe(II)-EDTA, which then serves as the reducing agent causing the reductive dissolution of magnetite.

The results show that as the dissolution proceeds the ferrous ion released to solution causes the reaction rate to progressively rise as the Fe(II)-EDTA concentration is increased.

Further support for the operation of a solute induced reductive dissolution (SIRD) reaction in EDTA solutions comes from the work of Regazzoni and Matijević [36]. The dissolution of a non-stoichiometric nickel ferrite ($Ni_{0.53}Fe_{2.47}O_4$) in mildly acidic EDTA solutions at 80°C was investigated. The dissolution rates were observed to rise throughout the dissolution process. This was taken to suggest that Fe(II)-EDTA species generated by the release of iron participate in a reductive dissolution process. Further, it was observed that the addition of hydrazine to the EDTA solution significantly promoted the dissolution process. It was proposed that this effect arises due to hydrazine reduction of Fe(III)-EDTA complexes to Fe(II)-EDTA complexes. The operation of this reductive dissolution process is further supported by the observation that in the presence of mild solution oxidizing agents only a slow oxide dissolution occurs.

The studies presented in this section clearly demonstrate that magnetite can dissolve in both oxalate and EDTA solutions by a rapid SIRD process involving Fe(II) complexes. This reaction is orders of magnitude faster than direct dissolution by acidic solutions of the same complexing agents.

The work of Baumgartner et al. [24] suggests that this process is sensitive to pH, the dissolution rate increasing dramatically as the pH is reduced from 8 to 4. The rate of this process is inhibited by the presence of solution oxidizing agents and promoted by the presence of reducing agents. This is due to their impact upon the solution concentration of Fe(II) complexes.

6.3 SOLUTE INDUCED REDUCTIVE DISSOLUTION (SIRD) INVOLVING SIMPLE REDUCING AGENTS

Baumgartner et al. [39] studied the dissolution of magnetite in thioglycollic acid (mercaptoethanoic acid, $HS{\cdot}CH_2{\cdot}COOH$). This reagent is a very strong complexing agent for iron, particularly at high pH. Both Fe(II) and Fe(III) are complexed, the latter being reduced by intramolecular electron transfer.

The dissolution of magnetite in thioglycollic acid proceeds by the following overall reaction:

$$Fe_3O_4 + 5HSCH_2CO_2H \rightarrow 3Fe(II)(SCH_2CO_2) + HO_2CCH_2SSCH_2CO_2H + 4H_2O \quad . \qquad (6.23)$$

The kinetic data obtained during dissolution experiments was consistent with the shrinking core model of dissolution, suggesting strongly that the rate of reaction was proportional to the instantaneous surface area of oxide. The rate of reaction exhibited a dependence upon

thioglycollate concentration. The form of the dependence was thought to originate from an adsorption process controlled by a Langmuir type adsorption isotherm.

The results and mechanisms proposed by Baumgartner et al. [39] do not distinguish between a solution or a solid state reduction of Fe(III) to Fe(II). Thus, thioglycollate could be acting as a reductive dissolution reagent or simply as a strong complexing agent that reduces Fe(III) once dissolved.

Oxalate can also act as a reducing agent, equation (6.12). The work of Sellers and Williams [38] indicates that, at 140°C, oxalic acid completely reduces solution Fe(III) species to Fe(II), while the work of Baumgartner et al. [24] indicates that at 30°C this reaction is negligible. Therefore, it is possible that at high temperatures oxalate acts directly as a reductive dissolution reagent,

$$2(>Fe(III)) + C_2O_4^{2-} \rightleftharpoons (>Fe(III))_2\text{-}C_2O_4^{2-} \qquad (6.24)$$

$$(>Fe(III))_2\text{-}C_2O_4^{2-} \rightarrow 2(>Fe(II)) + 2CO_2 \quad . \qquad (6.25)$$

During an investigation of spinel oxide dissolution in oxalic acid at 140°C, Sellers and Williams [38] were unable to distinguish between: (i) a direct dissolution process followed by solution reduction of Fe(III), and (ii) a reductive dissolution process involving oxalate.

The reductive dissolution of oxides directly by simple reducing agents has yet to be demonstrated. Such reactions however, remain strong possibilities in several incompletely understood dissolution processes.

6.4 AUTOREDUCTION

In 1925 Evans [99] found that electrochemical reduction of iron oxide films in hydrochloric acid produced a progressive film thinning. In 1930 Evans [100] observed that while iron oxide films on iron dissolved rapidly in dilute sulphuric acid, identical films detached from the substrate iron resisted dissolution. It was proposed that rapid destruction of the oxide film on iron was due to the establishment of local cells at discontinuities in the film, the ferric oxide undergoing cathodic reduction, the iron, anodic dissolution. Thus, all the iron species passed into solution as Fe(II), equations (6.26 and 6.27)

$$>Fe(0) \rightarrow Fe(II)(aq) + 2e^- \quad \text{Anodic Half-Reaction} \qquad (6.26)$$

$$>Fe_2O_3 + 6H^+(aq) + 2e^- \rightarrow 2Fe(II)(aq) + 3H_2O \quad \text{Cathodic Half-Reaction.} \qquad (6.27)$$

Evans [101] supported this proposal with electrochemical experiments with oxide films grown on iron in acidic solutions. Film dissolution was promoted by the application of cathodic potentials and prevented by

applied anodic potentials. It was observed that strong solution oxidizing agents had a similar inhibiting effect on the dissolution process.

The term "autoreduction" originated from a paper published by Pryor and Evans [102] in 1930. The term is used exclusively for situations in which film and substrate dissolution processes are coupled. This paper represented the first detailed study of autoreductive dissolution. Experiments were performed with iron oxide films composed principally of hematite (α-Fe_2O_3). The films were grown on iron disks in air at 300°C, the film thicknesses ranging from 440-725 Å. These films displayed interference tints, the colour of the tint providing a semiquantitative determination of film thickness. Dissolution experiments were performed in dilute hydrochloric acid, and the autoreductive process followed visually. The autoreductive dissolution of very thin films occurred uniformly across the disk surface. For thicker films autoreduction was not uniform, but could be seen to originate and spread outwards from certain surface points. This behaviour was attributed to the anisotropic growth of the original oxide film caused by the grain structure of the iron. This was readily apparent on microscopic examination of the films.

It was recognized that the thicker films used were duplex in form, a layer of magnetite existing between the iron and the outer hematite layer. Following an initial rapid autoreductive dissolution process, these thicker films left a black residue on the iron that was

extremely resistant to reductive dissolution. This residue was eventually released to solution as a solid due to undermining. It was noted that this solid was highly magnetic. It was suggested that the residue was magnetite.

Pryor and Evans proposed that the thin films conducted electrons uniformly and rapidly to the oxide solution interface, causing uniform dissolution. For thicker films it was proposed that the greater resistance of the film caused reductive dissolution at discontinuities or places where the film was abnormally thin.

The studies revealed that the rate of autoreduction increased rapidly with increasing temperature. The activation energy was calculated to be 35.6 $kJ \cdot mol^{-1}$.

A strong pH effect was observed, the autoreductive dissolution process requiring < 2 seconds at pH = 1, while at pH = 4 no noticeable dissolution occurred in 24 hours.

The corrosion potential was monitored throughout the autoreductive dissolution processes. It was proposed that during autoreduction the cathodic oxide dissolution process was highly polarized, while the anodic metal dissolution reaction was only slightly polarized. Under these circumstances the cathodic reduction of oxide would be the rate-controlling process. The very significant pH effect on the rate of

autoreduction was explained by the significant pH dependence of the cathodic oxide reduction process, equation (6.27).

Pryor and Evans [103] performed a second investigation of autoreduction. On this occasion separate but electrically connected electrodes of hematite and iron were used. The dissolution process in acid solutions was investigated by intermittently monitoring the current flowing between the electrodes and measuring the potential of the electrodes. By comparing the current passed to the quantity of iron released to solution the efficiency of the autoreduction process could be determined. There are two alternative cathodic processes available in such systems in addition to the reductive dissolution of hematite, equation (6.27): (i) the reduction of dissolved molecular oxygen,

$$O_2 + 4H^+ + 2e^- \rightarrow 2H_2O \qquad (6.28)$$

and (ii) the reduction of protons to hydrogen gas

$$2H^+ + 2e^- \rightarrow H_2 \quad . \qquad (6.29)$$

The efficiency measures the percentage of the anodic current generated, equation (6.26), that is consumed by the oxide reduction reaction, equation (6.27). The cathode consisted of a measured quantity of hematite floating on a pool of mercury, and an iron plate was used as the anode. Various samples of hematite, formed by a precipitation process and calcined at various temperatures, were used.

The results indicated that proton reduction was insignificant. However, the current efficiency was observed to change as the concentration of dissolved oxygen changed. With oxygen present, the current efficiency never exceeded 50% and seldom 25%. It was noted that these low efficiencies could, to some extent, be an artifact of the experiment, with the large mercury surface area available for oxygen reduction, equation (6.29).

The rate of reductive dissolution and the percentage efficiency decreased as the calcining temperature of the hematite increased. It was also observed that the efficiency initially falls rapidly as a function of time during dissolution.

Work by Bevan, Shelton and Anderson [104] found that the surface conductivity of hematite greatly exceeds the bulk conductivity, and that this is largely due to the high concentration of defects at the surface. Increased calcining temperatures reduce the concentration of surface defects and therefore decrease the surface conductivity in addition to reducing the number of active sites for dissolution. Therefore, both the initially rapid decline in dissolution rate and the efficiency can be attributed to the dissolution of the surface layer with a high concentration of defects. Pryor and Evans proposed that for solutions with a pH < 2, the rate of reductive dissolution is controlled by the surface conductivity, and hence, the concentration of defects.

Both the efficiency and the rate of the reductive dissolution process increased as the pH decreased. Both oxygen reduction, equation (6.28), and the reductive dissolution of hematite, equation (6.27), are promoted as the pH decreases. However, it appears that the oxygen reduction rate becomes limited by oxygen depletion at the electrode surface. Therefore, as the pH decreases the oxygen reduction process becomes proportionally less significant, and the efficiency rises as a consequence.

The dissolution behaviour in sulphuric, perchloric and hydrochloric acids was investigated, the results being identical within the limits of experimental error.

The authors comment on the possible identity of the rate-controlling process during autoreduction, suggesting that the oxide dissolution process probably involves two stages, an initial reduction reaction followed by direct dissolution of the reduced oxide. They claim that galvanostatic reduction of hematite films can be achieved at a pH at which no autoreduction is observed. This indicates that under these conditions direct dissolution of the reduced oxide cannot be the rate-controlling process.

The authors did not attribute much significance to the identical dissolution behaviour observed in the three acids studied, assuming that all three were essentially non-complexing. However, subsequent studies have demonstrated significant differences in the

abilities of these anions to promote the direct dissolution of hematite, Warren et al. [4,6,91]. The independence of the dissolution rate on the identity of the anion is further evidence that the direct dissolution of reduced oxide is not rate controlling.

A third paper by Pryor [105] proposed a mechanism for the reductive dissolution of hematite. The principal reaction steps are envisaged to be: (i) the conduction of electrons through the oxide; (ii) the reduction of the surface layers of oxide; and (iii) the direct dissolution of the reduced oxide. It is proposed that step (i) is likely to be rate controlling only for thick oxide films. The previous study indicated that step (iii) was not rate limiting at low pH. On the basis of this evidence, Pryor proposed that step (ii) will mainly control the rate of the reductive dissolution of hematite. He proposed that the electrons generated by metal dissolution, equation (6.26), did not reduce the oxide Fe(III) ions directly, but that the electrons discharged hydrogen ions on the oxide surface,

$$2H^{+}_{(aq)} + 2e^{-} \rightarrow 2H_{(adsorbed)} \quad . \tag{6.30}$$

The hydrogen atoms then reacted with the oxide to liberate water,

$$>O^{2-} + 2H_{(adsorbed)} \rightarrow H_2O + 2e^{-} \quad , \tag{6.31}$$

and the electrons from this process then brought about Fe(III) reduction

$$>Fe(III) + 2e^- \rightarrow >Fe(II) \quad . \qquad (6.32)$$

It was proposed that this process produced accelerated oxide dissolution by the continual creation of surface defects.

The cathodic behaviour of iron, magnetite (Fe_3O_4), hematite (α-Fe_2O_3) and maghemite (γ-Fe_2O_3) was investigated by Stockbridge, Sewell and Cohen [106]. Films of each oxide were grown on atomically smooth iron electrodes and reductively dissolved using electrochemical techniques. The current efficiencies for hematite, maghemite and magnetite were $\sim$ 100%, 40-60% and 8-17%, respectively. For the magnetite films the variation in efficiency was attributed to changes in film morphology and thickness. It was found that the efficiency decreased as the film thickness increased. Similar experiments were performed with a single, natural crystal of magnetite, current efficiencies of $< 5\%$ being obtained.

An open-circuit electrochemical investigation of magnetite film dissolution was performed. Two well defined potential plateaus were observed on the corrosion potential versus time plots. It was proposed that autoreduction was occurring and that the first potential arrest involved the coupling of metal dissolution, equation (6.27), to the cathodic reduction of a surface layer of maghemite (γ-Fe_2O_3)

$$>\gamma\text{-}Fe_2O_3 + 6H^+(aq) + 2e^- \rightarrow 2Fe(II)(aq) + 3H_2O \qquad (6.33)$$

while the second potential arrest was due to the coupling of metal dissolution and the reductive dissolution of magnetite

$$>Fe_3O_4 + 8H^+(aq) + 2e^- \rightarrow 3Fe(II)(aq) + 4H_2O \quad . \qquad (6.34)$$

Although an autoreductive dissolution process is almost certainly occurring, the suggestion that autoreductive processes involving reactions (6.33) and (6.34) are responsible for the potential plateaus is suspect.

Shoesmith et al. [34] studied the dissolution of magnetite films grown on iron in acidic solutions of EDTA and citrate. The open circuit potential was followed throughout the dissolution process. The iron release data and the corrosion potential clearly defined three distinct phases during the dissolution process.

In region I the corrosion potential was > -100 mV vs SCE and no detectable release of iron was observed. The duration of this region ranged from ∿ 30 minutes for porous films up to several hours for non-porous films. It was thought that during region I a barrier of oxide at the base of pores prevented solution penetration to the metal.

Region II commenced when the solution penetrated the barrier layer of oxide initiating the autoreductive dissolution of magnetite, equations (6.26) and (6.34). It was demonstrated that magnetite

reduction was the only thermodynamically feasible cathode reaction available at the potentials observed.

It was proposed that the iron release rate was potential dependent, clearly identifying an electrochemical process as the rate-controlling step. The metal dissolution reaction, equation (6.26), was claimed to be the potential determining reaction during region II. The dissolution behaviour was consistent with potential control by the metal dissolution reaction occurring at the base of constricted pores. The local chemistry within the pore was thought to be significantly different from the solution bulk due to the restricted transport of reactants and products to and from the pore. The autoreduction was claimed to be rate restricted during region II by the limited area of metal exposed. The oxide dissolution process in region II was inefficient, only 10-15% of the oxide being dissolved. Increasing the temperature was shown to raise the efficiency to 60% at 85°C. Region III commenced with an abrupt cathodic shift in potential. This was attributed to the increased exposure of metal, brought about in region II, causing the initiation of active corrosion, equations (6.27) and (6.30). It was proposed that an inefficient reductive dissolution of oxide persisted in region III causing the slow dissolution observed.

Although unable to propose any definite dissolution mechanism on the basis of the experimental results obtained, Shoesmith was able to demonstrate that the mechanism of autoreduction proposed by Pryor [105] involving the participation of atomic hydrogen was not thermodynamically

feasible during region II. Thus, during this region the electrons liberated by metal dissolution must directly reduce the magnetite Fe(III) ions.

Shoesmith et al. [40] studied the dissolution of magnetite films on iron in oxalic acid and oxalic acid/EDTA mixtures. The potential transients observed in this study were similar in general form to those observed in EDTA and citrate solutions. It was proposed that at high oxalate concentrations the dominant dissolution process occurring in the region prior to the major cathodic shift in potential was the direct dissolution of magnetite,

$$>Fe_3O_4 + 6H^+(aq) + 2HC_2O_4^-(aq) \rightarrow 2(FeC_2O_4)^+(aq) + Fe^{2+}(aq) + 4H_2O \quad . \qquad (6.35)$$

This dissolution process at 25°C removed between 40 and 50% of the magnetite present on the disk.

Reductive dissolution involving oxalate decomposition to CO_2, equation (6.12), was shown to be thermodynamically feasible, but no evidence could be found for its occurrence.

Rapid potential fluctuations were observed in solutions of oxalic acid prior to the major cathodic shift in potential. This was attributed to a pore-opening and repassivation process caused by the local precipitation of β-ferrous oxalate dihydrate. Microscopic and

X-ray diffraction studies confirmed the presence of this precipitate. It was observed that the presence of EDTA reduced the precipitation of ferrous oxalate. This period of potential fluctuation was followed by a sustained cathodic shift occurring when active corrosion became dominant.

Autoreductive dissolution of magnetite was thought to be the dominant dissolution process in EDTA solutions containing low concentrations of oxalate. This was attributed to the low surface coverage by oxalate which was assumed to be too low to cause significant direct dissolution.

The presence of oxalate in EDTA solutions significantly increased the rate and efficiency of oxide removal. It was postulated that oxalate facilitates dissolution by adsorbing on the oxide surface. The decrease in the dissolution rate following the major cathodic shift in potential was thought to arise from a potential-induced desorption of oxalate, leading to a reduction in the significance of direct dissolution and an increase in the relative significance of autoreduction.

The work of Pryor and Evans provided many insights into the reductive dissolution of hematite films on iron. They identified the cathodic oxide reduction process as the rate-controlling process, and explained the strong pH dependence in terms of its impact upon this half-reaction. Although the films were very thin, the importance of local dissolution processes was established. The conductivity of the

oxide was recognized and thought to play an important part in the dissolution process. It appeared that, for hematite, the conductivity could be the limiting process during the autoreduction process at low pH. The mechanism proposed by Pryor [105] for the autoreductive dissolution of hematite involves the participation of atomic hydrogen.

Pryor and Evans [103], Stockbridge et al. [106] and Shoesmith et al. [34] galvanostatically reduced iron oxides and oxide films on iron. The efficiency of the process varied as a function of chemical identity of the oxide, oxide preparation, oxide film thickness, oxide film morphology, pH, temperature, solution speciation, concentration of dissolved oxygen and the applied current. The reductive dissolution of magnetite was observed to be inefficient, typically $< 15\%$ of the current going to oxide reduction. Stockbridge attributed this to the high conductivity of magnetite permitting the passage of electrons right through the film to cause proton reduction. Shoesmith et al. [34] showed that for the reductive dissolution of magnetite films on iron in EDTA solutions, the mechanism proposed by Pryor involving hydrogen atoms was not thermodynamically feasible. It appears most probable that such reactions involve the direct reduction of oxide Fe(III) by the electrons generated by the anodic dissolution process.

CHAPTER 7

EXPERIMENTAL

7.1 GROWTH OF OXIDE FILMS ON CARBON STEEL DISKS

7.1.1 Disk Preparation

A large number of disks were machined from CS-A-105 grade carbon steel, the disk diameter being 12.5 mm, the disk depth 4 mm. One flat surface of the disk featured a centrally located short threaded stub, permitting good electrical connection to the disk.

Following machining, the disks were thoroughly degreased. The flat surface and sides of the disk were polished using grades of abrasive paper down to 600 grit. This procedure was continued until all machining marks were removed, leaving a surface with a mirror finish.

7.1.2 Autoclave Film Growth Process

The degreased and polished disks were located on Teflon mounts attached to an autoclave lid, Figure 7.

The autoclave was loaded with a 1 $mol \cdot dm^{-3}$ solution of sodium hydroxide in triply distilled water. The autoclave was filled to a

level that ensured immersion of the disks throughout the oxide film growth process.

After sealing, the gas space above the solution was evacuated, following which the gas void and solution were purged with hydrogen for 30 minutes. The hydrogen pressure was adjusted to 150 $kN \cdot m^{-2}$ ($\sim$ 22 psi) prior to heating, ensuring magnetite, as opposed to hematite, film growth. The internal autoclave temperature was monitored and a temperature of 275°C maintained for 14 days.

Following the oxide film growth process, the autoclave was allowed to cool and the disks removed. The disks were repeatedly washed with triply distilled water to remove the film growth solution.

7.1.3 Magnetite Film Growth Mechanism

A factor that has been found to have a major impact on the morphology of the oxide films grown during this process is the surface pretreatment of the autoclave carbon steel liner.

The surfaces of a clean carbon steel liner exposed to the aqueous alkali corrode during the course of the disk preparation process, releasing significant quantities of iron into the autoclave solution. At the end of this growth process, inspection of the disks reveals a surface completely covered with numerous discrete well-formed magnetite crystals, Micrographs 1 and 2. The liner acts as a source of

iron, causing the bulk solution iron concentration to rise rapidly to levels at or close to saturation. The liberation of iron from the concurrent disk corrosion leads to local supersaturation of the solution at the disk surface, permitting nucleation and growth of discrete magnetite crystals on the disk surface.

It is probably the disk itself rather than the liner that provides the majority of the iron for the growth of these upper-layer crystals. The discrete crystal growth process under these conditions is established quickly enough to prevent the growth of passivating film on the disk surface. A base-layer of oxide does form, but is sufficiently porous to permit the continued growth of the upper-layer crystals. Close inspection of scanning electron micrographs of these disks following partial dissolution of the upper-layer crystals reveals the presence of a porous base-layer oxide beneath the upper-layer, Micrograph 13. This fact, linked with the obvious porosity of the upper-layer crystals, suggests that this oxide film would not act as an impermeable barrier to ions in an aqueous medium. This type of disk is referred to as a double-layer disk, Figure 8.

At the end of the process described above, the inner surface of the liner is covered with a thin but mechanically robust film of magnetite. If the liner is used in this condition in an otherwise identical film growth process, the disk surfaces are found to be devoid of the upper-layer of crystals, Micrographs 3 and 4. The absence of these regular crystals is presumably because the iron supply from the

liner to the bulk solution is much more restricted under these conditions. Thus, the bulk solution iron concentration does not rise to levels at, or close to, saturation prior to the establishment of a passive film on the disk surface. Once the iron supply from the disk surface has been inhibited by this film formation, local supersaturation of the solution at the disk surface is not achieved. Hence, no nucleation and growth of discrete magnetite crystals on the disk surface is observed.

This base-layer oxide does not feature the crystallinity of the upper-layer crystals. Close inspection of this base-layer oxide reveals the still discernable scratch marks introduced to the metal during polishing, Micrograph 4, supporting the claim that this base-layer oxide grows via a solid-state process, not via metal dissolution followed by crystal growth as in the case of the upper layer. Scanning electron micrographs indicate that this oxide layer has no obvious porosity, suggesting it might be a more impermeable barrier in aqueous systems than the oxide films on double-layer disks. This type of disk is referred to as a single-layer disk, Figure 8.

7.1.4 Influence of Metal Structure on Magnetite Film Growth

The grade of carbon steel used to fabricate the disks used throughout these experiments is CS-A-105. This is one of a class of hypo-eutectoid plain carbon steels, i.e., a steel containing less than 0.8 atomic percent carbon. When such steels are slow cooled, two

distinctly different types of grain precipitate, alpha-iron and pearlite. The proportion of pearlite increases as the carbon content of the steel rises, until the steel is composed entirely of pearlite at 0.8 atomic percent carbon. Pearlite grains contain alpha-iron and iron carbide, which appear as discrete alternating bands within the grain. Thus, pearlite grains have a regular lamellar structure, the volume of the grain being divided approximately equally between the two components. The metal surface will dissect many pearlite grains, the presence of which can be revealed by various forms of chemical etching. The iron carbide component of the grain resists dissolution under conditions where the alpha-iron component will dissolve freely. Selective dissolution in this fashion leaves exposed ridges of iron carbide within the boundaries of pearlite grains. During the oxide film growth process it is highly probable that film formation over dissected pearlite grains will be affected both by the diminished iron release and the intrusions of insoluble iron carbide.

Inspection of scanning electron micrographs of the oxide films prior to oxide dissolution show a faint but discernable patchiness, Micrograph 3. This may well be caused by the presence of pearlite grains. Close inspection, Micrograph 4, indicates that the oxide film within these patches appears more porous than the film formed over the remainder of the carbon steel surface. Thus, it can be seen that the structure of the base metal plays a significant role in determining the nature of the oxide film produced.

When the oxide film on a carbon steel disk is subjected to dissolution, solution penetration to the metal would be expected to occur at sites that exhibited thin and/or porous oxide films. Figure 9 illustrates the impact of steel structure on the film growth and subsequent dissolution reactions, as observed in this report.

7.2 SOLUTION IRON CONCENTRATIONS

7.2.1 Significance of the Total Iron Release

The measurement of the total iron concentration at intervals throughout the course of a dissolution experiment provides some indication of the extent of oxide dissolution. The iron release data require careful interpretation. Both oxide and metal dissolution processes can contribute to increases in the solution iron concentration. Until metal exposure only oxide dissolution releases iron to solution, and after metal exposure both oxide and metal dissolution can release iron. The relative significance of these processes is influenced by the mechanism of oxide dissolution, film structure, solution composition, temperature and other parameters. If autoreduction is the only dissolution process, then the stoichiometry of this mechanism requires that one quarter of the iron released originates from the metal.

7.2.2 Significance of the Fe(II):Fe(III) Ion Ratio

The rate of a ligand-bridge assisted dissolution (LBAD) process would be expected to show a rate dependence upon the solution ferrous ion concentration. In an attempt to determine whether this mechanism was occurring during the dissolution process, a series of dissolution experiments was performed in which the initial solution ferrous concentration was systematically varied. If the LBAD process contributes significantly to oxide dissolution, the iron release rate should increase as the initial ferrous concentration is increased. This procedure necessitates the quantitative determination of the iron release to a solution that initially contains a significant background concentration of iron. Additionally, determining the quantities of ferrous and ferric ions liberated from the disks during the dissolution process provides valuable information as to which dissolution mechanism is occurring. Quantitatively determining the ferrous and ferric ion releases during dissolution under these experimental conditions is a demanding task.

7.2.3 The Impact of Dissolved Oxygen on the Ferrous:Ferric Ion Ratio

Determining the quantities of ferrous and ferric ions liberated during film dissolution is complicated by the rapid oxidation of ferrous to ferric ions by dissolved molecular oxygen in the presence of EDTA, Kurimura et al. [107]. Thus, to ensure that the ratio of ferric to ferrous ions released during the dissolution process was not

distorted prior to analysis, it was necessary to rigorously exclude oxygen from all cell solutions. This difficulty was compounded by the fact that the dissolution process produced only small quantities of iron in several hundred cubic centimeters of solution.

7.2.4 Experimental Procedures Used to Exclude Oxygen

It was determined that normal purging of aqueous solutions with ultra high purity argon for 72,000 seconds (20 hours) is ineffective at removing the initial inventory of dissolved oxygen, as the oxygen concentration at the end of this period exceeded 5 ppm (1.5×10^{-4} mol$\cdot$dm^{-3} O_2). To reduce the concentration of dissolved oxygen to acceptable levels, it was found necessary to degas all solutions by reflux. Triply distilled water was refluxed in a gas tight system with a continuous UHP argon purge. Following a reflux process lasting not less than 3 hours, the water was allowed to cool and was stored for subsequent use in the reflux flask with a continuous argon purge. Degassing of aqueous solutions by this method was found to reduce the dissolved oxygen concentration to $\leq$ 0.05 ppm ($\leq 1.5 \times 10^{-6}$ mol$\cdot$dm^{-3} O_2).

Transfer of the water to the electrochemical cell was achieved without exposure to air. The transfers were made to argon-purged sealed cells that had been prefilled with measured quantities of the appropriate reagents in dry solid form.

The use of a rotating electrode assembly was precluded due to the substantial oxygen ingress that would occur through the bearing assembly. A static electrode assembly that could be raised and lowered within the cell without breaking cell containment was used. This permitted the cell to be filled with the appropriate volume of water without immersion of the disk. The experiment was commenced by plunging the disk electrode into the solution.

Samples were periodically taken from the cell and analyzed for ferrous and ferric ion concentrations. Samples were withdrawn into an argon-flushed plastic syringe through a stainless steel hypodermic needle. The cell containment was maintained by sampling through a rubber septum cap. The sample was immediately introduced, through a septum cap, to a small glass test tube that was continuously purged with argon.

7.2.5 Further Investigation of the Oxygen Problem

During the course of a series of experiments designed to examine the impact of the ferrous ion concentration on the dissolution of magnetite films, further information on the manner in which oxygen reacts with ferrous ions was revealed. This set of experiments entailed the systematic variation of the initial ferrous ion concentration in systems containing 1×10^{-3} mol·dm^{-3} EDTA. As previously noted, rapid oxidation of Fe(II) to Fe(III) would be anticipated if dissolved oxygen were present.

The concentration of oxygen in the solutions used was determined by means of a commercially available dissolved oxygen assay kit. The results indicated that the concentration was < 0.05 ppm (< 1.5×10^{-6} mol•dm^{-3}). The technique was not sufficiently sensitive to exactly determine the oxygen concentration. Literature evidence [108] suggests that it was highly improbable that the concentration was < 0.01 ppm (< 3×10^{-7} mol•dm^{-3}). For a reaction of overall stoichiometry:

$$4Fe^{2+} + O_2 + 4H^+ = 4Fe^{3+} + 2H_2O \qquad (5)$$

an oxygen concentration in the range 0.05 ppm (1.5×10^{-6} mol•dm^{-3}) to 0.01 ppm (3×10^{-7} mol•dm^{-3}) would be expected to cause the solution ferrous ion concentration to decrease by 6×10^{-6} mol•dm^{-3} to 1.2×10^{-6} mol•dm^{-3}.

In the experiments to be described, known masses of solid ferrous ammonium sulphate were introduced to purged EDTA solutions. Immediately after dissolution, solution samples were taken and analyzed for ferric and ferrous ion concentrations. On this basis, it was possible to quantify the extent of the initial oxidation of ferrous to ferric ions, and hence to calculate the apparent oxygen concentration in the solution.

The first disconcerting observation was that the apparent oxygen concentration was lower than could be reasonably anticipated. It would be reasonable to expect that this apparent oxygen concentration

would be fairly constant from one experiment to the next, displaying only a slight random variation. However, it was observed that the apparent oxygen concentration rose as the initial ferrous ion concentration increased. This result suggests that the consumption of the initial oxygen inventory in the solution was not complete at the lower ferrous ion concentrations used. The consequence of this is that, as the dissolution of the disk proceeds, the residual oxygen will most probably oxidize a proportion of the ferrous ion released, causing a distortion of the apparent ratio of ferrous and ferric ions.

7.2.6 Analytical Procedure to Determine the Solution Ferrous and Ferric Ion Concentrations

Procedures for the quantitative determination of both ferrous and ferric species in aqueous solutions have been developed by a number of workers including Hey [109,110] and Stucki et al. [111,112]. The analytical procedures recommended initially determine the ferrous concentration colorimetrically as the intensely red phenanthroline complex $Fe(II)(phen)_3^{2+}$. Following the ferrous determination, all ferric species are reduced to ferrous either by chemical or photochemical reduction. A second colorimetric determination yields the total iron concentration, and the ferric concentration is available by difference. No detailed studies of the susceptibility of this procedure to interference from EDTA have been identified. However, Buxton et al. [37,81] used this technique in the presence of EDTA with apparent success, employing hydroxylamine hydrochloride as the reducing agent. Buxton et

al. [37] noted that in the presence of EDTA the reduction step took 1 hour to achieve completion.

Due to lack of published information it was considered prudent to investigate the influence of EDTA upon this analytical procedure.

The reaction scheme below outlines the equilibria between the major iron complexes present in systems containing EDTA/Fe(II)/Fe(III)/ phenanthroline. It is important to know the significance of each of these species, and the rates of the interconversion processes in the solutions under investigation.

$$[Fe^{2+}(EDTA)^{n-}]^{(2-n)} + 3(phen) \rightleftharpoons [Fe^{2+}(phen)_3]^{2+} + (EDTA)^{n-}$$

$+e^-$ ⇅ $-e^-$ $\qquad\qquad$ $+e^-$ ⇅ $-e^-$

$$[Fe^{3+}(EDTA)^{n-}]^{(3-n)} + 3(phen) \rightleftharpoons [Fe^{3+}(phen)_3]^{3+} + (EDTA)^{n-}$$

The stability constants for the four complexes of principal interest at 20°C are [93]:

$$\frac{[Fe(II)(phen)_3]}{[Fe(II)][phen]^3} = 10^{21}$$

$$\frac{[Fe(III)(phen)_3]}{[Fe(III)][phen]^3} = 10^{14} - 10^2$$

$$\frac{[(Fe(II)EDTA)^{2-}]}{[Fe(II)][(EDTA)^{4-}]} = 10^{14}$$

$$\frac{[(Fe(III)EDTA)^{-}]}{[Fe(III)][(EDTA)^{4-}]} = 10^{25}$$

The stability constants indicate that in an equilibrated Fe(II)/Fe(III)/EDTA/phenanthroline system, ferrous ions will be predominantly complexed by phenanthroline and ferric ions by EDTA.

The ferrous ion determination requires the displacement of EDTA from ferrous species by phenanthroline. The success of the total iron determination depends upon the conversion of the Fe(III)EDTA complex to $Fe(II)(phen)_3$. This reaction involves reduction and ligand exchange processes. In view of the stability of the Fe(III)EDTA complex it was considered possible that reduction of this complex might be slow. This process was investigated experimentally, the results indicating that the complete conversion of Fe(III)EDTA to $Fe(II)(phen)_3$ took several hours when the reducing agent hydroxylamine hydrochloride was used. The studies further indicated that a slow reduction of ferric to ferrous species occurred in the absence of an added reducing agent. It is probable that this reduction is a photochemical process, Stucki [112].

The analytical procedure outlined provided accurate total iron values when applied to iron-EDTA solution standards. In the absence of EDTA, ferrous ion standards were also accurately determined. When

attempting to determine the relative amounts of ferrous and ferric ion released during dissolution, the greatest source of error is unquestionably rapid post-dissolution oxidation. This problem cannot be eliminated, but it can be reduced to acceptable proportions by good experimental method.

7.3.1 Electrochemical Cell

Figure 10 is a sketch of a typical electrochemical cell used for these experiments. The reference electrode used throughout these experiments was a saturated calomel electrode. The reference electrode was separated from the main body of the cell by a glass frit and length of glass capillary tubing. A Luggin capillary was used to probe the potential close to the surface of the disk electrode.

The disk was accommodated within an accurately toleranced recess at one end of a cylindrical Teflon rotor. This holder provided a liquid tight seal around the circumference of the disk, preventing solution penetration to the electrical contact. The disk surface was flush with the adjacent Teflon surface, thereby ensuring laminar flow at the rotating disk surface. These conditions allow the calculation of the Reynolds number for this experimental arrangement.

All glass cells were used throughout, ensuring minimum contamination of the cell solutions. All solutions were made using triply distilled water. The reagents used were Analar grade materials.

EDTA was always used in the form of the disodium dihydrogen salt. The cell solutions were purged with ultra high purity argon (UHP argon) for a minimum of 10,000 seconds (3 hours) unless otherwise stated.

7.3.2 Corrosion Potential Measurement

The corrosion potential was measured with a DANA model 5330 high impedance voltmeter, the input resistance of which is $\sim 10^9 \Omega$. The output from the voltmeter was fed to a chart recorder, allowing the corrosion potential to be monitored throughout the duration of the experiment. At the midpoint of the experimental program, an EG&G Model 276 interface was obtained for an EG&G Model 173 potentiostat, allowing the data acquisition to be digitized. This system has a very short sampling time, the frequency of which is controllable. Both the high impedance voltmeter and the chart recorder had relatively slow response times. Thus, these devices gave smoothed outputs, the high-frequency noise component of the signal being lost. As a consequence of the aforementioned characteristics, this equipment change radically improved the detection of natural high-frequency noise in the corrosion potential signal.

CHAPTER 8

MAGNETITE FILM DISSOLUTION IN EDTA AND Fe(II)-EDTA SOLUTIONS

8.1 INTRODUCTION

The work reported in the chapter was performed primarily to investigate the following:

(i) Examine the reproducibility of film dissolution behaviour. Previous work by Shoesmith et al. [34,40] had observed significant variations in dissolution behaviour between apparently similar magnetite film covered iron disks.

(ii) Determine the effect of film morphology on dissolution behaviour. This was investigated by performing identical experiments with both single-layer and double-layer disks. Also, by performing similar experiments with static and rapidly rotating disks.

(iii) Investigate the relative significance of autoreduction and SIRD reactions at various solution concentrations of Fe(II)-EDTA; hence, improving the general understanding of reductive dissolution processes in solutions of strong complexing agents.

8.2 GENERAL FORM OF THE CORROSION POTENTIAL-TIME TRANSIENT

For both single-layer and double-layer oxide-covered carbon steel disks the corrosion potential time relationships in 1×10^{-3} $mol \cdot dm^{-3}$ EDTA, pH $\sim$ 3, are of a common form, as shown in Figure 11. The majority of dissolution experiments were performed in aqueous EDTA solutions at a pH $\sim$ 3. For these conditions, the following general observations can be made about each of the three well defined phases.

Phase I

The exact form of the corrosion potential trace during phase I varies even for apparently identical experiments. Both well-defined plateaus and sharp anodic peaks have been observed. At present, it is not clear which parameter governs the behaviour of the corrosion potential during this phase. The value of the corrosion potential during phase I is denoted as E_1.

The duration of phase I falls in the range 30 to 200 seconds. The transition to phase II behaviour is normally rapid, involving a cathodic shift in corrosion potential of $\sim$ 100 mV. T_1 is the time at which this transition occurs.

Phase II

This phase is characterized by a sustained period of corrosion potential invariance, the value of which is in the range -30 to -140 mV. The corrosion potential (E_2) has been observed to drift slowly in both the anodic and cathodic directions during this phase.

The duration of phase II falls in the range 1000 to 2700 seconds (17 to 45 minutes). The transition to phase III behaviour is generally sharp, involving a cathodic shift in corrosion potential of > 300 mV within a period of 30 seconds. T_2 is defined as the time at which this transition occurs.

Phase III

The value of the corrosion potential during phase III is ≤ -500 mV.

8.3 STATIC SINGLE-LAYER DISKS

8.3.1 Corrosion Potential Behaviour

One noticeable feature of the corrosion potential versus time traces for single-layer disks, both at pH = 3.0±0.3 and pH = 4.7±0.3, is a slight, but sustained, cathodic drift that was consistently observed

during phase II. In all other respects the behaviour of the single-layer disks conformed well to the general description given.

A major difference between this set of experiments and the normal experimental procedure is that a rotating disk electrode holder was not used. The disk was static and the solution was agitated using a magnetic bar stirrer. Avoiding the use of a rotating disk assembly facilitated the exclusion of oxygen from the cell.

8.3.1.1 pH Effect

Only two pH values have been investigated, pH = 3.0±0.3 and pH = 4.7±0.3. The data reveal that in the presence of 1×10^{-5} mol·dm^{-3} ferrous ion a powerful pH effect was observed, Figures 12 and 13.

The general form of the corrosion potential as described in Section 8.2 was observed at both pH values. The pH change produced a significant change in the duration of phase II, as Figure 12 and 13 clearly illustrate. The change from pH = 3.0±0.3 to pH = 4.7±0.3 caused the duration of phase II to increase by a factor of $\sim$ 10.

The pH change appears to have a slight impact on the value of the corrosion potential, the potential shifting in the cathodic direction as the pH decreases.

The nature of the transition from phase II to phase III differed considerably at the two pH values studied. At pH = 3.0±0.3 the transition was extremely sharp, compared to the higher pH where the transition was rounded in form, requiring < 3,000 seconds (50 minutes) rather than < 30 seconds to complete a 500 mV cathodic shift in corrosion potential.

In contrast to the behaviour just described, no pH effect was observed in the presence of 1×10^{-4} mol·dm^{-3} ferrous ion, Figures 12 and 13. At both pH = 3.0 and 4.7 the form of the corrosion potential trace was rounded, featuring poorly defined phases.

8.3.1.2 Fe(II)-EDTA Concentration, pH ∿ 4.7

Five separate experiments were performed at pH = 4.7±0.3 with an initial ferrous ion concentration of ∿ 1×10^{-5} mol·dm^{-3}. The corrosion potential versus time traces obtained conformed well to the general description given earlier in Section 8.2. A well defined transition from phase II to phase III lasting $\leq$ 3,000 seconds was observed at times ranging from 11,000 to 15,000 seconds (190 to 250 minutes). This small variation in the duration of phase II could be readily accounted for by a variation in oxide film properties alone.

The major reason for undertaking five repetitions of the same experiment was to determine the level of consistency in the dissolution behaviour of individual disks from the same autoclave run. The

invariance of T_2 is a reassuring indication of the consistency in oxide film properties.

When the initial ferrous ion concentration was raised from $1x10^{-5}$ to $1x10^{-4}$ $mol \cdot dm^{-3}$, the duration of phase II fell dramatically to $\sim$ 350 seconds ($\sim$ 6 minutes), Figure 12. The second major impact of the rise in the initial ferrous ion concentration was a shift in the value of the corrosion potential during phase I and phase II. In both cases the potential shifted $\sim$ 100 mV in the cathodic direction.

8.3.1.3 Fe(II)-EDTA Concentration, pH $\sim$ 3.0

At this pH four experiments were performed employing three different initial ferrous ion concentrations, the results of which are shown in Figure 13.

Increasing the ferrous ion concentration from 0 to $1x10^{-5}$ $mol \cdot dm^{-3}$ caused the value of E_2 to shift $\sim$ 100 mV in the cathodic direction and the value of T_2 to decrease by a factor > 4. However, a further increase in ferrous ion concentration from $1x10^{-5}$ to $1x10^{-4}$ $mol \cdot dm^{-3}$ did not produce changes of comparable magnitude. At this higher concentration phase II was beginning to lose its definition, the corrosion potential featuring a sustained cathodic drift throughout the experiment.

8.3.1.4 Impact of pH on Fe(II)-EDTA Concentration Effect

Figures 12 and 13 clearly show a similar impact of ferrous ion concentration on the corrosion potential behaviour. In both cases the value of T_2 decreases and E_2 shifts in the cathodic direction as the initial ferrous ion concentration rises. The pH effect is clearly detectable, giving generally reduced values of T_2 as the hydrogen ion concentration rises.

As seen previously, the value of T_2 decreases by a factor > 10 when the pH is lowered from ∿ 4.7 to ∿ 3.0 in the presence of $1x10^{-5}$ $mol \cdot dm^{-3}$ ferrous ions. However, in the presence of $1x10^{-4}$ $mol \cdot dm^{-3}$ ferrous ions, there is almost no change in the duration of T_2.

There appears to be a minimum value for T_2 (300 to 500 seconds) that is maintained irrespective of the values to which the hydrogen and ferrous ion concentrations are raised. It is possible that some transport process either from the disk surface to the solution bulk, or possibly within the oxide film pores, becomes rate controlling.

8.3.2 Iron Release Behaviour

8.3.2.1 pH ∿ 4.7

For three of the five experiments performed at pH = 4.7±0.3 and an initial ferrous ion concentration ∿ $1x10^{-5}$ $mol \cdot dm^{-3}$, samples were

recovered from the electrochemical cell at regular intervals. The samples were analyzed for both ferrous and ferric ion concentrations. The results obtained are shown in Figure 14.

Emphasis was placed upon the acquisition of a sufficient number of samples prior to the conclusion of phase I (100 to 300 seconds) to give an indication of the rate of ferric and ferrous ion release during this phase. Although there is a suggestion that up to T_1 ferric ion release exceeds ferrous ion, the results must be considered inconclusive. If this observation is substantiated, it would be evidence for the operation of a ligand-bridge assisted dissolution or a direct dissolution process during phase I. The release of total iron to the conclusion of phase II, $\sim$ 12,000 seconds ($\sim$ 200 minutes), appears to be linear.

The iron release rate data shed little light on what is occurring during phase I. However, this is not the case for phase II. The data indicate that the solution ferric ion concentration remains essentially constant throughout phase II, while the ferrous ion concentration rises in an approximately linear fashion. Very similar and constant release rates of iron were observed in three repetitions of the same basic experiment.

Infrequently the experiments were allowed to proceed beyond the transition to phase III. The small amount of data obtained for the rate of iron release during phase III suggests that, at least initially,

a linear release of iron is observed, the rate being lower than exhibited during phase II.

8.3.2.2 pH ∿ 3.0

Experiments were performed at three different initial ferrous ion concentrations. Attempts to follow the release of ferrous and ferric ions proved difficult due to the short duration of the experiments, the results being generally inconclusive.

8.3.3 Post-Dissolution Disk Morphology

Study of post-dissolution disks using a scanning electron microscope (SEM) revealed that the oxide films had a patchy appearance. Close inspection revealed that this effect is due to preferential attack on the oxide at certain sites, giving rise to shallow recesses in the oxide film, typically 5-20 μm in diameter. Within the recesses it is possible to discern a regular lamellar structure (see Micrographs 5, 6 and 7), indicating strongly that these regions are partially dissolved pearlite grains. The remainder of the oxide film, ∿ 50% of the disk surface, appears relatively unaffected. The polish marks made on the carbon steel during disk preparation prior to the oxide film growth are still clearly visible following dissolution.

It is difficult to estimate the extent of oxide dissolution in the case of a single-layer disk, due to their relatively featureless

appearance. Analytical determinations of the total iron release during the course of dissolution were performed on a number of occasions. As well as can be determined, the extent of the attack, as revealed by the SEM work, correlates well with the analytically determined total iron release.

Inspection of Micrographs 5 to 8 suggests that the nature of the attack upon the oxide layer does not obviously change as either the pH or the initial ferrous ion concentration is varied. Note that Micrograph 8 shows a disk surface following dissolution in a solution containing 1×10^{-4} $mol \cdot dm^{-3}$ ferrous ions. Inspection of this micrograph reveals the presence of what appear to be a number of localized bulges in the oxide film. Presently, the origin of these features is not known. It is possible that they existed prior to the dissolution process.

8.4 STATIC DOUBLE-LAYER DISKS

8.4.1 CORROSION POTENTIAL BEHAVIOUR

8.4.1.1 General Characteristics

The corrosion potential traces conformed well to the general form described earlier in Section 8.2. A sustained corrosion potential drift in the anodic direction was observed in all experiments during phase II.

8.4.1.2 pH Effect

In the presence of $1x10^{-5}$ mol•dm^{-3} ferrous ion the pH effect for double-layer disks is very similar to that observed for single-layer disks under comparable conditions, as can be seen from Figures 12 and 13 and Figures 15 and 16. For double-layer disks the value of T_2 can be seen to decrease by a factor of > 10 as the pH is lowered from ∿ 4.7 to ∿ 3.0. The corrosion potential during phase II, E_2, shifts in the anodic direction by > 100 mV as the pH decreases (recall that the single-layer disks feature a potential shift in the opposite direction). The pH effect in the presence of $1x10^{-4}$ mol•dm^{-3} ferrous ions was not investigated for double-layer disks.

8.4.1.3 Fe(II)-EDTA Concentration, pH ∿ 4.7

Only two experiments were performed at this pH, the initial ferrous ion concentration being 0 and $1x10^{-5}$ mol•dm^{-3}. This increase in ferrous ion concentration has very little effect on the corrosion potential behaviour. The difference between the two corrosion potential traces are slight, Figure 15. The iron free system takes marginally longer to commence the phase II to phase III transition, and the corrosion potential is 10 to 50 mV more anodic throughout phase II. Both systems exhibit a prolonged phase II to phase III transition.

8.4.1.4 Fe(II)-EDTA Concentration, pH ∿ 3

A series of five experiments was performed, each experiment featuring a different initial ferrous ion concentration in the range 0 to $1x10^{-2}$ mol•dm^{-3}, Figure 16. The similarity in the corrosion potential behaviour obtained is remarkable, no discernable trend being observed in the values of T_1, E_1 and E_2 as a function of initial ferrous ion concentration. All E_2 values are within a potential range of only 40 mV. T_2 displays only a slight dependence on initial ferrous ion concentration, T_2 increasing from ∿ 1,200 to 2,200 seconds (21 to 36 minutes) as the ferrous concentration increased from 0 to $1x10^{-2}$ mol•dm^{-3}. Unlike the comparable results obtained for single-layer disks, in this instance the lowest value of T_2 is observed when the initial ferrous ion concentration is zero.

8.4.1.5 Comparison of Single-Layer and Double-Layer Disk Behaviour, pH ∿ 4.7

With the exception of systems containing ferrous ion concentrations >> $1x10^{-5}$ mol•dm^{-3}, identical experiments with single- and double-layer disks yield similar corrosion potential behaviour, Figures 12 and 15. Two differences are consistently observed.

Firstly, the direction of the corrosion potential drift during phase II. As already noted for single-layer disks, the drift is in the

cathodic direction, while that for double-layer disks is in the anodic direction.

In solutions containing an initial ferrous ion concentration of $1x10^{-5}$ $mol \cdot dm^{-3}$ the form of the phase II to III potential transition differs for the two disk types, Figures 12 and 15 . The corrosion potential trace for single-layer disks shows a well defined transition to active corrosion commencing at T $\backsim$ 12,000 seconds and lasting $\backsim$ 3,000 seconds. The transition in the case of double-layer disks commences after the same period of dissolution, but then proceeds through a protracted transition lasting $\backsim$ 15,000 seconds. The use of logarithmic scales in Figures 12 and 15 conceals the magnitude of this major effect.

8.4.1.6 Comparison of Single-Layer and Double-Layer Disk Behaviour, pH $\backsim$ 3.0

The manner in which the corrosion behaviour responds to increases in ferrous ion concentration differs very significantly between the two disk types, see Figures 13 and 16.

8.4.2 Iron Release Behaviour

8.4.2.1 pH $\backsim$ 4.7

Figure 17 shows the ferrous and ferric ion releases during dissolution in the presence of 0 and $1x10^{-5}$ $mol \cdot dm^{-3}$ added ferrous ion.

The curves are very similar in form. As already noted, a protracted transition between phases II and III is observed for both types of disk, commencing at T $\sim$ 12,000 seconds and lasting $\sim$ 15,000 seconds. Thus, in these two experiments, the iron release was followed well into phase III.

The iron release in the initial stages of the reaction proved difficult to follow. Comparing the two plots it can be seen that when the initial ferrous ion concentration is 1×10^{-5} mol$\cdot$dm^{-3} the ratio of ferrous:ferric ions in the iron released by dissolution is > 1, while in the system with no added ferrous ion this ratio is initially clearly < 1. Further experimental data are required to determine whether these observations genuinely reflect different dissolution behaviour, or arise from experimental inconsistencies.

On the basis of these iron release data, it is difficult to assess whether acceleration of the oxide dissolution occurs as a consequence of the addition of ferrous ion. The iron release rate in the solutions containing an initial ferrous ion concentration of 1×10^{-5} mol$\cdot$dm^{-3} is twice that seen in the solutions containing no added iron, this margin being maintained up to 12,000 seconds. At the conclusion of the experiments at $\sim$ 70,000 seconds, the total quantities of iron released do not reflect this initial disparity in rate, the total amounts of iron released being identical. It must be noted that active corrosion is operative for most of this period.

8.4.2.2 pH ∿ 3.0

A series of five experiments was performed, each experiment featuring a different initial ferrous ion concentration in the range 0 to 1×10^{-2} mol·dm^{-3}. Ferrous and ferric ion concentration data were obtained from the three experiments featuring the lowest initial ferrous ion concentrations, Figure 18. At the higher initial ferrous ion concentrations the background concentration became too large to permit detection of the iron arising from oxide dissolution. The results in all three cases are very similar, no significant impact of ferrous concentration upon the iron release rate is observed.

As was seen in the experiments utilizing single-layer disks, the data obtained from selectively analyzing for both ferrous and ferric ion concentrations are insufficiently accurate to provide an insight into the oxide dissolution mechanism active during phase I.

The iron release rate in the three systems studied is constant, the rate being in excess of an order of magnitude greater than the rates observed at the higher pH of 4.7±0.3. Although the time scale is significantly extended at the higher pH, the form of the iron releases is very similar (compare Figure 17 with Figure 18). The total amount of iron released up to T_2 is approximately equal at pH ∿ 3.0 and ∿ 4.7, the increase in iron release rate caused by falling pH being compensated for by the decreasing value of T_2.

It should be noted that the total amount of iron dissolved appears to rise slightly as a function of the initial ferrous ion concentration, although iron release rate data are only available for initial ferrous ion concentrations of 0, 3.3×10^{-5} and 1.9×10^{-4} $mol \cdot dm^{-3}$. The total quantities of iron dissolved at time T_2 are 9.7×10^{-6}, 11.2×10^{-6} and 13.1×10^{-6} moles, respectively.

8.4.2.3 Comparison of Single-Layer and Double-Layer Disk Behaviour, pH $\sim$ 4.7

The iron release data reinforce the similarity in behaviour between the single-layer disks and double-layer disks up to 12,000 seconds (200 minutes). Both the total amount of iron released and the amount of ferrous ion released for the two disk types are very similar, the majority of the iron being released in the form of ferrous ions, compare Figure 17 with Figure 14. This is consistent with the similarity in corrosion potential behaviour, up to $\sim$ 12,000 seconds, previously noted.

For single-layer disks the rate of iron release slowed following the rapid transition to phase III behaviour. For double-layer disks the rate of iron release increased as the slow phase II to phase III transition commenced, although data are only available for the first 6,000 seconds (100 minutes) of this transition.

8.4.3 Post-Dissolution Disk Morphology

Due to the initial presence of discrete well formed magnetite crystals, a reasonable measure of the attack upon the upper layer of crystals could be obtained by inspection of post-dissolution disk scanning electron micrographs.

Table 8.1 indicates how the post-dissolution appearance of the upper layer of crystals changed as the initial ferrous ion concentration was systematically varied. Some dissolution was observed in solutions free from added ferrous ions, only a modest increase in the extent of oxide dissolution being observed as the ferrous ion concentration increased. At the highest initial ferrous ion concentration used, the attack appears to be significantly more aggressive, patches of the base layer of oxide being exposed. When viewing these figures, the values of T_2 (given in Table 8.1) should be taken into consideration, remembering that for these experiments the value of T_2 defines the duration of the experiment.

8.4.4 Summary of Corrosion Potential Behaviour

8.4.4.1 pH Effect

In the presence of 1×10^{-5} mol·dm^{-3} ferrous ion the corrosion potential behaviour of both single-layer and double-layer disks is strongly pH dependent in the pH range 3.3 to 4.7, the pH decreasing as

the value of T_2 falls. Only in the case of double-layer disks is a dependence of E_2 upon pH observed, although poorly defined, as the pH decreases the value of E_2 shifts in the anodic direction.

Table 8.1

Extent of Oxide Dissolution

Experimental Conditions: double-layer disks, pH = 3.00±0.05, initial ferrous ion concentration range 0 to $1x10^{-2}$ mol•dm^{-3}.

MICROGRAPH#	INITIAL [Fe(II)] (mol•dm^{-3})	T_2 (s)	IRON RELEASE (μmoles)	EXTENT OF OXIDE DISSOLUTION INDIVIDUAL CRYSTALS & GENERAL
9	0	1230	9.7	Slight rounding. Upper layer complete.
10	$3x10^{-5}$	1860	11.2	Moderate rounding. Upper layer complete.
11	$2x10^{-4}$	2070	13.1	Moderate rounding. Upper layer complete.
12	$1x10^{-3}$	1890	-	Moderate rounding. Upper layer complete.
13	$1x10^{-2}$	2220	-	Moderate rounding. ∿ 20% upper layer removed, exposing base oxide layer.

It is interesting to observe that at the lower pH both types of disk display a very rapid potential transition from phase II to phase III, lasting < 30 seconds. At the higher pH, the duration of the transition for single-layer disks is ≤ 3,000 seconds, while double-layer

disks exhibit a significantly more protracted transition lasting ∿ 15,000 seconds.

The pH effect in the presence of $1x10^{-4}$ mol•dm^{-3} ferrous ion was only investigated for single-layer disks. In contrast to the behaviour described above, the corrosion potential does not appear to be pH dependent.

8.4.4.2 Impact of the Initial Ferrous Ion Concentration

Single-layer disk corrosion potential behaviour is sensitive to the solution ferrous ion concentration, a characteristic not shown by double-layer disks. For single-layer disks at pH ∿ 4.7, increasing the initial ferrous ion concentration from $1x10^{-5}$ to $1x10^{-4}$ mol•dm^{-3} causes a decrease in the value of T_2 by more than an order of magnitude, additionally causing the values of both E_1 and E_2 to shift cathodically by > 100 mV.

For single-layer disks at pH ∿ 3.0, increasing the initial ferrous ion concentration from 0 to $1x10^{-5}$ mol•dm^{-3} causes a decrease in the value of T_2 by a factor of ∿ 5, additionally causing the value of both E_1 and E_2 to shift cathodically by > 100 mV. A further increase in initial ferrous ion concentration from $1x10^{-5}$ to $1x10^{-4}$ mol•dm^{-3} only reduces the value of T_2 by a factor < 2, and has little impact on the value of E_2.

In contrast to the behaviour described above, the value of T_2 observed for double-layer disks falls by a factor of 2 as the ferrous ion concentration rises from 0 to $1x10^{-2}$ $mol \cdot dm^{-3}$. The value of E_2 shows no systematic change as the initial ferrous ion concentration is varied, all the values obtained falling in a very narrow range of potential.

8.4.5 Summary Iron Release Behaviour

8.4.5.1 pH Effect

The pH effect on the iron release rate is clearly revealed when Figures 17 and 18 are compared, noting the factor of 10 difference in the time scales. The similarity in the form of the releases is readily apparent, suggesting that similar dissolution processes are operating at both pH $\curvearrowleft$ 3 and pH $\curvearrowleft$ 4.7.

8.4.5.2 Fe(II)-EDTA Concentration

Inherent analytical difficulties mean that investigation of the iron release rate dependence upon initial ferrous concentration is difficult. For this reason, an accurate evaluation of this dependence was not possible. At pH $\curvearrowleft$ 4.7 in the case of double-layer disks a modest iron release rate sensitivity to ferrous ion concentration is detected, an increase in the ferrous ion concentration from 0 to $1x10^{-5}$ $mol \cdot dm^{-3}$ doubling the iron release rate. For single-layer disks at

pH $\backsim$ 3, an increase in the iron release rate by a factor of $\backsim$ 3 is observed when the initial ferrous ion concentration is raised from 0 to $1x10^{-5}$ $mol \cdot dm^{-3}$.

The relatively narrow spread of iron release rates observed over a considerable ferrous ion concentration range is indicated by Figures 17 and 18.

The evidence gained by SEM examination of post-dissolution disks indicates quite strongly that there is no major acceleration of the oxide dissolution rate as the initial ferrous ion concentration is increased from 0 to $1x10^{-2}$ $mol \cdot dm^{-3}$.

The iron release behaviour during phase I could not be accurately determined due to the short duration of the phase. In all the experiments performed the total iron release rate during phase II was approximately linear.

The determinations of the quantities of ferrous and ferric ions released during the disk dissolution processes must be viewed with caution due to the analytical problems discussed in Sections 7.2.3 and 7.2 6. These data tentatively suggest that initially the majority of the iron appears in solution as ferric ions. However, these data more unambiguously indicate that the majority of the iron dissolved during phase II is released in the form of ferrous ions, Figures 17 and 18.

8.5 ROTATED DOUBLE-LAYER DISKS

8.5.1 Corrosion Potential Behaviour

8.5.1.1 General Form

The general form of the corrosion potential trace conforms well to that described in Section 8.2. The corrosion potential during phase II features a sustained anodic drift, spanning 10 to 30 mV in total.

8.5.1.2 pH Effect

The pH was closely controlled throughout to a value of 3.00±0.05 for all but one of the experiments. This one exception provides the only suggestion of a significant pH effect under these conditions. Two experiments were performed, the first at pH = 3.00±0.05 and the second, an otherwise identical experiment, at pH = 2.85±0.05. The values of T_2 observed in these experiments differ by a factor of > 2, the lower pH giving the lower T_2 value.

8.5.1.3 Fe(II)-EDTA Concentration

Figure 19 shows the manner in which the corrosion potential varied with the initial ferrous ion concentration. The three plots are representative samples from a total of eight experiments that were

performed to evaluate this effect in the ferrous ion concentration range 0 to 1×10^{-2} mol·dm^{-3}.

The values of E_1, E_2 and T_2 observed in each of the experiments are given in Table 8.2. Inspection of the data in this table reveals that no consistent trend in the value of T_2 is observed as the ferrous ion concentration rises. This is not the case for the values of E_1 and E_2, both of which exhibit a dependence on the ferrous ion concentration. The value of E_2 progressively rises from -110 to -30 mV as the initial ferrous ion concentration increases from 0 to 1×10^{-2} mol·dm^{-3}. The value of E_1 exhibits the opposite dependence, the potential falling from +210 to -35 mV as the initial ferrous ion concentration increases from 0 to 1×10^{-2} mol·dm^{-3}.

It should be noted that slight variations in experimental procedure have little effect on the value of E_2, but can significantly change the value of E_1. The corrosion potential at the start of these experiments suffered distortion when one or more of a number of commonly encountered difficulties arose. The most frequent was the formation of a stable gas bubble masking the surface of the disk and/or the end of the reference electrode capillary. This problem took anywhere from 10 to 100 seconds to rectify. In such circumstances the definition of time zero becomes rather arbitrary, thus causing a distortion of the corrosion potential behaviour observed during the brief phase I.

Table 8.2

Corrosion Behaviour as a Function of Fe(II) Concentration

Experimental Conditions: pH = 3.00±0.05 (unless otherwise stated). Value of E_1 taken at T=20 seconds, value of E_2 taken at T=250 seconds.

INITIAL [Fe(II)] ($mol \cdot dm^{-3}$)	ROTATING DISKS			STATIC DISKS		
	T_2 (s)	E_1 (mV)	E_2 (mV)	T_2 (s)	E_1 (mV)	E_2 (mV)
0	1500	+210	-110	1230	+90	-45
$1x10^{-5}$	1440	+150	-115	-	-	-
$3x10^{-5}$	-	-	-	1860	+40	-60
$1x10^{-4}$	1630	+160	- 85	-	-	-
$2x10^{-4}$	-	-	-	2070	-55	-85
$5x10^{-4}$	1940	+135	- 75	-	-	-
$1x10^{-3}$	1980	+ 35	- 30	1890	-60	-80
$5x10^{-3}$ ($)	2720	+ 35	+ 7	-	-	-
$1x10^{-2}$	1600	- 20	- 30	2220	-40	-50
$1x10^{-2}$ (*)	640	- 35	- 30	-	-	-

(*)Experiment performed at pH = 2.85±0.05. ($) Suspect disk.

8.5.1.4 Comparison of Static and Rotated Disk Behaviour

Figures 16 and 19 indicate considerable similarity in behaviour of rotated double-layer disks and static double-layer disks. One significant difference between the systems is that for the rotated disks the value of E_2 shows a systematic change as the initial ferrous ion concentration varies, the spread of values being ∿ 70 mV rather than ∿ 30 mV observed for static disks over the same concentration range.

The spread of E_1 values in the rotating disk system was much greater than that seen for static disks. The value of E_1 for rotated disks clearly showed a dependence upon the ferrous ion concentration. Static disks showed the same basic trend, but in a less pronounced manner, see Table 8.2.

8.5.2 Iron Release Behaviour

The iron release was not followed during these experiments.

8.5.3 Post-Dissolution Disk Morphology

The SEM results reveal that the extent of the oxide dissolution increases significantly as the initial ferrous ion concentration is increased from 0 to $1x10^{-5}$ $mol \cdot dm^{-3}$, compare Micrograph 14 and Micrograph 15. Further increases in the initial ferrous ion concentration only produced modest increases in the dissolution of the upper layer of crystals, Micrographs 16 to 18 and Table 8.3.

Two experiments were performed with an initial ferrous ion concentration of $1x10^{-2}$ $mol \cdot dm^{-3}$. The solution pH differed slightly between the two experiments, at pH = 3.00±0.05, T_2 = 1,600 seconds and at pH = 2.85±0.05, T_2 = 640 seconds. Micrographs 17 and 18 reveal that the extent of oxide dissolution is significantly greater for the experiment that exhibited the larger value of T_2.

Table 8.3

Extent of Oxide Dissolution

Experimental Conditions: double-layer disk, rotated 33.3 Hz, pH=3.00±0.05, initial ferrous ion concentrations = 0 to $1x10^{-2}$ $mol \cdot dm^{-3}$.

MICROGRAPH#	INITIAL [Fe(II)] ($mol \cdot dm^{-3}$)	T_2 (s)	EXTENT OF OXIDE DISSOLUTION INDIVIDUAL CRYSTALS & GENERAL
14	0	1500	Very slight rounding. Layer complete.
15	$1x10^{-5}$	1440	Moderate rounding. Layer complete.
	$1x10^{-4}$	1630	Moderate rounding. Layer complete.
	$5x10^{-4}$	1940	Moderate rounding. Layer complete.
16	$1x10^{-3}$	1980	Moderate rounding. Layer complete.
	$5x10^{-3}$	2720	Moderate rounding. Layer complete.
17	$1x10^{-2}$	640	Moderate rounding. Layer complete.
18	$1x10^{-2}$	1600	Considerable rounding. ∿ 5% surface bald.

8.6 DISCUSSION

As indicated by the potential-time relationship shown schematically in Figure 11, the behaviour of magnetite-covered carbon steel surfaces in EDTA solutions can be divided into three phases.

Phase I

The potential in phase I decreases with added ferrous ion for double-layer disks, Figure 19. One interpretation of this dependence is

that penetration to the steel surfaces occurs via a ligand-bridge assisted oxide dissolution process, involving electron transfer to a ferric ion in the lattice from a ferrous-EDTA species in solution, i.e.,

$$>Fe^{3+} + (Fe^{2+}EDTA)^{2-} = >Fe^{2+} + (Fe^{3+}EDTA)^{-} \qquad (8.1)$$

followed by dissolution of the reduced iron species:

$$>Fe^{2+} + (H_nEDTA)^{(4-n)-} = (Fe^{2+}EDTA)^{2-} + nH^{+} \quad . \qquad (8.2)$$

With no ferrous ion initially present in solution, this process requires the initial release of ferrous ion by direct dissolution in order to start, but would be expected to be rapid when ferrous ion is initially present. Our attempts to prove this point by analyzing the extent of ferric ion release show that initially there is a tendency for dissolved iron to appear as ferric ions. However, the analytical problems suggest the ferric ions may be produced by the oxidation of solution ferrous ions. Consequently, the production of ferric ions cannot be considered conclusive proof that LBAD is occurring.

The duration of phase I is in the range 30 to 200 seconds, this interval being determined by the time taken for solution penetration to the underlying steel. Solution interaction with the metal initiates autoreduction (reaction (8.3)), causing a change in the value of the corrosion potential:

$$>Fe_3O_4 + 8H^+ + >Fe = 4Fe^{2+} + 4H_2O \quad . \qquad (8.3)$$

Solution penetration to the underlying steel occurs preferentially at the pearlite regions. Micrograph 4 indicates that the pearlite grains are covered by a porous oxide film which is less protective than the film covering the adjacent alpha-iron grains. This behaviour is in contrast to that observed on magnetite-covered pure iron disks which show a more general attack [34,40]. Also, this attack is often slower for films formed on pure iron disks, consistent with a more uniform, more protective, oxide film.

Phase II

(a) General Behaviour

The majority of the iron dissolved in this region is in the form of ferrous ions with very little release of ferric ions. This strongly suggests that the predominant reaction occurring in this region is autoreduction, reaction (8.3), and that if ligand-bridge assisted oxide dissolution (reactions (8.1) and (8.2)) is occurring, it is a relatively minor process. Confirmation of the source of ferric ions is required before the extent of the ligand-bridge assisted dissolution process can be determined.

The autoreductive process occurs preferentially at the pearlite sites, leading to the characteristic layered structure shown in

Micrograph 5 and Figure 9. This layered structure can be attributed to the preferential dissolution of the alpha-iron from the pearlite region, the iron carbide remaining relatively untouched. The more protective oxide film covering the alpha-iron regions appears to be unattacked at the conclusion of phase II.

In general, the behaviour of both single-layer and double-layer disks is similar. Initially, double-layer disks will be considered and in the subsequent discussion of single-layer disks an attempt will be made to rationalize the observed differences between the two types of disk.

(b) Double-Layer Disks

The post-dissolution micrographs show that, for static disks, there is evidence for upper-layer crystal dissolution (rounding of the crystal edges), even when the initial ferrous ion concentration is zero. The micrographs also indicate that the extent of upper-layer crystal dissolution does not increase as the ferrous ion concentration rises, except at the highest concentration used, 1×10^{-2} mol·dm^{-3}, when patches of the base-layer oxide are visible. The release rate of iron in phase II for static disks was only measured for initial ferrous ion concentrations up to 1×10^{-4} mol·dm^{-3} and at two pH values. Except for the first $\sim$ 750 seconds of the dissolution process, iron is released to solution as ferrous ions, confirming that dissolution is predominantly via an autoreduction process. The release rate of iron in this region is

effectively independent of the initial ferrous ion concentration, at least up to $1x10^{-4}$ $mol \cdot dm^{-3}$, the limit of our measured range (see Table 8.4). This is consistent with the observation that the extent of dissolution is independent of the initial ferrous ion concentration over this range. In contrast, the iron release rate is strongly dependent on the hydrogen ion concentration (see Table 8.4).

For rotated disks, micrographs show a significant change in the extent of dissolution of the upper-layer crystals upon increasing the solution ferrous ion concentration from 0 to $1x10^{-5}$ $mol \cdot dm^{-3}$, see Table 8.2, and Micrographs 14 and 15. Further increases in ferrous ion concentration up to $1x10^{-2}$ $mol \cdot dm^{-3}$ caused little additional dissolution, see Micrographs 16 to 18.

For both static and rotated disks there appears to be a better correlation between the extent of oxide dissolution and the duration of phase II, than between the extent of oxide dissolution and the initial ferrous ion concentration. This correlation can be seen by comparing the amount of upper-layer crystal dissolution, crudely obtained from visual inspection of the micrographs, to the transition times, T_2. The values of T_2, Table 8.2, are independent of the initial ferrous ion concentration, which is consistent with the SEM evidence, but again strongly dependent on pH.

Table 8.4

Iron Release Behaviour of Double-Layer and Single-Layer Disks

DISK TYPE	pH	[Fe(II)] INITIAL ($mol \cdot dm^{-3}$)	T_2 (10^3 s)	IRON RELEASE TO TIME ₮ (μmoles)	₮ (10^3 s)	AV IRON RELEASE RATE TO ₮ ($\mu moles \cdot s^{-1}$)
SLD	∿4.7	$1x10^{-5}$	10.4	7.3	10.4	$7.0x10^{-4}$
SLD	∿4.7	$1x10^{-5}$	11-14	10.0	13.7	$7.3x10^{-4}$
SLD	∿4.7	$1x10^{-5}$	12.5-12.7	11.0	13.7	$8.0x10^{-4}$
SLD	∿4.7	$1x10^{-5}$	13.0	9.5	12.0	$7.9x10^{-4}$
SLD	∿4.7	$1x10^{-4}$	0.36	∿1.0	0.42	$\sim 2.4x10^{-3}$
SLD	3.3	0	2.40	4.7	2.40	$2.0x10^{-3}$
SLD	3.3	$1x10^{-5}$	0.51	2.5	0.51	$4.9x10^{-3}$
SLD	3.3	$1x10^{-4}$	∿0.42	∿1.3	0.51	$\sim 2.5x10^{-3}$
SLD	2.9	$1x10^{-5}$	0.24	∿0.4	0.30	$\sim 1.3x10^{-3}$
DLD	∿4.7	0	13-50	3.1	11.0	$2.8x10^{-4}$
DLD	∿4.7	$1x10^{-5}$	12-48	6.6	11.3	$5.8x10^{-4}$
DLD	3.0	0	1.23	9.7	1.23	$7.9x10^{-3}$
DLD	3.0	$3x10^{-5}$	1.86	11.2	1.86	$6.0x10^{-3}$
DLD	3.0	$2x10^{-4}$	2.07	13.1	2.07	$6.3x10^{-3}$

Note: All disks static.
SLD: Single-layer disk.
DLD: Double-layer disk.
₮: Time solution sample taken, $T_2 \sim$ ₮.

All this evidence indicates that added ferrous ion has little impact on the oxide dissolution process and that the parameter most

important in accelerating oxide dissolution is pH. The absence of a ferrous ion dependence suggests that the ligand-bridge assisted dissolution process, reactions (8.1) and (8.2), is unimportant, as expected from the very small amounts of ferric ion released. The dependence of the iron release rate, and T_2, on pH under autoreductive conditions can be rationalized in terms of a depolarization of the oxide dissolution reaction, reaction (8.6). The rate of the metal dissolution reaction can be considered independent of pH.

Although the oxide dissolution process will be a complex multi-step reaction, it can be broken down into three basic reactions:

(i) Reduction of the ferric ions in the oxide lattice, the electrons being supplied by the metal dissolution process:

$$>Fe^{3+} + e^- = >Fe^{2+} \qquad (8.4)$$

(ii) Transfer of ferrous species from the solid to the solution, assisted by complexation with EDTA:

$$>Fe^{2+} + (H_nEDTA)^{(4-n)-} = (Fe^{2+}EDTA)^{2-} + nH^+ \quad . \qquad (8.5)$$

According to Matijević et al. [16,36] and Blesa et al. [79] the EDTA will be surface adsorbed.

(iii) Neutralization of the lattice oxide species by protons:

$$>O^{2-} + 2H^{+} = H_2O \quad . \tag{8.6}$$

The strong dependence of the iron release rate on pH could arise if a reaction of type (iii) is rate determining. Also, according to Matijević [15,16,17,36] such a dependence could arise from pH-induced changes in the surface concentration of adsorbed EDTA, indicating that a reaction of type (ii) is rate determining. The possibility of a rate control by electron transfer, (i), or cation transfer, (ii), has not been tested. Rate control via reactions of type (i) would be possible if the rate of the metal dissolution reaction, and hence the supply of electrons for the reduction reaction, is limited by the surface area of exposed metal. It is conceivable that such a situation exists in the early stages of phase II, immediately following solution penetration to the steel.

The increase in extent of dissolution in a solution containing $> 1 \times 10^{-3}$ mol·dm^{-3} added ferrous ion can be explained without invoking the direct effect of ferrous ions on the dissolution rate, although the extent of ferric ion production in this experiment is unknown, the possibility of a ligand-bridge assisted dissolution process cannot be ruled out. However, complexation of ferrous ions by EDTA will lead to the liberation of protons at pH $\sim$ 3 by processes similar to that shown in reaction (8.5), leading to a significant increase in proton concentration, especially close to the dissolving oxide/metal interface.

This would be expected to lead to an acceleration of the oxide dissolution process.

Such variations in the local chemistry conditions would be expected to be more marked at static disks than at rotated disks, since the rate of convective transport of species to and from the static disk will be much lower than at the rotated disk. Such an effect could explain the observation that for zero added ferrous ion some dissolution of the upper-layer oxide is apparent on static disks but not on rotated disks. Under the limited convective transport conditions achieved, the local concentration of ferrous ions would be expected to build up at the surface, leading to the local release of protons via EDTA complexation, and hence to accelerated oxide dissolution. At rotated electrodes, this localized acidity buildup will be prevented by the convective transport of complexed ferrous ions to the bulk solution and of uncomplexed $H_nEDTA^{(4-n)-}$ to the disk surface.

Such an effect would also explain the relative invariance of the corrosion potential during phase II for static disks as the solution ferrous ion concentration is varied. The local concentration of ferrous and hydrogen ions is established mainly by the autoreductive dissolution process at the disk surface. These concentrations can be considered to be locally "buffered" and hence, to a large extent, independent of the bulk concentration of ferrous ions.

For rotated disks this local "buffering" of the chemical conditions is not so marked and consequently the potential in phase II responds to changes in the bulk concentration of ferrous ion. The shift to anodic potentials could be interpreted as due to an effect of added ferrous ion on either the metal dissolution or the oxide dissolution half-reactions. Ignoring the impact of the EDTA on the free iron concentration the equilibrium potential-pH relationships for the two reactions can be written [48]. For the metal dissolution reaction:

$$E_c = -0.44 + 0.0295 \log[Fe^{2+}] \text{ vs SHE} \qquad (8.7)$$

and for magnetite dissolution:

$$E_c = 0.980 - 0.2364 \text{ pH} - 0.0886 \log[Fe^{2+}] \text{ vs SHE} \quad . \qquad (8.8)$$

The measured corrosion potential is approximately equidistant from both these values, indicating a significant polarization of each reaction. An increase in the local ferrous ion concentration would shift the metal dissolution potential to more anodic values and the oxide dissolution potential to more cathodic values. The observed shift is in the anodic direction, suggesting that the added ferrous ion is increasing the polarization of the anodic reaction. This would not be unreasonable for a reversible metal dissolution process. If this was the case, it would suggest that the metal dissolution reaction is rate controlling, and that an increase in ferrous ion concentration should inhibit the rate of electron transfer to the ferric species in the oxide

lattice, thereby decreasing the rate of oxide dissolution. This is contrary to our conclusion that, if it has any effect at all, ferrous ion accelerates oxide dissolution. Also, rate control by metal dissolution is less likely than rate control by oxide dissolution unless the rate of metal dissolution is controlled by the very small area of exposed steel. This is unlikely for two reasons. Firstly, very high rates of metal dissolution can be achieved under pitting conditions [83], a situation very similar to the present one. Secondly, our iron release rate is constant throughout phase II, indicating a constant rate of oxide (and metal) dissolution, despite the fact that the surface area of exposed steel is changing throughout phase II.

An alternative explanation which would account for the observed positive shift in the corrosion potential in phase II is that the increased ferrous ion concentration is causing a local increase in hydrogen ion concentration via the complexation reactions outlined above. Such a decrease in pH at the site of oxide dissolution would shift the oxide dissolution potential to more positive values, leading to a depolarization of this reaction, and consequently to an increase in the oxide dissolution rate.

(c) Single-Layer Disks

Monitoring the corrosion potential and the iron release during dissolution experiments on double-layer disks gives no clear indication as to whether different processes are occurring in the base layer as

compared to those active on the upper layer. During phase II it is considered probable that the corrosion potential is strongly influenced by processes occurring at the base of pits in the oxide film. Hence, the "buffering" of local concentrations in pores and cracks in the base layer and in the voids and spaces in the upper layer could obscure real dependencies of parameters E_2 and T_2 on the concentrations of hydrogen and ferrous ions.

The limited results on single-layer disks, where the complications due to the presence of the upper layer are absent, are generally similar, but not identical, to those observed with double-layer disks. During comparable experiments the iron release rates for static single- and double-layer disks do not differ by more than a factor of $\sim$ 2 for all conditions investigated, see Table 8.4. For single-layer disks the pH effect on both the value of T_2 and iron release rate is similar to that observed for double-layer disks. This suggests that a similar sequence of reactions to those claimed for double-layer disks is occurring in the base layer.

The values of E_2 and T_2 observed during dissolution experiments with static single-layer disks show a significant sensitivity to the solution ferrous ion concentration, a characteristic not shared by static double-layer disks. The absence of the upper-layer crystals in the case of single-layer disks might well diminish the "buffering" effects described above, permitting the dependence of the corrosion potential upon bulk solution characteristics to be revealed.

As the autoreductive dissolution of the oxide film proceeds the area of carbon steel exposed to the solution will rise, eventually causing active corrosion to take over from autoreduction as the predominant reaction. It would not be unreasonable to expect that the switch to active corrosion follows the exposure of an essentially invariant area of metal. Hence, suggesting that for each type of disk an essentially constant amount of oxide dissolution would precede the phase II to III transition, the data in Table 8.4 for single-layer disks indicate that this is not the case. This observation could be explained by the operation of more than one oxide dissolution process, the first being a general oxide attack releasing the majority of the iron to solution, and secondly an attack within the confines of oxide pores that exposes the base metal. Thus, changes in solution characteristics, such as ionic strength, that have little impact upon the general iron release rate might selectively accelerate the oxide dissolution in pores, leading to significant changes in the value of T_2.

CHAPTER 9

TEMPERATURE EFFECT ON MAGNETITE FILM DISSOLUTION IN EDTA SOLUTIONS

9.1 INTRODUCTION

9.1.1 General

The work reported in the previous chapter was an investigation of magnetite film dissolution from carbon steel disks in acidic EDTA solutions at room temperature. As reactor decontaminations are performed at ~ 85°C, it is necessary to investigate the impact of temperature upon such dissolution processes. A series of thermostatted dissolution experiments were performed, each at a preselected temperature in the range 23°C to 85°C. The dissolution process was followed by monitoring the corrosion potential of the oxide-covered metal, measuring the quantity of iron released to solution, and by pre- and post-dissolution examination of the disk surface using a scanning electron microscope. These experiments were performed with single-layer and double-layer disks.

9.1.2 Experimental

The cell used for these experiments was similar to that described in Chapter 7. The only major modification was the use of a cell with an integral water jacket, Figure 10. Water from a

thermostatically controlled reservoir was circulated through the jacket, permitting control of the cell-solution temperature to ± 1°C. To obtain reproducible transport conditions the disks were rotated at 16.67 Hz.

The solution used throughout these experiments was a 2×10^{-3} $mol \cdot dm^{-3}$ aqueous solution of EDTA, pH = 3.00±0.05. It should be noted that all experiments on a particular type of disk were performed successively in the same solution. Sufficient time was allowed between each experiment to permit readjustment of the solution temperature.

For each experiment samples of the cell solution were taken before and after dissolution and analyzed for total iron. Thus, only the total quantity of iron released in the dissolution process at each temperature was determined, not the iron release as a function of time during dissolution.

The iron analyses were obtained by inductively-coupled plasma spectrometry (ICPS) using a Plasma-Therm Inc. Model 2500/APCS-3 instrument. The analyses were performed by the Analytical Science Branch, Whiteshell Nuclear Research Establishment (WNRE). No attempt was made to analyze selectively for ferrous and ferric ions.

9.2 CORROSION POTENTIAL BEHAVIOUR

9.2.1 Single-Layer Disks

For all temperatures examined in the range 23°C to 85°C the corrosion potential trace has a common form. The value of E_2 is constant at -120±10 mV, Figure 20. Both the values of T_1 and T_2 progressively decline as the temperature rises from 23°C to 55°C. Thereafter, further increases in temperature have little additional effect, Figures 22 and 23. At temperatures greater than 55°C the values of T_1 and T_2 remain essentially constant at $T_1 \backsim 50$ seconds and $T_2 \backsim 150$ seconds.

It should be noted the value of T_2 ($\backsim 1200$ seconds), obtained at 23°C, is consistent with the results reported in Chapter 8.

9.2.2 Double-Layer Disks

For all temperatures examined in the range 23°C to 85°C the corrosion potential trace produced is of a common form, similar to that seen for single-layer disks. The value of E_2 is constant at -100±10 mV, Figure 21.

Both the values of T_1 and T_2 progressively decline as the temperature rises from 23°C to 55°C. Thereafter, further increases in temperature have little additional effect, Figures 22 and 23. Above

55°C, the values of T_1 and T_2 remain essentially constant at ∿ 20 and ∿ 450 seconds, respectively.

9.2.3 Comparison of the Two Disk Types

The corrosion potential traces observed for single-layer disks and double-layer disks are similar in form and the values of T_1 and T_2 for each of the two disk types display a common dependence upon temperature, Figures 22 and 23.

At each temperature investigated the value of T_1 obtained for a single-layer disk is greater than the corresponding value for a double-layer disk. However, the reverse is true for values of T_2, Figures 22 and 23, respectively.

9.3 IRON RELEASE BEHAVIOUR

9.3.1 General

The iron release is the total quantity of iron released to solution from time zero to T_2, i.e., the total iron released throughout phases I and II. The work reported in the previous chapter revealed that at room temperature the iron release during phase I is considerably less than that during phase II. Consequently, the iron release rate is calculated as the average iron release rate from time 0 to T_2. This quantity is approximately equal to the average iron release rate in

phase II, iron release during phase I having been assumed to be negligible.

9.3.2 Single-Layer Disks

The total quantity of iron dissolved up to T_2 shows a slight initial rise with temperature up to 55°C, thereafter remaining essentially constant, Figure 25. All values fall in the range 5.4×10^{-7} moles (23°C) to 2.45×10^{-6} moles (65°C), a factor of ~ 4 difference. The iron release rate increases by a factor of 40 as the temperature rises, with values ranging from 4.9×10^{-10} mol·s^{-1} at 23°C to 1.9×10^{-8} mol·s^{-1} at 65°C, Figure 25.

9.3.3 Double-Layer Disks

The total quantity of iron dissolved prior to T_2 rises linearly from 2.4×10^{-6} to 1.57×10^{-5} moles as the temperature increases from 23°C to 85°C, a 7-fold increase, Figure 24. These values yield iron release rates which increase linearly as the temperature rises throughout the temperature range 23°C to 85°C, Figure 25.

9.3.4 Comparison of the Two Disk Types

In the temperature range 23°C to 65°C, the iron release observed from both disk types increases, for a given temperature, the iron release from a double-layer disk exceeding that from a single-layer

disk by a factor of $\sim$ 4. At higher temperatures the iron release from double-layer disks continues to increase, while that for single-layer disks declines slightly, the iron releases differing by a factor $>$ 10 at 85°C.

At each temperature studied the iron release rate for double-layer disks exceeds that for single-layer disks by a factor of 2.0±0.8. The data presented in Figure 25 for a single-layer disk could be interpreted a number of ways. It is considered most probable that the value obtained at 65°C is a spuriously high point. Therefore, the basic trend observed for a single-layer disk is similar to that for a double-layer disk, the gradient being lower by a factor of $\sim$ 2.

9.4 POST-DISSOLUTION DISK MORPHOLOGY

9.4.1 Single-Layer Disks

For all the temperatures studied, the oxide film removal is incomplete, the post-dissolution oxide films all having a distinctly patchy appearance. Close inspection of SEM micrographs reveals that this is due to the presence of local regions of significant oxide film penetration in a film that has otherwise only experienced a modest general attack. As noted in the previous chapter, the areas of significant oxide film penetration occur at sites where the surface intersects pearlite grains. Study of the high magnification micrographs reveals the characteristic lamellar structure of the partially dissolved

pearlite grains. The severity of the attack of these sites does not appear to alter significantly as the temperature is increased from 23°C to 85°C. Micrographs 1 and 2 are of pre-dissolution films, and Micrographs 19 to 21 show post-dissolution films.

The greater part of the oxide film is grown on alpha-iron. This oxide film appears much less susceptible to penetration than the oxide film grown over the pearlite grains.

At 23°C the extent of oxide dissolution from the alpha-iron appears very slight, little visible change having been caused by the dissolution process. As the temperature at which the dissolution is performed rises to 75°C, there is a steady rise in the extent of oxide dissolution from the alpha-iron, leaving the entire film with a mottled appearance due to the presence of numerous, small, shallow pits. The appearance of post-dissolution disks reveals that increasing the temperature of the dissolution process from 75°C to 85°C markedly promotes the general oxide dissolution process. At the higher temperature this general dissolution process is sufficiently extensive to blur the previously well-defined boundaries of pearlite grains.

9.4.2 Double-Layer Disks

For all temperatures studied the oxide film removal is incomplete, the extent of oxide dissolution varying greatly, from a modest attack at 23°C to a substantial dissolution at temperatures

> 65°C. Micrographs 3 and 4 are of pre-dissolution films, and Micrographs 22 to 24 show post-dissolution films.

Dissolution at 23°C resulted in little discernible attack of the upper-layer crystals, only a very slight rounding of the sharp crystal edges being detectable. As the temperature is raised to 55°C a significant increase in the extent of crystal dissolution is observed, the regular form of the magnetite crystals being completely lost. Throughout this temperature range the dissolution of the upper-layer crystals is insufficient to expose the base-layer oxide.

Dissolution at 65°C produced a disk that featured large areas of complete upper-layer crystal dissolution, the remainder of the surface being covered by patches of partially dissolved upper-layer crystals. Dissolutions performed at 75°C and 85°C produced similar results. At these higher temperatures the large areas of exposed base-layer oxide reveal the presence of partially dissolved pearlite grains. Inspection of the micrographs suggests that there is no correlation between the areas in which complete upper-layer crystal dissolution is observed and the pearlite grain sites.

The dramatic change in the apparent extent of dissolution observed between 55°C and 65°C is probably exaggerated by uncontrollable variations in the oxide film characteristics of the pre-dissolution disks.

The extent of oxide film dissolution, as indicated by the post-dissolution micrographs, correlates well with the quantities of soluble iron released.

9.5 DISCUSSION

For both types of disk the duration of phase I diminishes significantly as the temperature rises in the range 23°C-55°C, Figure 22, suggesting that the rate-controlling process in phase I is thermally activated below 55°C. The most probable process is an oxide dissolution reaction. For temperatures above 55°C the value of T_1 shows little dependence upon temperature, suggesting rate control by a temperature insensitive transport process.

The values of T_1 for both types of disk display a similar dependence upon temperature, Figure 22, indicating that similar processes are occurring. For a specified temperature, T_1 values for single-layer disks are consistently greater than those for double-layer disks, indicating that the upper-layer crystals do not impede the penetration of the solution to the carbon steel. Indeed, it suggests that the base-layer oxide for double-layer disk is thinner, or differs significantly in morphology, from that grown on single-layer disks.

The effect of increasing temperature upon the value of T_2 is similar for both disk types, T_2 declining sharply in the temperature

range 23°C-55°C, and thereafter remaining essentially constant up to 85°C, Figure 23.

The work reported in Chapter 8 indicated that the value of T_2 is determined by dissolution processes occurring in the base-layer oxide. The observed dependence of T_2 upon temperature suggests that below 55°C the rate of this base-layer oxide dissolution is controlled by a thermally activated process. As the temperature rises above $\sim$ 55°C, the rate of base-layer oxide dissolution increases to the point where a thermally insensitive process, probably a transport process, becomes rate determining.

For a given temperature the value of T_2 for double-layer disks consistently exceeds that for single-layer disks. This difference can be explained a number of ways. One possibility is that the base layer morphology differs between the two disk types. However, this argument would conflict with that made in the previous section, which suggested that, of the two disk types, the base-layer oxide film present on double-layer disks is more easily penetrated by the solution. A more probable explanation is that, for double-layer disks, reactions occurring within the upper-layer of crystals modifies the solution composition at the surface or in the pores and cracks of the base layer of oxide. Thus,

$$Fe_3O_4 + 3(H_2EDTA)^{2-} + 2H^+ + 2e^- \rightarrow 3(FeEDTA)^{2-} + 4H_2O \quad . \quad (9.1)$$

The ferrous ion concentration and pH will be higher within the base-layer oxide when an additional overlying carpet of oxide crystals is present, since the dissolution of the upper oxide layer will both consume protons and release ferrous ions.

The value of the potential E_2 remains constant throughout phase II for both disk types, and is approximately the same in both cases. Similar behaviour was observed in the work reported in the previous chapter.

For both disk types the value of the potential E_2 is unaffected by temperature in the range 23°C to 85°C. This suggests that the identity of the potential-determining reaction in phase II does not change in the temperature range studied. As noted previously, this does not completely eliminate the possibility of an additional non-electrochemical oxide dissolution process.

For temperatures below 55°C both the iron release rate increase, Figure 25, and the declining values of T_1 and T_2, Figures 22 and 23, suggest that a thermally-activated process is rate controlling. For temperatures above 55°C, the iron release rate continues to rise, but T_1 and T_2 remain constant. A possible explanation is that, for temperatures below 55°C, temperature increases accelerate the oxide dissolution process occurring within the oxide pores, causing the values of T_1 and T_2 to diminish. At $\sim$ 55°C the pore oxide dissolution process becomes rate limited by a transport process. Thus, little further

change in the values of T_1 and T_2 is observed. The oxide dissolution that gives rise to the increasing iron release rate at temperatures above 55°C cannot therefore arise from the pore dissolution process, and must come from a general oxide dissolution process spread more uniformly across the entire oxide surface.

Micrographs of post-dissolution disks reveal insignificant dissolution of the upper-layer crystals on double-layer disks at 23°C, suggesting strongly that under these conditions all oxide dissolution is occurring in the base-layer oxide.

At temperatures below 55°C, single-layer disks appear to experience distinctly localized oxide dissolution. The oxide dissolution seems to occur exclusively at pearlite grain sites. This observation is consistent with the results reported in the previous chapter.

At temperatures above 55°C, micrographs for both types of disk show a general oxide dissolution process, the extent of which increases with temperature, suggesting that the site of oxide dissolution if influenced by temperature, changing from a base-layer to a more general dissolution process as the temperature rises.

9.4 POSSIBLE DISSOLUTION MECHANISM

On the basis of the work reported in this and the previous chapter the following model is proposed for the oxide dissolution process.

An initial, short-lived, oxide dissolution process exposes areas of metal at the base of oxide pores to the solution (phase I). Solution contact with the metal immediately initiates autoreduction (phase II). As the autoreductive dissolution process commences only small areas of steel are exposed to the solution at the base of pores in the oxide film. The corrosion potential is initially at a value that excludes the possibility of proton reduction, the only cathodic half-reaction available being magnetite reduction. Thus, the electrons liberated by the metal dissolution reaction migrate to the magnetite-solution interface causing reductive dissolution.

There are two distinctly different sites available for oxide dissolution, locally within the pores where the metal dissolution is occurring and generally over the entire surface of the film. The conductivity of 99.99% alpha-iron is approximately $1 \times 10^5\ \Omega^{-1} \cdot cm^{-1}$ at 300 K, while that for magnetite at the same temperature is approximately $300\ \Omega^{-1} \cdot cm^{-1}$ [62]. Thus, the resistance to electron migration within the magnetite is sufficient to ensure that the electrons generated by metal dissolution will preferentially react at the nearest oxide/solution interface.

The experimental observations can be rationalized in terms of a change in the relative significance of the local and general oxide dissolution processes, Figure 26.

The local process is a pore-oxide dissolution process, during which both the metal and oxide dissolution half-reactions occur in close proximity, leading to the enlargement of pores in the oxide film and hence to a growth in the surface area of exposed metal. The surface area of exposed metal plays a major role in determining whether active corrosion or autoreduction is the predominant reaction. Thus, such a pore-oxide dissolution process would facilitate a rapid switch to active corrosion, thereby yielding low values of T_2.

For temperatures up to $\sim$ 55°C, the autoreduction process appears to be rate controlled by a step within the oxide dissolution reaction. For higher temperatures, the pore-oxide dissolution appears to become limited by a transport process for both double and single-layer disks. Either the transport of ferrous ions from the pore to the bulk solution, or the reverse process for protons, might well become rate determining. The evidence to date suggests that proton migration is the most probable candidate for the rate-limiting step in the pore-oxide dissolution process.

Such transport limitations on the pore-oxide dissolution process leads to the onset of a more general oxide dissolution at sites more remote from the metal dissolution site at the base of the oxide

pore, Figure 26. The probability of proton or ferrous ion transport becoming rate determining at these surface sites is markedly less than for pore-oxide dissolution.

General oxide dissolution requires the long-range migration of electrons generated by metal dissolution. The exposure of metal to the solution would occur far more slowly under these conditions as opposed to a pore dissolution process. Since it is the pore dissolution process which determines the switch to active corrosion at T_2, the limitation on rate of the process leads to T_2 becoming independent of temperature, while the overall oxide dissolution rate increases with temperature due to the increasing importance of the general oxide dissolution process.

For both double-layer and single-layer disks under the conditions used, general oxide dissolution is a minor component of the oxide dissolution process at 23°C. Above ~ 55°C its significance grows rapidly with increasing temperature. At 85°C the majority of oxide dissolution appears to occur by this process.

CHAPTER 10

MAGNETITE FILM DISSOLUTION IN EDTA AND MIXED EDTA/OXALATE SOLUTIONS

10.1 INTRODUCTION

10.1.1 General

The work of Baumgartner et al. [24] and Warren et al. [38] have demonstrated that magentite powders dissolve in oxalic acid by a SIRD reaction involving Fe(II)-oxalate complexes. It is also thought possible that oxalic acid can promote a direct dissolution process, Shoesmith et al. [40] and Baumgartner et al. [24]. Shoesmith et al. [40] demonstrated that the addition of oxalate to EDTA solutions increases both the rate and efficiency of magnetite film dissolution by autoreduction.

Hence, three distinct oxide dissolution mechanisms have been claimed for magnetite dissolution in oxalate solutions: (a) direct dissolution, (b) LBAD, and (c) autoreduction. Also, the above discussion suggests that the dissolution of free magnetite and magnetite films on iron sufaces may proceed by different mechanisms. The purpose of the work presented in this chapter is to determine the mechanism of magnetite dissolution from carbon steel surfaces in oxalate and oxalate/EDTA solutions.

10.1.2 Experimental

Double-layer, oxide-covered, carbon steel disks grown in the same autoclave batch were used throughout these experiments. The disks were prepared and characterized as described in Chapter 7, Micrographs 1 and 2.

Experiments were performed in mixed EDTA-oxalate solutions. The EDTA concentration was 1×10^{-3} mol·dm^{-3} and the oxalate concentration was varied from 0 to 1×10^{-2} mol·dm^{-3}. Some experiments were performed in solution free from EDTA at an oxalate concentration of 1×10^{-3} mol·dm^{-3}.

On two occasions crystalline ferrous ammonium sulphate was added to oxalate solutions during the course of dissolution experiments. Analar grade oxalic acid and Na_2H_2EDTA were used to produce the solutions, and the pH was adjusted to 3.00±0.10 with sulphuric acid or sodium hydroxide as appropriate.

Disks were allowed to corrode on open circuit, and the corrosion potential was monitored continuously. All potential measurements were made with respect to the saturated calomel electrode (SCE). Experiments were allowed to run until a major negative shift in the corrosion potential to a value < -500 mV was observed. The iron release during dissolution was monitored by periodic sampling of the cell solution, and subsequent quantitative determination of total iron.

The iron analyses were performed by the Analytical Science Branch by means of inductively-coupled plasma spectrometry (ICPS).

10.2 MIXED EDTA-OXALATE SOLUTIONS

10.2.1 Corrosion Potential Behaviour

The form of the corrosion potential versus time traces obtained are similar, Figure 27, and exhibit the three phases as defined in Figure 11 and discussed in Chapters 8 and 9.

The value of T_1 does not show any clear dependence upon the oxalate concentration. There is a suggestion that E_1 shifts in the positive direction as the oxalate concentration rises. This dependence is difficult to evaluate due to the short duration of phase I (typically 150 seconds) and the sustained decline in the value of E_1 throughout this phase.

In solutions possessing an oxalate concentration $> 3 \times 10^{-3}$ $mol \cdot dm^{-3}$, a previously unobserved event appears on the corrosion potential versus time traces. The phase I to phase II transition appears to reverse, the corrosion potential recovering in the positive direction, Figure 27. At oxalate concentrations $\leq 7.5 \times 10^{-3}$ $mol \cdot dm^{-3}$ the recovery is ≤ 20 mV, whereas at 1×10^{-2} $mol \cdot dm^{-3}$ the recovery is 70 mV.

Initially, phase II is characterized by a sustained period of E_2 invariance. Towards the end of phase II, the corrosion potential moves at a progressively increasing rate in a negative direction, culminating in an abrupt potential transition to phase III that commences at -180±40 mV. In oxalate free solutions this final drift in the negative direction occurs within ∿ 200 seconds, whereas at an oxalate concentration of $1x10^{-2}$ mol•dm^{-3} the corresponding interval is ∿ 2,000 seconds.

E_2 displays a clear dependence upon the oxalate concentration, Figure 28 and Table 10.1. The relationship between E_2 and the oxalate concentration is complex, the logarithmic plot displaying two distinct linear regions. The best fit line for the five data points in the oxalate concentration range $1x10^{-3}$-$1x10^{-2}$ mol•dm^{-3} has a gradient of +85.5 mV/decade. The gradient for the best fit line for the three data points in the oxalate concentration range $1x10^{-5}$-$1x10^{-4}$ mol•dm^{-3} is +4.0 mV/decade, Figure 28.

T_2 also exhibits a dependence upon the solution oxalate concentration, Figure 29 and Table 10.1. The value of T_2 rises as a function of the oxalate ion concentration for concentrations $> 1x10^{-4}$ mol•dm^{-3}.

Table 10.1

T_2, E_2 and Total Iron Release as a Function of Oxalate Concentration

Experimental Conditions: Disks Rotated at 16.67 Hz; pH=3.12±0.10; Room Temperature

Solution Composition		T_2	E_2†	Total Iron Release
Oxalate ($mol \cdot dm^{-3}$)	EDTA ($mol \cdot dm^{-3}$)	(seconds)	(mV)	(up to $t = T_2$) (μmoles)
0	1×10^{-3}	2620	-127±11	5.3
1×10^{-5}	1×10^{-3}	2300	-123±11	6.1
3×10^{-5}	1×10^{-3}	2280	-121±15	9.1
1×10^{-4}	1×10^{-3}	2030	-119±12	11.5
3×10^{-4}	1×10^{-3}	2370	-91±16	15.2
1×10^{-3}	1×10^{-3}	2750	-91±12	17.3
3×10^{-3}	1×10^{-3}	2950	-55±8	17.6
5×10^{-3}	1×10^{-3}	3130	-31±5	18.2
7.5×10^{-3}	1×10^{-3}	4000	-18±4	18.5
1×10^{-2}	1×10^{-3}	5860	-6±5	19.4

†The value of E_2 was recorded at T = 1000 seconds. There is 95% confidence that the values fall within the defined limits.

10.2.2 Iron Release Behaviour

For systems containing oxalate concentrations in the range 0 to 3×10^{-4} $mol \cdot dm^{-3}$ the iron release is linear with time following a short induction period. The iron release rate rises with oxalate concentration within this concentration range, Figure 30. The slope and time-axis intercept (T*) of the best fit straight line for each data set is given in Table 10.2. Each data set was edited prior to linear

regression to ensure that only data obtained during phase II were used. All data obtained in the initial 500 seconds of each experiment, and the last data point in each set (often taken following the switch to phase III) were discarded. The high values obtained for the correlation coefficients attest to the linearity of the iron release behavior in phase II.

The values of T_1 and T* reported in Table 10.2 indicate that the iron release during phase I is low, and that the iron release during phase II must commence with an induction period of < 250 seconds duration.

Table 10.2

Iron Release Rate, T_1 and T* as a Function of Oxalate Concentration for Oxalate Concentration < 3×10^{-4} mol·dm^{-3}

Oxalate Concentration (mol·dm^{-3})	Iron Release Rate (moles·s^{-1})	T_1 (seconds)	T* (seconds)
0	2.3×10^{-9}	180	340
1×10^{-5}	3.1×10^{-9}	110	330
3×10^{-5}	4.1×10^{-9}	170	305
1×10^{-4}	5.6×10^{-9}	80	265
3×10^{-4}	6.8×10^{-9}	120	245

At oxalate concentrations above 3×10^{-4} mol·dm^{-3} a distinct change in behaviour is observed, increases in concentration causing the initial iron release rate to diminish. Also, the form of the iron

release vs time plots progressively depart from linearity as the concentration rises, the iron release rate rising progressively throughout the course of a dissolution, Figure 31.

The total quantity of iron released prior to the switch to active corrosion (phase III) rises as a function of the oxalate concentration, Figure 32.

10.2.3 Post-Dissolution Disk Morphology

Dissolution in an EDTA solution free from any oxalate caused little discernible attack on the upper-layer crystals, only a slight rounding of the sharp crystal edges being detectable, Micrograph 25. The extent of the upper-layer crystal dissolution increases significantly as the oxalate concentration is raised from 0 to 3×10^{-4} mol$\cdot$dm^{-3}, Micrograph 26. At this latter concentration more than 50% of the disk surface is devoid of upper-layer crystals, the remaining crystals having suffered considerable attack. No further increase in the extent of upper-layer crystal dissolution is observed as the oxalate concentration is increased from 3×10^{-4} mol$\cdot$dm^{-3} to 1×10^{-2} mol$\cdot$dm^{-3}, Micrograph 27. Indeed, on the basis of SEM evidence, there is a suggestion that the extent of upper-layer crystal dissolution diminishes slightly as the oxalate concentration is increased from 1×10^{-3} mol$\cdot$dm^{-3} to 1×10^{-2} mol$\cdot$dm^{-3}.

10.3 OXALATE SOLUTIONS

10.3.1 Corrosion Potential

Two distinctly different types of corrosion potential behaviour were observed.

In two cases no transition from phase II to phase III occurred, the corrosion potential remaining at a value > +120 mV for the duration of the experiment (in one case up to ∿ 24 h (85,000 s)), Figure 33.

In the remaining experiments, the corrosion potential versus time behaviour displayed the characteristic three phases previously observed in all EDTA containing systems, Figure 34. As observed in the EDTA/oxalate mixtures with an oxalate concentration > 3×10^{-3} $mol \cdot dm^{-3}$ (Figure 27), the corrosion potential recovered in a positive direction immediately following the phase I to II transition.

In two experiments ferrous ammonium sulphate was added to the cell solution once it appeared that the potential was going to remain above +100 mV. The addition of this salt immediately caused the corrosion potential to drop by ∿ 100 mV, Figure 35. Following this the corrosion potential behaviour suggests that the dissolution proceeds as if the potential transition had occurred spontaneously.

In two experiments that exhibited sustained positive corrosion potentials, a small but distinct potential perturbation is apparent. The corrosion potential exhibits a sharp negative shift of ∿ 20 mV, followed by a recovery to its previous value, Figures 33 and 35.

10.3.2 Iron Release Behaviour

The iron release behaviour, shown in Figure 36, is very similar to that previously observed for the EDTA-oxalate mixtures containing high oxalate concentrations, Figure 31.

At the conclusion of experiments that feature a corrosion potential which remains above 120 mV, the quantity of iron in solution is below the detection limit of the analytical procedure used (i.e., $< 5 \times 10^{-7}$ moles).

10.3.3 Post-Dissolution Disk Morphology

The disks which maintain a positive corrosion potential for the duration of the experiment show no discernible attack on the upper-layer crystals, Micrograph 28. Disks that show a potential transition from phase II to III suffer extensive magnetite dissolution. The majority of the upper-layer crystals are completely dissolved, and the base-layer oxide suffers significant attack revealing the pearlite grain structures, Micrograph 29.

Studies of the two disks from the experiments in which ferrous ammonium sulphate was added show that only minor dissolution of the upper-layer crystals occurs, Micrograph 30.

10.4 STIRRING EFFECTS

10.4.1 EDTA-Oxalate Solutions

During dissolution experiments the disks were rotated to enhance the transport of both reactant and product species between the solution bulk and the surface of the disk, thus reducing the possibility of a rate-determining transport process.

The impact of stirring was studied in two experiments; the first in a 1×10^{-3} mol·dm^{-3} solution of EDTA, the second in 1×10^{-3} mol·dm^{-3} of oxalate. The corrosion potential was monitored throughout the dissolution process. On a number of occasions during each experiment the rotation was briefly halted, but restarted once the corrosion potential had achieved a stable value. For both the EDTA and oxalate solutions the termination of rotation caused a step change in potential, Figures 37 and 38, respectively.

In the EDTA solution the corrosion potential jumped 60-90 mV in the positive direction in $\sim$ 10 seconds. This change was reversible, the reverse shift requiring a similar interval of time. As shown in Figure 37, this behaviour was reproducible throughout phase II.

Following the transition to phase III a similar but opposite rotation dependence was observed, the corrosion potential changing by ∿ 20 mV.

In oxalate solutions the dependence of the corrosion potential on rotation speed during phase II was opposite to that observed for EDTA solutions, Figure 38. Immediately following the transition to phase II the corrosion potential was almost unaffected by the termination of rotation. As the dissolution proceeds the potential change becomes increasingly significant, a potential shift of ∿ 300 mV being observed just prior to the transition to phase III. The behaviour in phase III was similar to that observed for EDTA.

10.5 SOLUTION PROPERTIES

10.5.1 Ionic Strength

As the oxalate concentration is varied in the EDTA-oxalate mixtures the solution ionic strength changes. Speciation calculations have been performed, yielding the ionic strengths of each of the mixtures used, Figure 39. The results indicate that the ionic strength remains essentially constant in the oxalate concentration range 0 to 1×10^{-3} mol·dm^{-3}. This result suggests that neither the iron release rate nor corrosion potential changes observed can be attributed to changes in the solution ionic strength.

10.6 SOLUTION ANION COMPOSITION

10.6.1 General

To investigate the impact of ionic strength upon chemical and electrochemical processes, it is desirable to systematically vary ionic strength without changing the activities of reacting species. Both Na_2SO_4 and $NaClO_4$ contain anions that are generally regarded as poor complexing agents, these salts being commonly used to systematically alter solution ionic strength in such studies.

In this investigation four experiments were performed in solutions of the composition indicated in Table 10.3.

Table 10.3

Solution Compositions

Experiment	[EDTA] ($mol \cdot dm^{-3}$)	[Oxalate] ($mol \cdot dm^{-3}$)	[Na_2SO_4] ($mol \cdot dm^{-3}$)	[$NaClO_4$] ($mol \cdot dm^{-3}$)
A	3×10^{-4}	3×10^{-4}	0	0
B	3×10^{-4}	3×10^{-4}	1×10^{-3}	0
C	0	0	1×10^{-3}	0
D	0	0	0	1×10^{-3}

10.6.2 Corrosion Potential Behaviour

The presence of 1×10^{-3} mol·dm^{-3} sulphate in a mixed EDTA-oxalate solution causes a significant decrease in the value of T_2, while the value of E_2 remains unaffected, Figure 40.

The impact of sulphate was sufficient that a further dissolution was performed in a solution containing only 1×10^{-3} mol·dm^{-3} sodium sulphate. The value of T_2 obtained in this solution is less than that observed in the 3×10^{-4} mol·dm^{-3} equimolar mixture of EDTA and oxalate. This result is unexpected in view of the claim that sulphate is a poor complexing agent, suggesting that sulphate is promoting the oxide dissolution process. In an attempt to determine whether the sulphate anion participates directly in the dissolution process, a fourth experiment was performed in a 1×10^{-3} mol·dm^{-3} sodium perchlorate solution, since perchlorate is considered to be a weaker complexing anion than sulphate. The values of T_2 observed in the 1×10^{-3} mol·dm^{-3} solutions of sulphate and perchlorate differ very considerably, 3900 and 7600 seconds, respectively. The studies performed allow a comparison to be made between the corrosion potential behaviour observed during dissolutions performed in 1×10^{-3} mol·dm^{-3} solutions of EDTA, oxalate, sulphate and perchlorate, Figure 41. The values of E_2 differ considerably, the lowest E_2 value being observed for EDTA solution, perchlorate giving an intermediate value and sulphate the highest, approximately 150 mV higher than the values observed in EDTA solutions,

Table 10.4. The values of T_2 alter considerably. There does not appear to be any correlation between the value of E_2 and T_2, Table 10.4.

Table 10.4

T_2, E_2 Values as a Function of Anion Identity in 1×10^{-3} mol·dm^{-3} Solutions, pH=3.00±0.10, Room Temperature

Anionic Species	E_2† (mV)	T_2 (seconds)
EDTA	-127±11	2620
oxalate	variable	variable
sulphate	+13±8	3910
perchlorate	-58±17	7600

†E_2 value recorded at T = 1000 s.

10.6.3 Iron Release Behaviour

The iron release rates obtained are presented in Figure 42. The results indicate that the iron release rate observed in the 3×10^{-4} mol·dm^{-3} equimolar mixture of EDTA and oxalate is significantly increased by the addition of 1×10^{-3} mol·dm^{-3} sulphate.

The iron release behaviours observed in 1×10^{-3} mol·dm^{-3} solutions of EDTA, oxalate, sulphate and perchlorate do not reflect the relative complexing abilities of these species, Figure 43. The iron

releases observed in oxalate, sulphate and perchlorate all exhibit a significant induction period, and the iron release rate rises progressively throughout phase II. This behaviour contrasts with that observed for EDTA, Section 10.2.2. Figure 43 indicates that there are significant changes in the rates of iron release and the total quantities of iron released prior to the onset of active corrosion.

10.6.4 Post-Dissolution Disk Morphology

The mixed EDTA-oxalate solution dissolved a significant proportion of the upper-layer crystals, exposing the base-layer oxide on approximately 50% of the disk's surface area, Micrograph 31. Using adhesive materials it proved possible to remove the residual upper-layer and expose the base-layer oxide for examination. Dissolution does not occur generally over the entire base-layer oxide surface. A small percentage of the surface is covered by individual pits or small clusters of pits that have a diameter of 1-2 μm. There does not appear to be any correlation between the location of these features and the position of the pearlite grains. The remaining oxide film covering α-iron grains shows no visible signs of dissolution. Within the confines of the pearlite grains, many small pits are apparent, with pit diameters of approximately 0.1 μm, Micrograph 32.

Following dissolution in the EDTA-oxalate-sulphate system, only about 10% of the disk surface is free of upper-layer crystals, the residual crystals being well rounded, Micrograph 33. Following removal

of the residual upper-layer crystals, study of the base-layer oxide reveals that the attack has been less aggressive than that seen in the previous experiment. The larger pits, of the type observed in the previous experiment, are fewer in number, Micrograph 34. The extent of visible oxide attack following dissolutions in $1x10^{-3}$ $mol \cdot dm^{-3}$ solution of EDTA, oxalate, sulphate and perchlorate differ considerably, Micrographs 25, 29, 35 and 37, respectivly. The extent of upper-layer crystal dissolution is significantly greater in oxalate solutions than for any of the other solutions. The SEM evidence suggests that the extent of upper-layer crystal dissolution in EDTA, sulphate and perchlorate are comparable.

Dissolution in a sodium sulphate solution produces only moderate rounding of the upper-layer crystals, Micrograph 35. The base-layer oxide was exposed for examination, and the appearance of this oxide layer is as described for the previous experiment, Micrograph 36.

Dissolution in a sodium perchlorate solution produced only slight rounding of upper-layer crystals, Micrograph 37. No areas of base-layer oxide are exposed. It proved impossible to remove the upper-layer crystals using the techniques developed, suggesting that little dissolution occurs to weaken the attachment of the upper-layer crystals to the base-layer.

10.7 DISCUSSION

The work reported in chapters 8 and 9 indicates that autoreduction is the dominant dissolution process occurring during phase II, equations (10.1) and (10.2),

$$>Fe \rightarrow Fe^{2+} + 2e^{-} \qquad (10.1)$$

$$>Fe^{2+}(Fe^{3+})_2O_4 + 8H^{+} + 2e^{-} \rightarrow 3Fe^{2+} + 4H_2O \qquad (10.2)$$

and suggests that the rate-determining step is associated with the oxide dissolution half-reaction.

The iron release behaviour is difficult to rationalize if the principal oxide dissolution mechanism is direct dissolution.

$$>Fe_3O_4 + 8H^{+} \rightarrow 2Fe^{3+} + Fe^{2+} + 4H_2O \qquad (10.3)$$

This mechanism provides no ready explanation for the induction period observed at low oxalate concentrations or the accelerating iron release rates observed in more concentrated oxalate solutions.

The form of the iron release in oxalate solutions and oxalate-rich EDTA-oxalate mixtures is the same as that observed by Baumgartner for the dissolution of oxide particle suspensions in initially ferrous ion free oxalate solutions [24]. Hence, the mechanism proposed by

Baumgartner involving an SIRD process is one possible explanation of our experimental observations, i.e.,

$$Fe^{II}(C_2O_4)_{adsorbed} + >Fe^{III}(C_2O_4)$$

$$\rightleftharpoons Fe^{III}(C_2O_4)_{adsorbed} + >Fe^{II}(C_2O_4) \qquad (10.4)$$

$$>Fe^{II}(C_2O_4) \rightleftharpoons Fe(C_2O_4)_{adsorbed}$$

$$\rightleftharpoons Fe(C_2O_4)_{solution} \cdot \qquad (10.5)$$

Baumgartner found that the presence of ferrous species introduced to oxalate solutions prior to the start of magnetite dissolution experiments caused the immediate initiation of SIRD. To determine whether such a process could be activated in our case, solid ferrous ammonium sulphate was added to oxalate solutions following immersion of the disk, but prior to the initiation of a significant dissolution process. Thus, if SIRD is the principal oxide dissolution process during phase II, the anticipated result of this act would be accelerated oxide dissolution. This is not observed experimentally. The presence of ferrous species in oxalate solutions does not change the form of the corrosion potential-time trace, and the duration of phase II remains unchanged. Also, the extent of visible oxide dissolution at the conclusion of the experiment is less than in ferrous free solutions.

The similarities of the corrosion potential behaviour in EDTA-oxalate mixtures and in oxalate solutions (with and without added ferrous species) to that observed in EDTA alone, Chapters 8 and 9, suggests that a common dissolution mechanism is occurring and that autoreduction is the dominant process even in the presence of oxalate.

The experimentally observed corrosion potential is a mixed potential. Its dependence upon the reactant and product species concentrations is, therefore, influenced by the dependencies of both the anodic and cathodic half-reactions upon these parameters. In a simple system with only two active half-reactions, the corrosion potential adopts a value between the two half-reaction equilibrium potentials. The mixed potential will tend to the value of the equilibrium potential for the half-reaction that features the highest exchange current. The magnitude of this current is influenced by the surface area available for that process, and the half-reaction exchange current density, this latter parameter being constant for a given electrochemical process.

Equations (10.1) and (10.2) can be rewritten to reflect the direct participation of oxalate in both the anodic and cathodic half-reactions, equations (10.6) and (10.7):

$$Fe + (CO_2)_2^{2-} \rightarrow Fe(CO_2)_2 + 2e^- \qquad (10.6)$$

$$Fe^{2+}(Fe^{3+})O_4 + 3(CO_2)_2^{2-} + 8H^+ + 2e^- \rightarrow 3Fe(CO_2)_2 + 4H_2O \quad . \qquad (10.7)$$

Assuming that half-reactions (10.1) and (10.2) are at equilibrium, it is possible to apply the Nernst equation, yielding expressions for the half-reaction equilibrium potentials, equations (10.8) and (10.9).

For metal dissolution:

$$E_e = E_a' + 0.0295 \log[Fe^{2+}] \quad \text{vs} \quad \text{SCE} \tag{10.8}$$

and for magnetite dissolution:

$$E_e = E_c' - 0.2364\ \text{pH} - 0.089 \log[Fe^{2+}] \quad \text{vs} \quad \text{SCE} \ . \tag{10.9}$$

Similarly, equations (10.6) and (10.7) yield the dependency of each half-reaction's equilibrium potential upon the solution oxalate concentration. The constants E_c' and E_a' are different from E_c'' and E_a'' due to the inclusion of different terms. The E" constants include a log K_{sp} term.

For metal dissolution:

$$E_e = E_a'' - 0.0295 \log[(CO_2)_2^{2-}] \quad \text{vs} \quad \text{SCE} \tag{10.10}$$

and for magnetite dissolution:

$$E_e = E''_c - 0.2364\ pH + 0.089\ \log[(CO_2)_2^{2-}]\ \ vs\ \ SCE \qquad (10.11)$$

Beta-ferrous oxalate is a sparingly soluble salt. Once the solubility product (K_{sp}) of this salt is exceeded, the free ferrous ion concentration will be inversely proportional to the oxalate concentration, i.e.,

$$K_{sp} = [Fe^{2+}] \cdot [(CO_2)_2^{2-}] \qquad (10.12)$$

By virtue of this relationship it can be seen that once the solubility product for beta-ferrous oxalate is achieved, the equilibrium potential dependencies upon free ferrous ion concentration are indistinguishable from those upon oxalate concentration. Thus, the experimentally determined corrosion potential dependence upon oxalate concentration cannot distinguish between a mechanism involving the direct participation of oxalate in the dissolution process from an indirect effect caused by changes in the free ferrous ion concentration. However, irrespective of which of the two mechanisms is operating, the equilibrium potential for the metal dissolution process moves in the negative direction as the oxalate concentration rises, and the equilibrium potential for the magnetite dissolution reaction moves in the positve direction. Figure 44 shows the dependencies of both half-reaction equilibrium potentials, equations (10.1) and (10.2), upon the ferrous ion concentration. The dependence of half-reaction equilibrium potentials, equations (10.6) and (10.7), will be similar to that shown

in Figure 44, although the absolute values will vary due to the differences between E' and E" terms.

Figure 28 illustrates that the dependence of potential E_2 upon the oxalate concentration is more complex than that suggested by the Nernst relationships. The potential does shift in a positive direction as a function of oxalate concentration, but not in a consistent manner. At oxalate concentrations $\leq 1 \times 10^{-4}$ mol·dm^{-3} the potential E_2 shows little or no dependence upon the oxalate concentration, whereas in the oxalate concentration range 1×10^{-3}-1×10^{-2} mol·dm^{-3} E_2 displays a linear dependence on the logarithm of the oxalate concentration. The best fit straight line for the five data points in this region has a gradient of 85.5 mV/decade. This is similar to the value of 89 mV/decade predicted for the cathodic magnetite dissolution half-reaction. This suggests that for oxalate concentrations $\geq 1 \times 10^{-3}$ mol·dm^{-3}, the potential determining reaction is the magnetite dissolution half-reaction, and consequently the metal dissolution half-reaction is rate determining. Since the surface area of metal available rises throughout the dissolution process, we would expect a change in the iron release rate with time if metal dissolution is rate determining because the rate of this process would be determined, in part, by the surface area of exposed metal. Figure 31 shows that the iron release rate does rise progressively throughout the dissolution process for oxalate concentrations $\geq 1 \times 10^{-3}$ mol·dm^{-3}.

Both the iron release data in Figures 30 and 31 and the corrosion potential results in Figure 28 show a significant change in dissolution behaviour in the oxalate concentration range $1x10^{-4}$ to $1x10^{-3}$ mol•dm^{-3}. It would be anticipated that the behaviour in mixed EDTA-oxalate systems containing low oxalate concentrations would be similar to that observed for EDTA solutions, Chapters 8 and 9, where the oxide dissolution half-reaction contains the rate-determining step. The constant iron release rate observed throughout the dissolution processes supports this claim.

Consequently, the rate-determining reaction appears to change from the oxide dissolution process to the metal dissolution process as the oxalate concentration increases. This switch can be understood in terms of the precipitation of beta-ferrous oxalate dihydrate at the higher oxalate concentrations.

Shoesmith et al. [40] determined that crystals of beta-ferrous oxalate were deposited on the surface of magnetite-covered iron disks during dissolution experiments performed in solutions similar to those used in this study. During this study no attempt was made to confirm the presence of beta-ferrous oxalate on the surface of disks. In acidic $1x10^{-2}$ mol•dm^{-3} oxalate solutions the precipitation of this salt can be anticipated when high free ferrous ion concentrations are generated. The presence of EDTA in mixed solutions will certainly inhibit the precipitation process by reducing the free ferrous ion concentration. Calculations performed to determine the speciation of mixed EDTA-oxalate

solutions (Appendix A) indicate that the precipitation of ferrous oxalate is possible for the oxalate-rich mixtures used.

It is envisaged that the dissolution process yields locally high ferrous ion concentrations within the pores in the base-layer oxide film. Thus, precipitation is most likely to occur at these sites. The metal dissolution half-reaction occurs at the base of these pores in the oxide film, and precipitation of ferrous oxalate effectively reduces the surface area of metal available, reducing the exchange current for the anodic process and thereby causing the corrosion potential to move in the positive direction, Figure 45. This reaction is slowed sufficiently that it replaces the magnetite dissolution half-reaction as the rate-limiting step in the autoreductive dissolution process. Thus, the initial iron release rates are low. As the dissolution proceeds, the rising area of metal available causes the iron release rate to rise. At some intermediate point in the autoreduction process, it is probable that the identity of the rate-determining process changes to the oxide dissolution half-reaction. This could account for the linear iron release rates observed in the final stages of the dissolution process. Figure 46 indicates that the final iron release rate rises as a function of oxalate concentration throughout the entire concentration range, consistent with the suggestion that the oxide dissolution half-reaction is rate controlling at the end of phase II for all the oxalate concentrations investigated. Both the initial iron release rate, and E_2 dependence upon oxalate concentration, exhibit discontinuities in the oxalate concentration range $1x10^{-4}$-$1x10^{-3}$ $mol \cdot dm^{-3}$, Figure 28 and Figure

46. This coincidence is good evidence for the change in identity of the rate-determining step.

Further evidence for the change in the identity of the rate-determining step is provided by the stirring effects observed. If the dissolving oxide disk is rotated, transport processes between the disk surface and the solution bulk are promoted. If the rate of rotation is reduced or stopped the concentration of reaction products at the disk's surface will rise and the concentration of reactant species will diminish, leading to an increase in the concentration of free ferrous ion and a decrease in concentration of chelating agent. In EDTA solutions the corrosion potential is observed to move in a positive direction when the rotation is halted, while in oxalate solutions the potential moves in the opposite direction. These observations are consistent with our suggestion that different half-reactions are potential controlling in the two systems. The Nernst equations for both the metal and oxide half-reactions have been written, Equations (10.8) and (10.9). These equations describe the half-reaction equilibrium potential dependence upon free ferrous ion concentration. As the free ferrous ion concentration rises, the equilibrium potential for the metal dissolution reaction moves positive, and that for the oxide dissolution reaction negative. This suggests that the metal dissolution reaction is potential-determining in EDTA solutions, and that oxide dissolution is potential-determining in oxalate solutions. The identities of the potential-determining reactions are consistent with our previous designation. Following the transition to phase III, both reactions

exhibit the same rotation-potential dependence, consistent with a mixed potential dominated by the metal dissolution half-reaction potential.

The recovery of the corrosion potential in the positive direction immediately following the phase I to phase II transition (see Figures 27 and 34) is a consequence of ferrous oxalate precipitation. The observed behaviour suggests that the ferrous ion concentration is low at the end of phase I. The switch to autoreduction causes the ferrous ion concentration in the pores to rise rapidly, causing precipitation. This precipitation process gives rise to the positive recovery in the corrosion potential as the metal dissolution reaction is inhibited. This behaviour suggests that little oxide dissolution is occurring during phase I. If this were not the case, ferrous oxalate precipitation would occur prior to the initiation of phase II and the potential transient would not be observed. Therefore, both this explanation for the corrosion potential behaviour observed in oxalate-rich systems, and the interpretation of the iron release behaviour observed in EDTA-oxalate mixtures containing $\leq 3 \times 10^{-4}$ mol·dm^{-3} oxalate indicate that the iron release during phase I is low, and is not significantly enhanced by the presence of oxalate.

Although SIRD cannot definitely be ruled out, the experimental observations can be consistently explained in terms of an autoreductive process. Figure 46 indicates that the iron release rates observed at the conclusion of phase II (under autoreductive conditions) rise as a function of oxalate concentration throughout the entire concentration

range, showing that oxalate is affecting the rate of the oxide dissolution process.

The oxalate concentration can affect the autoreductive dissolution process in a number of ways: the oxalate anion could participate directly in either of the two half-reactions, or could simply change the free ferrous ion concentration by complexation,

$$[Fe^{II}(H_2O)_6]^{2+} + C_2O_4^{2-} \rightleftharpoons [Fe^{II}(H_2O)_4(C_2O_4)] + 2H_2O \qquad (10.13)$$

$$[Fe^{II}(H_2O)_4(C_2O_4)] + C_2O_4^{2-} \rightleftharpoons [Fe^{II}(H_2O)_2(C_2O_4)_2]^{2-} + 2H_2O \qquad (10.14)$$

$$[Fe^{II}(H_2O)_2(C_2O_4)_2]^{2-} + C_2O_4^{2-} \rightleftharpoons [Fe^{II}(C_2O_4)_3]^{4-} + 2H_2O \qquad (10.15)$$

thereby indirectly affecting dissolution by increasing ferrous ion solubility.

The direct participation of anions in the anodic dissolution of transition metals has been proposed by a number of workers [116,117,118], although such proposals are currently the subject of dispute. Our studies indicate that the acceleration in iron release rate, observed as the oxalate concentration rises (for oxalate concentrations $\leq 1 \times 10^{-4}$ mol·dm^{-3}), must arise from the impact of oxalate on the oxide dissolution half-reaction.

Two different oxide dissolution mechanisms appear consistent with our observations that the reaction rate displays a dependence upon oxalate concentration, while E_2 is concentration independent in EDTA-oxalate mixtures containing $\leq 1 \times 10^{-4}$ mol·dm^{-3} oxalate. One mechanism requires that an electrochemical process is rate determining; the second that a chemical process following the electrochemical steps is rate limiting.

If the rate-determining step is an electrochemical process, the independence of E_2 from oxalate concentration can only be explained if the half-reaction potentials for both reactions respond in an equal but opposite manner to the oxalate (or free ferrous ion) concentration. The two half-reaction equilibrium potentials do exhibit opposite concentration dependencies. However, as equations (10.8) and (10.9) (or equations (10.10) and (10.11)) indicate, the equilibrium potential of the metal dissolution half-reaction changes by 29 mV for each decade change in oxalate concentration, the equivalent figure for the oxide dissolution equilibrium potential being 89 mV. Thus, it is difficult to visualize circumstances under which these effects of differing magnitude would cancel, and the credibility of this mechanism is reduced as a consequence.

A mixed potential independent of oxalate concentration would be anticipated if the rate-determining reaction is a chemical process that follows the electrochemical step. The increase in the iron release rate caused by the addition of low concentrations of oxalate to EDTA

indicate that oxalate is participating directly in the rate-determining step. The fractional rate order with respect to oxalate probably arises from the form of the oxalate adsorption isotherm and the competition for surface sites with EDTA.

Matijević et al. have studied the dissolution of colloidal hematite in oxalic and citric acids [15], in EDTA [16] and the dissolution of nickel ferrite in EDTA [36]. They interpret the dissolution behaviour of hematite using a surface complexation model [17]. Matijević claims that hematite dissolution in oxalic and citric acids does not arise because of the reduction in the solution free metal ion concentration caused by complexation, stating that these complexing agents are chemisorbed on the oxide and that the desorption of the surface complex is rate limiting. The rate of hematite dissolution in EDTA at 26°C increases with pH to a maximum at a pH $\sim$ 10, and this is interpreted as indicating that at 26°C hematite dissolution is taking place primarily from a non-complexed surface. At 100°C the dissolution of hematite in EDTA appears to occur via the desorption of ferric chelate complexes from the oxide surface, the pH sensitivity seen at 26°C being reversed.

Matijević et al. also claim that when oxide dissolution is occurring through the desorption of surface complexes the rate of reaction is directly proportional to the concentration of surface complexes. It is demonstrated that the oxide dissolution rate

sensitivity to pH can be wholly attributed to changes in the concentration of surface complexes.

Their work with citric acid and oxalic acid indicates that only anions carrying a negative charge of 2 or greater form surface complexes, further suggesting that the anions bond to the surface through two carboxyl groups. Steric effects are important in determining the maximum surface coverage, and hence the maximum rate of dissolution in the presence of a given anion. Oxalate achieves a maximum surface coverage $\sim$ 4 times greater than citrate.

A further significant result obtained by Matijević et al. is the form of the adsorption isotherms for oxalic and citric acid upon hematite. These isotherms relate the equilibrium surface and solution concentrations. The surface concentrations rise as a function of solution concentration, particularly in low pH solutions the initial rise in surface concentration being rapid. Following this the surface concentration is much less sensitive to the solution concentration changes. This indicates that below critical solution concentrations of complexing agents the concentration of the surface complex and hence the rate of dissolution decrease rapidly.

The work of Matijević et al. supports our suggestion that the autoreductive dissolution process is rate controlled by a chemical process in the oxide dissolution half-reaction.

Their work suggests that at 26°C EDTA behaves differently from oxalic and citric acids in that the rate-determining step does not involve the desorption of a surface complex. This does not appear to be the case for the autoreductive dissolution of magnetite. The work presented in Chapter 8 indicated that the rate of oxide dissolution is approximately directly proportional to the hydrogen ion concentration, and in this study, Figure 47 indicates that the reaction rate rises with increasing EDTA concentration in the presence of oxalate. Neither of these reaction rate dependencies would be expected if the dissolution of magnetite in EDTA proceeded by the mechanism suggested for hematite in EDTA at 26°C.

Dissolutions in EDTA differ from those performed in oxalate, sulphate and perchlorate. The iron release rate is essentially constant throughout phase II and the corrosion potential is more negative than that observed during dissolutions in the other reagents, Figures 41 and 43. The form of the iron release curves in oxalate, sulphate, and perchlorate all suggest that the metal dissolution half-reaction is rate determining throughout phase II. This does not appear to be the case for EDTA. It is possible that EDTA, by reducing the solution concentration of ferrous ion, enhances the rate of metal dissolution. The work with EDTA-oxalate mixtures containing low concentrations of oxalate indicated that the iron release during phase II commences with an induction period of < 250 seconds. Upon initiation of the autoreduction process, the minute area of metal available dictates that the metal dissolution process is rate controlling. The reaction rate

will initially increase in proportion to the growing area of metal. It is possible that EDTA enhances the metal dissolution reaction to such an extent that within the first 250 seconds of autoreduction the area of metal available is sufficient to support a reaction rate greater than the oxide dissolution half-reaction can sustain, and thus the oxide dissolution process becomes rate controlling and a linear iron release is observed. The claim that EDTA enhances the metal dissolution process is supported by the more negative corrosion potential observed during dissolutions in EDTA. Oxalate, sulphate, and perchlorate do not appear to promote the metal dissolution reaction, causing the metal dissolution process to remain rate determining for the greater part of phase II.

The model proposed by Matijević et al. explains the dissolution behaviour observed in multicomponent solutions. The addition of oxalate to EDTA promotes dissolution by increasing the concentration of surface complexes, thereby accelerating the rate-controlling oxide dissolution process. Sulphate behaves similarly. Under the conditions employed, the concentration of surface complexes appears to be well below saturation, as demonstrated by the significant iron release rate acceleration achieved by the addition of sulphate to a mixed EDTA-oxalate solution. The significant difference in the behaviour of sulphate and perchlorate is possibly due to the different ionic charges.

It is observed that as the rate of reaction increases, the site of magnetite dissolution becomes more general. It is possible to

rationalize this behaviour using the arguments developed in Chapter 9. The more general dissolution process suggests that pore dissolution becomes rate limited by transport processes, and thus further increases in the rate of oxide dissolution only promotes the dissolution of oxide outside the pores where the rate of oxide dissolution is not constrained by transport processes. Thus, accompanying the rise in the iron release rate, is an increase in the total amount of iron released prior to the initiation of active corrosion, Figure 32.

The addition of ferrous ammonium sulphate to disks that are exhibiting stable positive corrosion potentials causes the potential to abruptly shift in the negative direction, consistent with a mixed potential dominated by the oxide dissolution half-reaction. Following the addition of ferrous ammonium sulphate, the corrosion potential behaviour observed is similar to that seen when the autoreductive dissolution process commenced spontaneously. However, SEM evidence suggests that under these circumstances little visible oxide dissolution occurs. This behaviour can be attributed to the reduction in the solution oxalate concentration caused by complexation with the added ferrous ion. It is possible that following the addition of ferrous ammonium sulphate, the sulphate anion and not oxalate is primarily responsible for oxide dissolution.

CHAPTER 11

SUMMARY

Magnetite films present on carbon steel appear to consist of three principal structural components. A porous base-layer film, typically several microns in thickness, covers the carbon steel. The base-layer film grows from the substrate metal by a solid-state process, the metal structure significantly influencing the properties of the oxide film. The base-layer oxide overlying pearlite grains is thinner and more porous than that formed on α-iron. At the bottom of pores in the base-layer film the carbon steel appears to be covered by a very thin barrier-layer of oxide. Films can be grown with and without the third, upper-layer, of discrete magnetite crystals formed by a solution nucleation and precipitation process.

Phase I of film dissolution in acidic solutions appears to consist of solution migration to, and dissolution of, the barrier-layer film. The total time for these processes is typically less than 300 seconds. Penetration of the barrier-layer film involves the dissolution of very small quantities of oxide. The speed and scale of this dissolution process have, as yet, prevented the identification of the dissolution mechanism.

Penetration of the barrier-layer oxide exposes carbon steel to the electrolyte, causing the initiation of autoreduction, phase II.

During phase II autoreductive dissolution is dominant. If either SIRD, involving Fe(II) complexes, or direct dissolution are occurring they are only minor contributors to the total oxide dissolution process.

Autoreductive dissolution of base-layer oxide exposes increasing areas of metal to the solution throughout the dissolution process, causing the corrosion potential to move cathodically. The cathodic drift continues gradually until proton reduction becomes thermodynamically feasible. At this point a rapid and near complete switch in mechanism to active corrosion occurs, phase III.

In all the systems studied autoreduction is the dominant oxide dissolution process during phase II, and hence is the principal mechanism by which oxide dissolution occurs prior to the onset of active corrosion. The data strongly suggest that autoreduction in EDTA based solutions is rate-limited by the oxide, and not the metal, dissolution half-reaction.

Oxide dissolution during autoreduction occurs preferentially within pores in the base-layer. Thus, oxide dissolution occurs principally at pearlite grain sites, the remainder of the oxide grown on α-iron being little affected. Dissolution of upper-layer crystals, when present, does not contribute to the exposure of metal, and therefore does not directly affect the duration of the autoreductive process. However, the upper-layer crystal dissolution reaction causes significant changes in the solution composition in the base-layer, and in this way

influences its dissolution. The presence of upper-layer crystals effectively buffers the solution composition in the base-layer film, so that changes in the bulk solution chemistry do not necessarily cause corresponding changes at the site of oxide dissolution.

When reaction rates are low the oxide dissolution process is confined almost exclusively within pores in the base-layer. Such dissolution processes are inefficient, removing little oxide prior to the onset of active corrosion. The restricted geometry of these pores means that the reactions at such sites are prone to transport control. If autoreduction is accelerated either thermally or chemically the pore oxide dissolution process becomes transport limited. This causes the magnetite dissolution process to occur more generally over the entire surface area of oxide. In EDTA solutions a temperature increase from 25°C to 85°C caused oxide dissolution to change from essentially a pore process to a significant general dissolution process. Thus, thermal acceleration of autoreduction increases the efficiency of oxide dissolution.

A similar result was obtained when the reaction was chemically promoted. The addition of oxalate, at relatively low concentrations, to EDTA solutions increased both the rate and efficiency of oxide dissolution.

The addition of high oxalate concentrations to EDTA solutions caused the precipitation of ferrous oxalate dihydrate in the base-layer

pores during autoreductive film dissolution. This precipitate restricts the effective surface area of metal available to the electrolyte to such an extent that, initially, autoreduction is rate limited by metal dissolution, and low oxide dissolution rates are observed. In these circumstances the rate of reaction rises progressively as pore expansion exposes increasing areas of metal. Rate-control by the oxide dissolution process appears to be reestablished in the final stages of autoreduction before the onset of active corrosion.

It appears that the oxide dissolution half-reaction is rate limited by a chemical dissolution process, possibly involving the desorption of a surface cation complex. The observed rate dependencies on anion identity, anion concentration, and pH can be rationalized using the adsorption and dissolution model proposed by Matijević et al. [16,17,36,78].

On the basis of their data, the rate of dissolution would be proportional to the surface complex concentration. The pH and solution speciation effects on rate arise as a consequence of changes induced in the surface complex concentration. The results suggest, that under the conditions used, surface coverage of magnetite by surface complexes is low, such that increasing the solution concentration of complexing species increases the surface complex concentration.

At pH $\sim$ 3 EDTA, oxalate, and sulphate all appear to form surface complexes. The relative abilities of these species to form

surface complexes does not reflect the large differences in their solution complexation constants. This observation is clearly of importance when formulating decontamination reagents.

REFERENCES

1. J.W. Diggle (Ed.), Pub. Marcel Dekker, Inc., New York (1973), Oxides and Oxide Films, Vol. 2, The anodic behaviour of metals and semiconductors series.

2. G. Koch, Ber. Bunsenges. Physik. Chem., 69, (2), pp. 141-5 (1965), Kinetics and mechanism of the dissolution of beryllium oxide in acid.

3. E. Devuyst and I.H. Warren, Proc. Symp. Oxide - Electrolyte Interfaces (1972) (Pub. 1973), The leaching of iron and aluminum oxides.

4. I.H. Warren et al., Trans. Inst. Min. Metall. (Sect C, Mineral Process. Extr. Metall.), Vol. 78 (1969), pp. C21-27, Anisotropic dissolution of hematite.

5. I.H. Warren and G.I.D. Roach, Trans. Inst. Min. Metall. (Sect. C, Mineral Process. Extr. Metall.), Vol. 80 (1971), pp. C152-155, Physical aspects of the leaching of goethite and hematite.

6. I.H. Warren and A.J. Monhemius, Paper No. 5, The Conference of Metallurgists, Toronto (1966), The dissolution of iron oxide in aqueous solutions of sulphur dioxide.

7. V.S. Surana and I.H. Warren, Trans. Inst. Min. Metall. (Sect. C, Mineral Process. Extr. Metall.), Vol. 78 (1969), pp. C133-139, The leaching of goethite.

8. I.H. Warren and E. Devuyst, Paper presented at the Electrochemical Society Fall Meeting, Miami (1972), Abstract No. 182, pp. 446-448, The leaching of iron and aluminum oxides.

9. M.J. Pryor and U.R. Evans, J. Chem. Soc. (London) (1949), pp. 3330-3336, Passivity of metals. X. The mechanism of direct solution of ferric oxide.

10. K. Azuma and H. Kametani, Trans. AIME, Vol. 230 (1964), pp. 853-862, Kinetics of dissolution of ferric oxide.

11. D. Bradbury, Water Chem. Ncul. Reac. Syst., Proc. Int. conf. (1977) (Pub. 1978), Paper 44, The chemical dissolution of Fe(III) oxide.

12. I.G. Gorichev, V.S. Dukhanin, N.A. Kipriyanov, Russian Journal of Physical Chemistry, 54, (5) (1980), pp. 774-776, The influence of the pH of the medium on the kinetics of the dissolution of magnetite in a solution of sodium ethylenediaminetetra-acetate.

13. I.G. Gorichev, N.G. Klyuchnikov, Z.P. Bibikova and I.G. Boltovskaya, Russian Journal of Physical Chemistry, 50, (12) (1976), pp. 1853-1855, Kinetics of the dissolution of magnetite in sulphuric acid.

14. V.I.E. Bruyère and M.A. Blesa, Journal Electroanalytical Chemistry and Interfacial Electrochemistry.

15. Y. Zhang, N. Kallay and E. Matijević, Langmuir (1985), 1, pp. 201-206, Interactions of metal hydrous oxides with chelating agents. 7. Hematite-oxalic acid and-citric acid systems.

16. H.-C. Chang and E. Matijević, Journal of Colloid and Interface Science, Vol. 92, No. 2 (1983), pp. 479-488. Interactions of metal hydrous oxides with chelating agents. IV. Dissolution of hematite.

17. N. Kallay and E. Matijević, Langmuir (1985), 1, pp. 195-201, Adsorption at solid/solution interfaces. 1. Interpretation of surface complexation of oxalic and citric acids with hematite.

18. R. Gilbert and L. Ouellet, Nuclear Technology, Vol. 68 (1968), pp. 385-394, Dissolution of metal oxides accumulated in nuclear steam generators: study of solutions containing organic chelating agents.

19. B.A. Zabin and H. Taube, Inorganic Chemistry, Vol. 3, No. 7 (1964), pp. 963-968, The reactions of metal oxides with aquated chromium(II) ion.

20. D.F.A. Koch, Aust. J. Chem. (1957), 10, p. 150, Kinetics of the reaction between manganese dioxide and ferrous ion.

21. M.G. Segal and R.M. Sellers, J. Chem. Soc., Faraday Trans. 1 (1982), 78, pp. 1149-1164, Kinetics of metal oxide dissolution.

22. M.G. Segal and R.M. Sellers, Advances in Inorganic and Bioinorganic Mechanisms, Vol. 3, pp. 97-129, Redox reactions at solid-liquid interfaces.

23. M.G. Segal and R.M. Sellers, J.C.S. Chem. Comm. (1980), pp. 991-993, Reactions of solid iron(III) oxides with aqueous reducing agents.

24. E. Baumgartner, M.A. Blesa, H.A. Marinovich and A.J.G. Maroto, Inorganic Chemistry (1983), 22, pp. 2224-2226, Heterogeneous electron transfer as a pathway in the dissolution of magnetite in oxalic acid solutions.

25. T. Kishi, S. Shimizu and T. Nagai, Surface Technology, 16 (1982), pp. 23-29, Effects of anions on the anodic dissolution of nickel ferrous ferrite electrodes.

26. T. Kishi and T. Nagai, Surf. Technol., 15 (1982), p. 199-206, Anodic oxidation of nickel ferrous ferrite electrodes.

27. Y. Kawashima, T. Kishi and T. Nagai, Denki Kagaku Oyobi Kogyo Butsuri Kagaku, 45 (1977), p. 299-303, Anodic behaviour of iron-nickel ferrite electrodes.

28. S. Trasatti (Ed.), Studies in Physical and Theoretical Chemistry, No. 11, Part A, Electrodes of Conductive Metal Oxides, M.R. Tarasevich and B.N. Efremov, Chapter 5. Properties of spinel-type oxide electrodes.

29. A.C.C. Tseung and S. Jasem, Electrochimica Acta, Vol. 22 (1977), pp. 31-34, Oxygen evolution on semiconducting oxides.

30. J.G.D. Haenen, W. Visscher and E. Barendrecht, Journal of Applied Electrochemistry, 15 (1985), pp. 29-38, Oxygen evolution on $NiCo_2O_4$ electrodes.

31. J.B. Hiskey, Inst. Min. Metall. Trans. C., 89 (1980), p. 145, Hydrogen peroxide leaching of uranium in carbonate solutions.

32. M.J. Nicol and C.R.S. Needes, Electrochimica Acta, 20 (1975), p. 585, The anodic dissolution of uranium dioxide-I in perchlorate solutions.

33. S. Sunder, D.W. Shoesmith, M.G. Bailey, F.W. Stanchell and N.S. McIntyre, J. Electroanal. Chem., 130 (1981), p. 163, Anodic oxidation of UO_2. Part I. Electrochemical and X-ray photoelectron spectroscopic studies in neutral solutions.

34. D.W. Shoesmith, T.E. Rummery, W. Lee and D.G. Owen, Power Industry Research (1981), 1, pp. 43-63, Dissolution of oxide films on iron in aqueous solutions containing complexing anions - I. Magnetite in citrate and ethylenediaminetetra-acetate.

35. J. Rubio and E. Matijević, Journal of Colloid and Interface Science, Vol. 68, No. 3 (1979), pp. 408-421, Interactions of metal hydrous oxides with chelating agents. I. ß-FeOOH-EDTA.

36. A.E. Regazzoni and E. Matijević, Corrosion, National Association of Corrosion Engineers (NACE), Vol. 40, No. 5 (1984), Interactions of metal hydrous oxides with chelating agents. VI. Dissolution of a nickel ferrite in EDTA solutions.

37. G.V. Buxton, T. Rhodes and R.M. Sellers, Journal of the Chemical Society, Faraday Trans. 1 (1983), 79, pp. 2961-2974, Radiation chemistry of colloidal hematite and magnetite in water.

38. R.M. Sellers and W.J. Williams, Faraday Discussion Chem. Soc. (1984), 77, paper 21, High-temperature dissolution of nickel chromium ferrites by oxalic acid and nitrilotriacetic acid.

39. E. Baumgartner, M.A. Blesa and A.J.G. Maroto, J. Chem. Soc. Dalton Trans. (1982), pp. 1649-1654, Kinetics of the dissolution of magnetite in thioglycolic acid solutions.

40. D.W. Shoesmith, W. Lee and D.G. Owen, Power Industry Research (1981), 1, pp. 253-267, Dissolution of oxide films on iron in aqueous solutions containing complexing anions - II. Magnetite in oxalic acid and oxalic acid plus EDTA.

41. J.N. Butler, J. Chem. Phys., 35, p. 636 (1961).

42. U. Stimming and J.W. Schultze, Electrochimica Acta, Vol. 24, pp. 859-869 (1979), A semiconductor model of the passive layer on iron electrodes and its application to electrochemical reactions.

43. U. Stimming and J.W. Schultze, Ber. Bunsenges. Phys. Chem., 80, p. 1297 (1976).

44. H. Yoneyama, T. Fujimoto, K. Kubo and H. Tamura, J. Electroanal. Chem., 63 (1975), pp. 85-96, Adsorption of dicarboxylic acids on lithiated nickel oxide electrode.

45. D.A. Vermilyea, Journal of the Electrochemical Society. Vol. 113, No. 10 (1966), pp. 1067-1070, The dissolution of ionic compounds in aqueous media.

46. H.J. Engell, Z. Physik. Chem. N.F., 7, p. 158 (1956).

47. J. O'M. Bockris and A.K.N. Reddy, Plenum Publishing Corp., 3rd edn., Modern Electrochemistry.

48. M. Pourbaix, Atlas of Electrochemical Equilibria in Aqueous Solutions, Permagon Press, Oxford (1966).

49. P.S. Sidhu, R.J. Gilkes and A.M. Posner, J. Inorg. Nucl. Chem., Vol. 39, pp. 1953-1958 (1977), Mechanism of the low temperature oxidation of synthetic magnetites.

50. A.F. Wells, Clarendon Press, Oxford, 4th edn. (1975), Structural Inorganic Chemistry.

51. M.B. Robin and P. Day, Adv. Inorg. Chem. Radiochem., 10, p. 247 (1967), Mixed-valence chemistry - a survey and classification.

52. R. Bauminger, S.G. Cohen, A. Marinov, S. Ofer and E. Segal, Phys. Rev., Vol. 122, p. 1447 (1961), Study of the low-temperature transition in magnetite and the internal fields acting on iron nuclei in some spinel ferrites, using Mössbauer absorption.

53. B.J. Evans and S.S. Hafner, J. Appl. Phys., Vol. 40, No. 3, pp. 1411-3 (1969), Iron-57 hyperfine fields in magnetite (Fe_3O_4).

54. N.M. Kovtun, V.K. Prokopenko and A.A. Shamyakov, Solid State Commun. (1978), 26(12), pp. 877-8, Electroconductivity and electron exchange in spinel structures.

55. J.E. Huheey, Harper and Row (1972), Inorganic chemistry: principles of structure and reactivity.

56. G. Blasse, Philips Research Reports Supplements, (1964), No. 3, Crystal chemistry and some magnetic properties of mixed metal oxides with spinel structures.

57. E.J.W. Verwey and P.W. Haayman, Physica, 8, p. 979 (1941).

58. F. Walz and J. Rivas, Phys. Stat. Sol. (a) 37, p. 151 (1976), Magnetic after-effects in manganese ferrites.

59. J.M. Hastings and L.M. Carliss, Phys. Rev., 104, p. 328 (1956).

60. I.I. Yamzin et al, J. Phys. Soc. Japan (Suppl.) 17, B-III, p. 55 (1962).

61. C.P. Marshall and W.A. Dollase, American Mineralogist, Vol. 69, p. 928-936 (1984), Cation arrangement in iron-zinc-chromium spinel oxides.

62. T.E. Whall, K.K. Yeung and Y.G. Proykova, Philosophical Mag. B (1984), Vol. 50, No. 6, p. 689-707, The electrical conductivity and thermoelectric power of nickel ferrous ferrite.

63. J. Rivas, J. Iniguez and E. Moreno, IEEE Transactions on Magnetics Vol. MAG-20, No. 5, (1984), p. 1509-11, Some properties of sintered iron, manganese, nickel and cobalt spinel ferrites at low frequencies.

64. B.G. Street, Powder Metallurgy, Vol. 2, p. 62-67, (1979), Present technology of hard and soft ferrites.

65. G.H. Jonker, J. Phys. Chem. Solids, Vol. 9, p. 165-175, (1959), Analysis of the semiconducting properties of cobalt ferrite.

66. E.J.W. Verwey, Physica, Vol. 2, p. 1059 (1935).

67. D.M. Shub, A.N. Chemodanov and U.V. Shalaginov, Elektrokhimiya 14 (1978), p. 595.

68. A. Rosencwaig, Canadian Journal of Physics, Vol. 47, p. 2309-2317 (1969), Double exchange and electron hopping in magnetite.

69. K.J. Gallagher, W. Feitknecht and U. Mannweiler, Nature, 217, p. 1118 (1968), Mechanism of oxidation of magnetite to γ-Fe_2O_3.

70. H. Kronmüller, R. Schutzenauer and F. Walz, Phys. Stat. Sol. (a), 24, p. 487 (1974), Magnetic after-effects in magnetite.

71. C.F. Jones, R.L. Segall, R.St.C. Smart, P.S. Turner, Journal of the Chemical Society, Faraday Transactions I (1977), Vol. 73, p. 1710-1720, Semiconducting oxides.

72. H. Kametani and K. Azuma, Trans. Met. Soc. AIME (1968), 242, p. 1025.

73. J. Eisenlauer, E. Matijević, Journal of Colloid and Interface Science, Vol. 75, No. 1, (1980), p. 199-211, Interactions of Metal hydrous oxides with chelating agents II. α-Fe_2O_3 - low molecular and polymeric hydroxamic acid species.

74. H.-C. Chang, T.W. Healy, E. Matijević, Journal of Colloid and Interface Science, Vol. 92, No. 2, (1983), p. 469-478, Interactions of metal hydrous oxides with chelating agents III. Adsorption on spherical colloidal hematite particles.

75. P.S. Sidhu, R.J. Gilkes and A.M. Posner, J. Inorg. Nucl. Chem., Vol. 40, p. 429-435 (1978), The synthesis and some properties of Co, Ni, Zn, Cu, Mn, and Cd substituted magnetites.

76. I. David and A.J.E. Welch, Trans. Faraday Soc., 53, p. 1642 (1956).

77. T. Sugimoto and E. Matijević, Journal of Colloid and Interface Science, Vol. 74, No. 1, (1980), p. 227-243, Formation of uniform spherical magnetite particles by crystallization from ferrous hydroxide gels.

78. H.-C. Chang, E. Matijević, Finnish Chem. Lett., Vol. 6-8, p. 90-5 (1982), Interactions of metal hydrous oxides with chelating agents. Part V. Magnetite-EDTA.

79. M.A. Blesa, E.B. Borghi, A.J.G. Maroto, A.E. Regazzoni, Journal of Colloid and Interface Science, Vol. 98, No. 2, (1984), p. 295-305, Adsorption of EDTA and iron-EDTA complexes on magnetite and the mechanism of dissolution of magnetite by EDTA.

80. M.A. Blesa, A.J.G. Maroto, Congress on the Reactivity of Solids, The nature of reactive sites in the dissolution of metal oxides by acid chelating agents in aqueous solution.

81. G.V. Buxton, T. Rhodes, R.M. Sellers, Nature, Vol. 295, 18 February, 1982, p. 583-585, Radiation-induced dissolution of colloidal haematite.

82. G.C. Allen, R.M. Sellers, P.M. Tucker, Philosophical Magazine B (1983), Vol. 48, No. 4, L5-L9, Surface composition and morphology of magnetite crystals during dissolution.

83. K.J. Vetter and H.H. Strehblow, Proc. Symp. on "Localized Corrosion", NACE (pub.) Huston (1974), p. 240-251, Pitting corrosion in an early stage and its theoretical implications.

84. W.C. Mackrodt and P.W. Tasker, Chemistry in Britain, April 1985, p. 366-369, Surfaces and interfaces in oxides.

85. D.P. Benton and G.A. Horsfall, J. Chem. Soc., p. 3899 (1962), Sorption from some electrolyte solutions by synthetic magnetite.

86. E. Tronc, J.-P. Jolivet, J. Lefebvre, R. Massart, Journal of The Chemical Society, Faraday Transactions 1 (1984), 80, p. 2619-2629, Ion adsorption and electron transfer in spinel-like iron oxide colloids.

87. A.M. Riley and J.M. Sykes, Passivity of metals and semiconductors, Proceedings of the 5th International Symposium on Passivity, May 30 - June 3, 1983, Rotated ring-disk electrode studies of the passivation of low-alloy steels.

88. D.W. Shoesmith, unpublished.

89. D. Bradbury, M.G. Segal, R.M. Sellers, T. Swan, C.J. Wood, Electric Power Research Institute (EPRI), Palo Alto, California (1983), Report No. EPRI NP-3177.

90. D.G. Wickham, Inorganic Synthesis (1967), Vol. 9, p. 152, Metal Fe(III) oxides.

91. E. Devuyst and I.H. Warren, International Symposium on Hydrometallurgy, Avail. Nat. Libr. Canada, Ottawa, Ont., From Diss. Abstr. Int. B (1974), 34(12), 6022.

92. M.E. Wadsworth and D.R. Wadia, Trans. AIME, Vol. 203 (1955), p. 755-759, Reaction rate study of the dissolution of cuprite in sulfuric acid.

93. L.G. Sillen and A.E. Martell, The Chemical Society, London, Special Publication No. 17 (1964), Stability constants of metal-ion complexes.

94. R.L. Parfitt, V.C. Farmer, J.D. Russell, J. Soil Sci. 28 (1977), p. 24-39, Adsorption on hydrous oxides. I. Oxalate and benzoate on goethite.

95. R.L. Parfitt, A.R. Frazer, J.D. Russell, V.C. Farmer, J. Soil. Sci., 28 (1977), p. 40-47, Adsorption on hydrous oxides. II. Oxalate, benzoate and phosphate on gibbsite.

96. R.L. Parfitt, J.D. Russell, Journal of Soil Science (1977), 28, p. 297-305.

97. O. Siiman, L.A. Blumm, R. Callaghan, C.G. Blatchford, M. Kerkes, J. Phys. Chem. (1983), 87, p. 1014.

98. D.J. Bauer and R.E. Lindstrom, J. Metals, May 1971, p. 31-33, Use of chelating agents for recovery of copper from carbonate and silicate ores.

99. U.R. Evans, Proc. Roy. Soc. (1925), A, 107, p. 228.

100. U.R. Evans, Journal of the Chemical Society (1930), p. 478.

101. U.R. Evans, Journal of the Chemical Society (1930), p. 481.

102. M.J. Pryor and U.R. Evans, Journal of the Chemical Society (1950), p. 1259, The reductive solution of ferric oxide in acid. 1. The reductive solution of oxide films present on iron.

103. M.J. Pryor and U.R. Evans, Journal of the Chemical Society (1930), p. 1266, The reductive dissolution of ferric oxide in acid. Part II. The reductive dissolution of powdered ferric oxide.

104. D.J.M. Bevan, J.P. Shelton and J.S. Anderson, Journal of the Chemical Society (1948), p. 1729-1741, Properties of some simple oxides and spinels at high temperatures.

105. M.J. Pryor, Journal of the Chemical Society (1930), p. 1274, The reductive dissolution of ferric oxide in acid. Part III. The mechanism of reductive dissolution.

106. C.D. Stockbridge, P.B. Sewell, M. Cohen, Journal of the Electrochemical Society, Vol. 108, No. 10 (1961), p. 928-933, Cathodic behaviour of iron single crystals and the oxides Fe_3O_4, gamma-Fe_2O_3, and alpha-Fe_2O_3.

107. Y. Kurimura, R. Ochiai and N. Matsuura, Bulletin of the Chemical Society of Japan, Vol. 41, No. 10, p. 2234-39 (1968), Oxygen oxidation of ferrous ions induced by chelation.

108. E. Bjergbakke, Proceedings of an Interdisciplinary Symposium, Odense University, Denmark, September 1974, Measurement of oxygen.

109. M.H. Hey, Mineralogical Magazine, March 1982, Vol. 46, p. 111-118, The determination of ferrous and ferric iron in rocks and minerals; and a note on sulphosalicyclic acid as a reagent for Fe and Ti.

110. M.H. Hey, Mineralogical Magazine, December 1982, Vol. 46, p. 512-13, The determination of ferrous and ferric iron in rocks and minerals: addendum.

111. J.W. Stucki and W.L. Anderson, Soil Sci. Soc. Am. J., Vol. 45, p. 633-637 (1981), The quantitative assay of minerals for Fe(II) and Fe(III) using 1,10-phenanthroline I. Sources of variability.

112. J.W. Stucki, Soil Sci. Soc. Am. J., Vol. 45, p. 638-641 (1981), The quantitative assay of minerals for Fe(II) and Fe(III) using 1,10-phenanthroline II. A photochemical method.

113. T. Swan, D. Bradbury, M.G. Segal, R.M. Sellers, C.J. Wood, C.E.G.B. Research, June 1982, P. 3-14, Chemical decontamination of water-reactor circuits: the development of LOMI reagents.

114. J.M. West, Pub. Van Nostrand Reinhold Company, London (1971), Electrodeposition and corrosion processes.

115. D. Bradbury, M.G. Segal, R.M. Sellers, T. Swan, C.J. Wood, British Nuclear Energy Society: London (1981), p. 403, Water chemistry of nuclear reactor systems 2.

116. A. Saraby-Reintjes, Electrochimica Acta., Vol. 30, No. 3, p. 387-401 (1985), The theory of competitive adsorption and its application to the anodic dissolution of Ni and other Fe-group metals. I. Active dissolution in acidic solutions under steady state conditions.

117. G.M. Florianovich, L.A. Sokolova and Ya. M. Kolotyrkin, Electrochimica Acta., Vol. 12, p. 879-887 (1967), Mechanism of the anodic dissolution of iron in acid solutions.

118. Ya. M. Kolotyrkin, Usp. Khim. Vol. 31, 3 (1962).

119. G.C. Allen and R.M. Mascall, CEGB Res., Vol. 11, p. 32 (1982).

Reagent	Concentration (10^3 x mol.dm^{-3})	pH
HCl	100	0
EDTA	100	5
Oxalate	200	5
TGA	100	3
Cr(II)-Cl^-	40	1
V(II)-ClO_4^-	10	1
Cr(II)(bipy)$_3$	4	5
V(II)(bipy)$_3$	4	4.5
V(II)(pic)$_3$	4	5
V(III)(citrate)	4	4
Fe(II)-EDTA	2	4

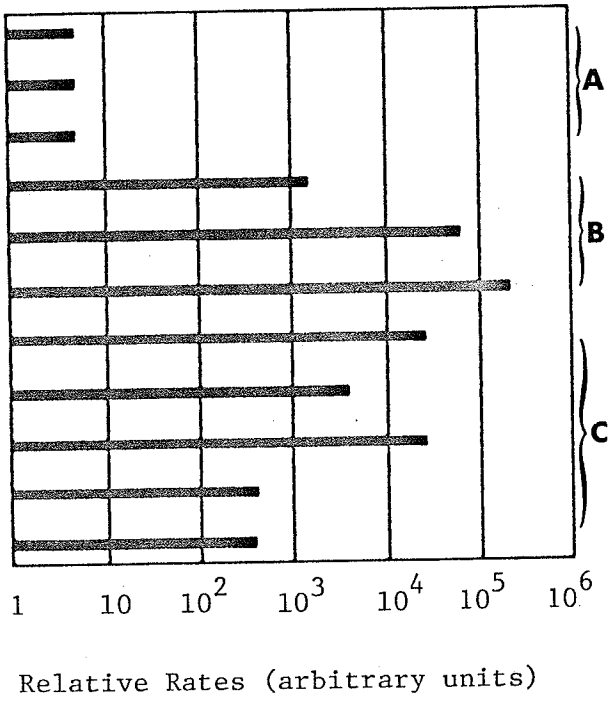

FIGURE 1

Relative rates of dissolution of stoichiometric nickel ferrite ($NiFe_2O_4$) in A: conventional acids and chelating agents at 'high' concentration, B: low pH one-electron reductants, and C: low-concentration one-electron reductants in the presence of a chelating reagent.

Note: TGA, Thioglycollic Acid; EDTA, Ethylenediaminetetra-acetic acid; bipy, bipyridyl; pic, picolinate.

Figure taken from: T. Swan et al [113].

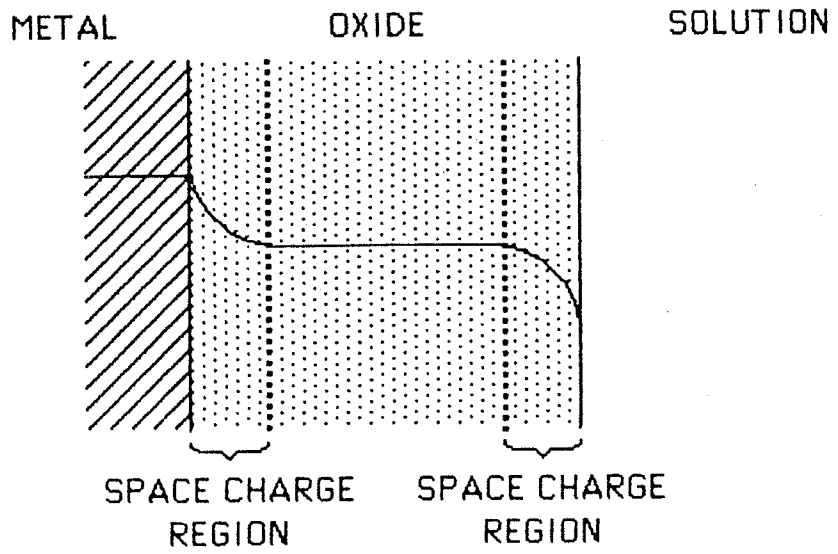

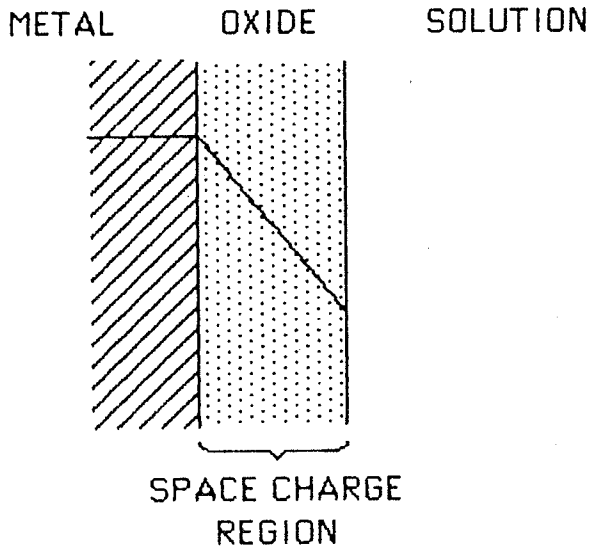

FIGURE 2

Distribution of potential in oxide films

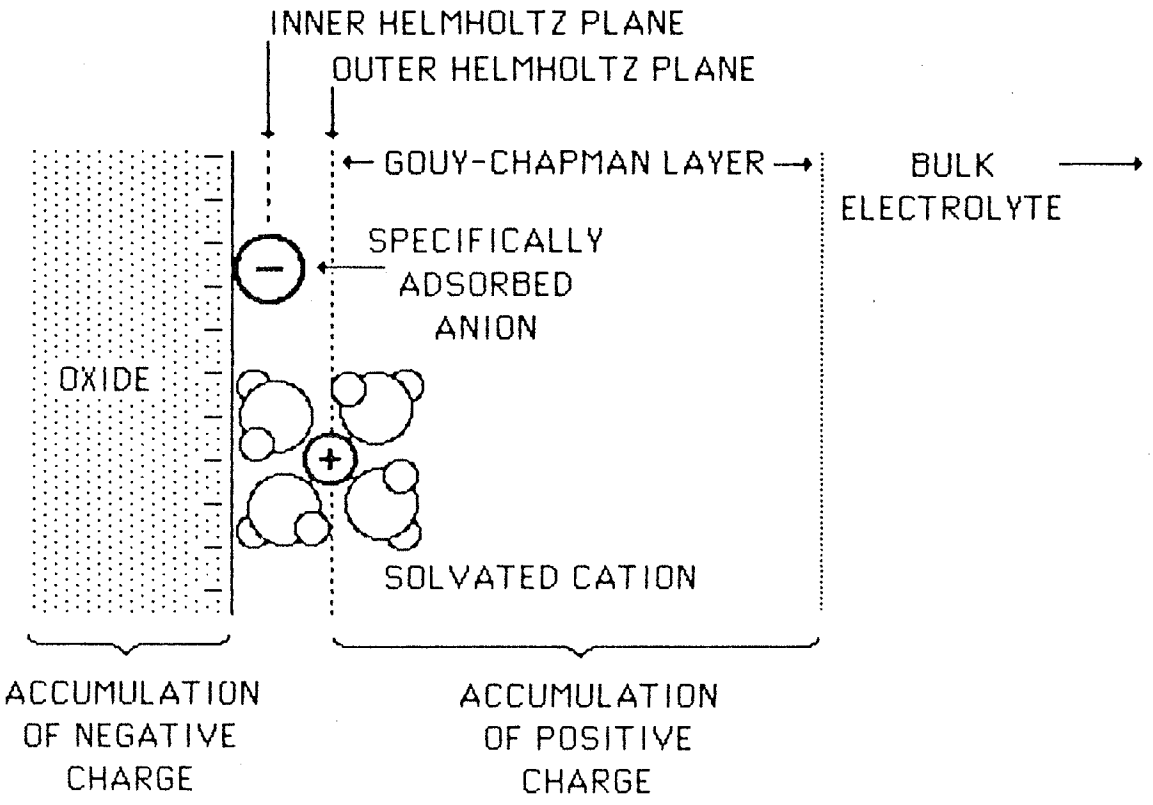

FIGURE 3

The structure of the electrical double layer. Figure taken from J.M. West [114].

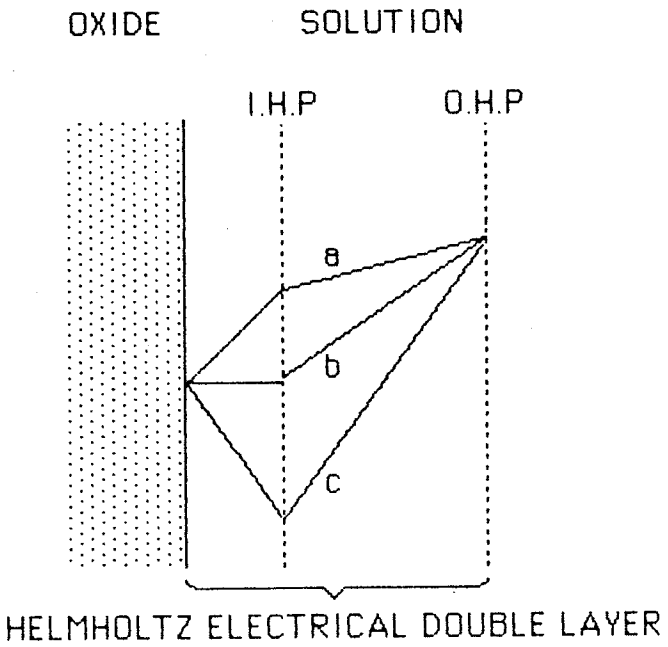

FIGURE 4

Simplified model of the potential distribution in the Helmholtz double layer: (a) with cations specifically adsorbed in the inner Helmholtz plane; (b) with no specific adsorption; (c) with anions specifically adsorbed in the inner Helmholtz plane. Figure taken from J.M. West [114].

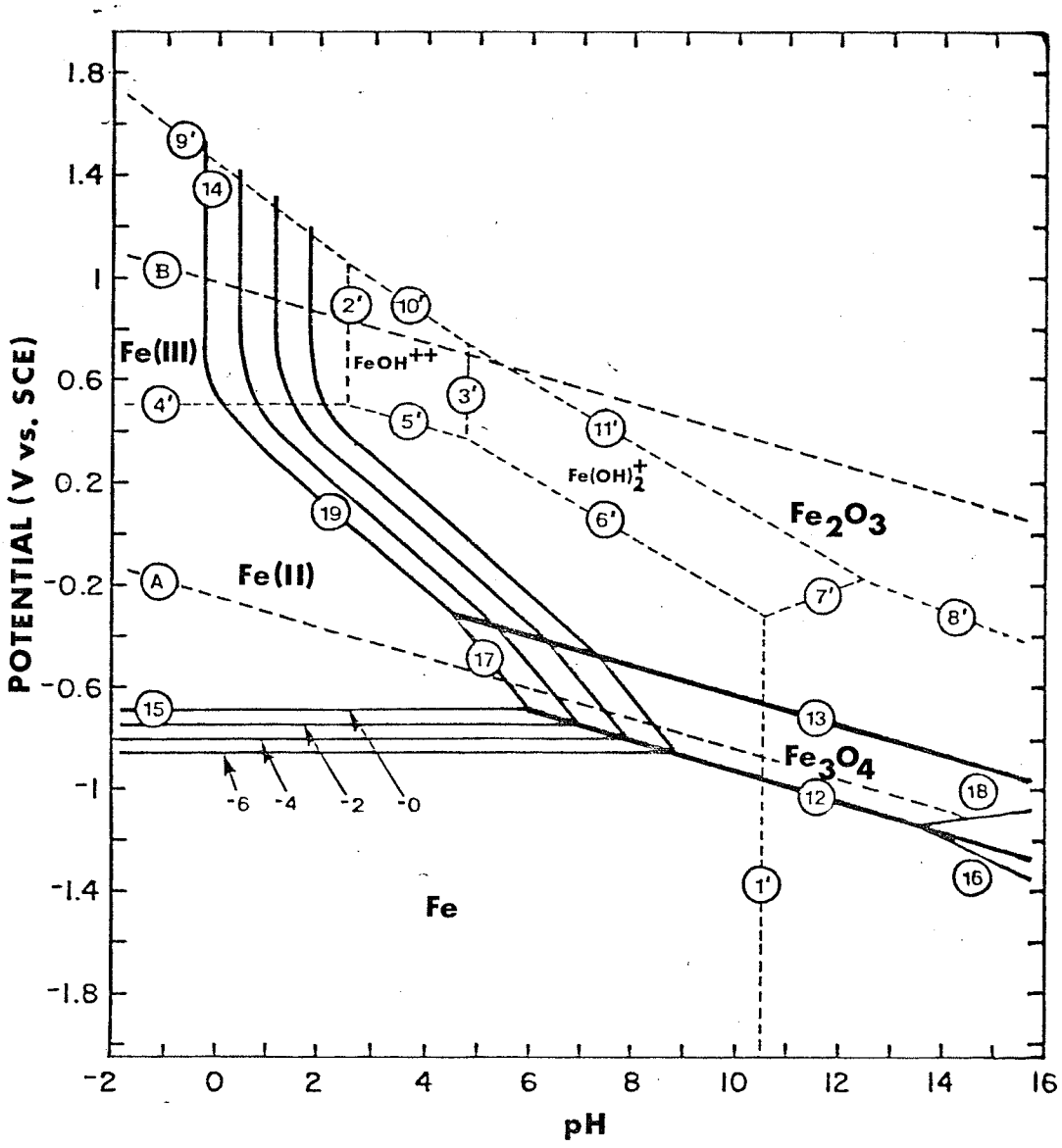

FIGURE 5

Potential-pH equilibrium diagram for the system iron-water, at 25°C (considering as solid substances only Fe, Fe_3O_4 and Fe_2O_3.)
Figure taken from "Atlas of Electrochemical Equilibria in Aqueous Solutions", M. Pourbaix [48]. See Ref. [48] for equations defining lines (1') - (19).

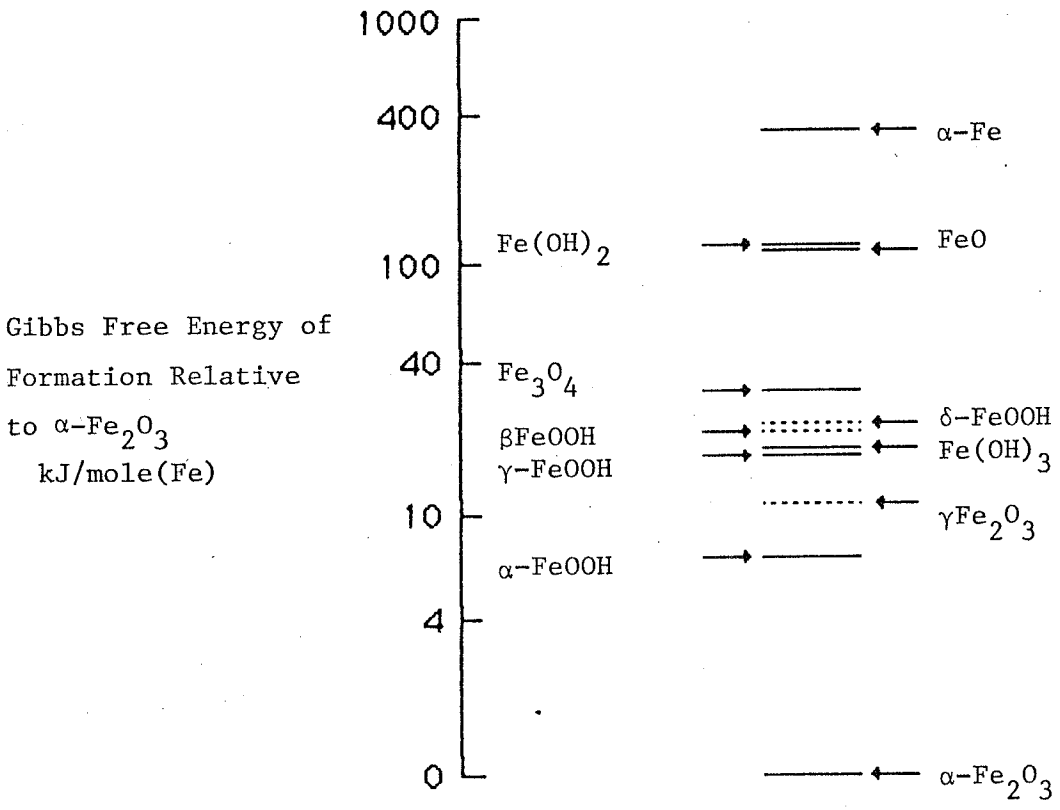

FIGURE 6

Gibbs free energy of formation relative to hematite (α-Fe_2O_3).
Dashed levels: exact value unknown.

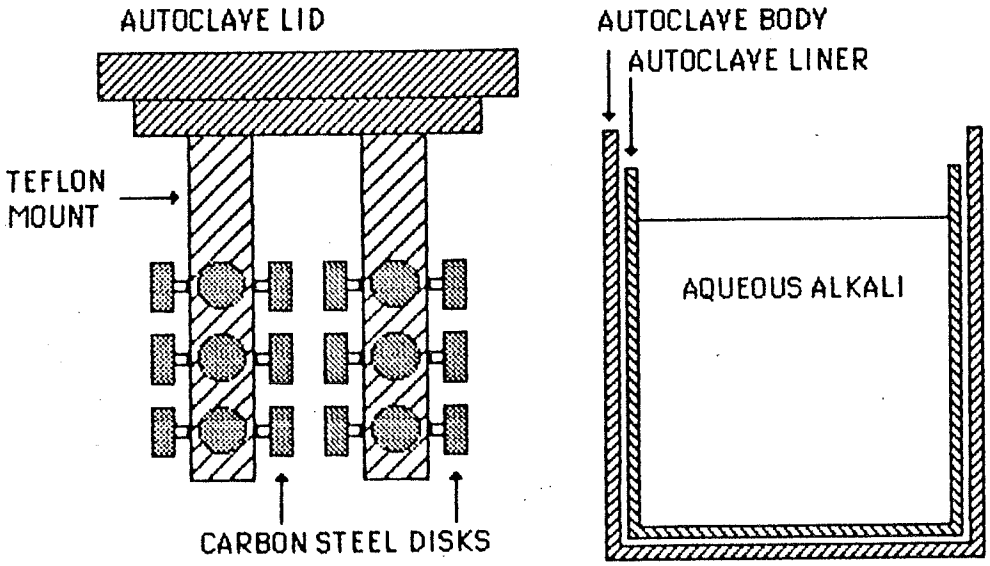

FIGURE 7

Autoclave assembly for magnetite film growth process.

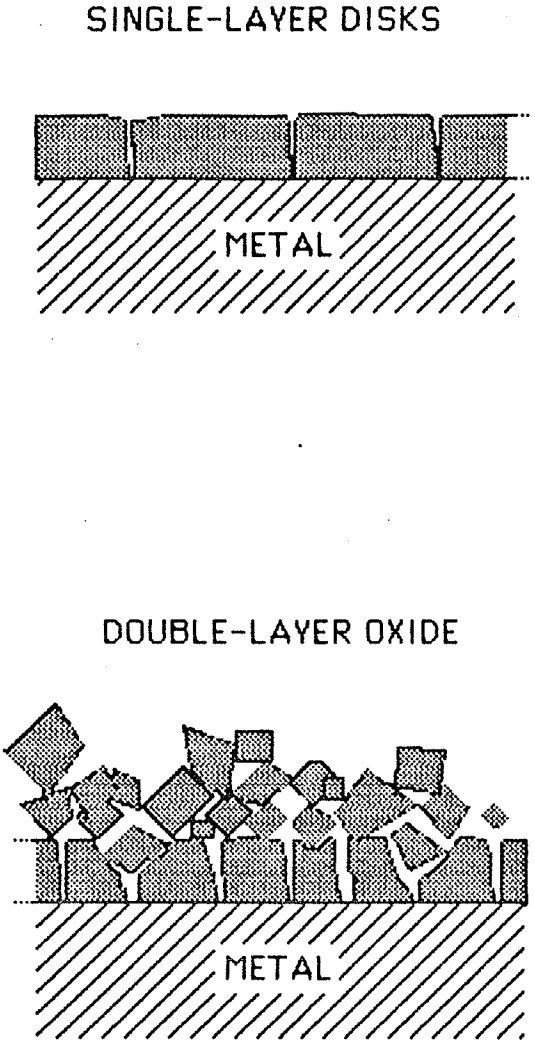

FIGURE 8

Oxide film structure.

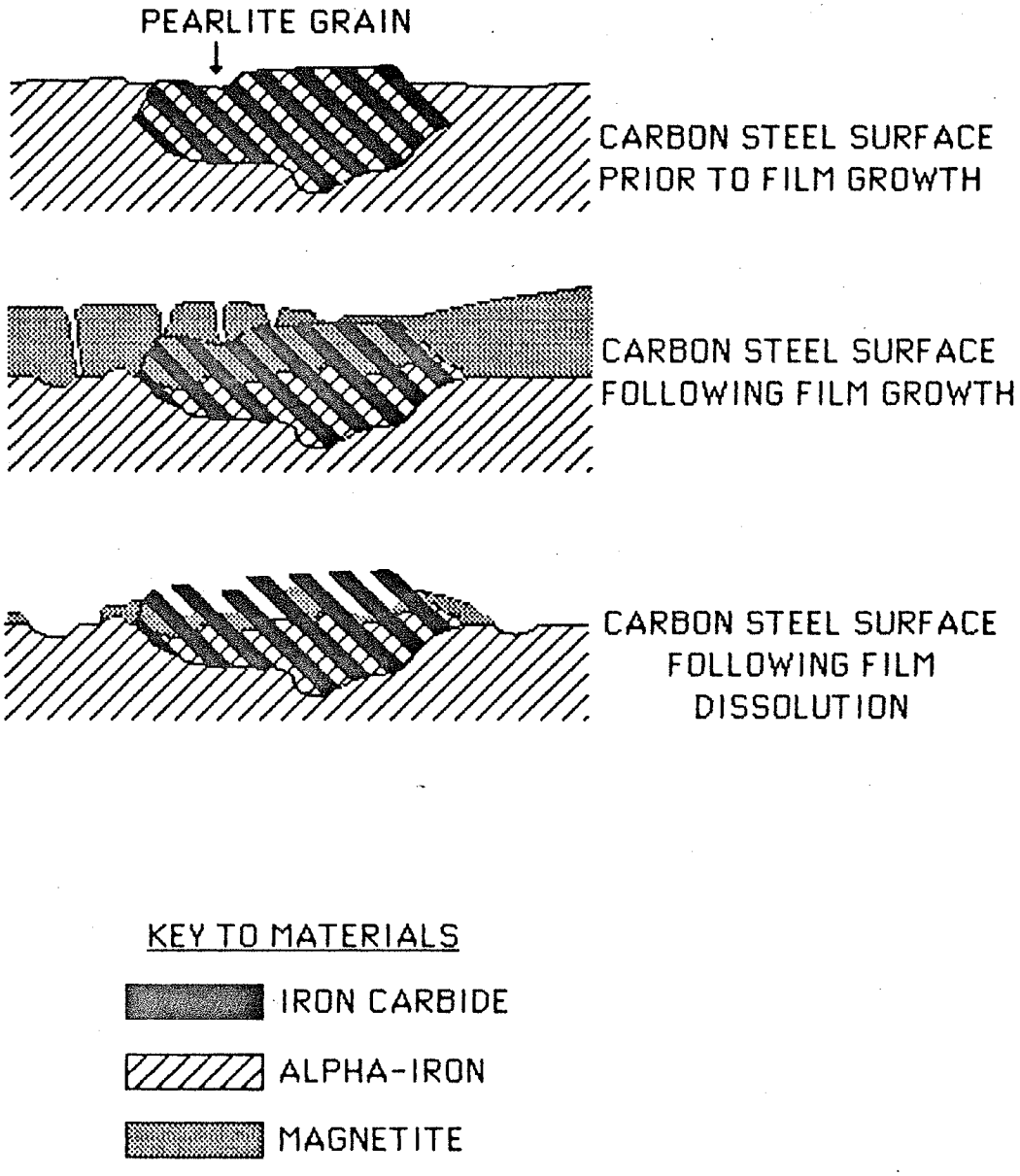

FIGURE 9

Influence of metal structure on oxide film growth and film dissolution processes.

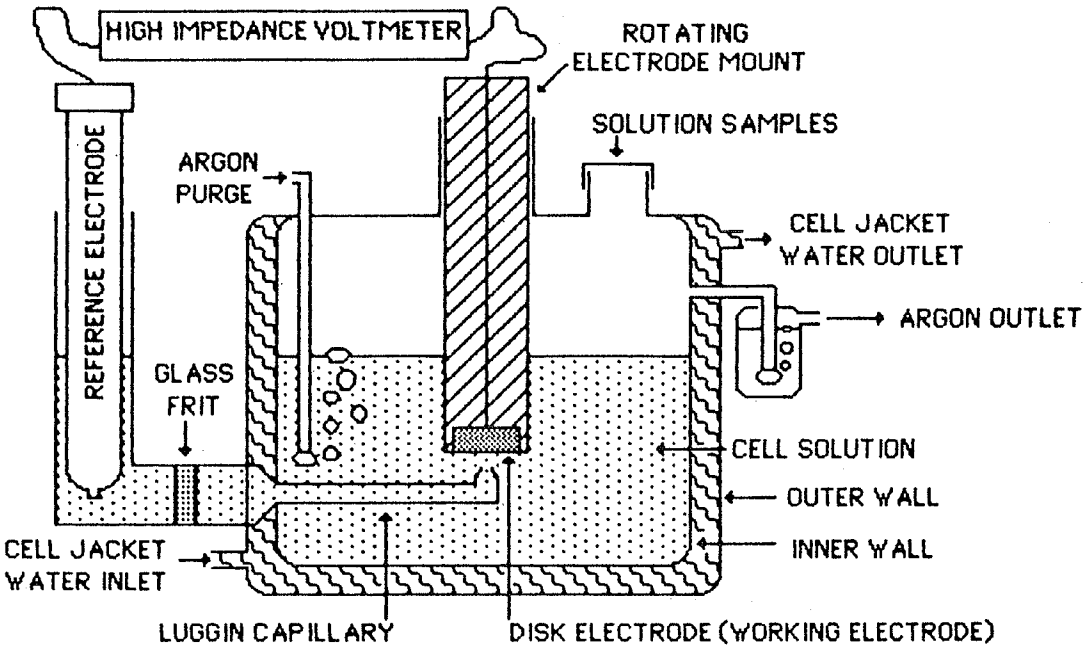

FIGURE 10

Electrochemical cell.

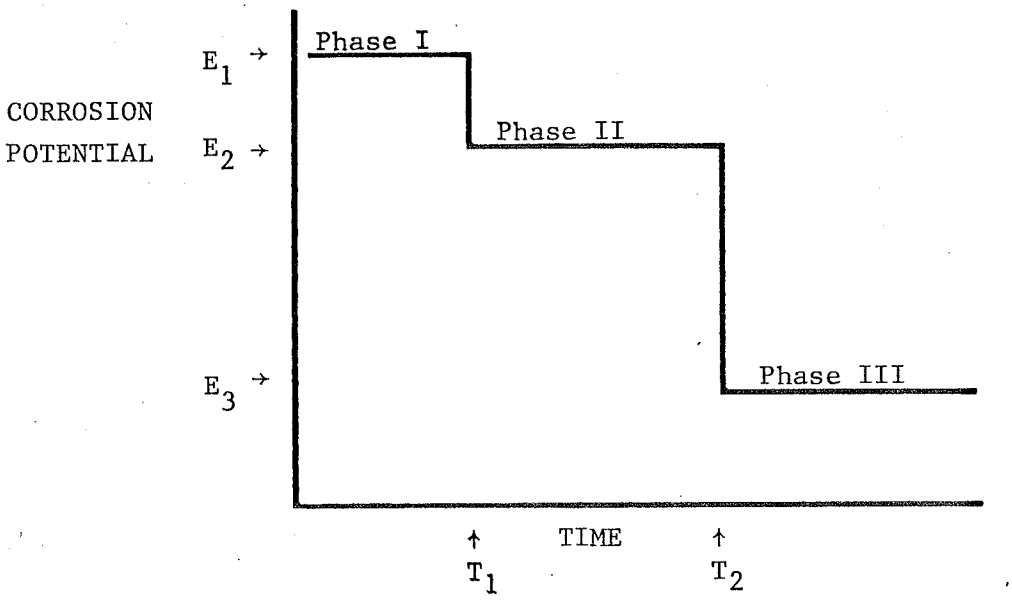

FIGURE 11

Schematic of a typical corrosion potential versus time trace

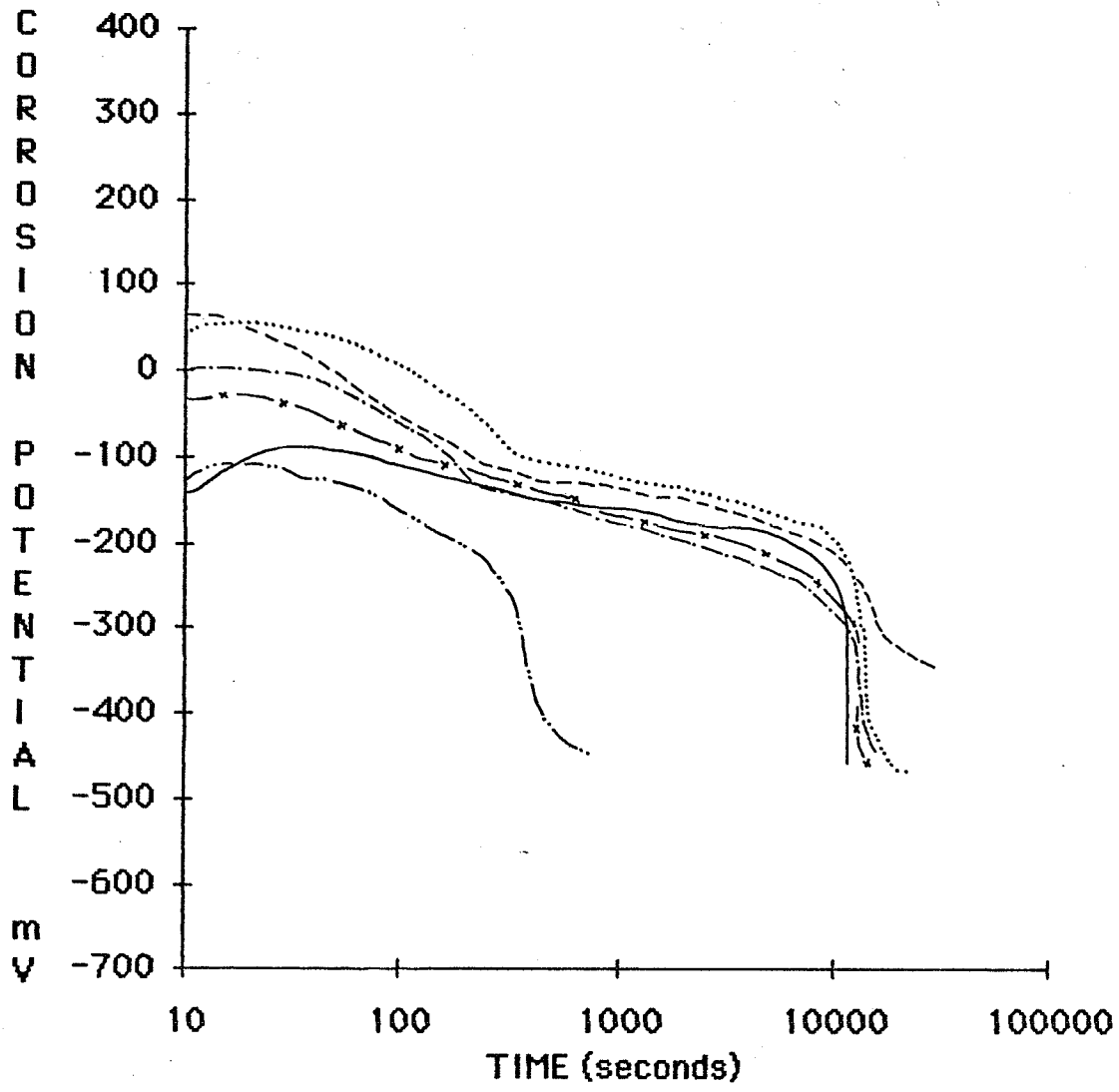

FIGURE 12

Corrosion potential (vs SCE) versus time as a function of initial Fe(II) concentration for static single-layer disks. Experimental conditions: 1 x 10^{-3} mol·dm^{-3} EDTA; pH = 4.7 ± 0.3; initial Fe(II) concentration; (-·· -·· -), 1 x 10^{-4}; (····), (----), (-·-·-), (-x-x-), (——), 1 x 10^{-5} mol·dm^{-3}.

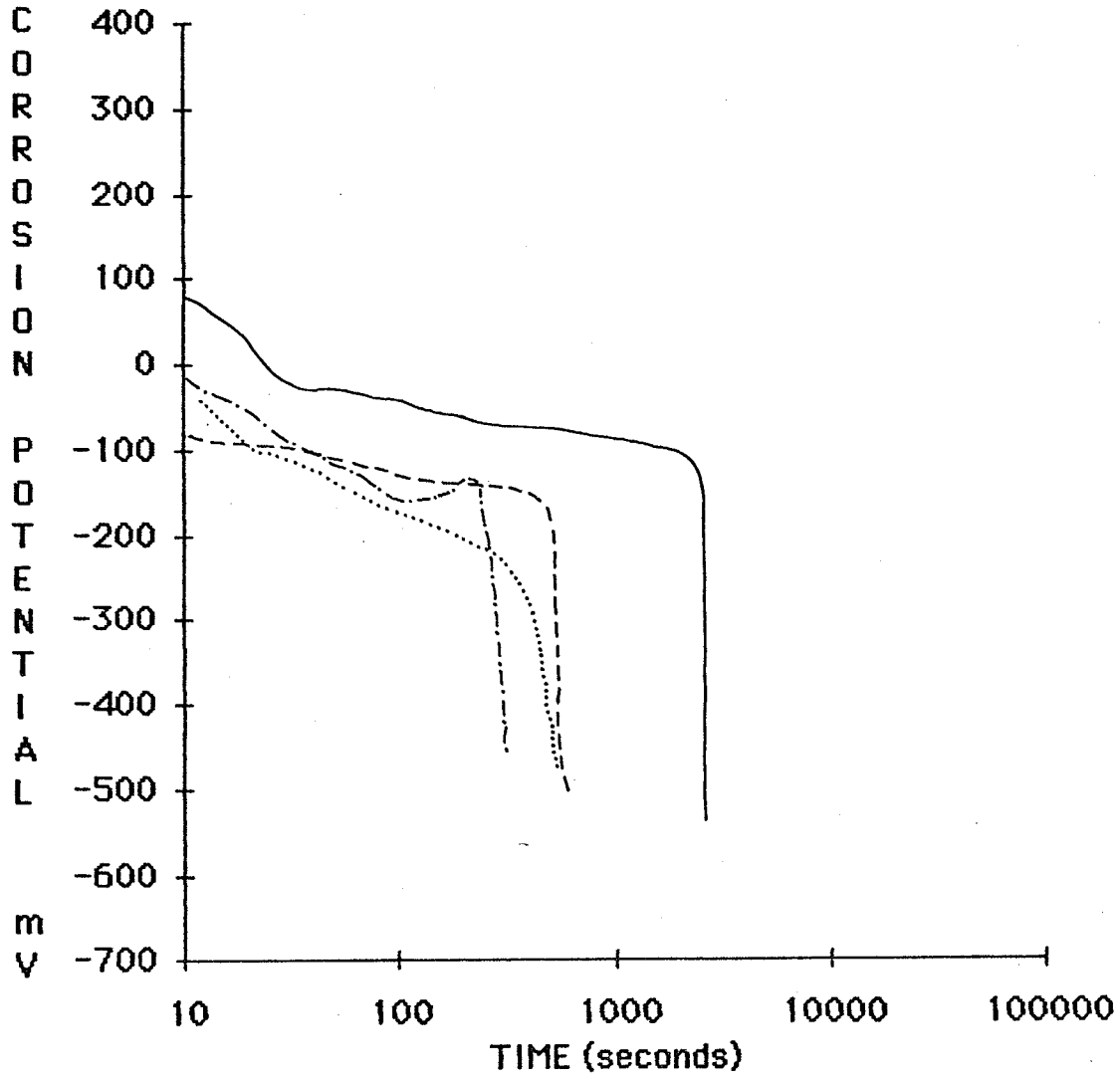

FIGURE 13

Corrosion potential (vs SCE) versus time as a function of initial Fe(II) concentration for static single-layer disks. Experimental conditions: 1 x 10^{-3} mol·dm^{-3} EDTA; initial Fe(II) concentration and initial pH; (——), 0 and 3.3; (---), 1 x 10^{-5} and 3.3; (-·-·-), 1 x 10^{-5} and 2.9; (····), 1 x 10^{-4} mol·dm^{-3} and 3.3.

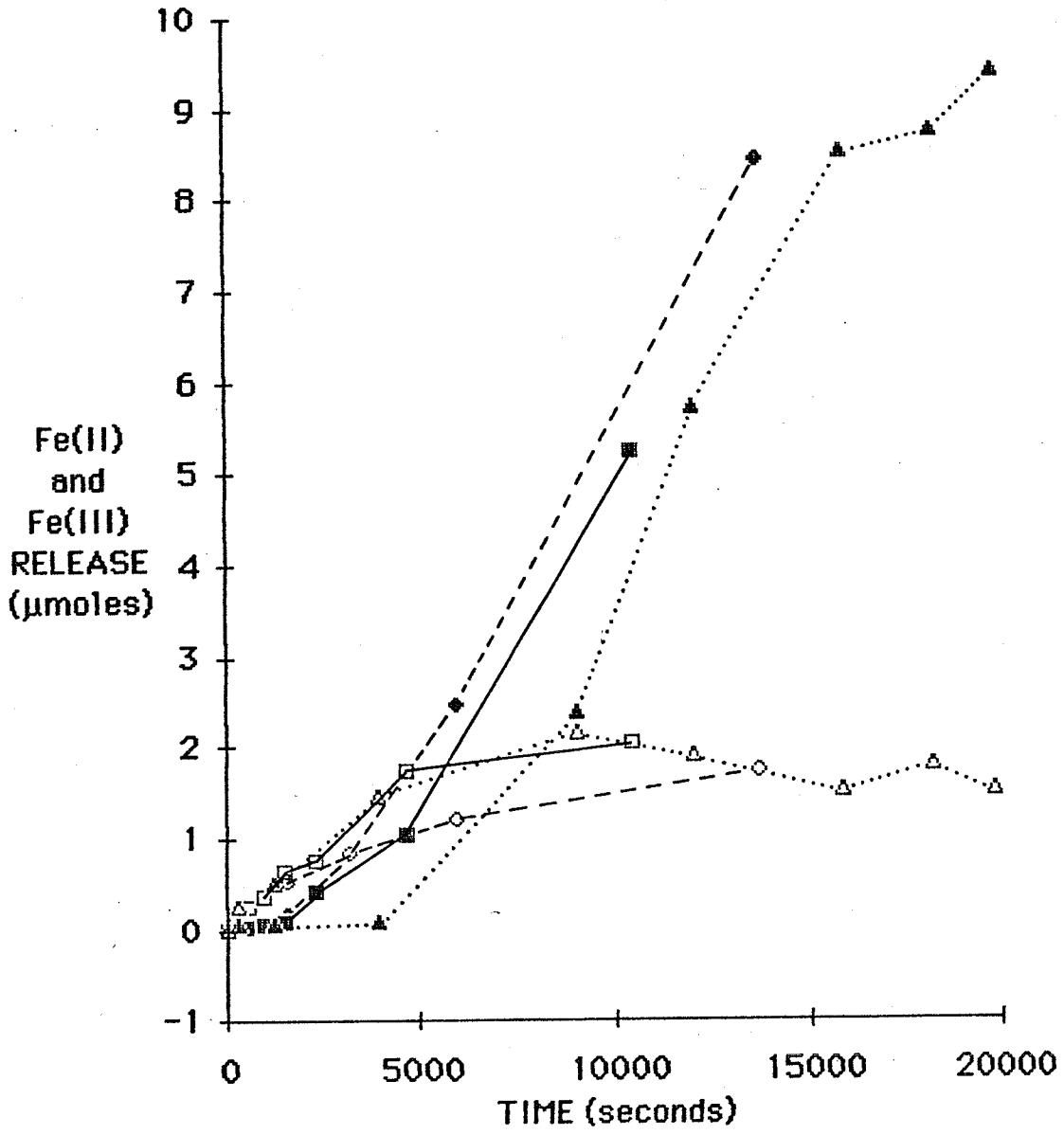

FIGURE 14

Quantity of Fe(II) and Fe(III) released versus time as a function of the initial Fe(II) concentration for static single-layer disks. Experimental conditions: 1 x 10^{-3} mol·dm^{-3} EDTA; pH = 4.7 $\pm$ 0.3; initial Fe(II) concentration; (····), (----), (——), 1 x 10^{-5} mol·dm^{-3}. Hollow symbols, Fe(III); solid symbols, Fe(II).

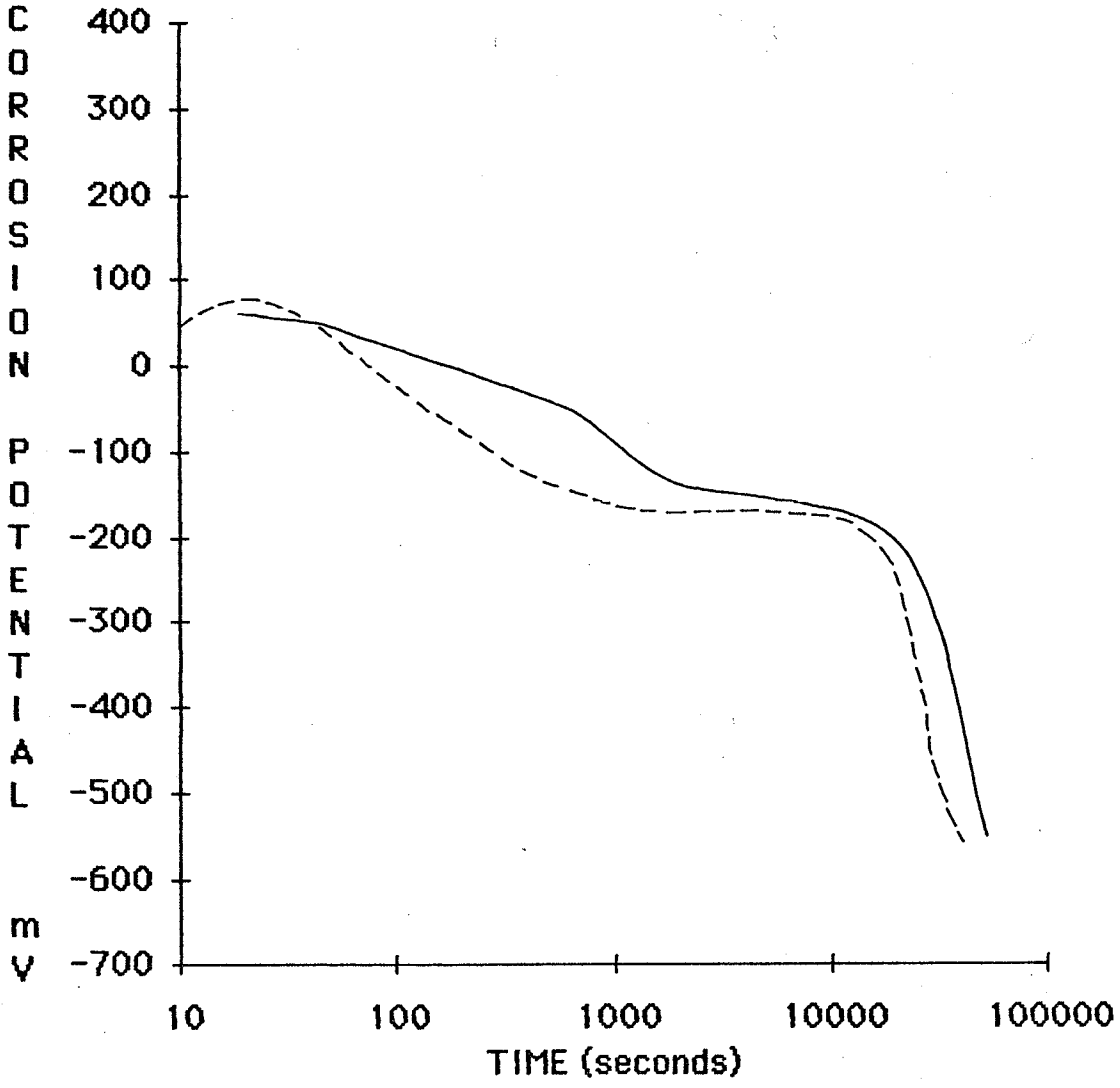

FIGURE 15

Corrosion potential (vs SCE) versus time as a function of initial Fe(II) concentration for static double-layer disks. Experimental conditions: 1 x 10^{-3} mol·dm^{-3} EDTA; pH = 5.0 $\pm$ 0.5; initial Fe(II) concentration; (——), 0; (----), 1 x 10^{-5} mol·dm^{-3}.

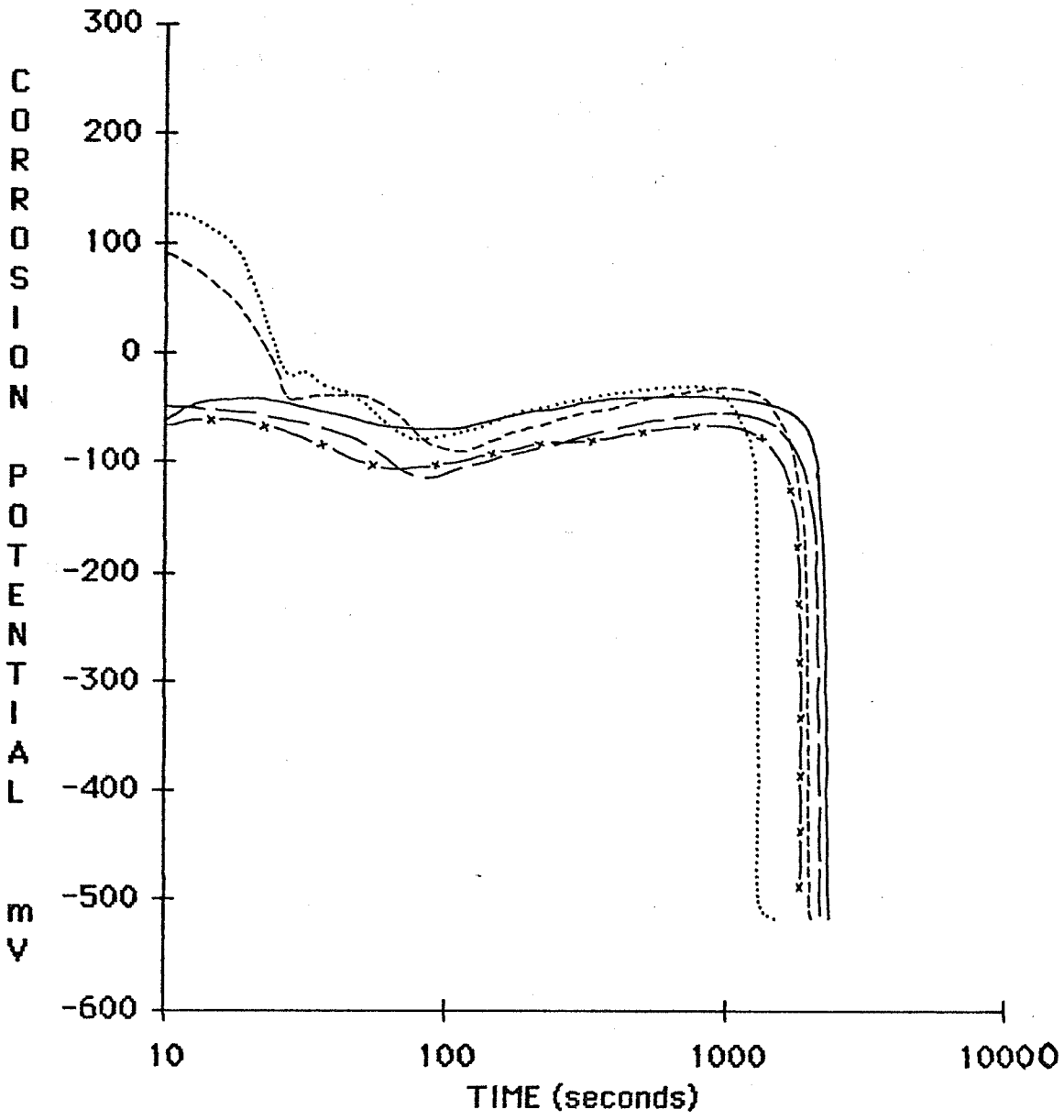

FIGURE 16

Corrosion potential (vs SCE) versus time as a function of initial Fe(II) concentration for static double-layer disks. Experimental conditions: 1 x 10^{-3} mol·dm^{-3} EDTA; pH = 3.0 ± 0.3; initial Fe(II) concentration; (····), 0; (----), 3 x 10^{-5}; (— —), 2 x 10^{-4}; (-x-x-), 1 x 10^{-3}; (——), 1 x 10^{-2} mol·dm^{-3}.

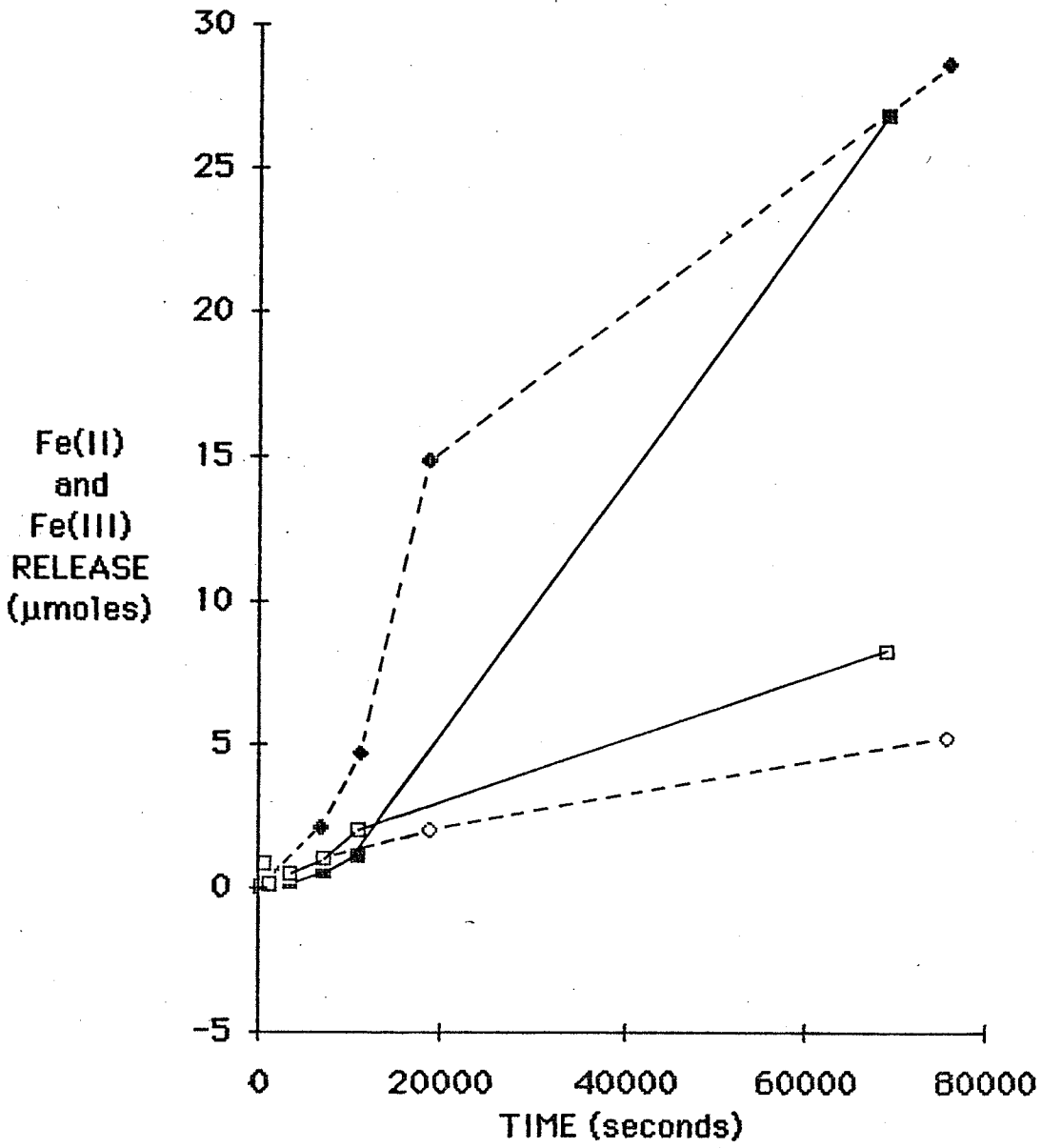

FIGURE 17

Quantity of Fe(II) and Fe(III) released versus time as a function of the initial Fe(II) concentration for static double-layer disks. Experimental conditions: 1×10^{-3} mol·dm^{-3} EDTA; pH = 5.0 ± 0.5; initial Fe(II) concentration; (——), 0; (----), 1×10^{-5} mol·dm^{-3}. Hollow symbols, Fe(III); solid symbols, Fe(II).

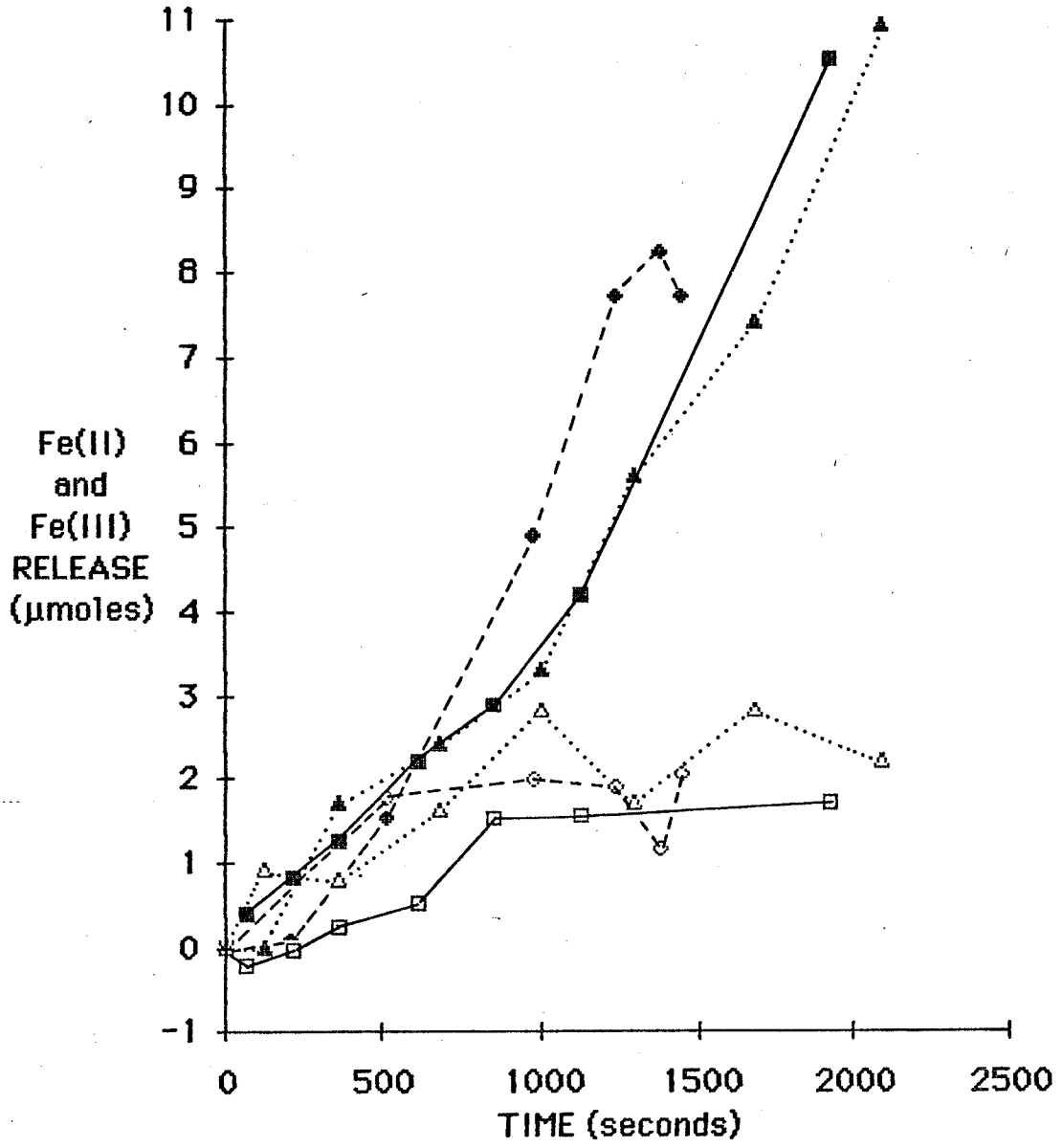

FIGURE 18

Quantity of Fe(II) and Fe(III) released versus time as a function of the initial Fe(II) concentration for static double-layer disks. Experimental conditions: 1 x 10^{-3} mol·dm^{-3} EDTA; pH = 3.0 ± 0.3; initial Fe(II) concentration; (----), 0; (____), 3.3 x 10^{-5}; (····), 1.9 x 10^{-4} mol·dm^{-3}. Hollow symbols, Fe(II); solid symbols, Fe(II).

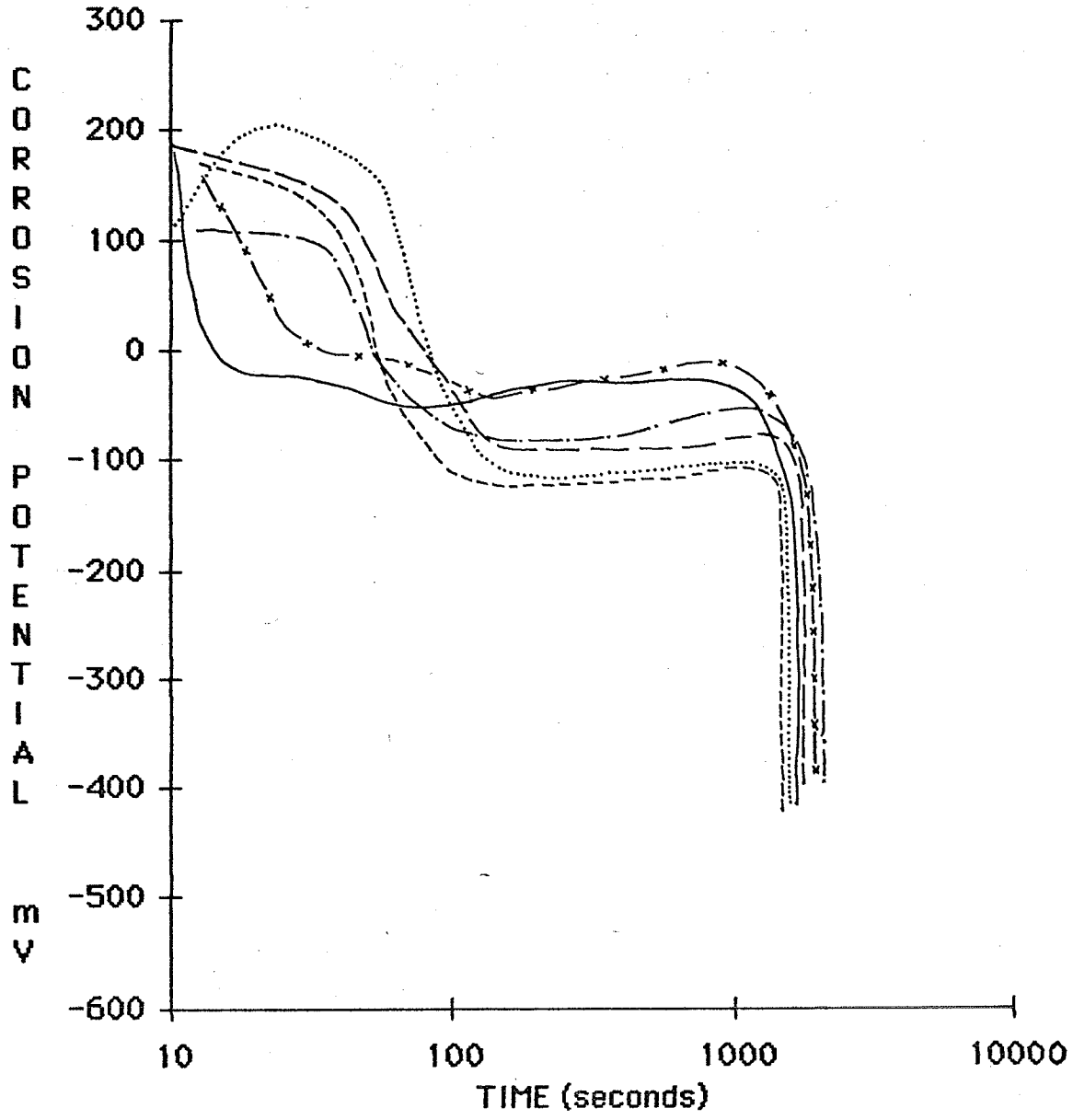

FIGURE 19

Corrosion potential (vs SCE) versus time as a function of initial Fe(II) concentration for rotated double-layer disks. Experimental conditions: 1 x 10^{-3} mol·dm^{-3} EDTA; disks rotated at 16.16 Hz; pH = 3.0 $\pm$ 0.3; initial Fe(II) concentration; (····), 0; (----), 1 x 10^{-5}; (— —), 1 x 10^{-4}; (-·-·-), 5 x 10^{-4}; (-x-x-), 1 x 10^{-3}; (——), 1 x 10^{-2} mol·dm^{-3}.

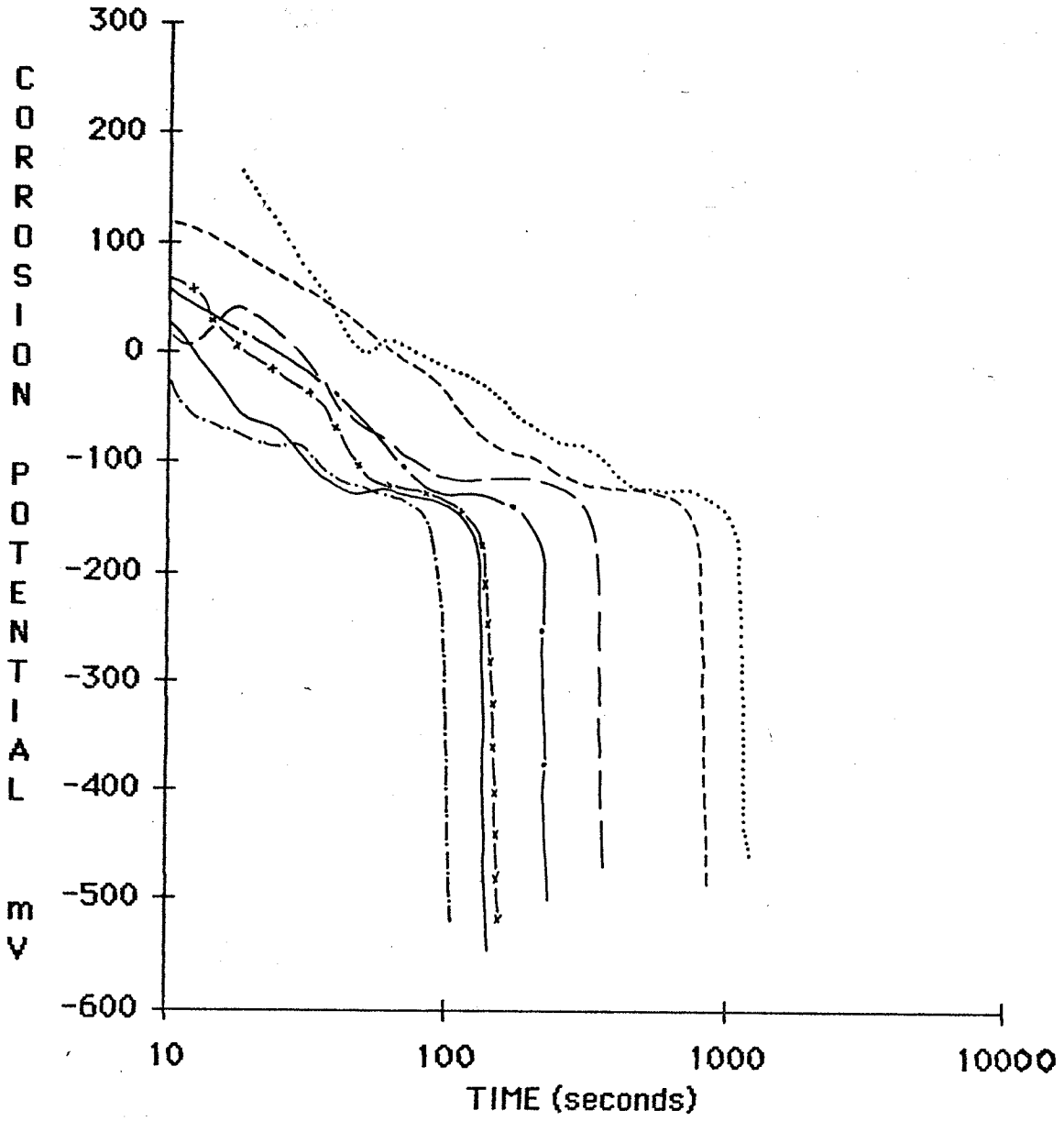

FIGURE 20

Corrosion potential (vs SCE) versus time as a function of temperature for rotated single-layer disks. Experimental conditions: 2×10^{-3} mol·dm^{-3} EDTA; disks rotated at 16.16 Hz; pH = 3.00 ± 0.05; temperatures; (····), 23°C; (----), 30°C; (— —), 40°C; (— · —), 55°C; (———), 65°C; (-x-x-), 75°C; (-·-·-), 85°C.

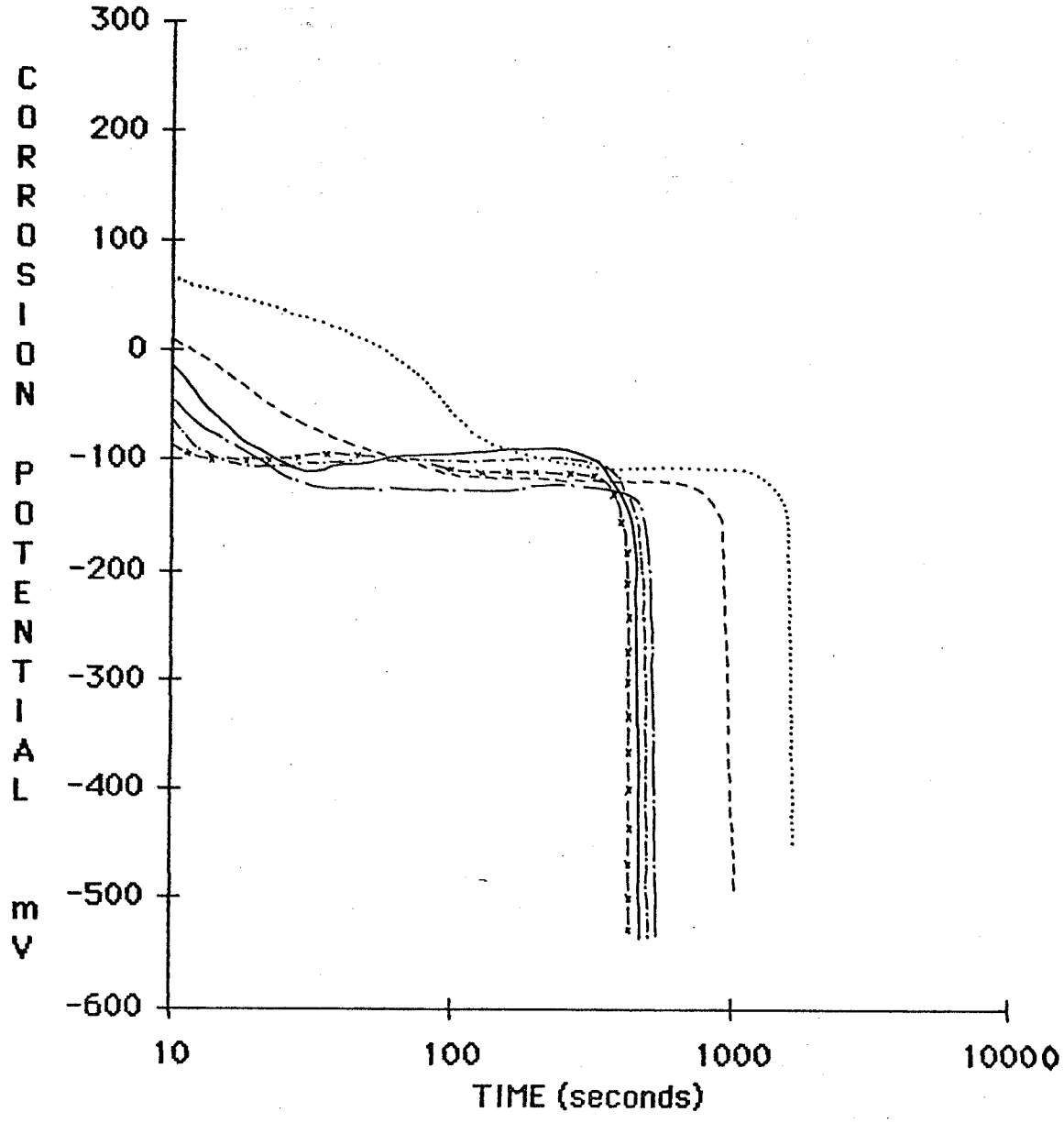

FIGURE 21

Corrosion potential (vs SCE) versus time as a function of temperature for rotated double-layer disks. Experimental conditions: 2×10^{-3} mol·dm^{-3} EDTA; disks rotated at 16.16 Hz; pH = 3.00 $\pm$ 0.05; temperature; (····), 23°C; (----), 29°C; (— · —), 55°C; (_____), 65°C; (-x-x-), 75°C; (-·-·-), 85°C

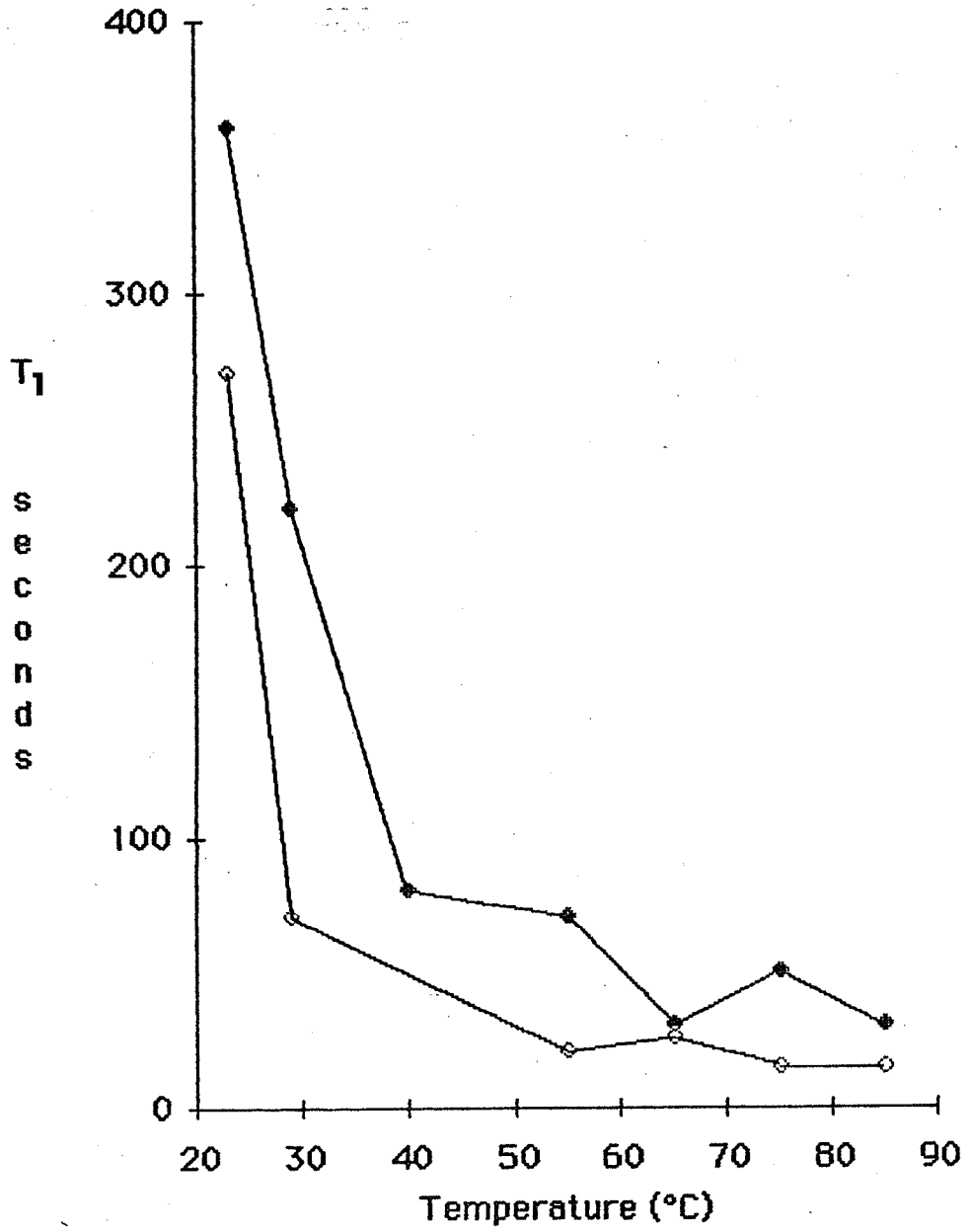

FIGURE 22

First potential transition time (T_1) versus temperature for double-layer and single-layer disks. Experimental conditions: 2×10^{-3} mol·dm^{-3} EDTA; disks rotated at 16.67 Hz; pH = 3.00 $\pm$ 0.05; (◆), single-layer disks; (◇), double-layer disks.

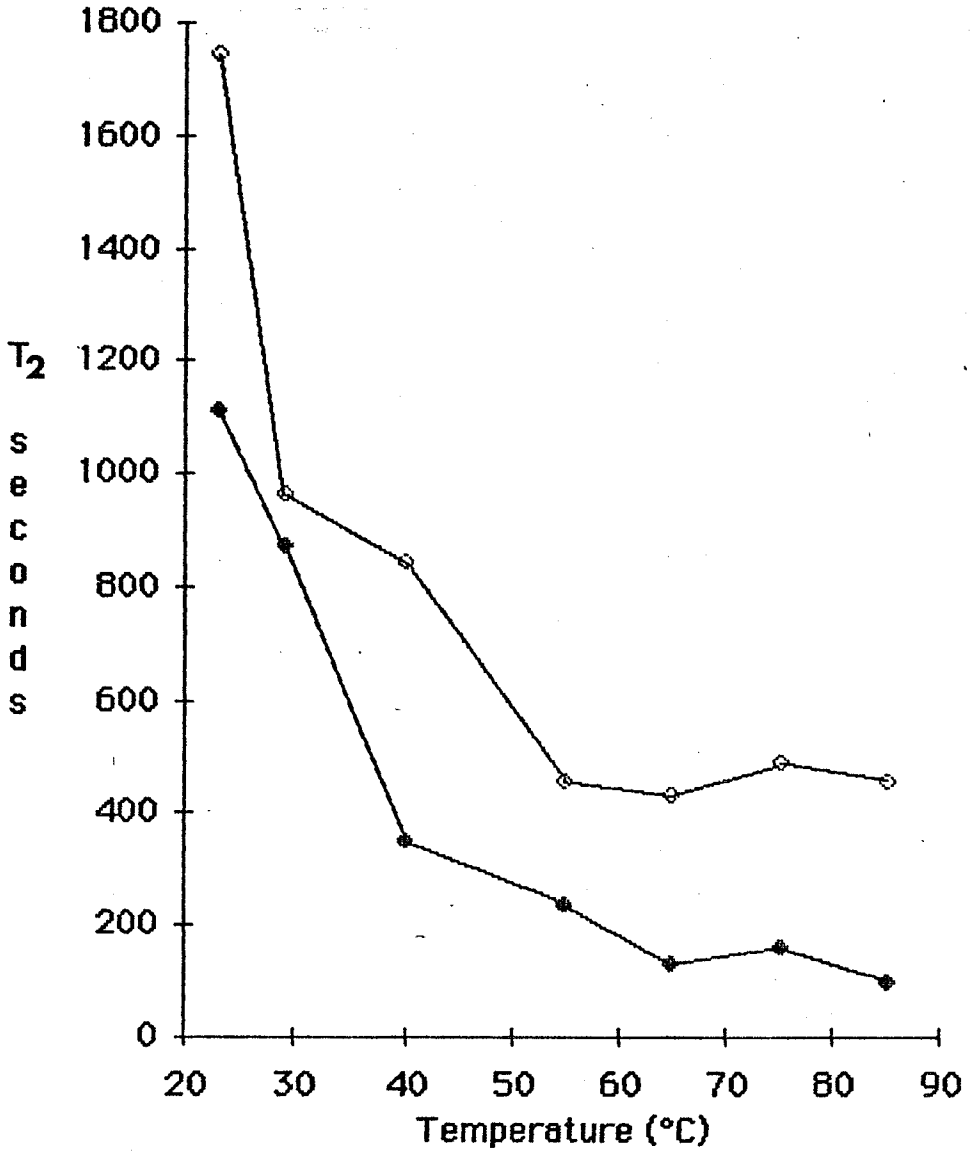

FIGURE 23

Second potential transition time (T_2) versus temperature for double-layer and single-layer disks. Experimental conditions: 2×10^{-3} mol·dm^{-3} EDTA; disks rotated at 16.67 Hz; pH = 3.00 ± 0.05; (◆), single-layer disks; (◇), double-layer disks.

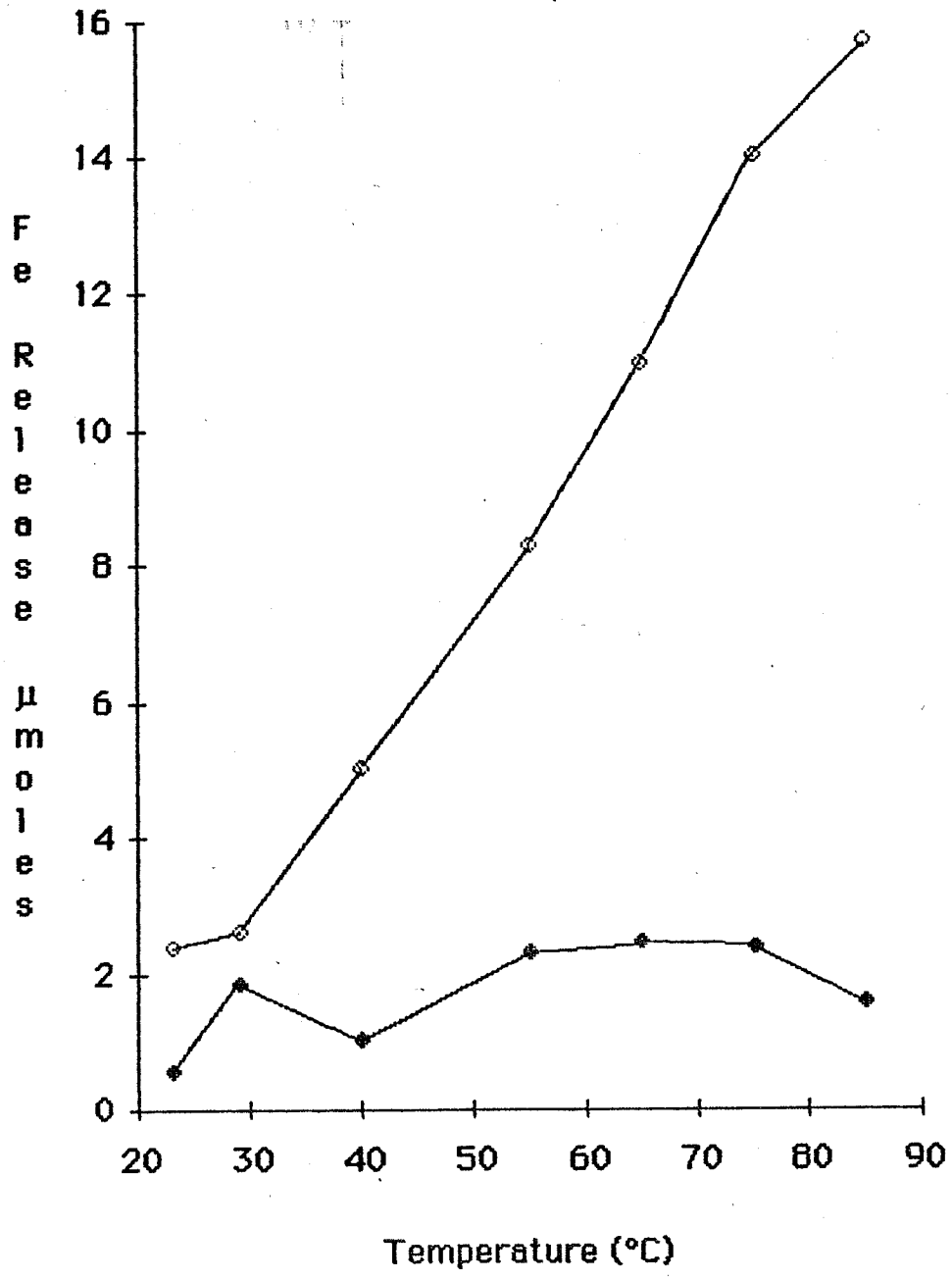

FIGURE 24

Total quantity of iron released during dissolution versus temperature for double-layer and single-layer disks. Experimental conditions: 2×10^{-3} mol·dm^{-3} EDTA; disks rotated at 16.67 Hz; pH = 3.00 $\pm$ 0.05; (◆) , single-layer disks; (◇) , double-layer disks.

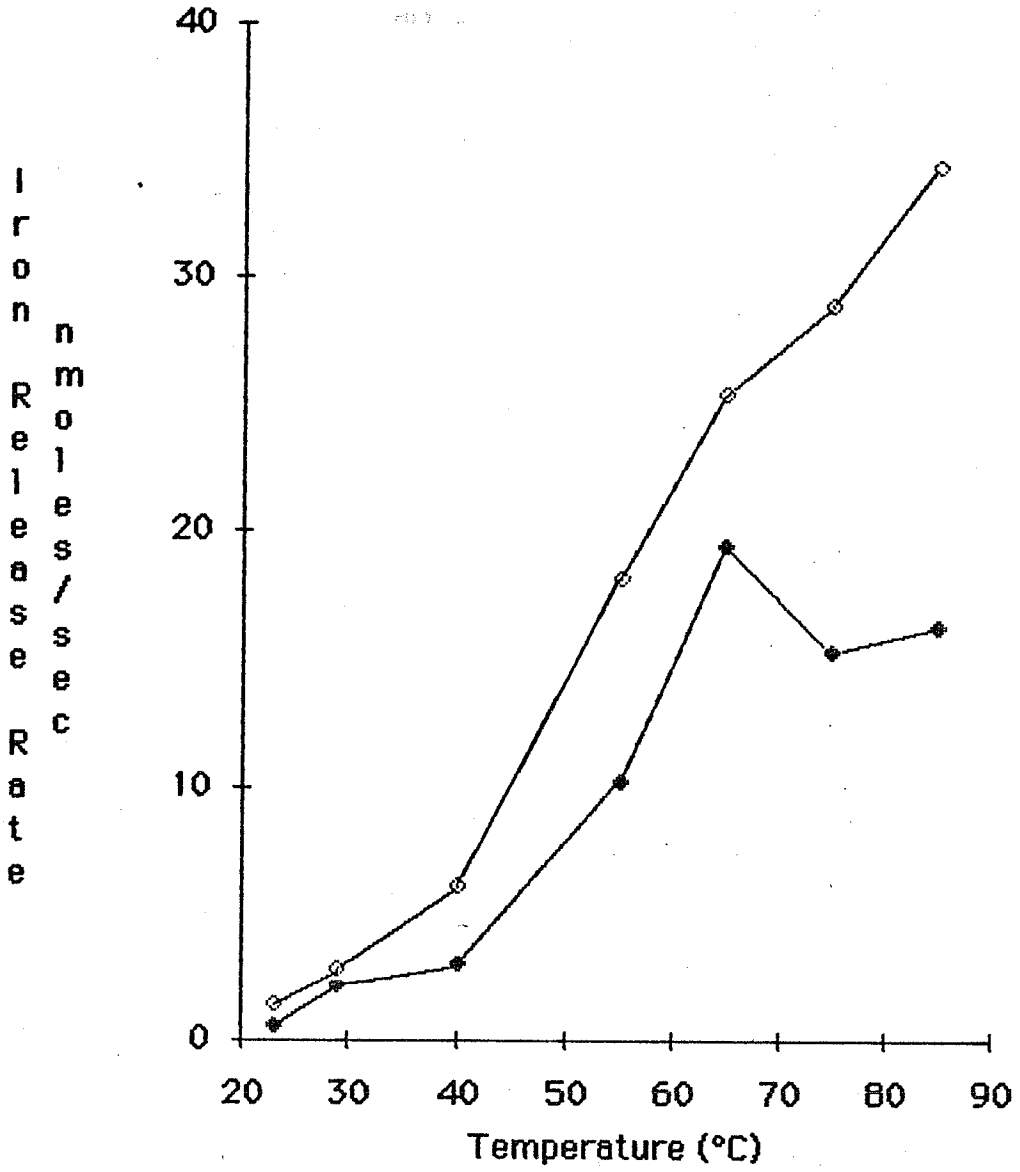

FIGURE 25

Average iron release rate versus temperature for double-layer and single-layer disks. Experimental conditions: 2 x 10^{-3} mol·dm^{-3} EDTA; disks rotated at 16.16 Hz; pH = 3.00 $\pm$ 0.05; (◆), single-layer disks; (◇), double-layer disks.

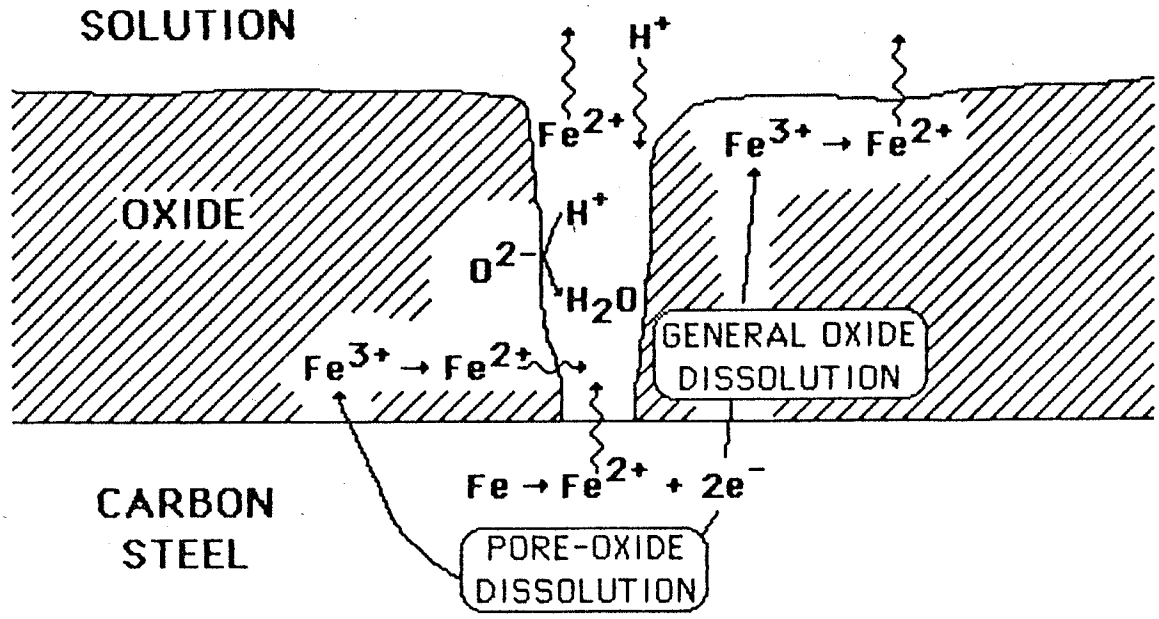

FIGURE 26

Schematic of pore-oxide and general-oxide dissolution processes.

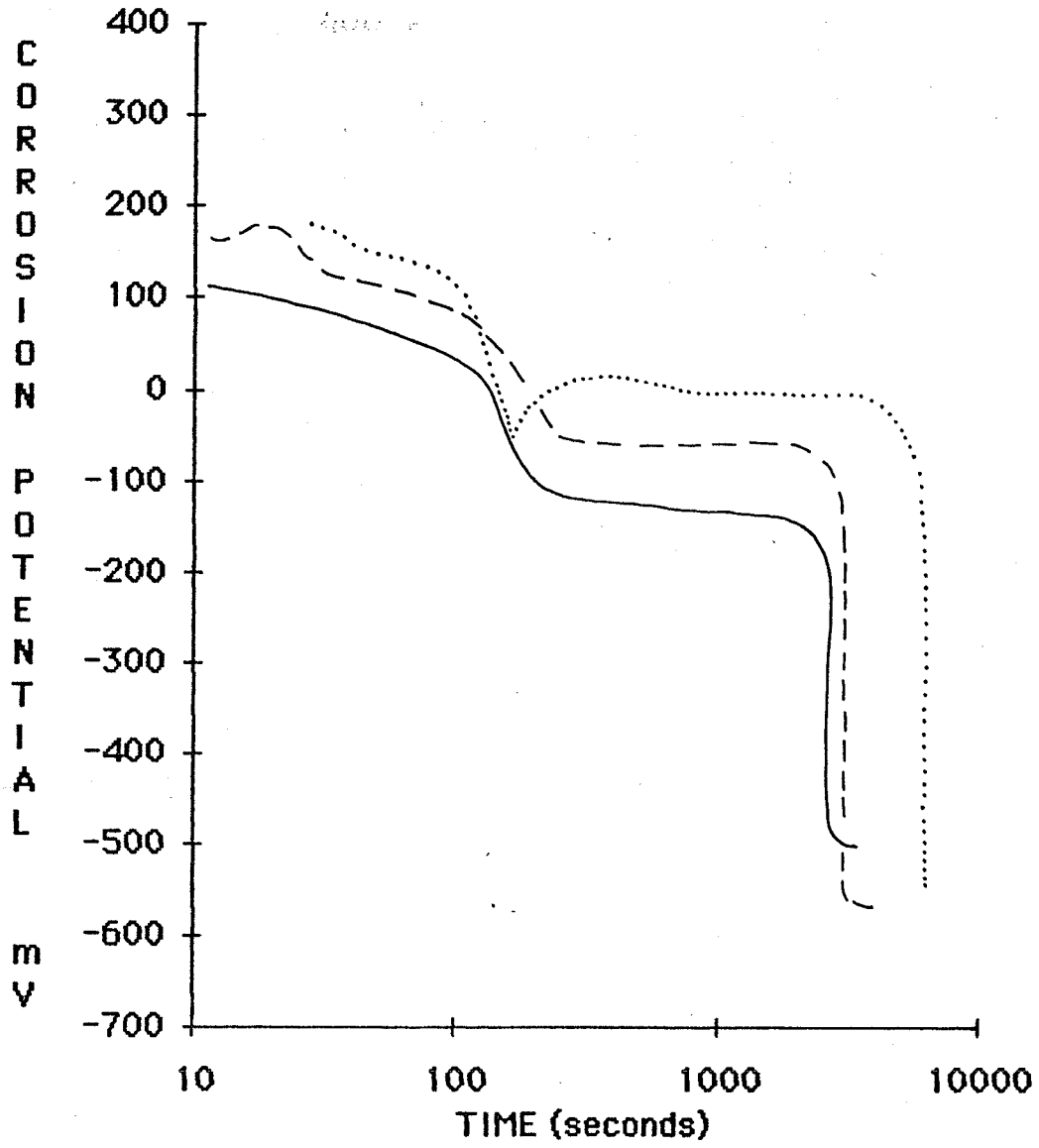

FIGURE 27

Corrosion potential (vs SCE) versus time as a function of oxalate concentration. Experimental conditons: 1 x 10^{-3} mol·dm^{-3} EDTA; disks rotated at 16.67 Hz; pH = 3.12 $\pm$ 0.10; room temperature; oxalate concentrations; (——), 0; (----), 3 x 10^{-3}; (····), 1 x 10^{-2} mol·dm^{-3}.

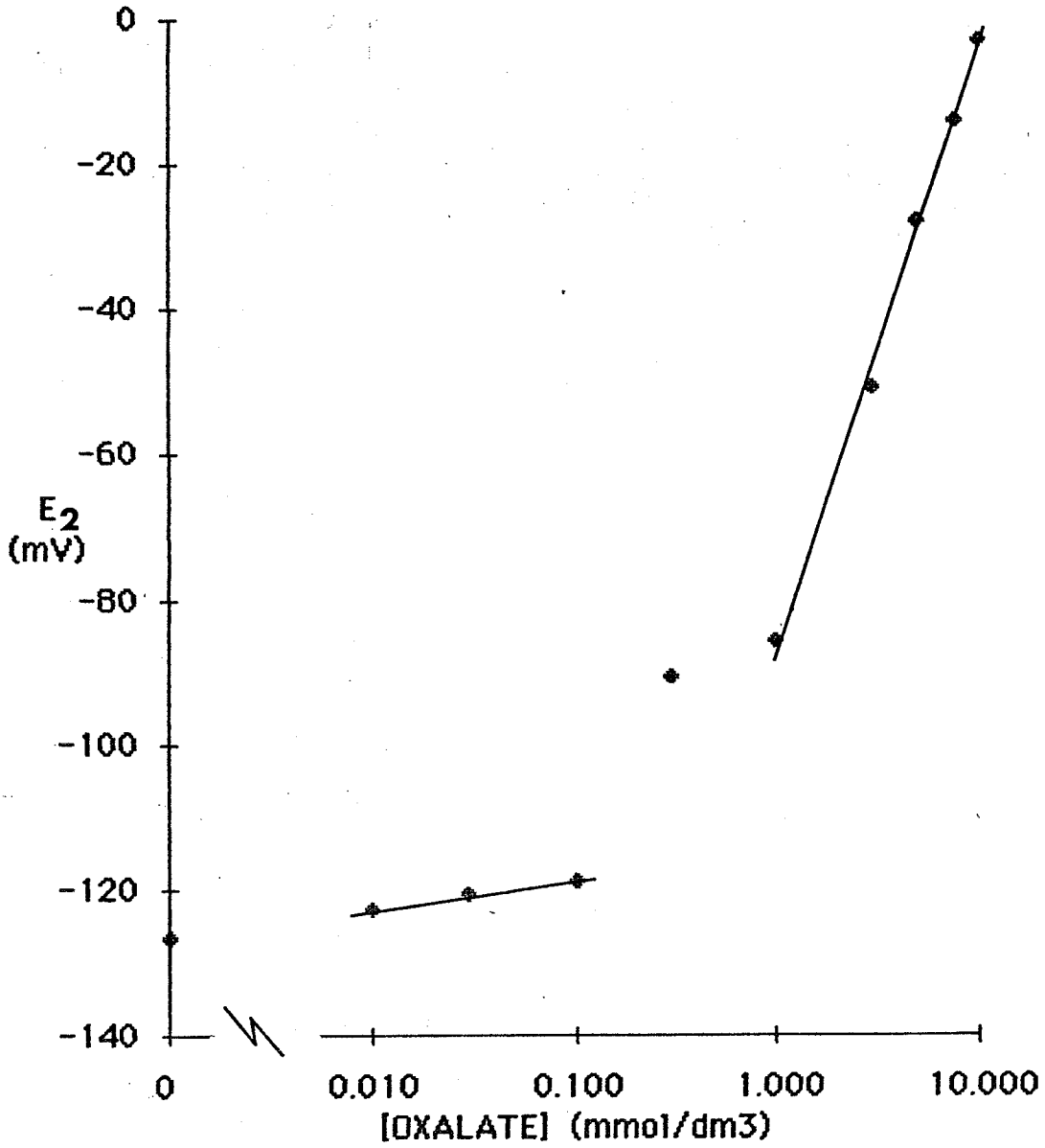

FIGURE 28

Potential E_2 (vs SCE) versus oxalate concentration. Experimental conditions: 1 x 10^{-3} mol·dm^{-3} EDTA; disks rotated at 16.67 Hz; pH = 3.12 ± 0.10; room temperature.

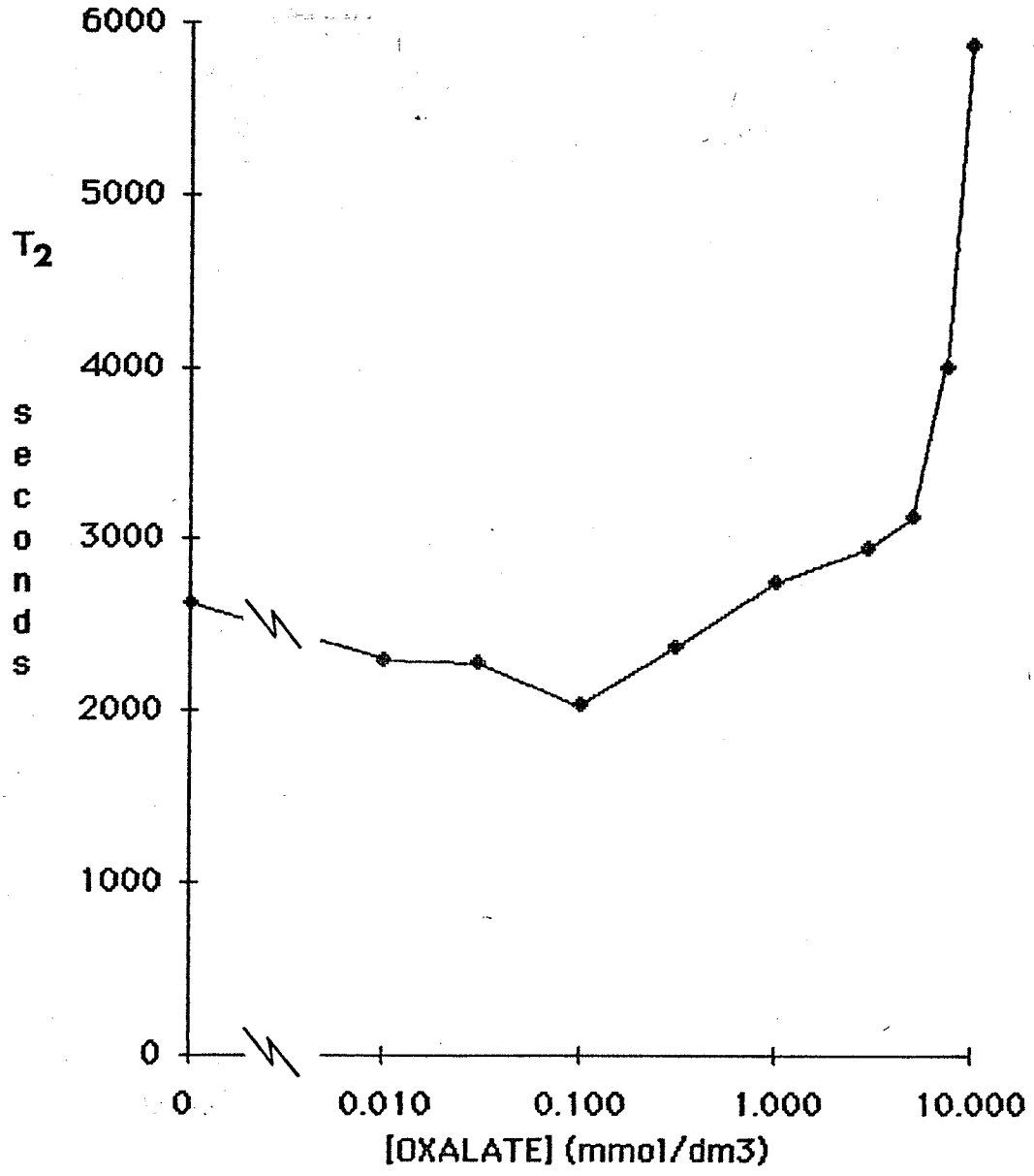

FIGURE 29

Time T_2 versus oxalate concentration. Experimental conditions: 1×10^{-3} mol·dm^{-3} EDTA; disks rotated at 16.67 Hz; pH = 3.12 $\pm$ 0.10; room temperature.

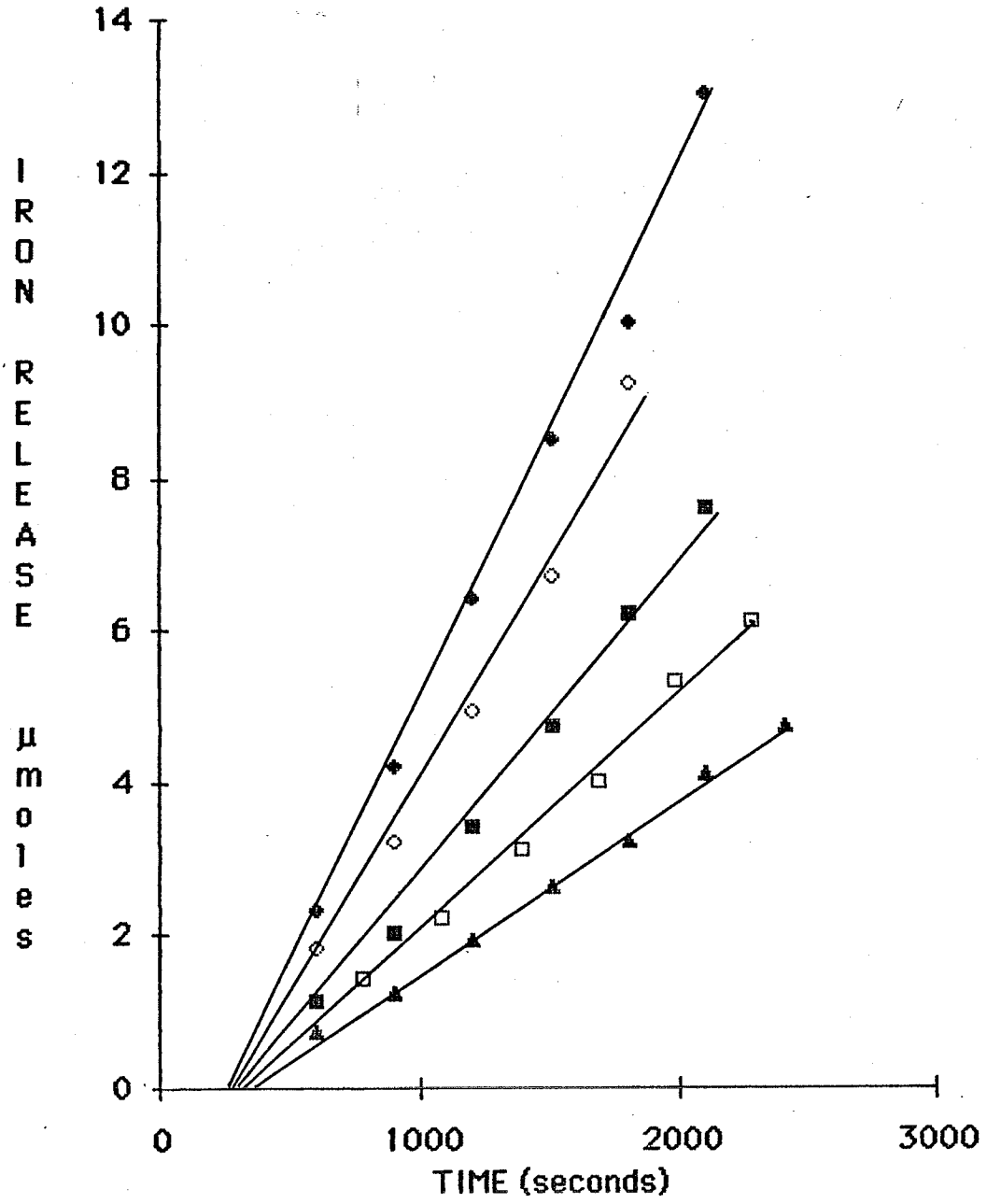

FIGURE 30

Iron release versus time as a function of oxalate concentration. Experimental conditions: 1 x 10^{-3} mol·dm^{-3} EDTA; disks rotated at 16.67 Hz; pH = 3.12 ± 0.10; room temperature; oxalate concentration: ▲, 0; □, 1 x 10^{-5}; ■, 3 x 10^{-5}; ◇, 1 x 10^{-4}; ◆, 3 x 10^{-4} mol·dm^{-3}.

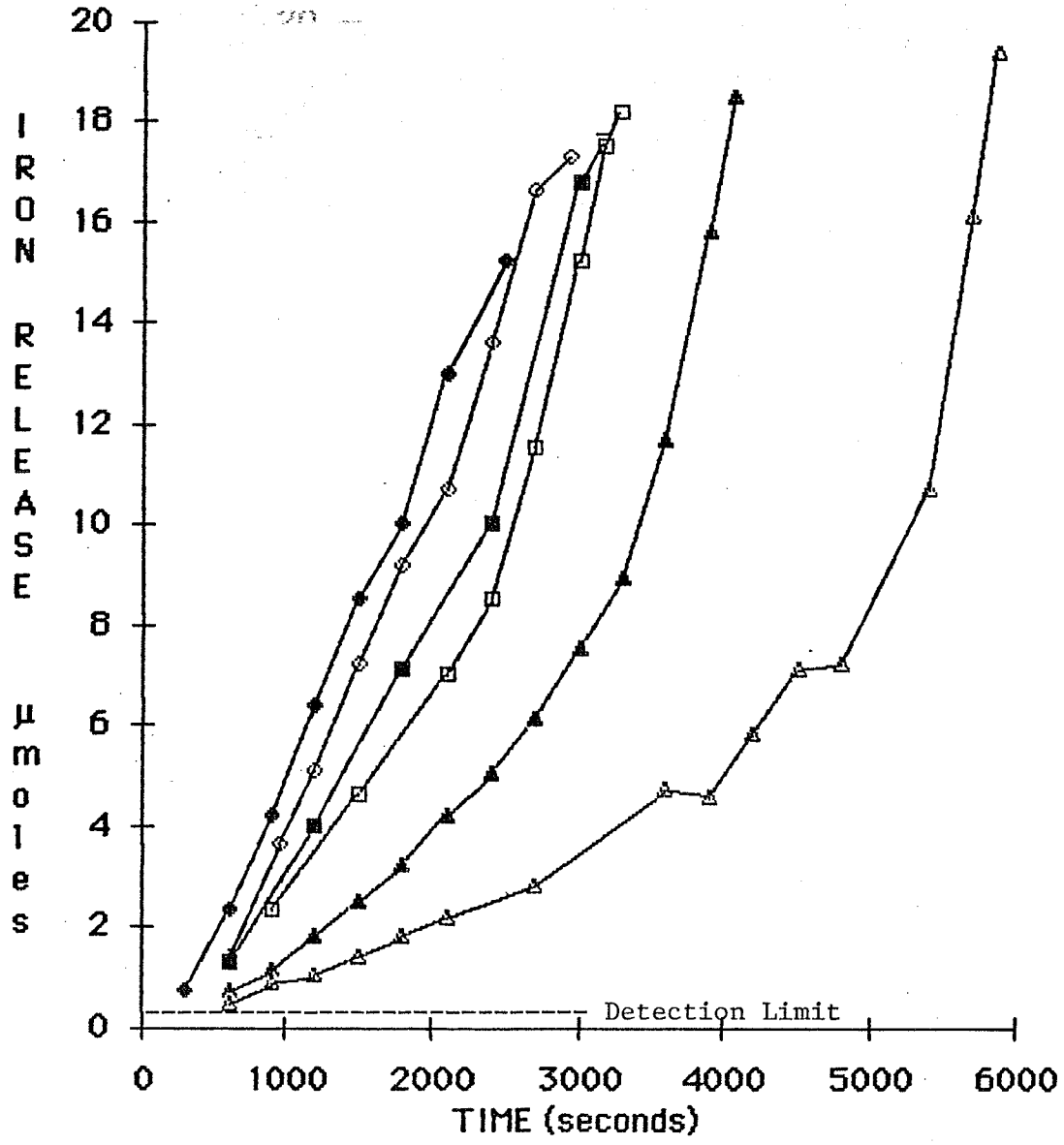

FIGURE 31

Iron release versus time as a function of oxalate concentration. Experimental conditions: 1 x 10^{-3} mol·dm^{-3} EDTA; disks rotated at 16.67 Hz; pH = 3.12 ± 0.10; room temperature; oxalate concentration: ◆, 3 x 10^{-4}; ◇ , 1 x 10^{-3}; ■ , 3 x 10^{-3}; □ , 5 x 10^{-3}; ▲ , 7.5 x 10^{-3}; △, 1 x 10^{-2} mol·dm^{-3}.

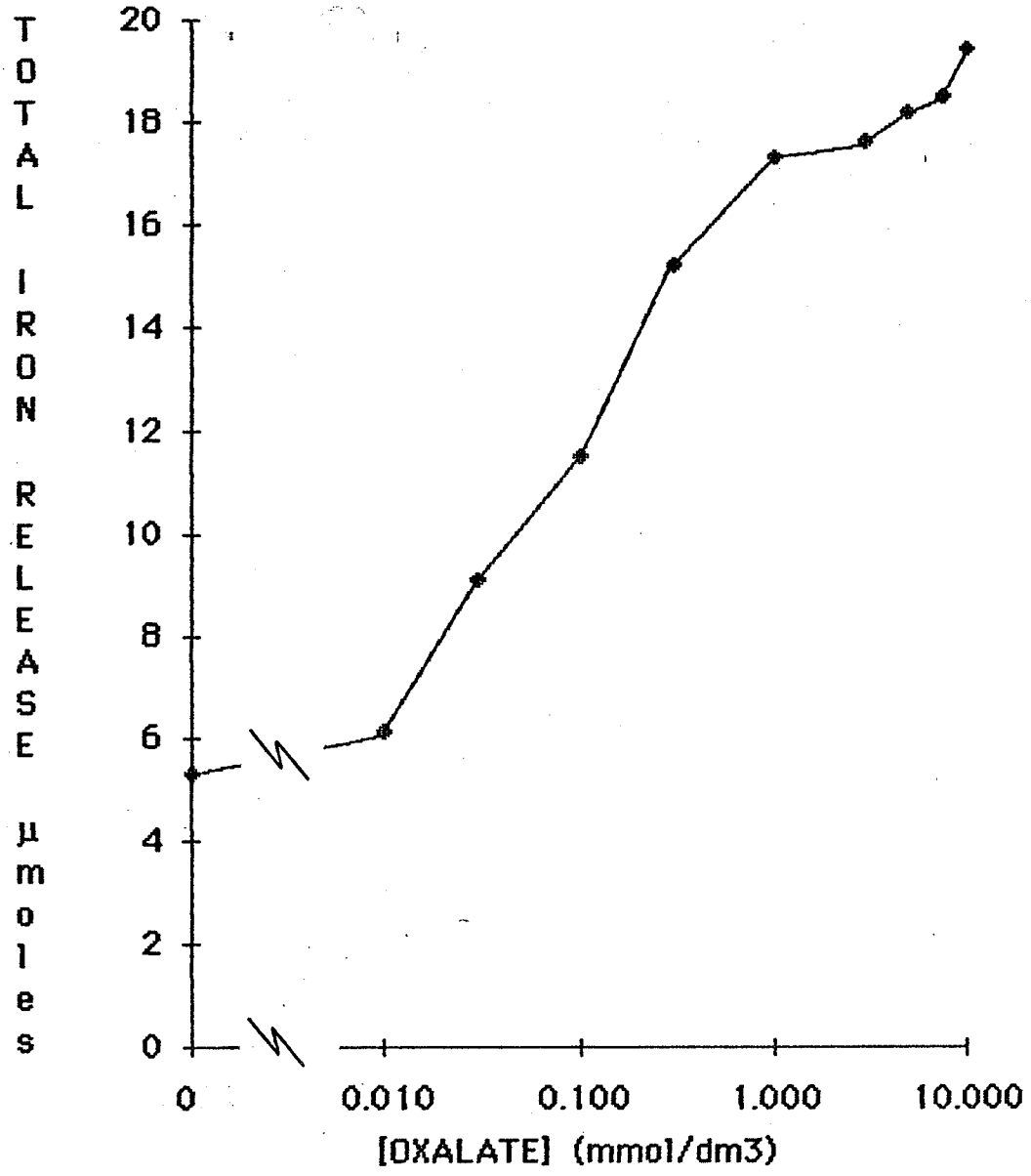

FIGURE 32

Total iron release versus oxalate concentration. Experimental conditions: 1×10^{-3} mol·dm^{-3} EDTA; disks rotated at 16.67 Hz; pH = 3.12 $\pm$ 0.10; room temperature.

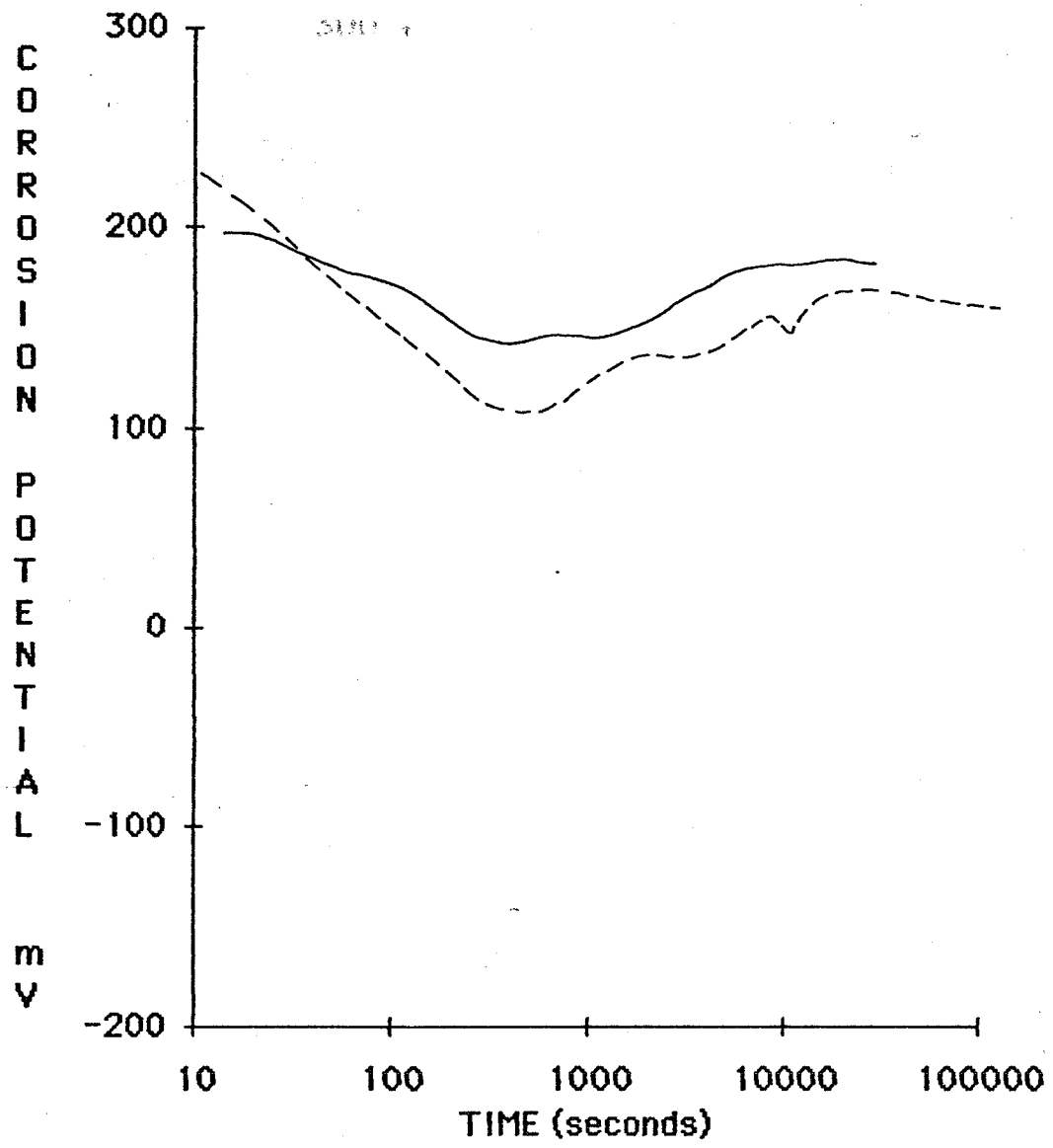

FIGURE 33

Corrosion potential (vs SCE) versus time. Experimental conditions: 1×10^{-3} mol·dm^{-3} oxalate; pH = 3.00 $\pm$ 0.05; room temperature; disks rotated at 16.67 Hz; (———; -----) repeat experiments.

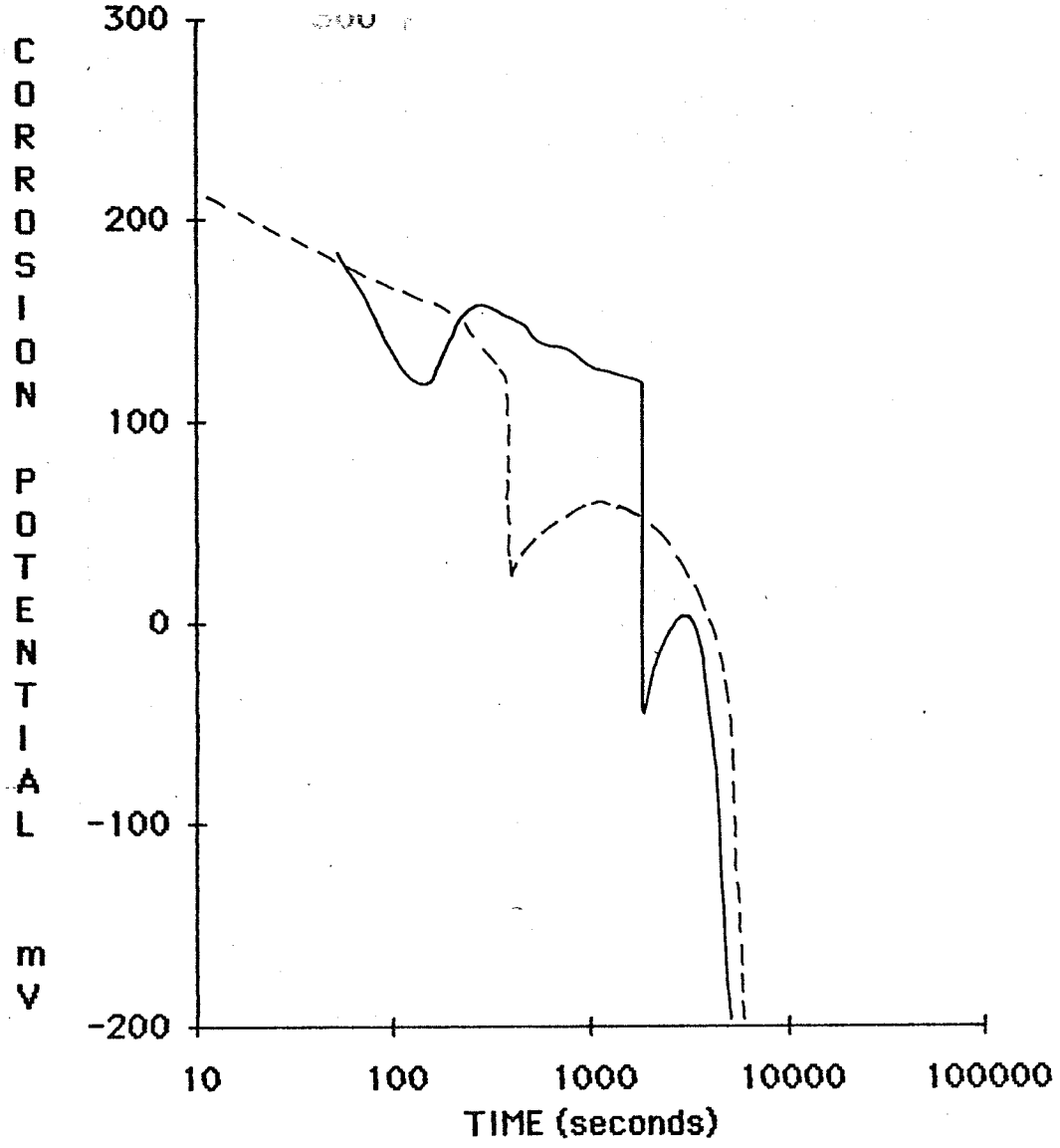

FIGURE 34

Corrosion potential (vs SCE) versus time. Experimental conditions: 1×10^{-3} mol·dm^{-3} oxalate; pH = 3.00 ± 0.05; room temperature; disks rotated at 16.67 Hz; (———— ; -------) repeat experiments.

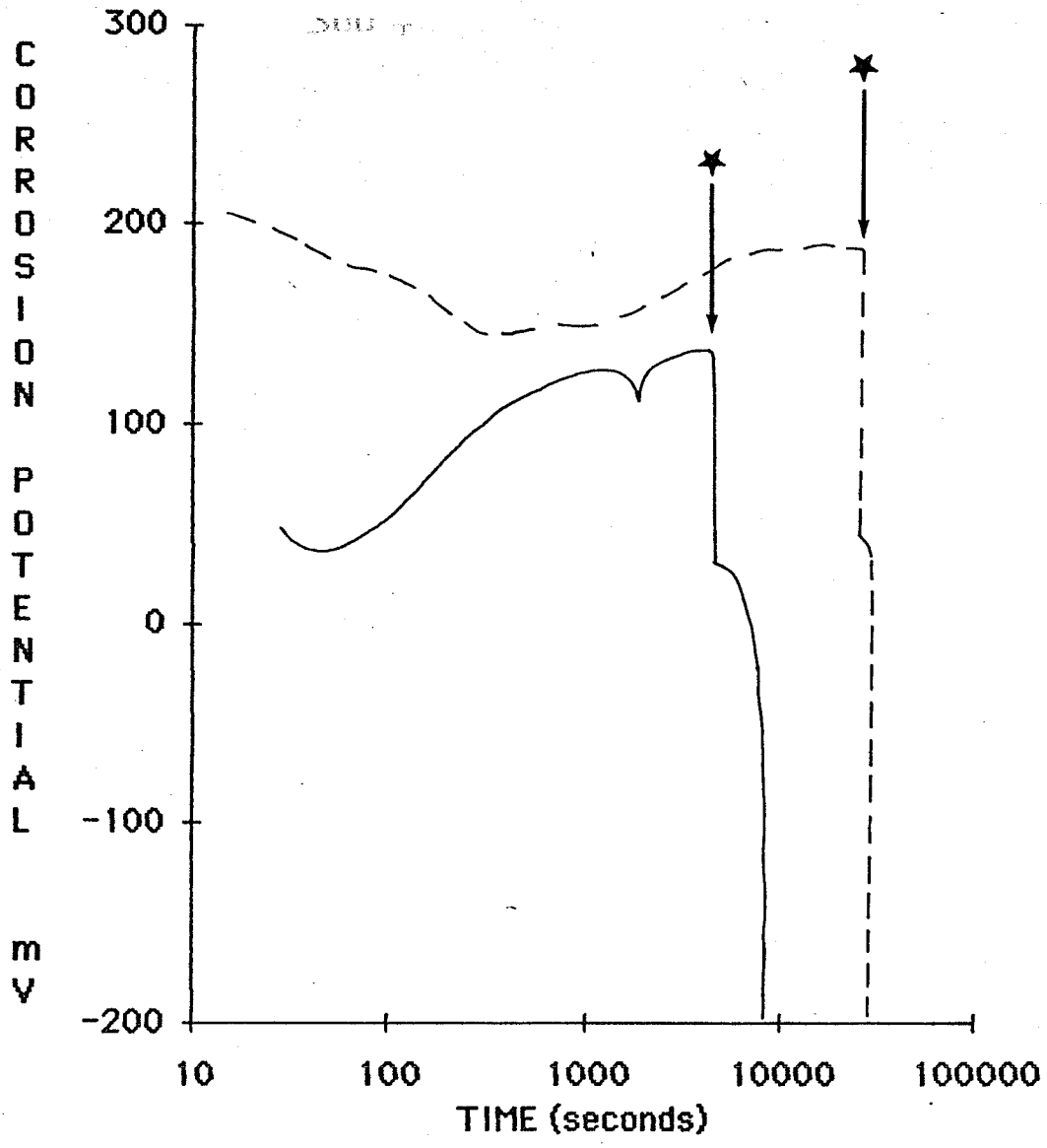

FIGURE 35

Corrosion potential (vs SCE) versus time. Experimental conditions: 1×10^{-3} mol·dm^{-3} oxalate; pH = 3.00 ± 0.05; room temperature; disks rotated at 16.67 Hz. Repeat experiments.

★ indicates the time at which ferrous ammonium sulphate was added.

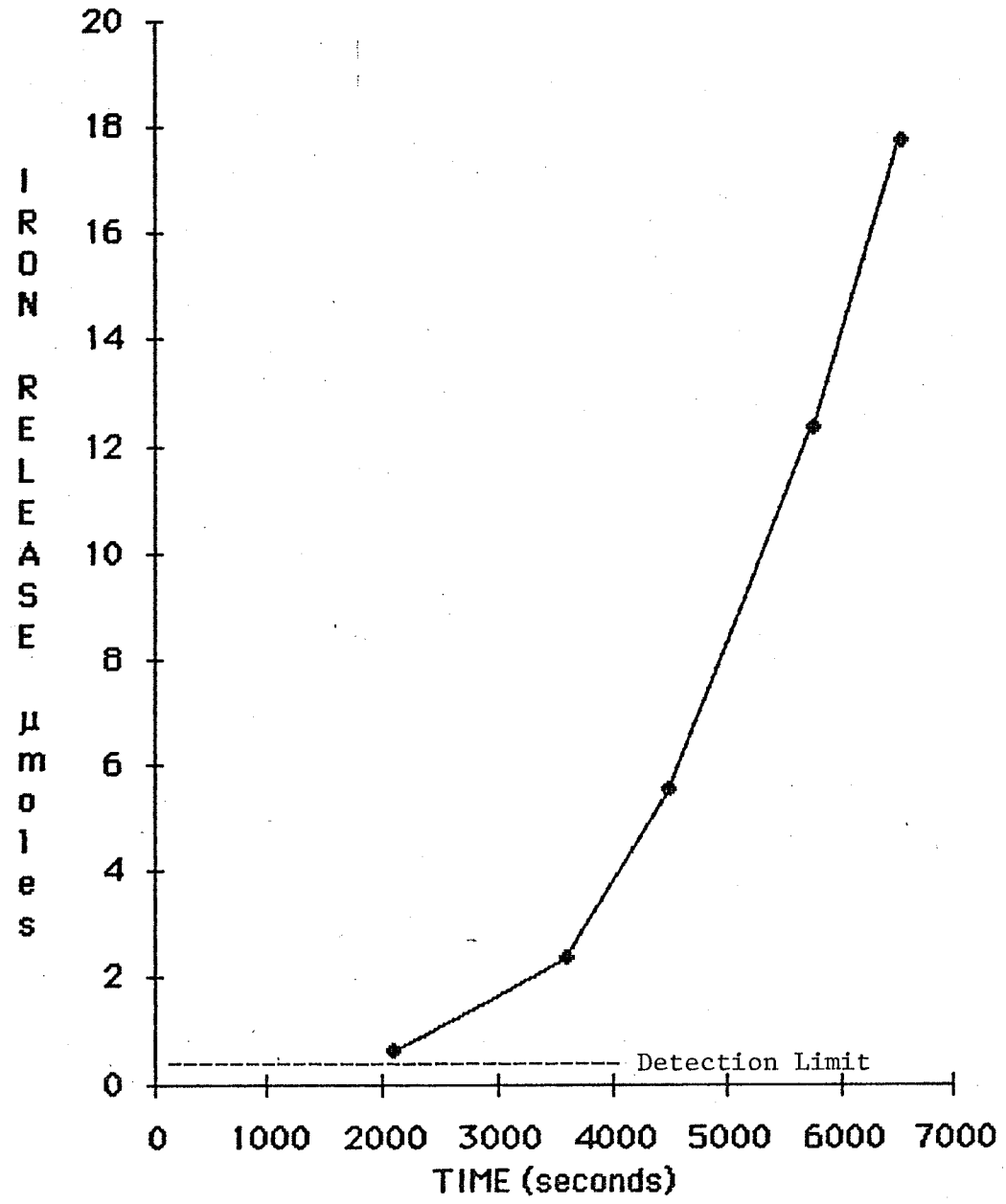

FIGURE 36

Iron release versus time. Experimental conditions: 1×10^{-3} mol·dm^{-3} oxalate; pH = 3.00 ± 0.05; room temperature; rotated at 16.67 Hz.

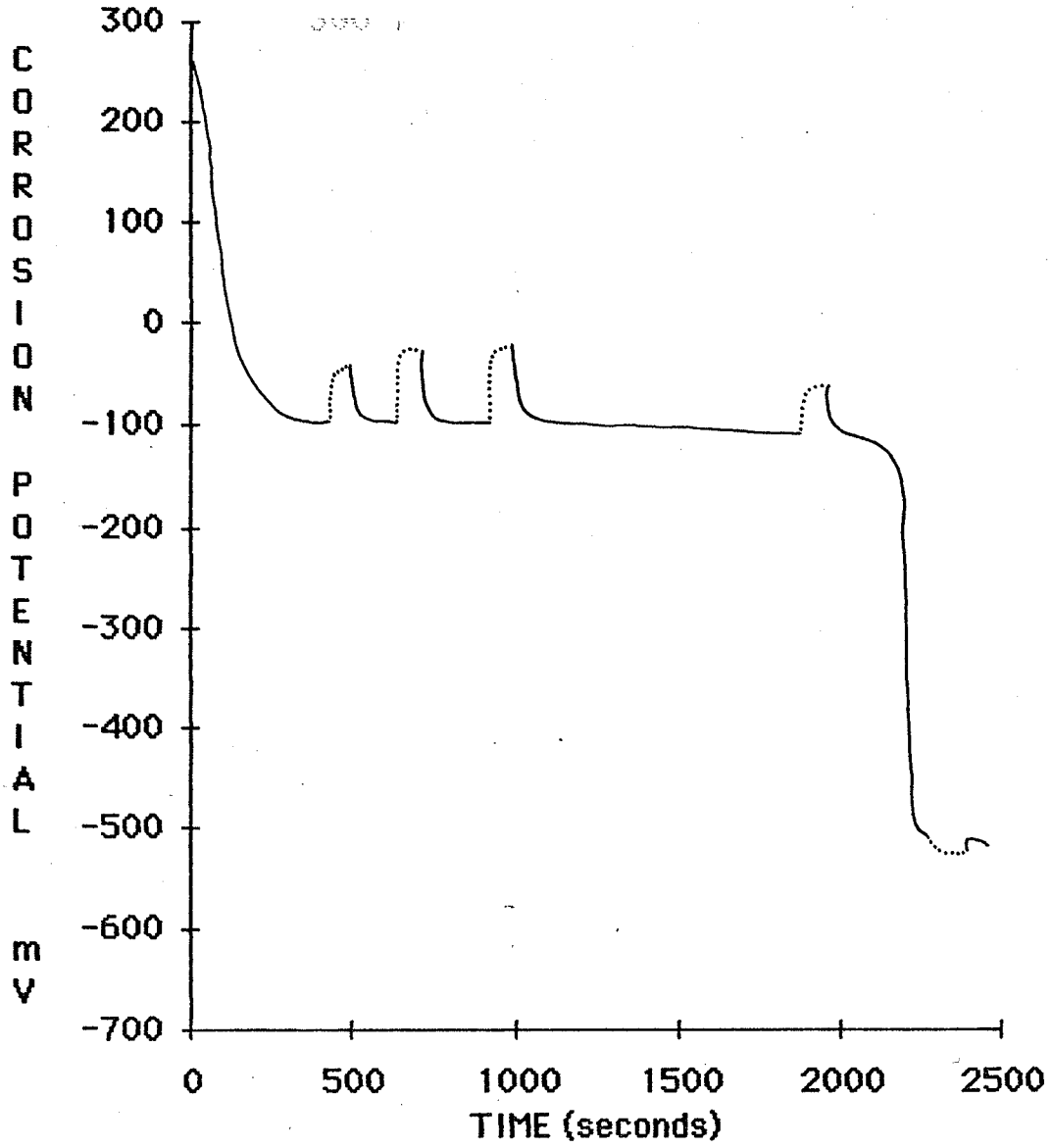

FIGURE 37

Corrosion potential versus time, with changes in disk rotation speed. Experimental conditions: 1 x 10^{-3} mol·dm^{-3} EDTA; pH = 3.00 ± 0.05; room temperature; (———), disk rotated 16.67 Hz; (·····), disk static.

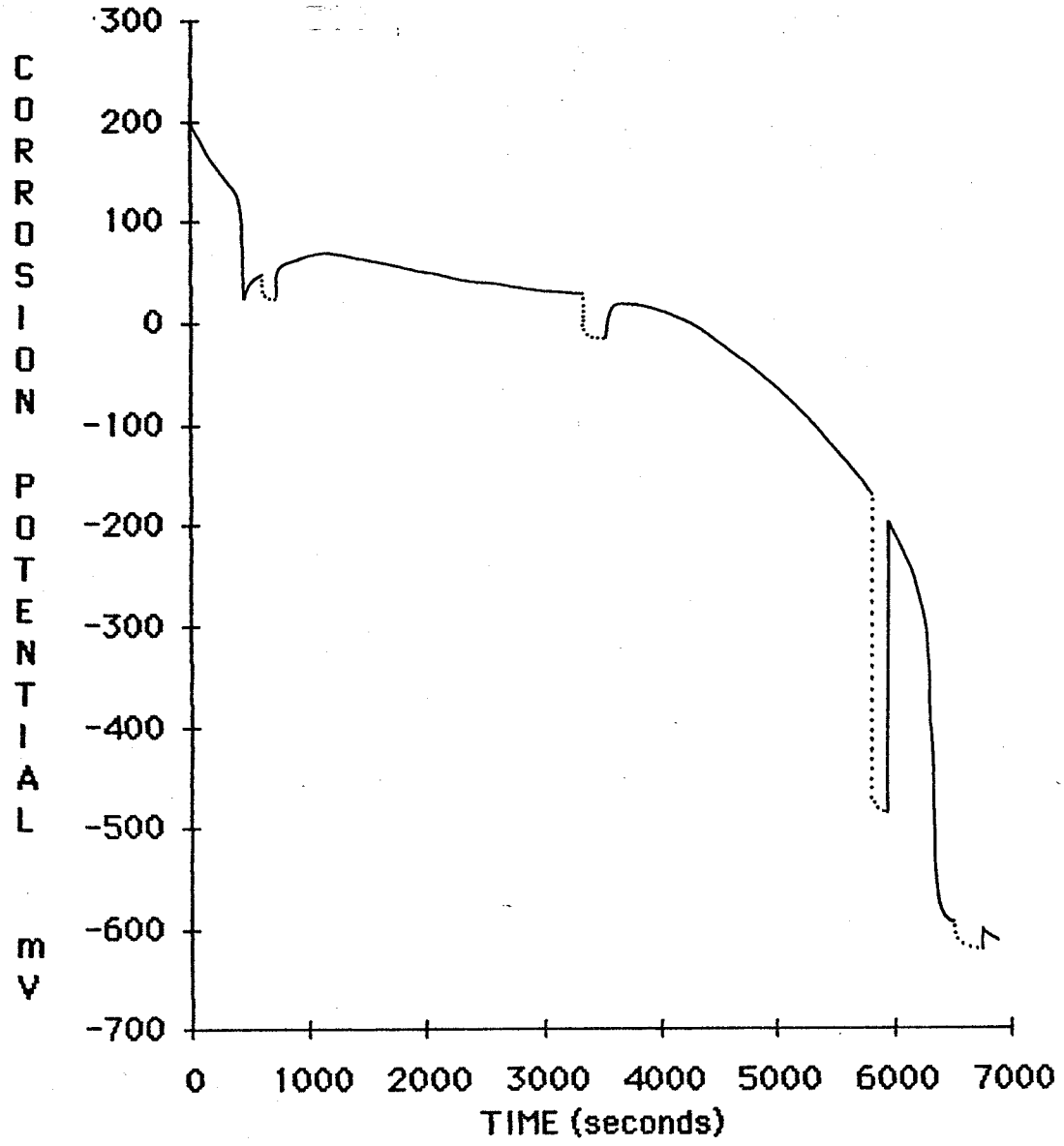

FIGURE 38

Corrosion potential versus time, with changes in disk rotation speed. Experimental conditions: 1×10^{-3} mol·dm^{-3} oxalate; pH = 3.00 ± 0.10; room temperature; (——), disk rotated 16.67 Hz; (····), disk static.

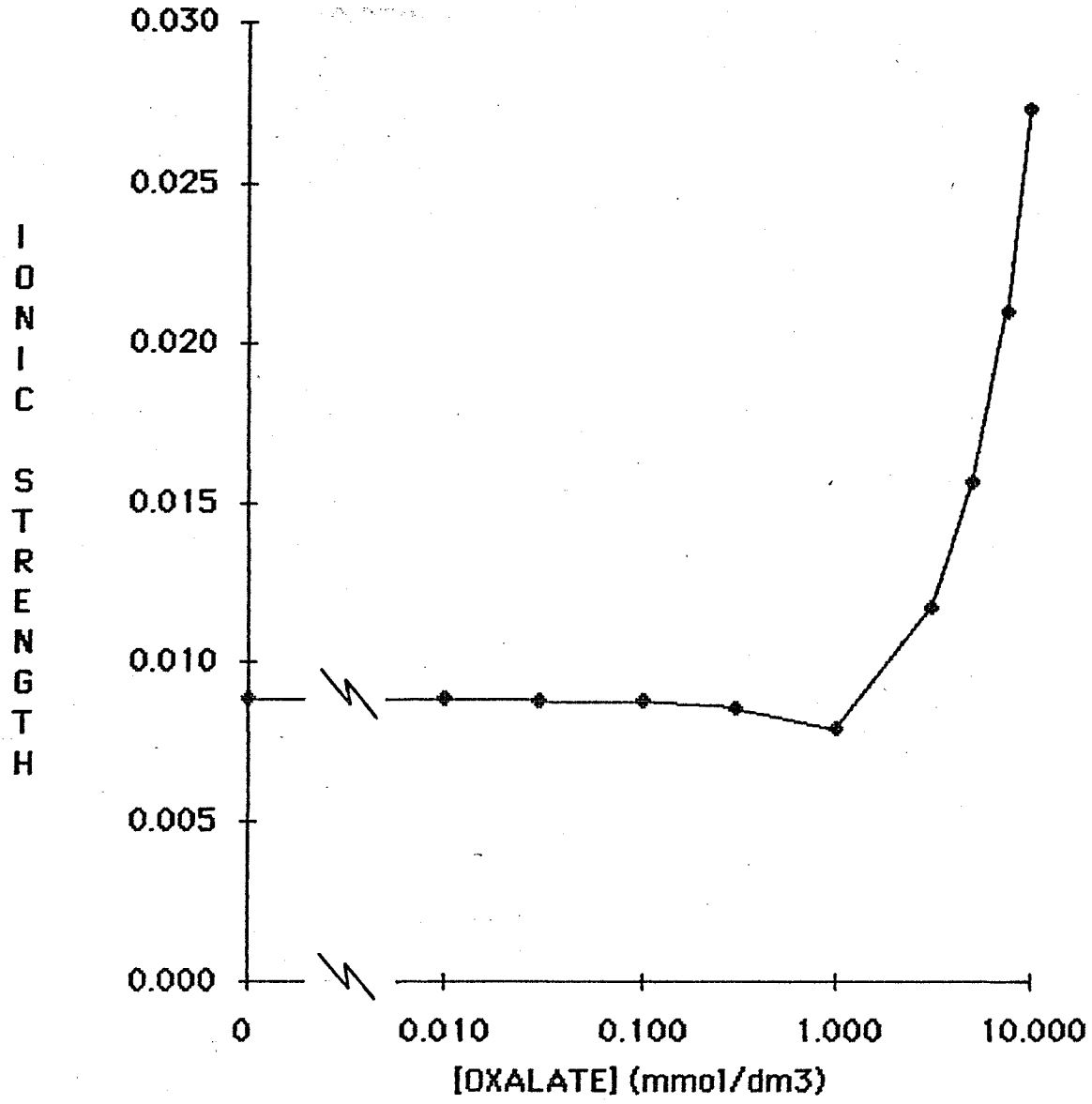

FIGURE 39

Ionic strength of mixed EDTA/oxalate solutions versus oxalate concentration. Experimental conditions: 1×10^{-3} mol·dm^{-3} EDTA; temperature 20°C; pH = 3.10 ± 0.10.

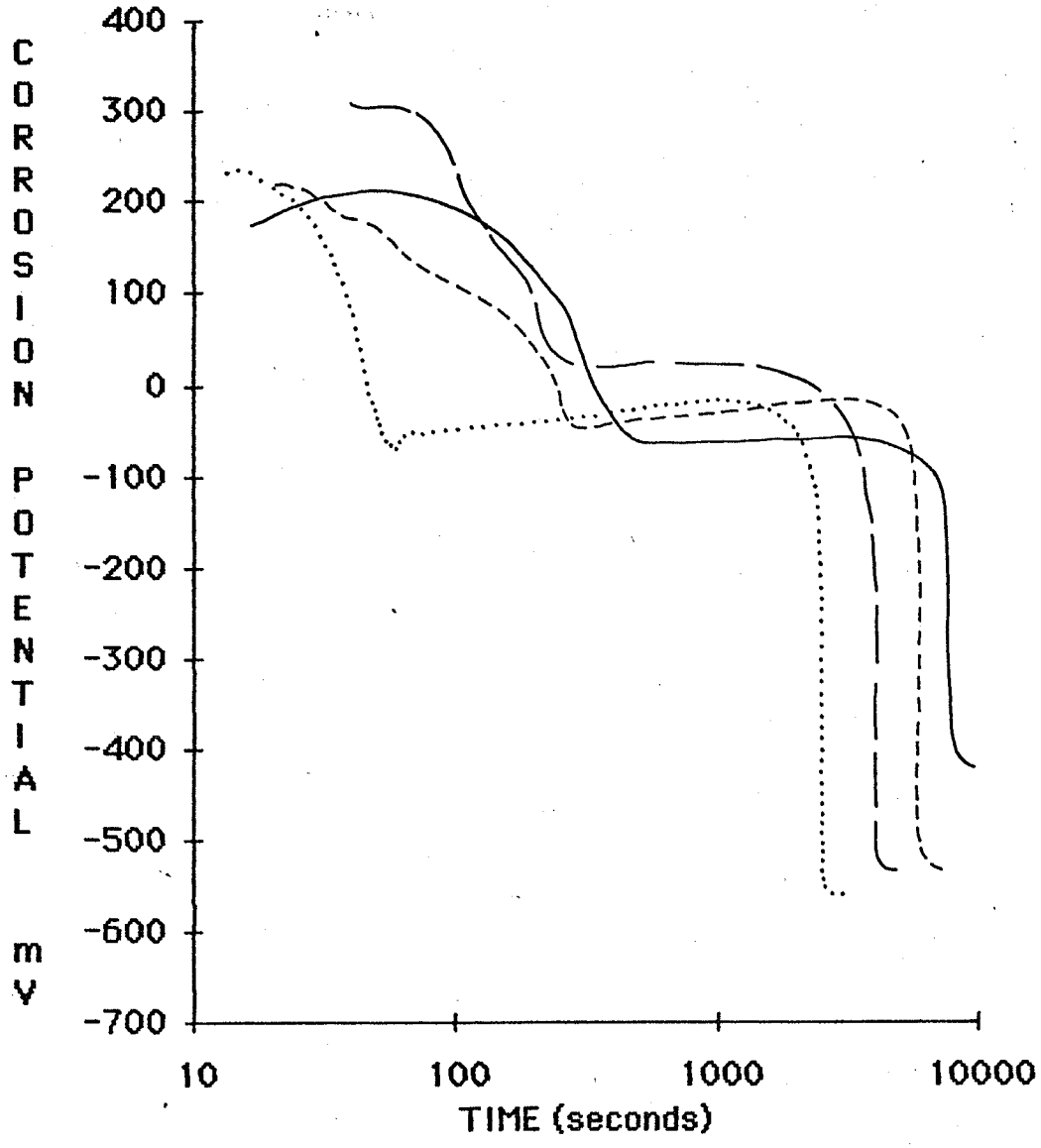

FIGURE 40

Corrosion potential (vs SCE) versus time. Experimental conditions: pH = 3.10 ± 0.05; room temperature; disks rotated at 16.67 Hz. Solution composition, concentrations ($mol \cdot dm^{-3}$); (----), 3×10^{-4} EDTA + 3×10^{-4} oxalate; (····), 3×10^{-4} EDTA + 3×10^{-4} oxalate + 1×10^{-3} sulphate; (— —), 1×10^{-3} sulphate; (——), 1×10^{-3} $mol \cdot dm^{-3}$ perchlorate.

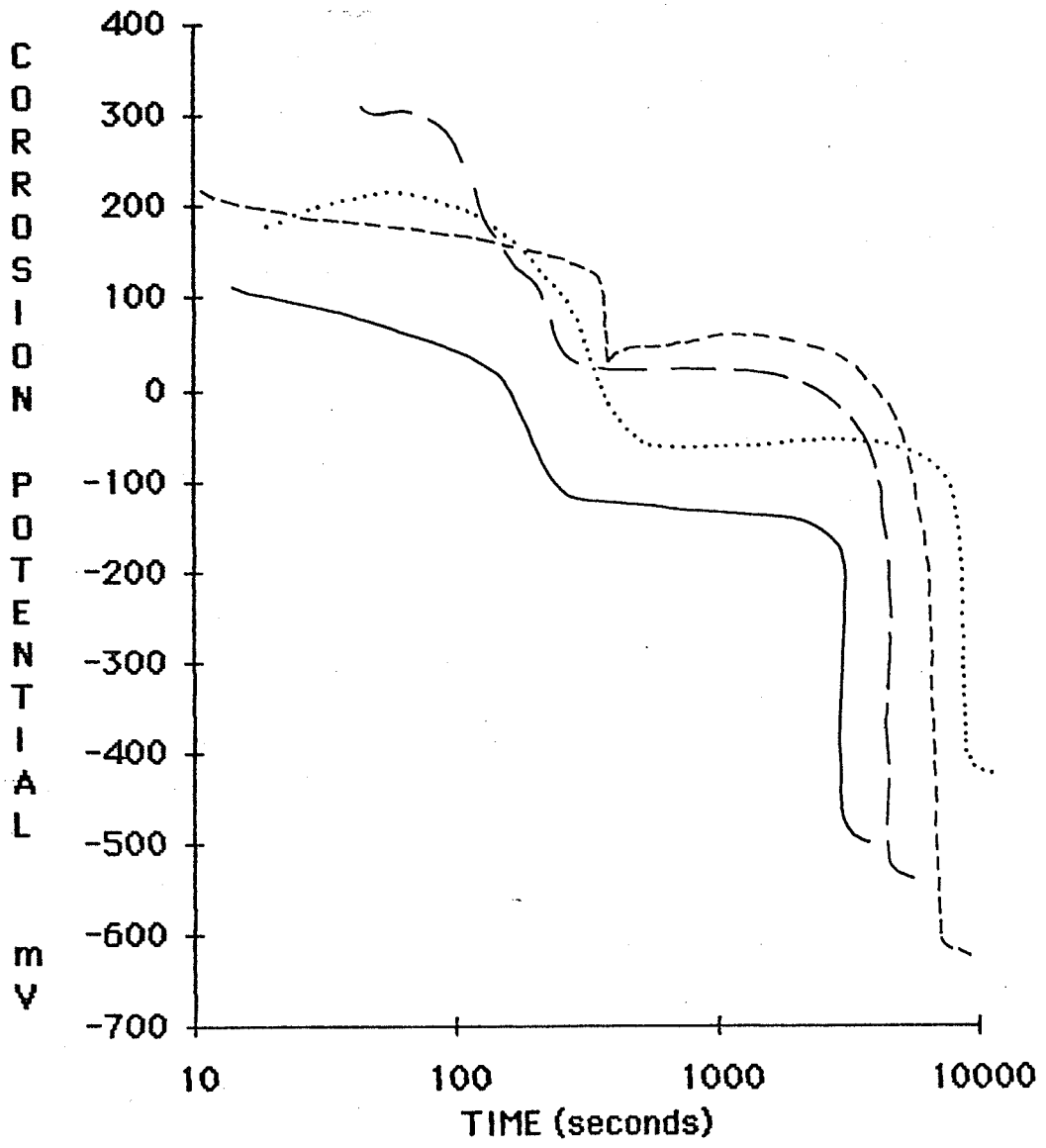

FIGURE 41

Corrosion potential (vs. SCE) versus time. Experimental conditions: pH = 3.10 ± 0.10; room temperature; disks rotated at 16.67 Hz. Solution compositions, concentrations ($mol \cdot dm^{-3}$); (——), 1×10^{-3} EDTA; (····), 1×10^{-3} perchlorate; (— —), 1×10^{-3} sulphate; (----), 1×10^{-3} oxalate.

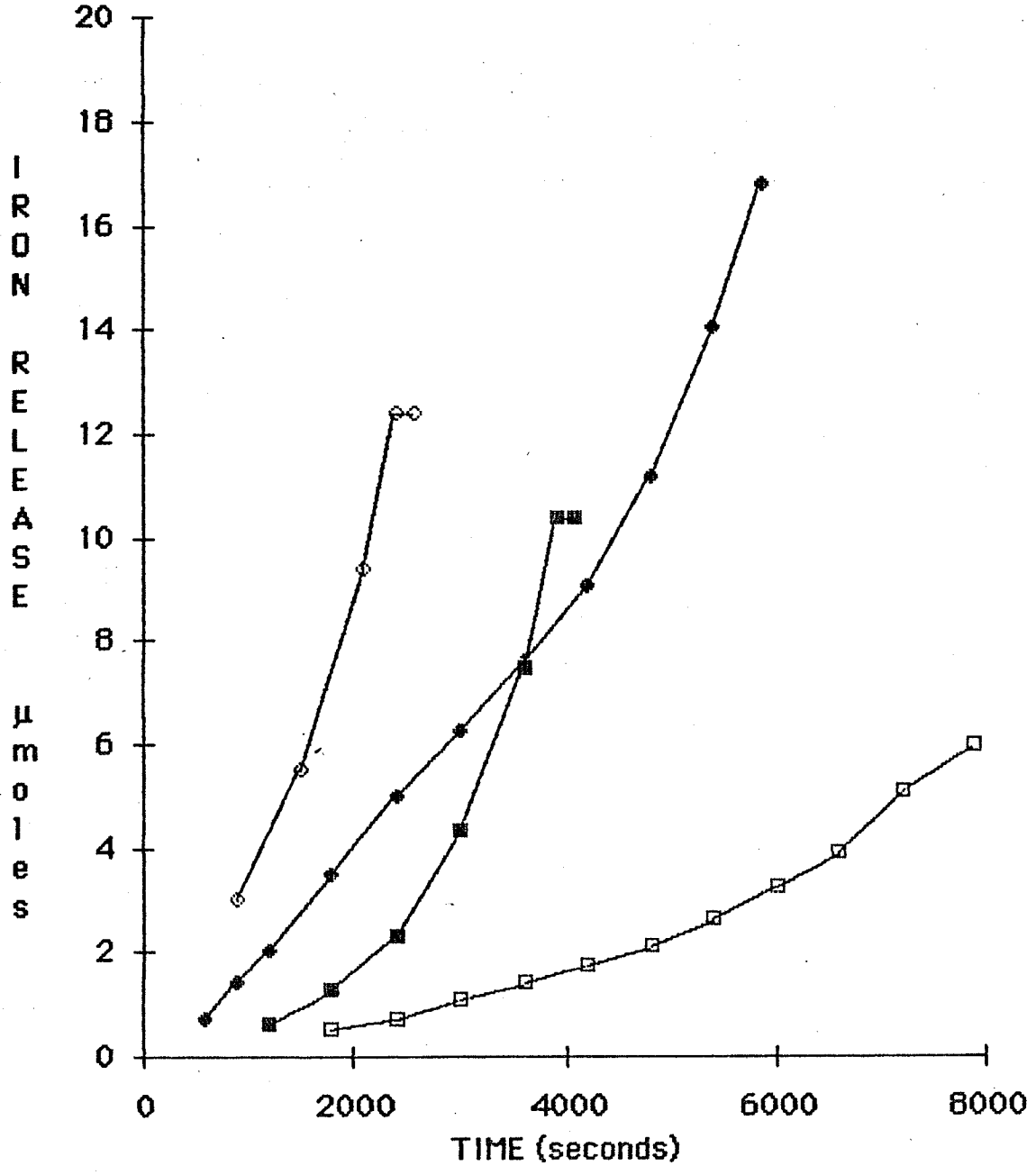

FIGURE 42

Iron release versus time. Experimental conditions: pH = 3.10 ± 0.10; room temperature; disks rotated at 16.67 Hz. Solution composition, concentrations ($mol \cdot dm^{-3}$); ◇ , 3×10^{-4} oxalate + 3×10^{-4} EDTA + 1×10^{-3} sulphate; ◆ , 3×10^{-4} oxalate + 3×10^{-4} EDTA; ■, 1×10^{-3} sulphate; □ , 1×10^{-3} perchlorate.

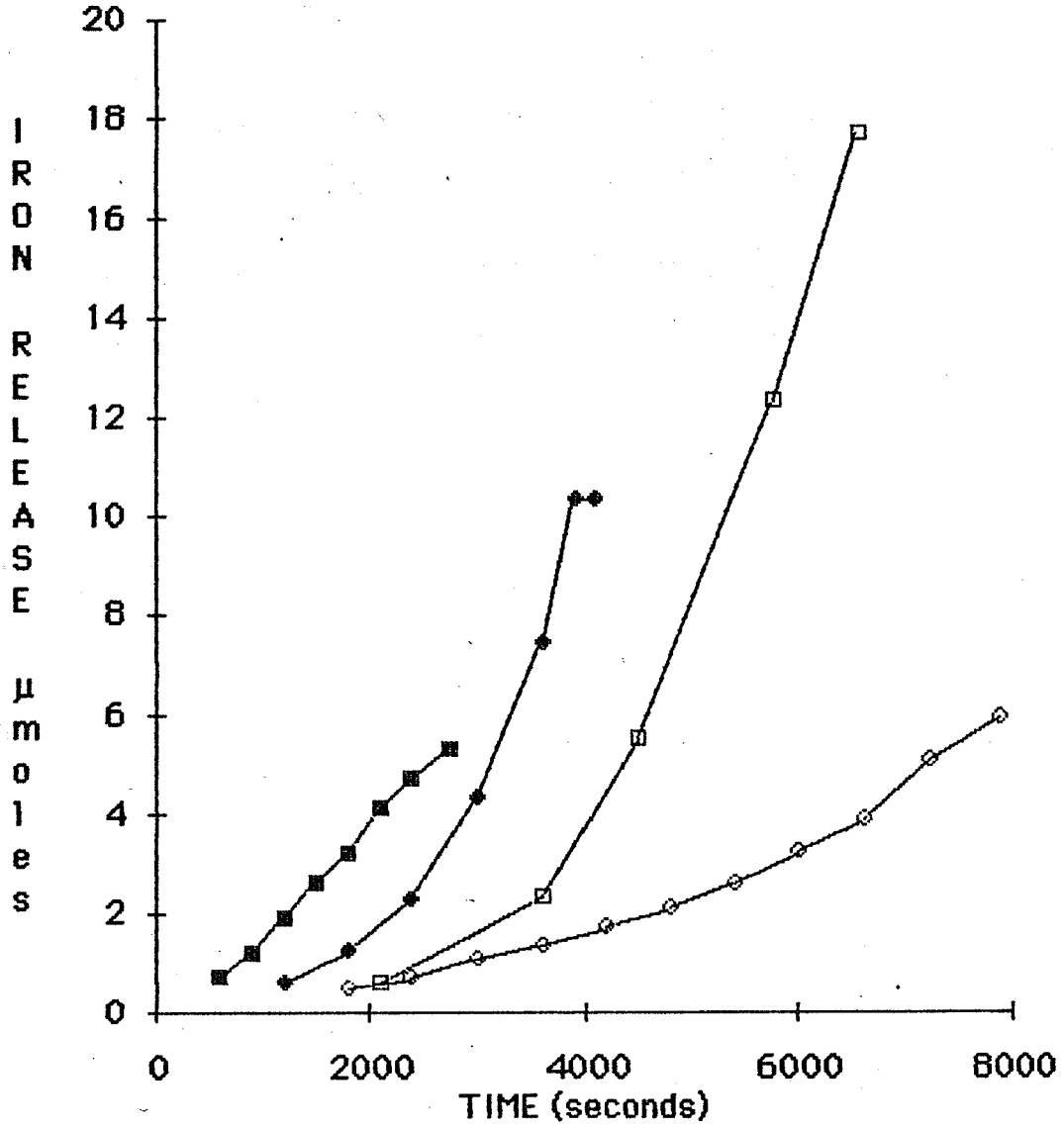

FIGURE 43

Iron release versus time. Experimental conditions: pH = 3.10 ± 0.10; room temperature; disks rotated at 16.67 Hz. Solution composition, concentrations ($mol \cdot dm^{-3}$): ■ , 1×10^{-3} EDTA; ◆ , 1×10^{-3} sulphate; □, 1×10^{-3} oxalate; ◇ , 1×10^{-3} perchlorate.

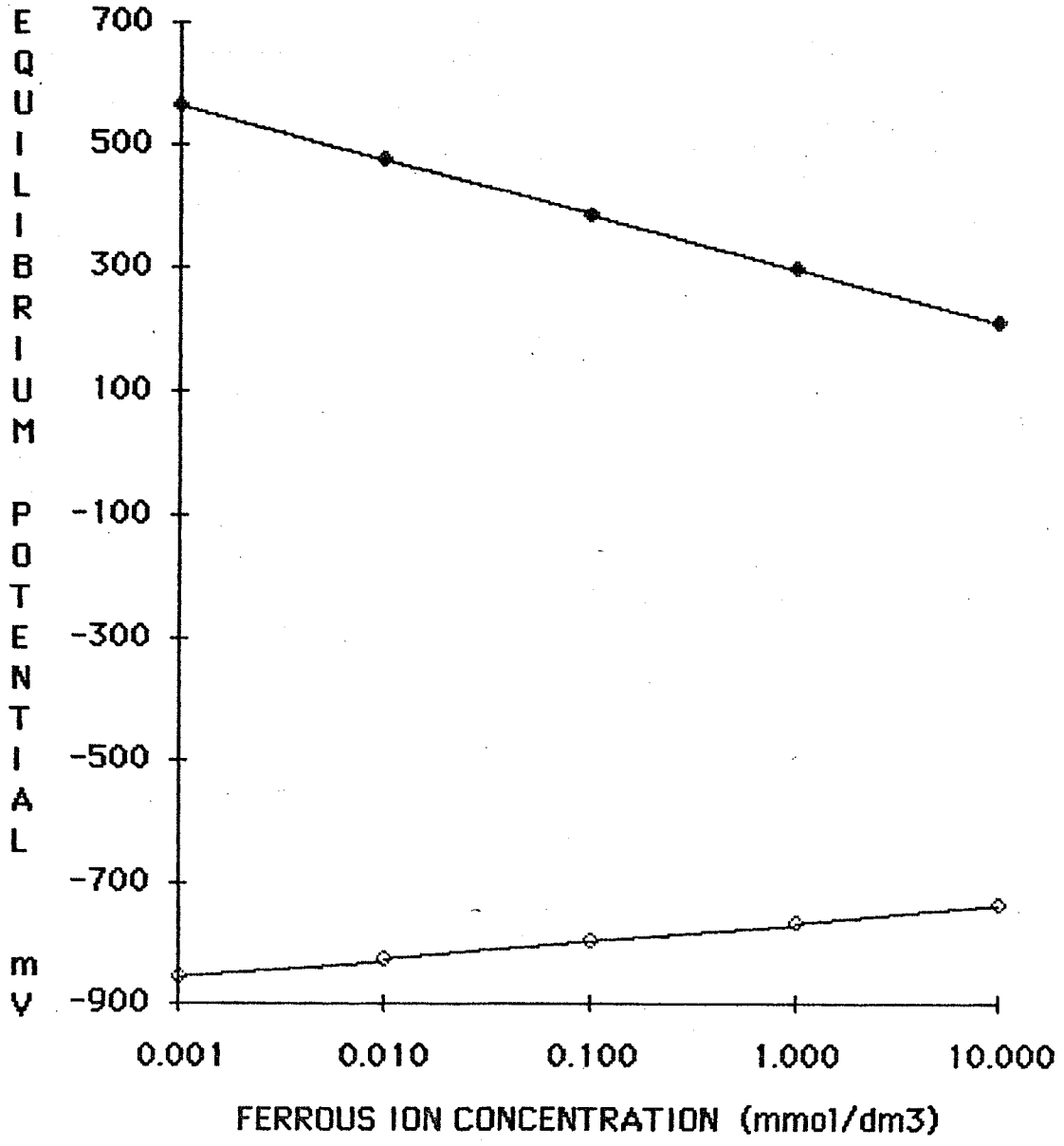

FIGURE 44

Half-reaction equilibrium potentials (vs SCE) versus ferrous ion concentration, temperature 20°C. Reactions: (◆), magnetite dissolution, equation (10.2); (◇), metal dissolution, equation (10.1).

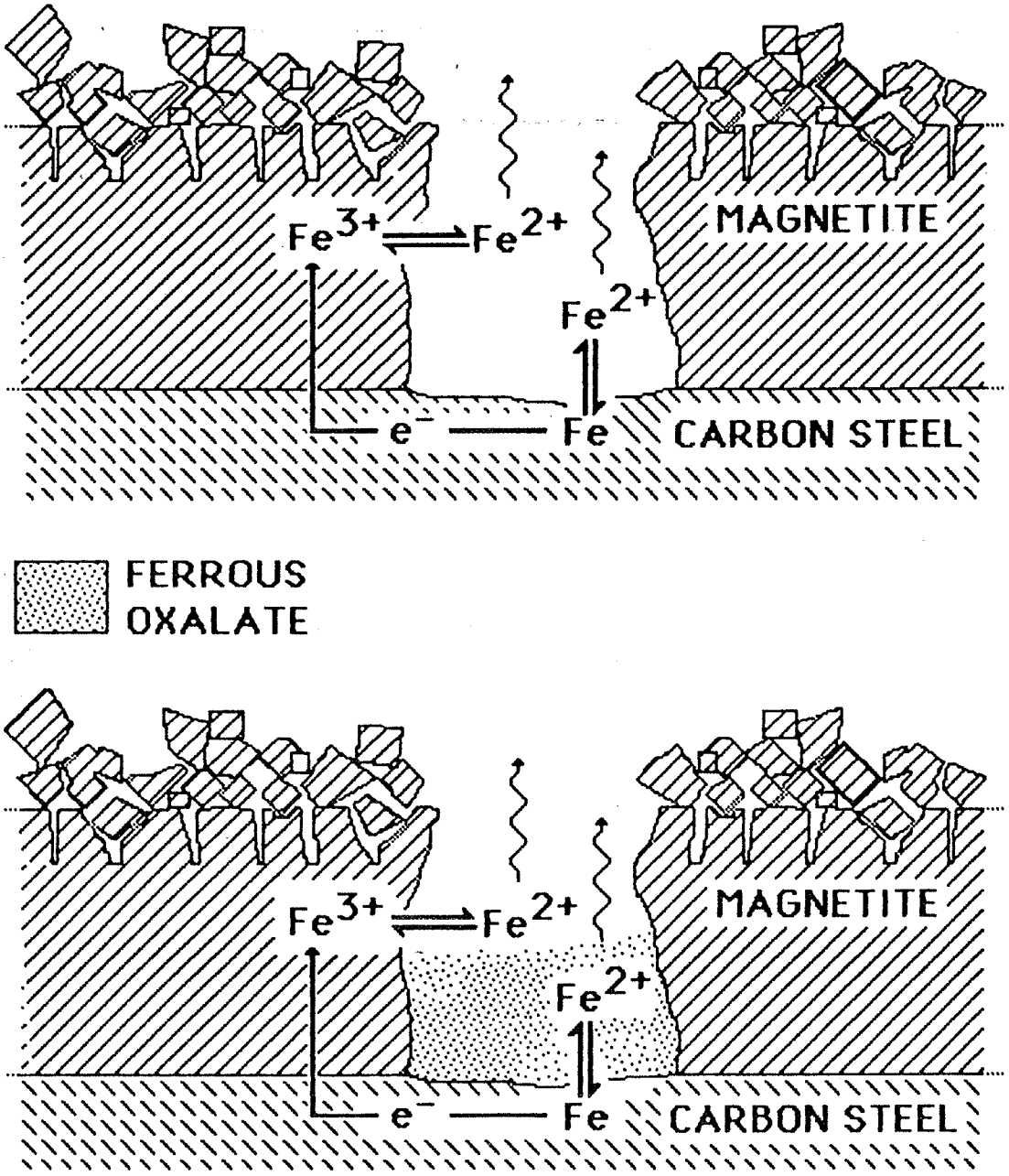

FIGURE 45

Schematic illustrating the inhibition of the anodic dissolution of carbon steel due to the precipitation of ferrous oxalate within the base-layer oxide pores. The top figure shows the dissolution process in the absence of precipitation, the bottom figure in the presence of precipitation.

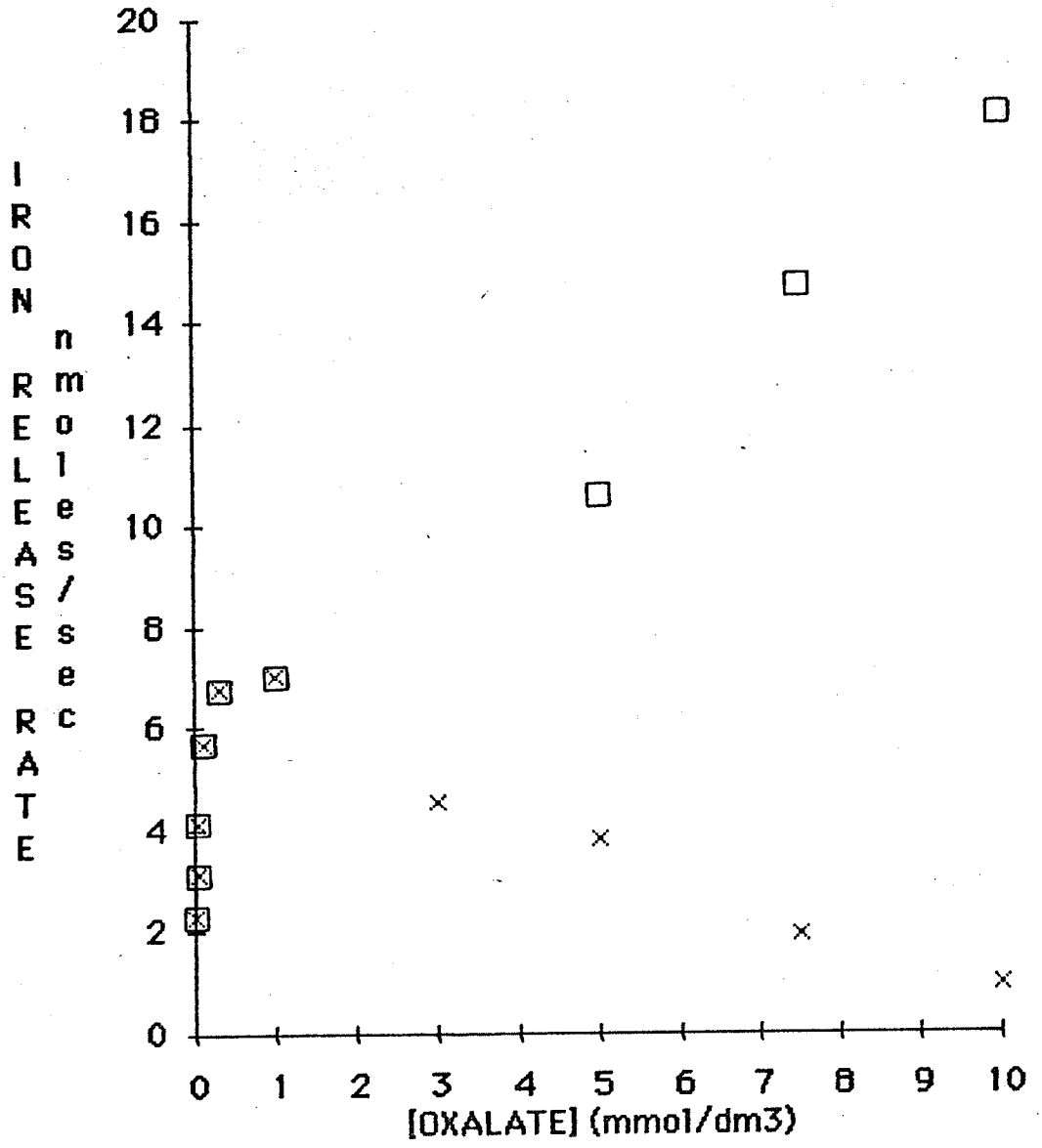

FIGURE 46

Initial and final iron release rates versus oxalate concentration. Experimental conditions: 1×10^{-3} mol·dm^{-3} EDTA; pH = 3.00 ± 0.10; room temperature. x, initial iron release rate; □ , final iron release rate.

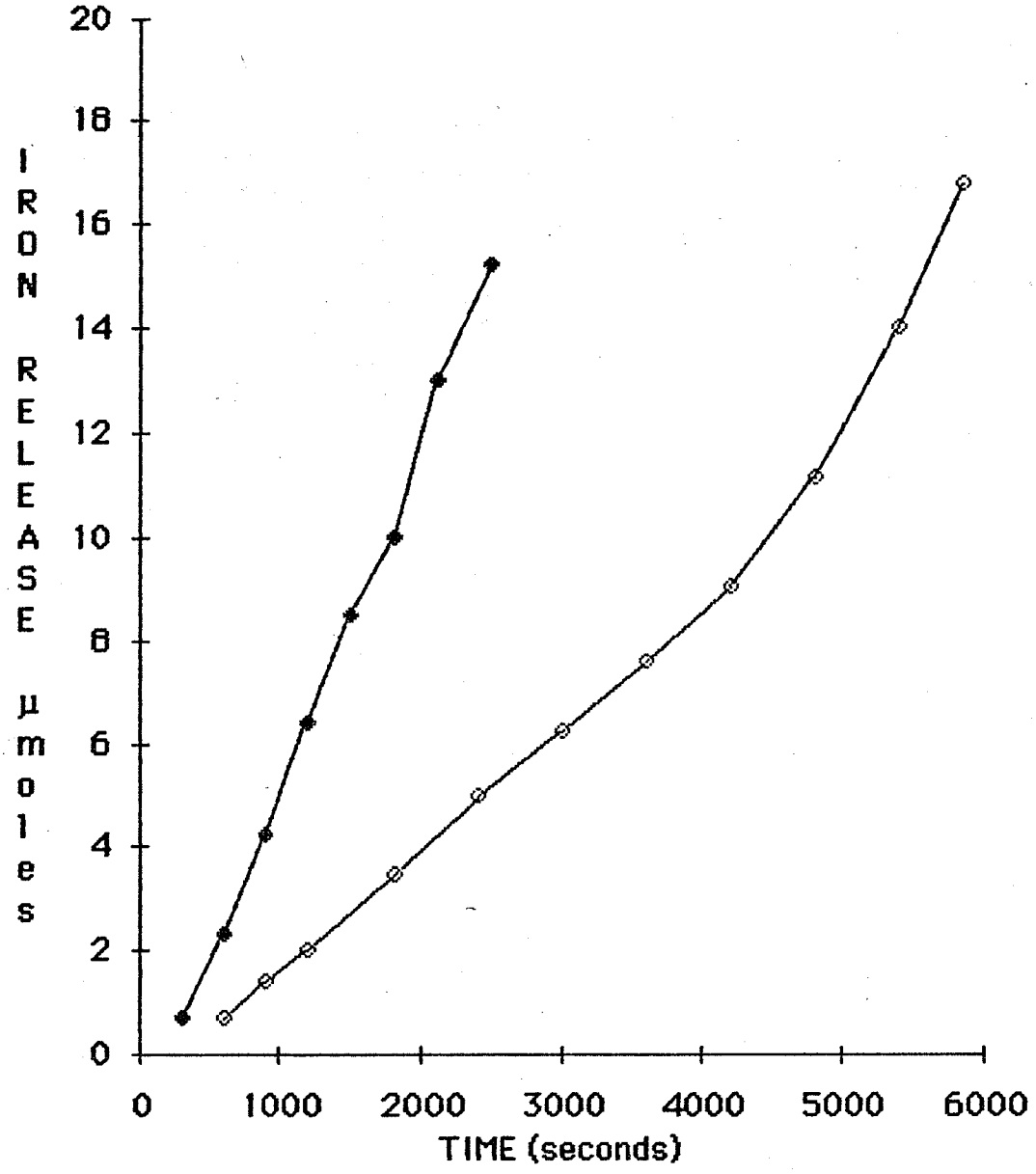

FIGURE 47

Iron release versus time as a function of EDTA concentration in mixed EDTA-oxalate solutions. Experimental conditions: 3×10^{-4} mol·dm^{-3} oxalate; pH = 3.10 ± 0.10; room temperature; disks rotated at 16.67 Hz; ◆ , 1×10^{-3} mol·fm^{-3} EDTA; ◇, 3×10^{-4} mol·dm^{-3} EDTA.

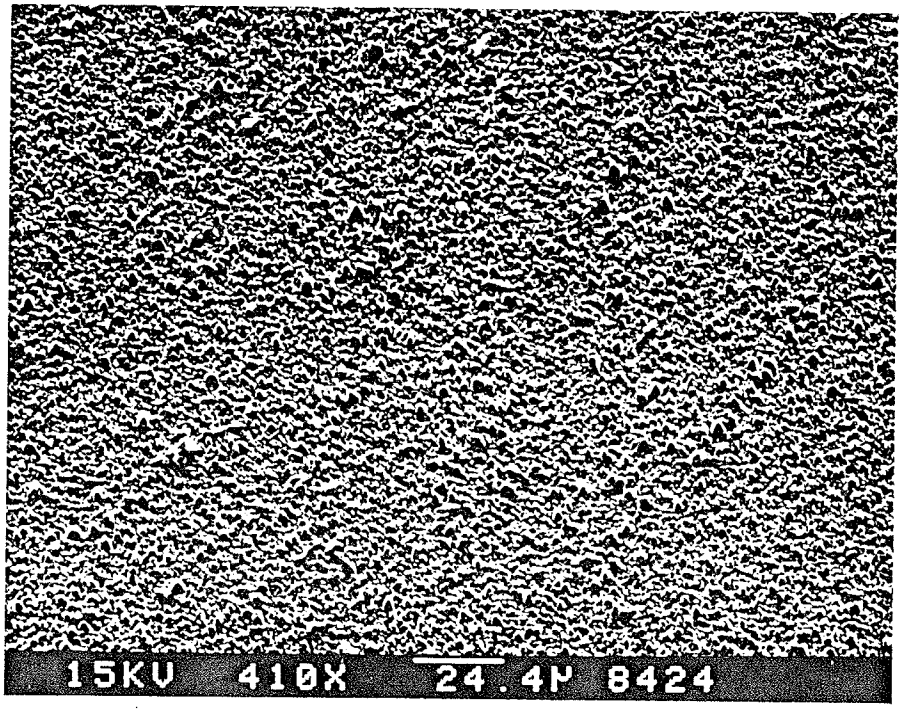

MICROGRAPH 1: Pre-dissolution double-layer magnetite film.

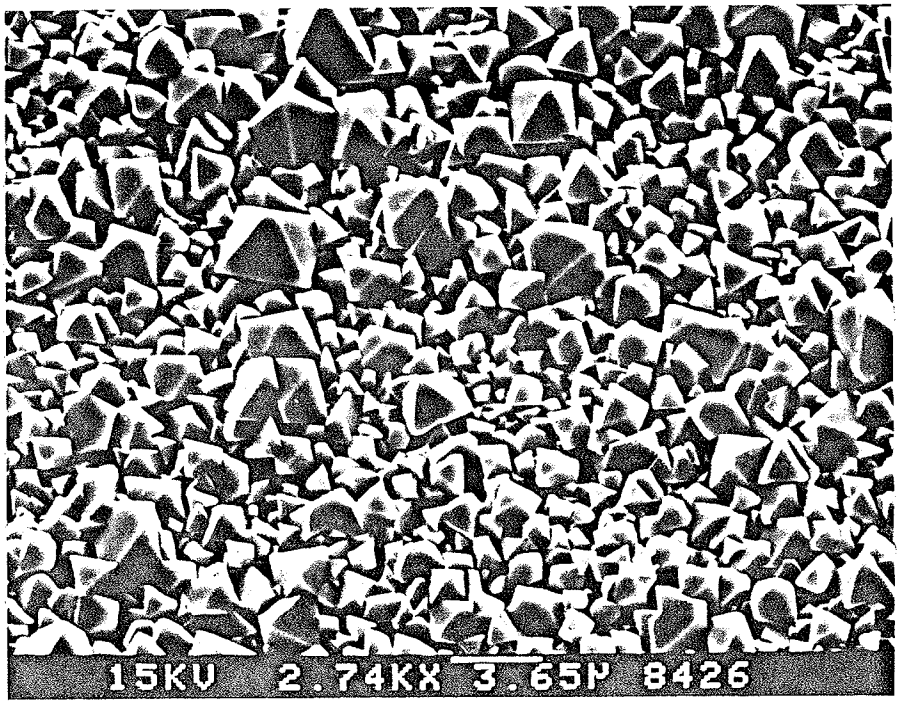

MICROGRAPH 2: Pre-dissolution double-layer magnetite film.

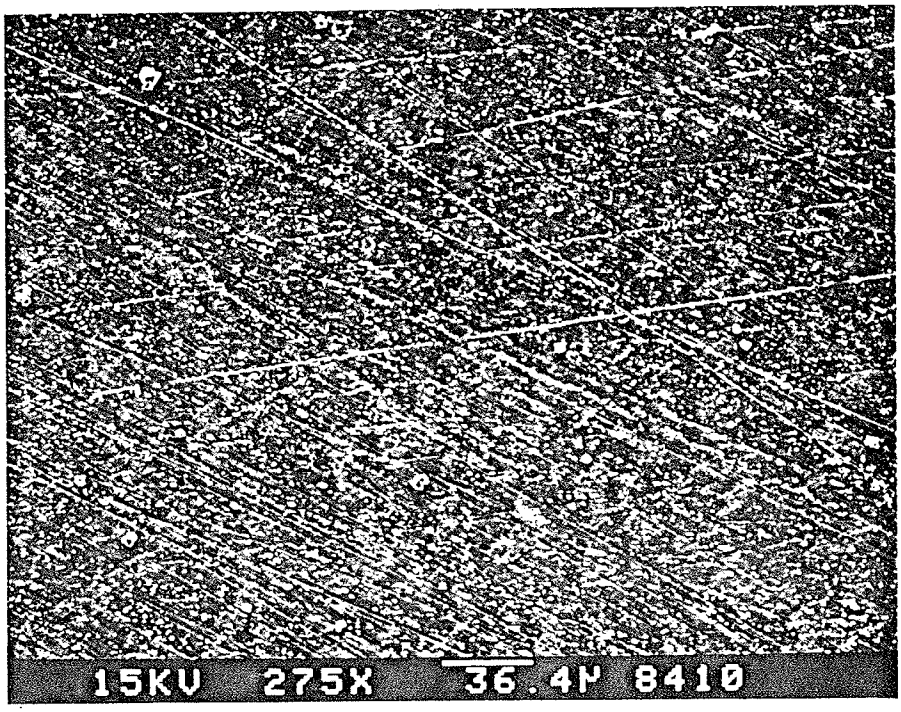

MICROGRAPH 3: Pre-dissolution single-layer magnetite film.

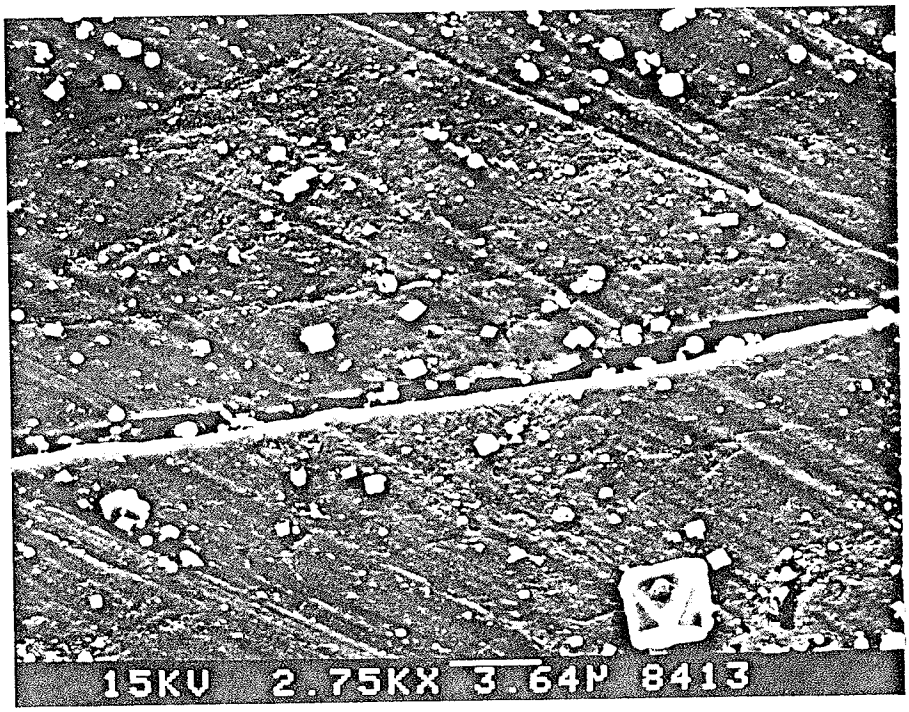

MICROGRAPH 4: Pre-dissolution single-layer magnetite film.

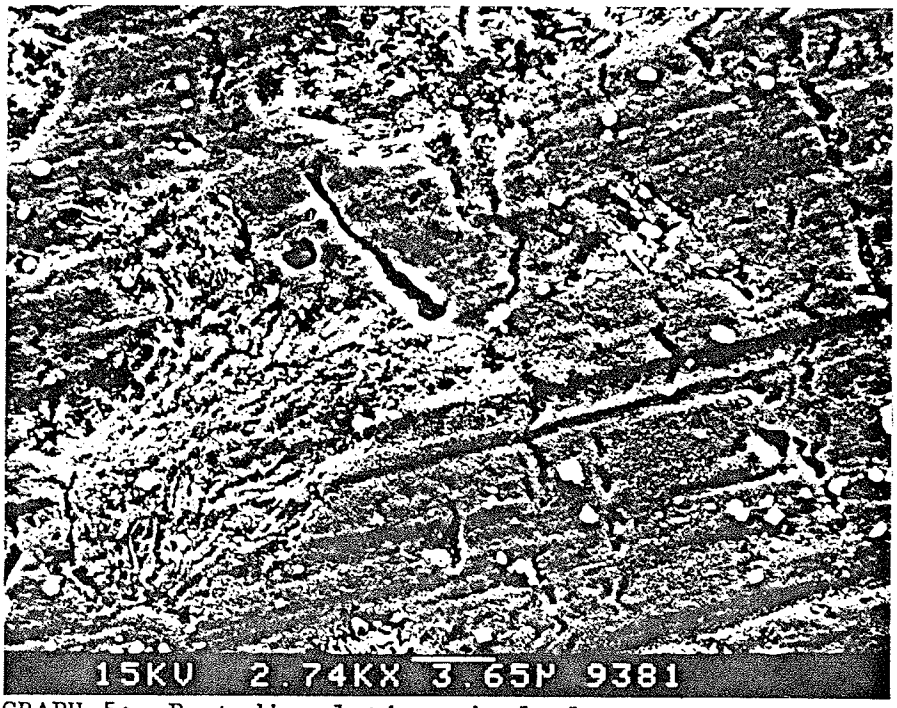

MICROGRAPH 5: Post-dissolution single-layer magnetite film.
Experimental conditions: room temperature; static disk; $1x10^{-3}$ $mol \cdot dm^{-3}$ EDTA; pH = 3.25 ± 0.05; initial Fe(II) concentration 0 $mol \cdot dm^{-3}$.

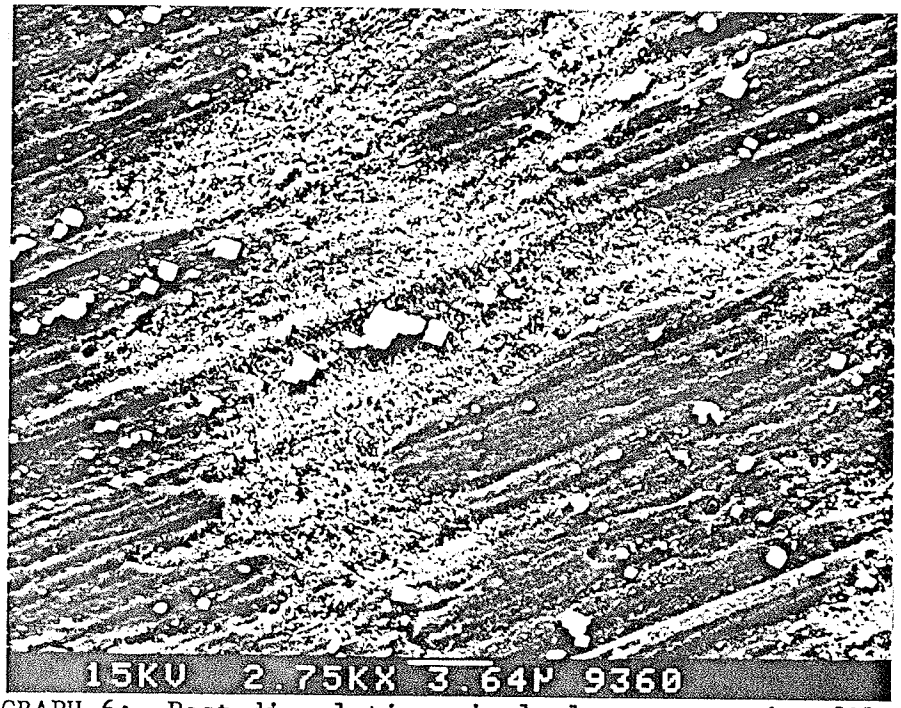

MICROGRAPH 6: Post-dissolution single-layer magnetite film.
Experimental conditions: room temperature; static disk; $1x10^{-3}$ $mol \cdot dm^{-3}$ EDTA; pH = 3.25 ± 0.05; initial Fe(II) concentration $1x10^{-5}$ $mol \cdot dm^{-3}$.

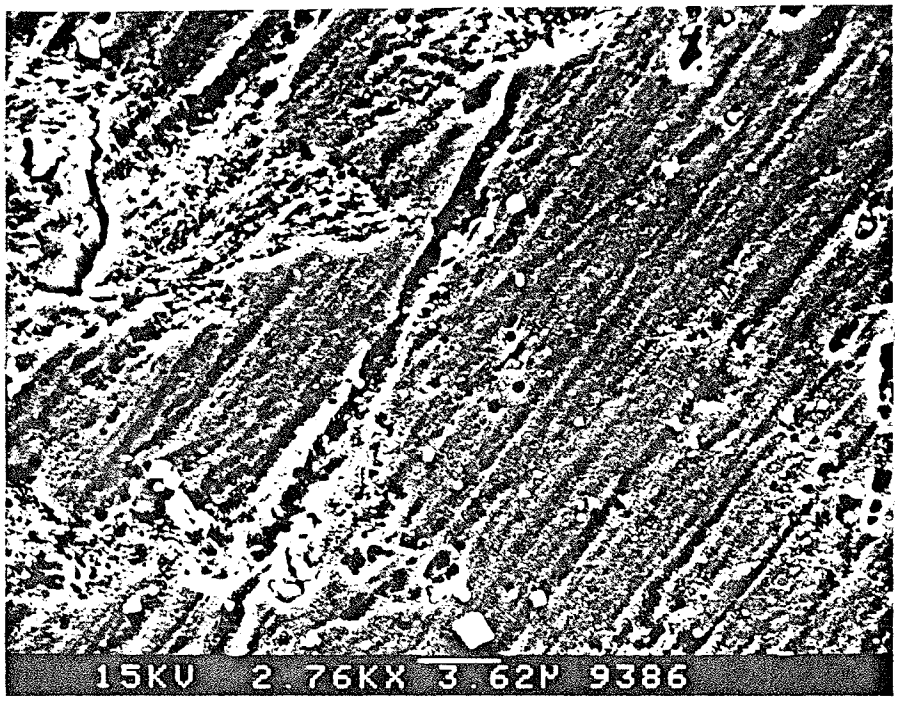

MICROGRAPH 7: Post-dissolution single-layer magnetite film. Experimental conditions: room temperature; static disk; $1x10^{-3}$ $mol \cdot dm^{-3}$ EDTA; pH = 5.00 ± 0.30; initial Fe(II) concentration $1x10^{-5}$ $mol \cdot dm^{-3}$.

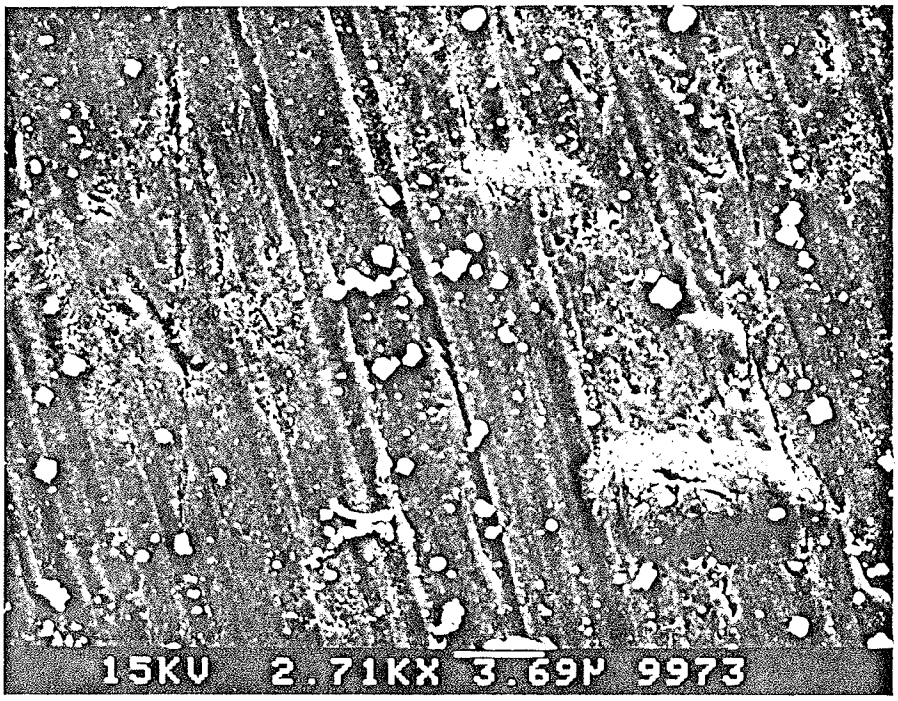

MICROGRAPH 8: Post-dissolution single-layer magnetite film. Experimental conditions: room temperature; static disk; $1x10^{-3}$ $mol \cdot dm^{-3}$ EDTA; pH = 4.40 ± 0.30; initial Fe(II) concentration $1x10^{-4}$ $mol \cdot dm^{-3}$.

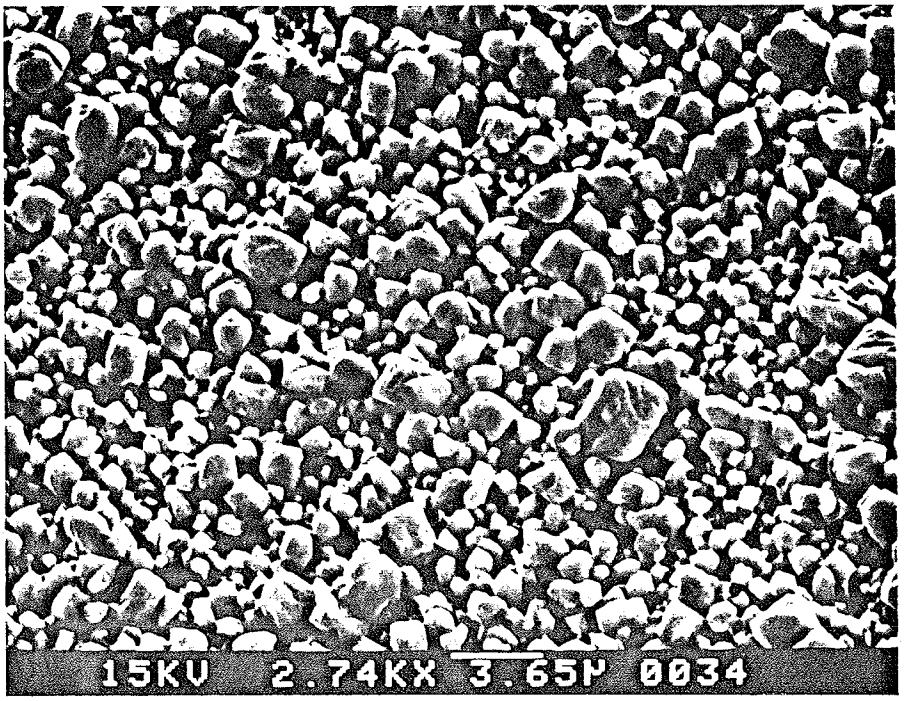

MICROGRAPH 9: Post-dissolution double-layer magnetite film. Experimental conditions: room temperature; static disk; 1×10^{-3} mol·dm^{-3} EDTA; pH = 3.00 ± 0.05; initial Fe(II) concentration 0 mol·dm^{-3}.

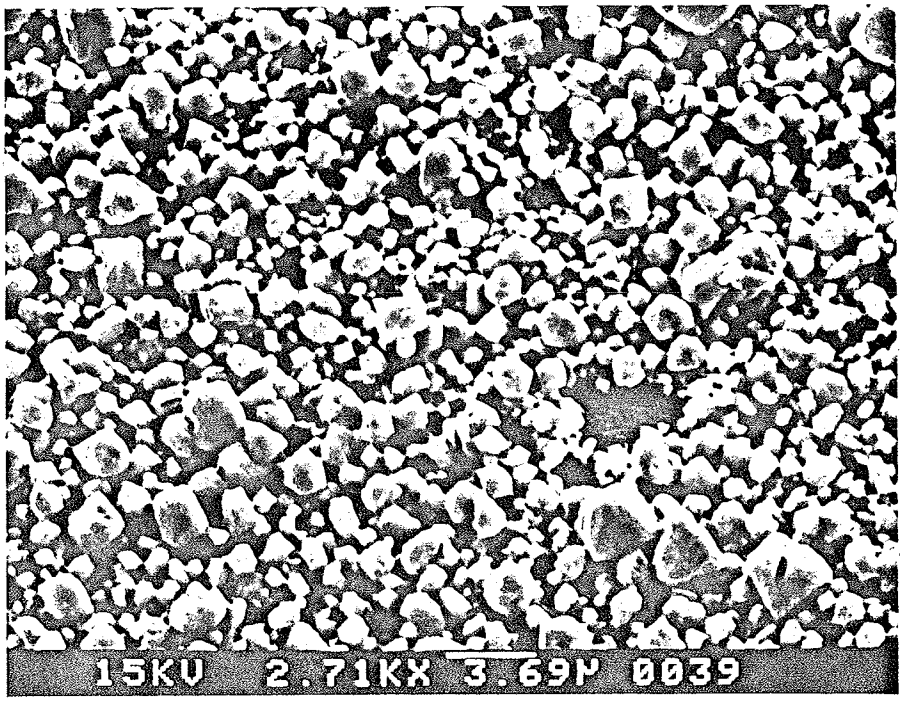

MICROGRAPH 10: Post-dissolution double-layer magnetite film. Experimental conditions: room temperature; static disk; 1×10^{-3} mol·dm^{-3} EDTA; pH = 3.00 ± 0.05; initial Fe(II) concentration 3×10^{-5} mol·dm^{-3}.

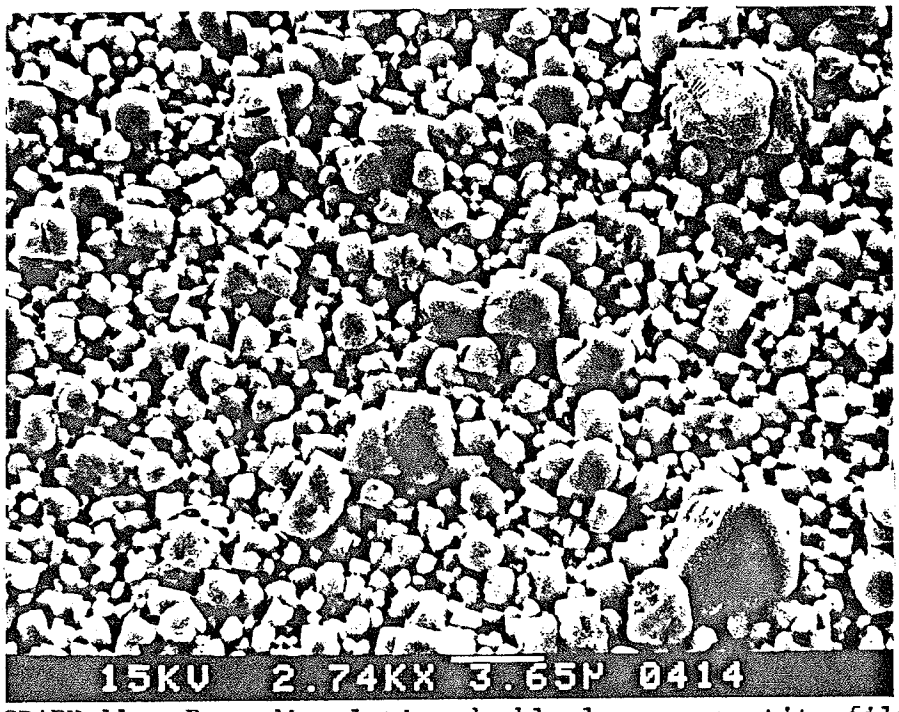

MICROGRAPH 11: Post-dissolution double-layer magnetite film. Experimental conditions: room temperature; static disk; 1×10^{-3} mol·dm^{-3} EDTA; pH = 3.00 ± 0.05; initial Fe(II) concentration 2×10^{-4} mol·dm^{-3}.

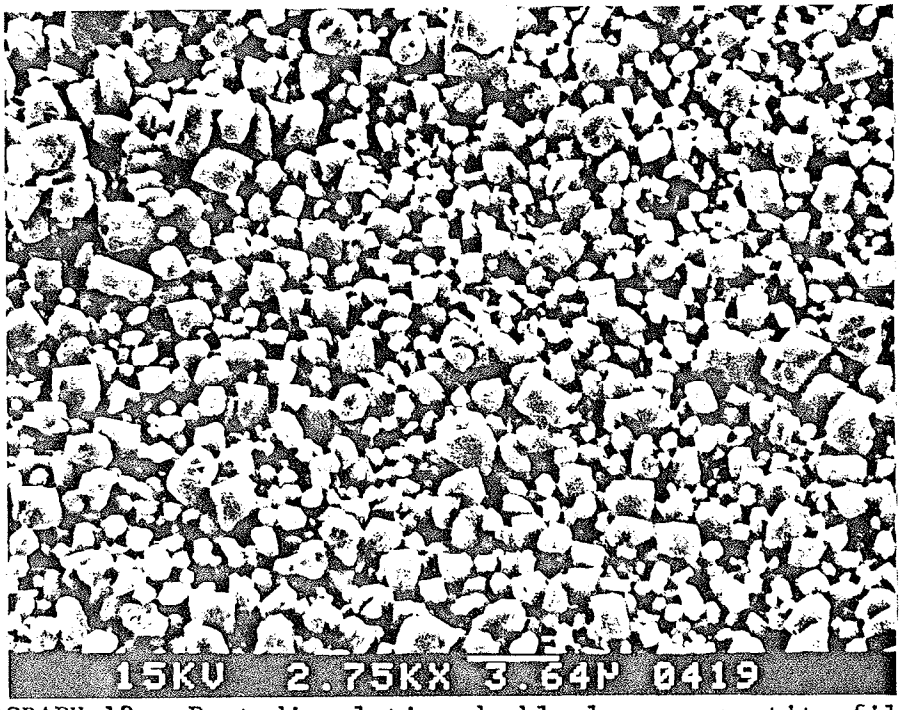

MICROGRAPH 12: Post-dissolution double-layer magnetite film. Experimental conditions: room temperature; static disk; 1×10^{-3} mol·dm^{-3} EDTA; pH = 3.00 ± 0.05; initial Fe(II) concentration 1×10^{-3} mol·dm^{-3}.

MICROGRAPH 13: Post-dissolution double-layer magnetite film. Experimental conditions: room temperature; static disk; $1x10^{-3}$ $mol \cdot dm^{-3}$ EDTA; pH = 3.00 ± 0.05; initial Fe(II) concentration $1x10^{-2}$ $mol \cdot dm^{-3}$.

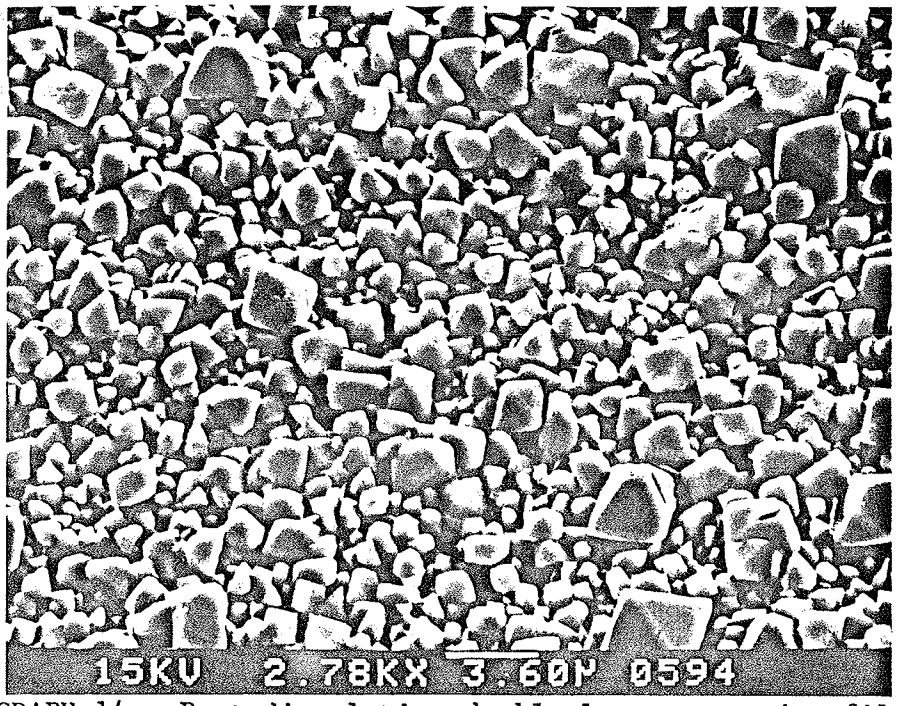

MICROGRAPH 14: Post-dissolution double-layer magnetite film. Experimental conditions: room temperature; disk rotated at 33.3 Hz; $1x10^{-3}$ $mol \cdot dm^{-3}$ EDTA; pH = 3.00 ± 0.05; initial Fe(II) concentration 0 $mol \cdot dm^{-3}$.

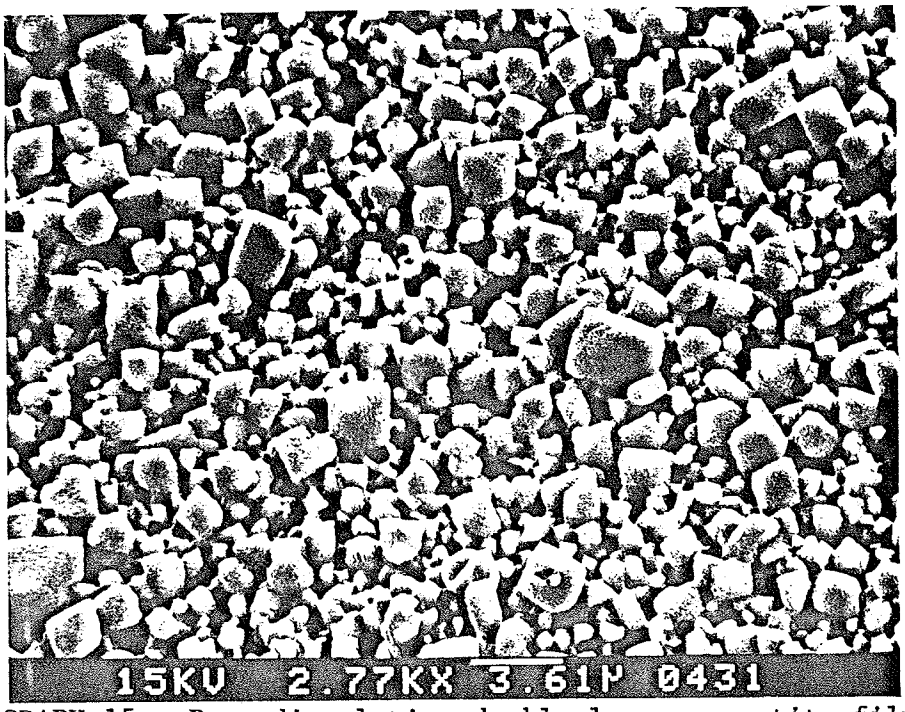

MICROGRAPH 15: Post-dissolution double-layer magnetite film.

Experimental conditions: room temperature; disk rotated at 33.3 Hz; $1x10^{-3}$ $mol \cdot dm^{-3}$ EDTA; pH = 3.00 ± 0.05; initial Fe(II) concentration $1x10^{-5}$ $mol \cdot dm^{-3}$.

MICROGRAPH 16: Post-dissolution double-layer magnetite film.

Experimental conditions: room temperature; disk rotated at 33.3 Hz; $1x10^{-3}$ $mol \cdot dm^{-3}$ EDTA; pH = 3.00 ± 0.05; initial Fe(II) concentration $1x10^{-3} mol \cdot dm^{-3}$.

MICROGRAPH 17: Post-dissolution double-layer magnetite film.

Experimental conditions: room temperature; disk rotated at 33.3 Hz; $1x10^{-3}$ mol·dm^{-3} EDTA; pH = 3.00 ± 0.05; initial Fe(II) concentration $1x10^{-2}$ mol·dm^{-3}.

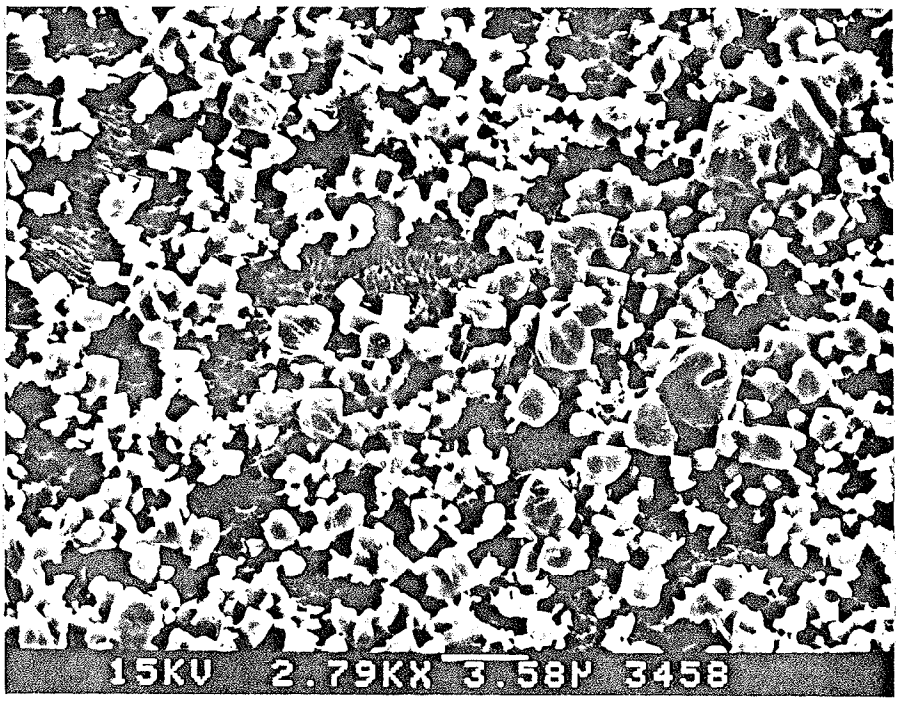

MICROGRAPH 18: Post-dissolution double-layer magnetite film.

Experimental conditions: room temperature; disk rotated at 33.3 Hz; $1x10^{-3}$ mol·dm^{-3} EDTA; pH = 3.00 ± 0.05; initial Fe(II) concentration $1x10^{-2}$mol·dm^{-3}.

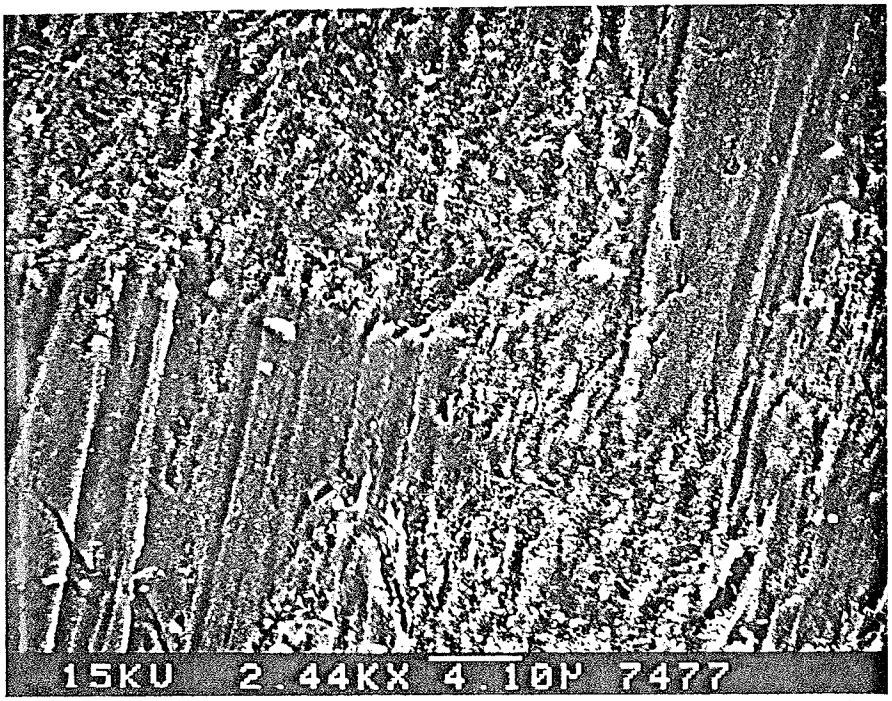

MICROGRAPH 19: Post-dissolution single-layer magnetite film.
Experimental conditions: temperature 23°C; disk rotated at 16.7 Hz; 2×10^{-3} mol·dm^{-3} EDTA; pH = 3.00 ± 0.05.

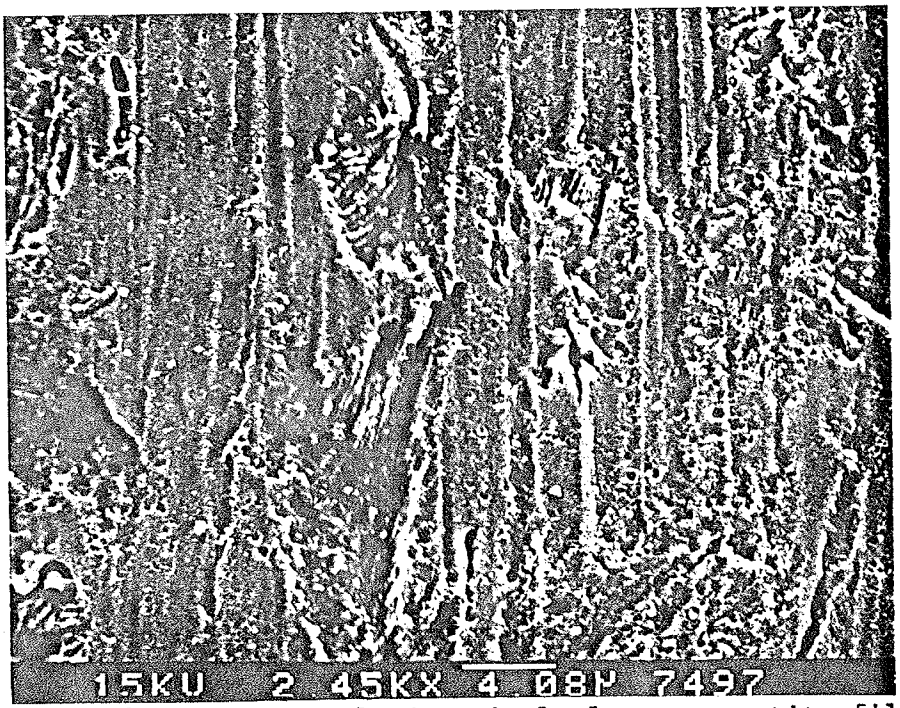

MICROGRAPH 20: Post-dissolution single-layer magnetite film.
Experimental conditions: temperature 65°C; disk rotated at 16.7 Hz; 2×10^{-3} mol·dm^{-3} EDTA; pH = 3.00 ± 0.05.

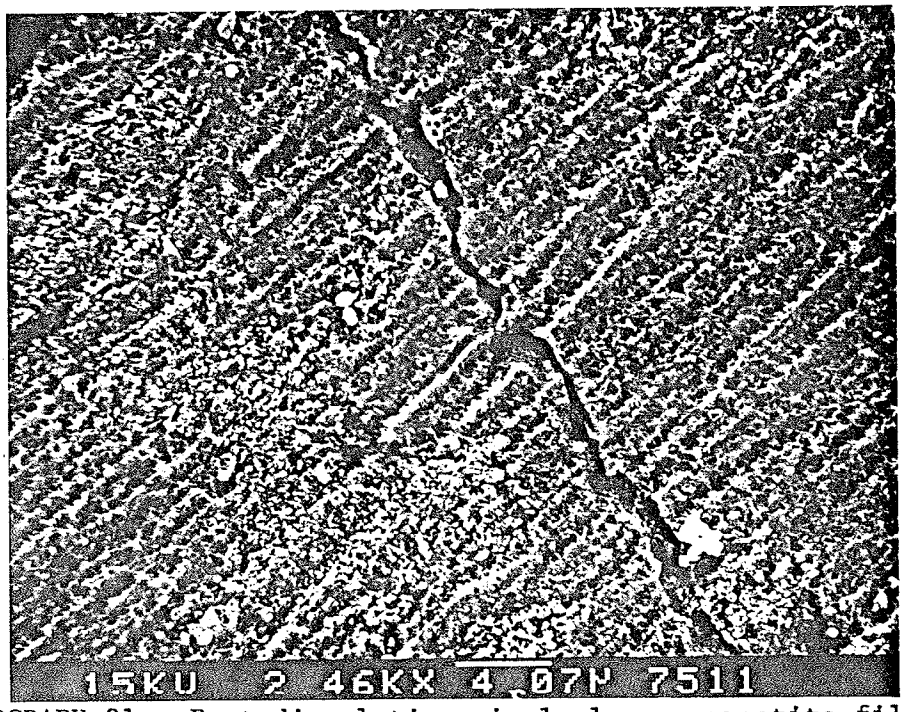

MICROGRAPH 21: Post-dissolution single-layer magnetite film.
Experimental conditions: temperature 85°C; disk rotated at 16.7 Hz; 2×10^{-3} mol·dm^{-3} EDTA; pH = 3.00 ± 0.05.

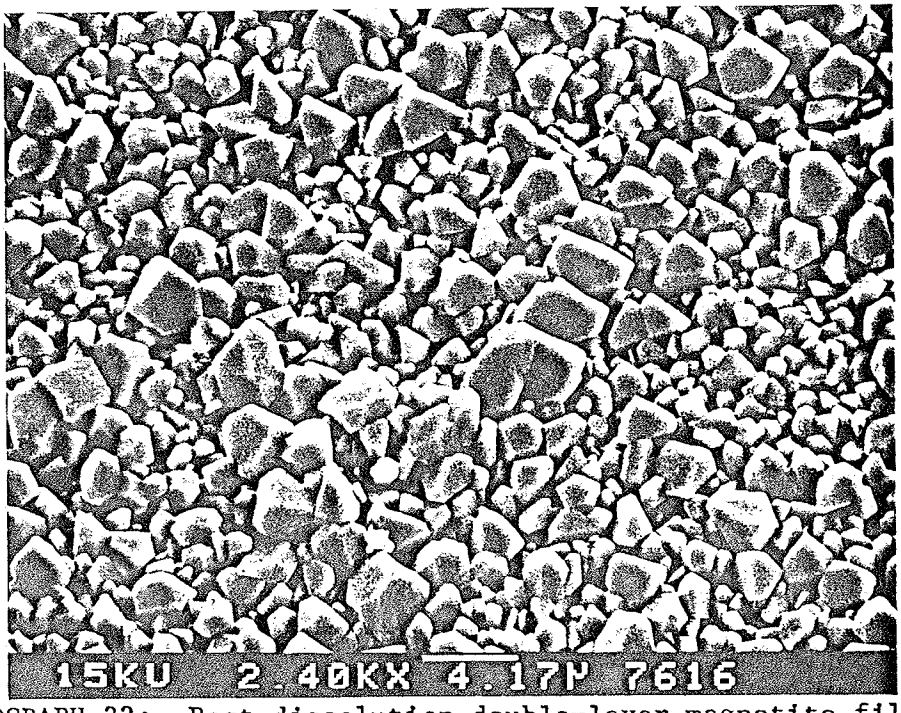

MICROGRAPH 22: Post-dissolution double-layer magnetite film.
Experimental conditions: temperature 23°C; disk rotated at 16.7 Hz; 2×10^{-3} mol·dm^{-3} EDTA; pH = 3.00 ± 0.05.

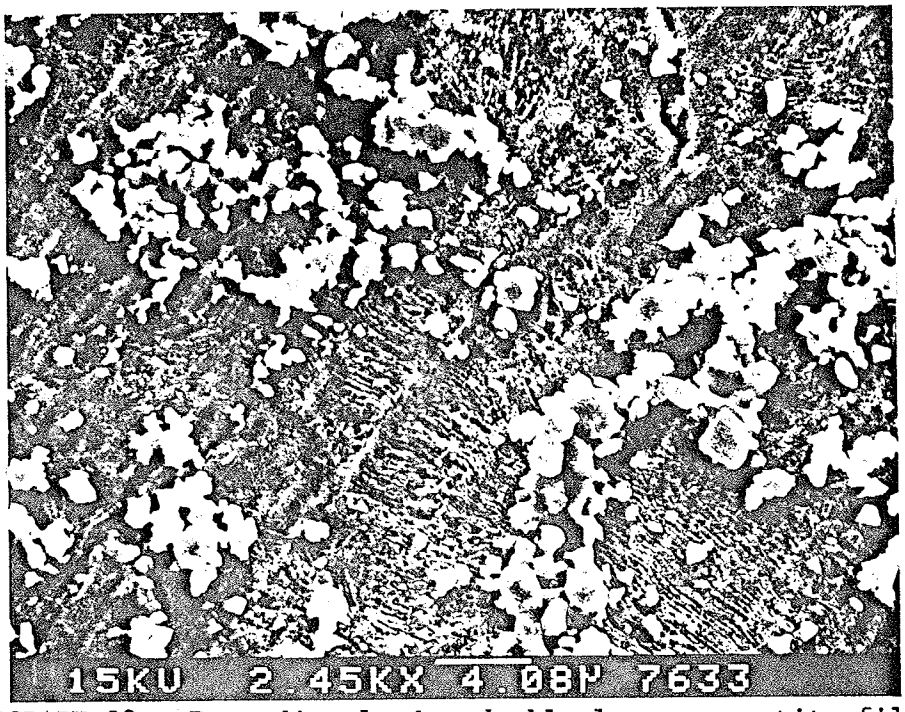

MICROGRAPH 23: Post-dissolution double-layer magnetite film.
Experimental conditions: temperature 65°C; disk rotated at 16.7 Hz;
2×10^{-3} mol·dm^{-3} EDTA; pH = 3.00 ± 0.05.

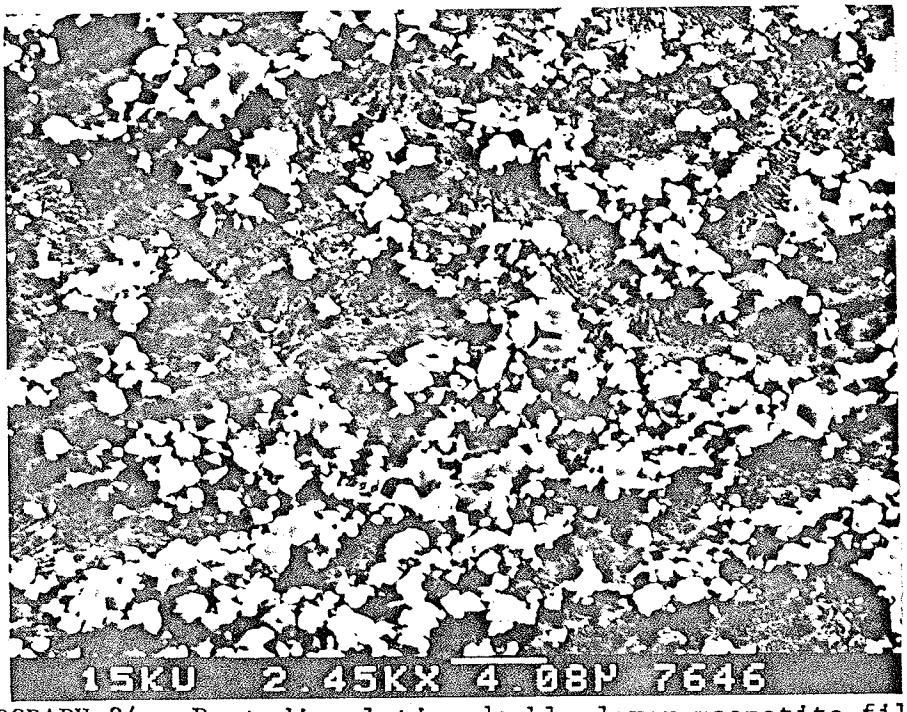

MICROGRAPH 24: Post-dissolution double-layer magnetite film.
Experimental conditions: temperature 85°C; disk rotated at 16.7 Hz;
2×10^{-3} mol·dm^{-3} EDTA; pH = 3.00 ± 0.05.

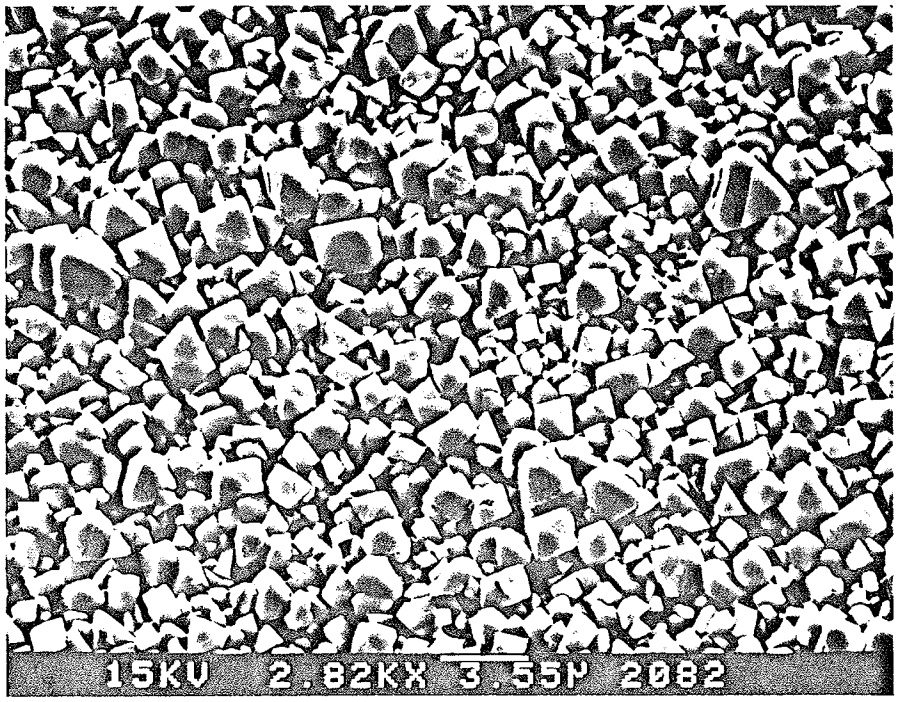

MICROGRAPH 25: Post-dissolution double-layer magnetite film.
Experimental conditions: room temperature; disk rotated at 16.7 Hz; $1x10^{-3}$ mol•dm^{-3} EDTA; pH = 3.12 ± 0.10.

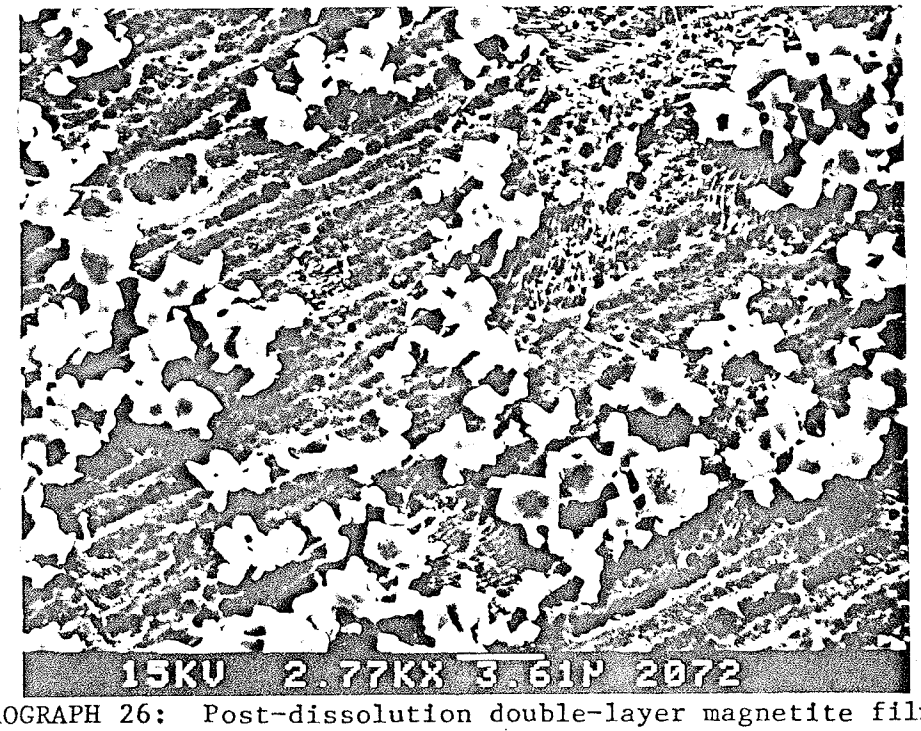

MICROGRAPH 26: Post-dissolution double-layer magnetite film.
Experimental conditions: room temperature; disk rotated at 16.7 Hz; $1x10^{-3}$ mol•dm^{-3} EDTA; $3x10^{-4}$ mol•dm^{-3} oxalate; pH = 3.12 ± 0.10.

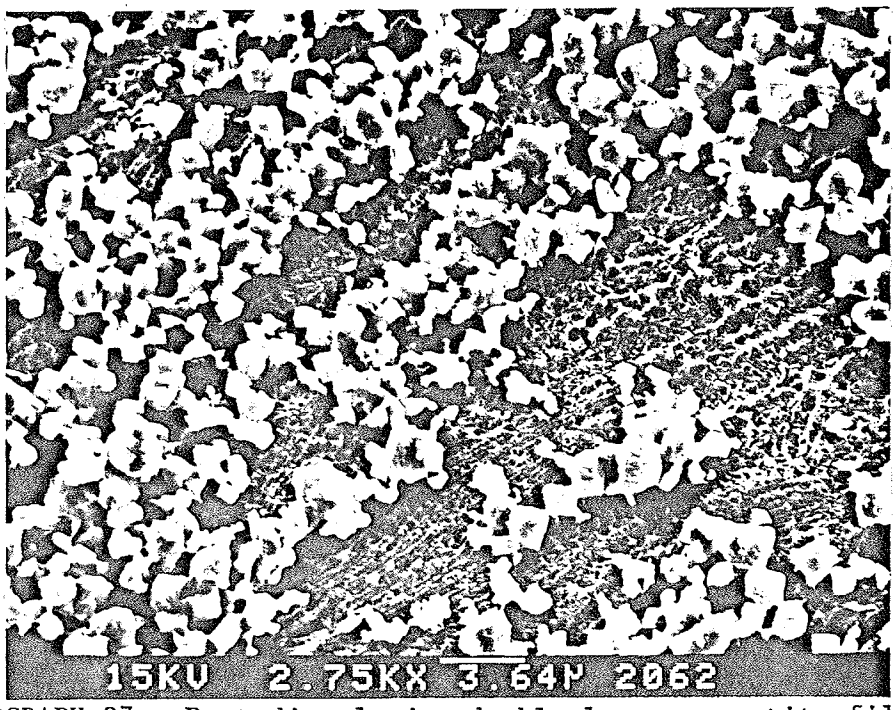

MICROGRAPH 27: Post-dissolution double-layer magnetite film.

Experimental conditions: room temperature; disk rotated at 16.7 Hz; $1x10^{-3}$ $mol \cdot dm^{-3}$ EDTA; $1x10^{-2}$ $mol \cdot dm^{-3}$ oxalate; pH = 3.12 ± 0.10.

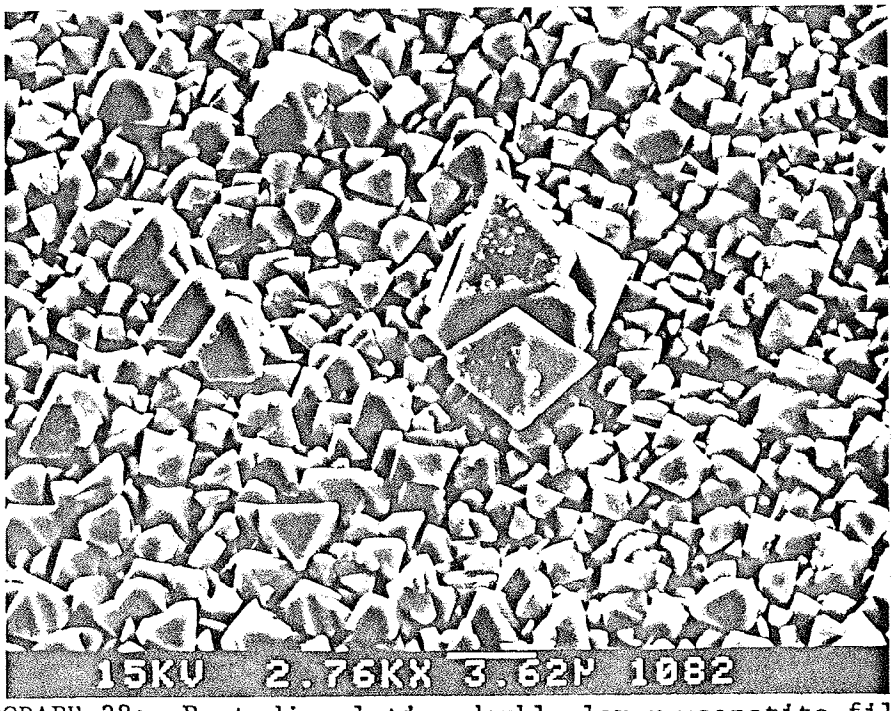

MICROGRAPH 28: Post-dissolution double-layer magnetite film.

Experimental conditions: room temperature; disk rotated at 16.7 Hz; $1x10^{-3}$ $mol \cdot dm^{-3}$ oxalate; pH = 3.00 ± 0.05; passive disk.

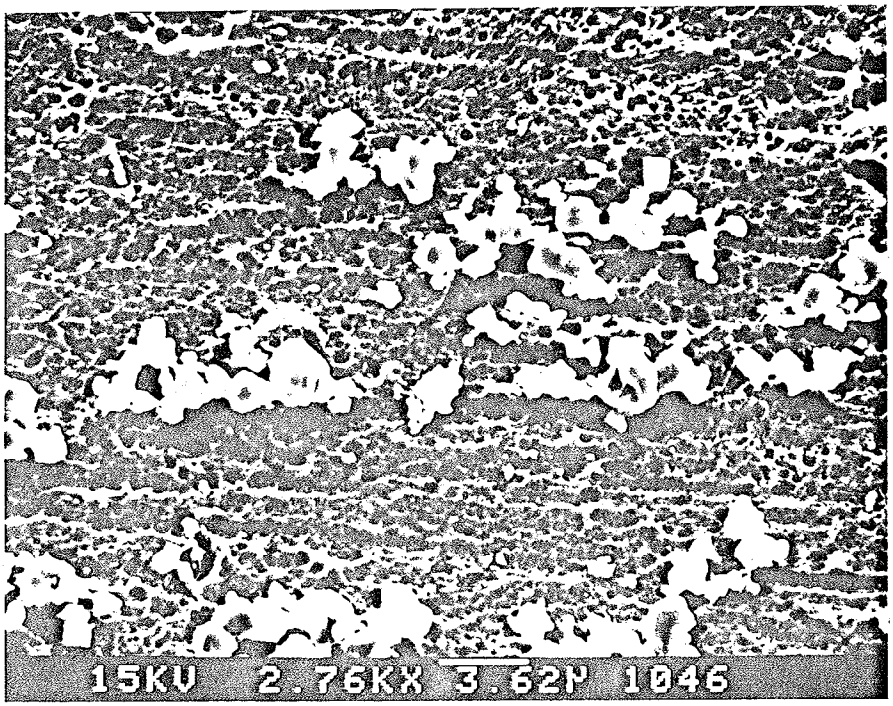

MICROGRAPH 29: Post-dissolution double-layer magnetite film. Experimental conditions: room temperature; disk rotated at 16.7 Hz; $1x10^{-3}$ mol•dm^{-3} oxalate; pH = 3.00 ± 0.05; active disk.

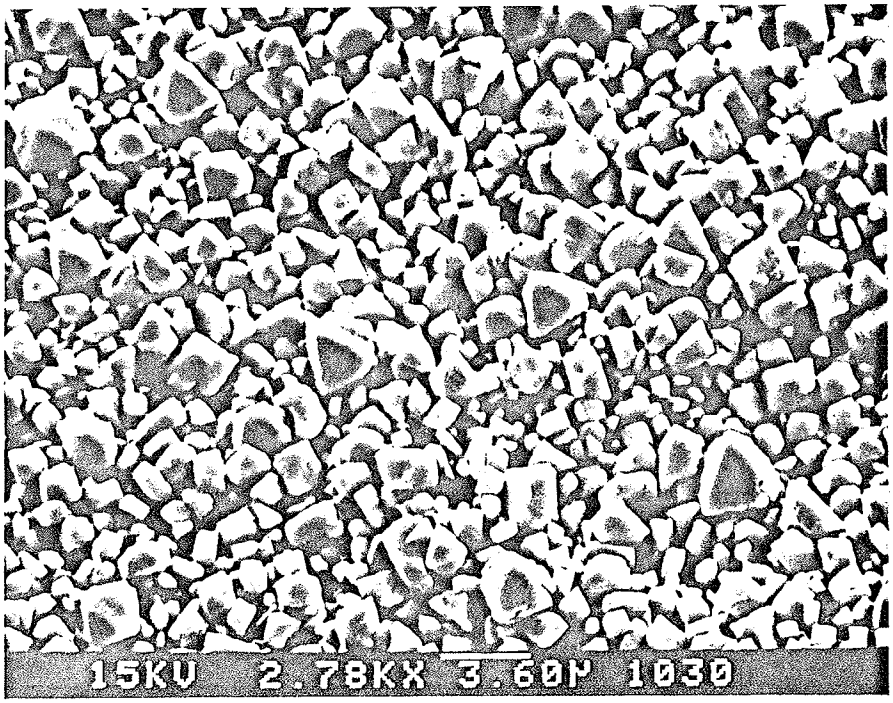

MICROGRAPH 30: Post-dissolution double-layer magnetite film. Experimental conditions: room temperature; disk rotated at 16.7 Hz; $1x10^{-3}$ mol•dm^{-3} oxalate; pH = 3.00 ± 0.05; ferrous ammonium sulphate added.

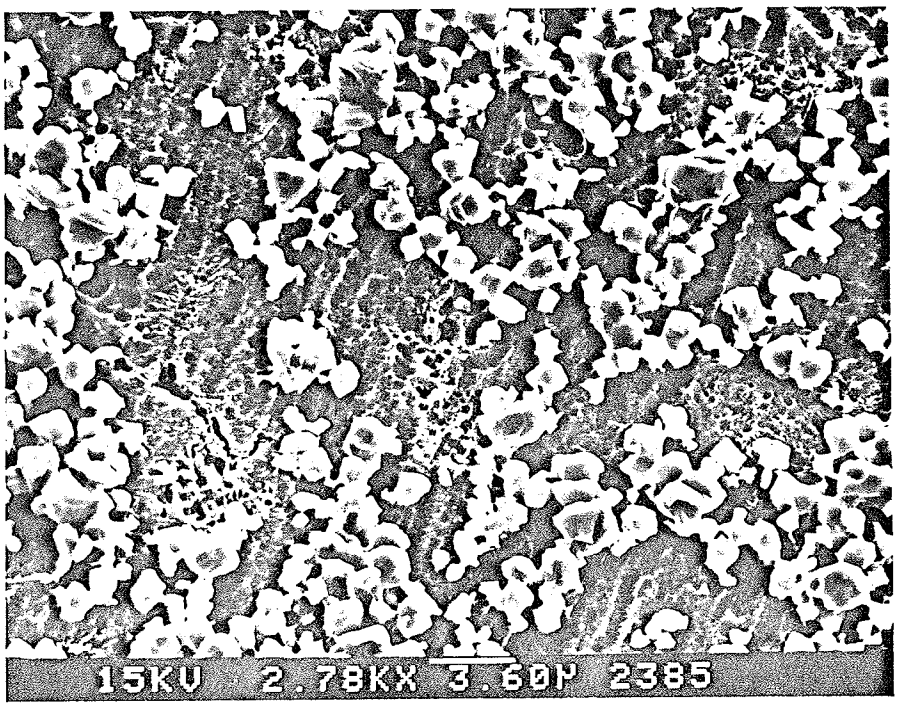

MICROGRAPH 31: Post-dissolution double-layer magnetite film.
Experimental conditions: room temperature; disk rotated at 16.7 Hz; $3x10^{-4}$ mol·dm^{-3} EDTA; $3x10^{-4}$ mol·dm^{-3} oxalate; pH = 3.10 ± 0.10.

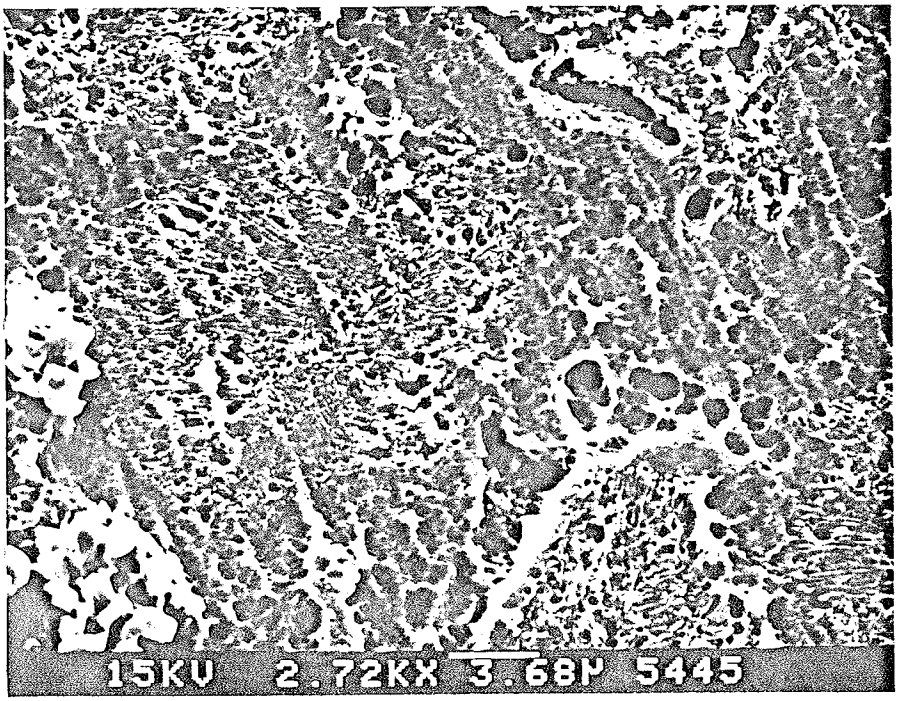

MICROGRAPH 32: Post-dissolution double-layer magnetite film.
Experimental conditions: room temperature; disk rotated at 16.7 Hz; $3x10^{-4}$ mol·dm^{-3} EDTA; $3x10^{-4}$ mol·dm^{-3} oxalate; pH = 3.10 ± 0.10; residual upper-layer crystals physically removed.

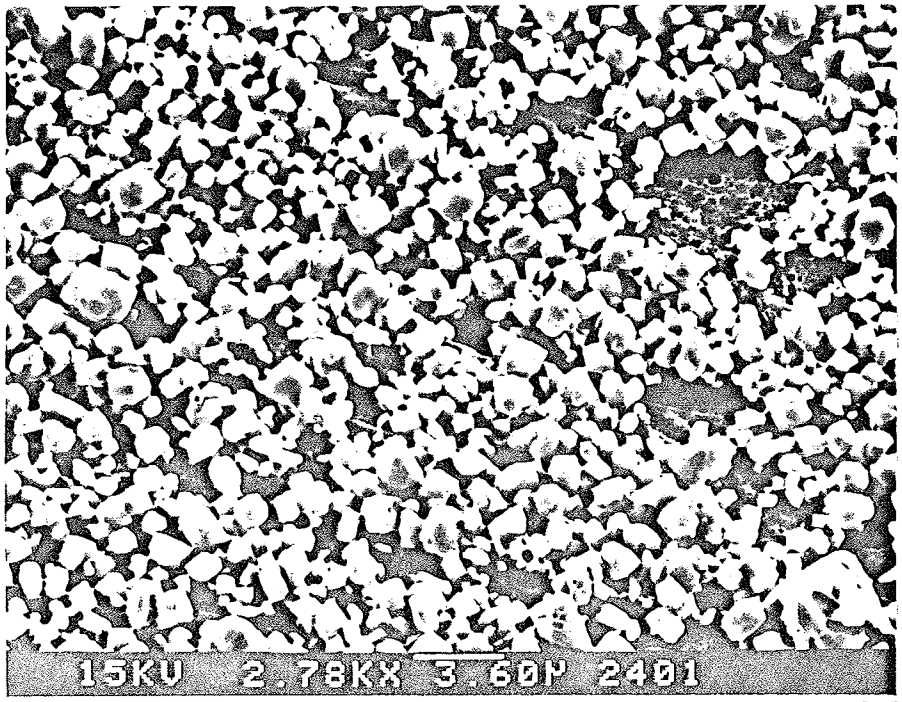

MICROGRAPH 33: Post-dissolution double-layer magnetite film.

Experimental conditions: room temperature; disk rotated at 16.7 Hz; $3x10^{-4}$ mol·dm^{-3} EDTA; $3x10^{-4}$ mol·dm^{-3} oxalate; $3x10^{-4}$ mol·dm^{-3} Na_2SO_4; pH = 3.10 ± 0.10.

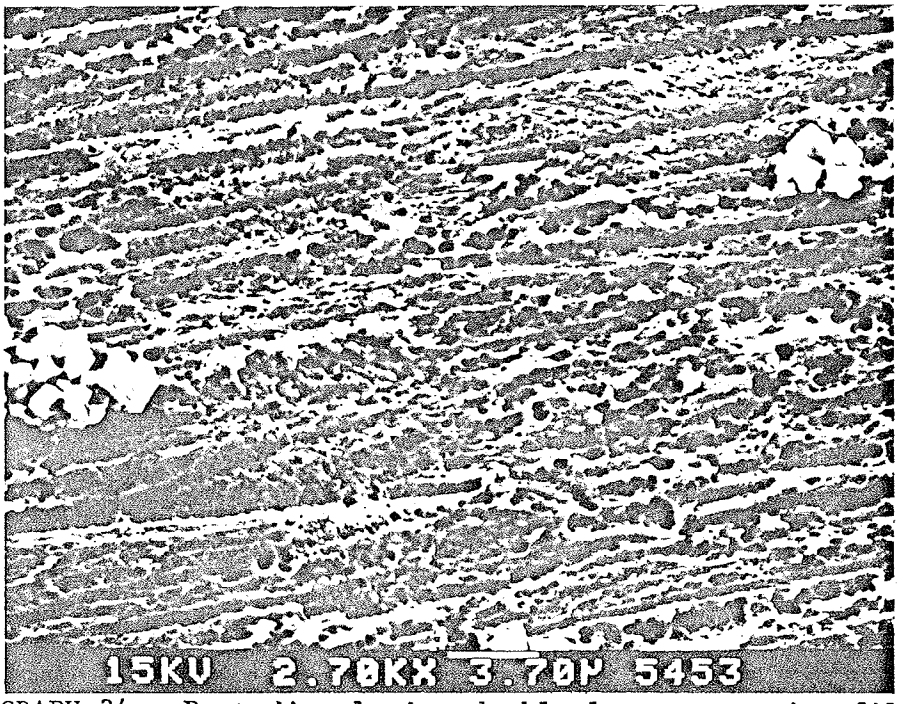

MICROGRAPH 34: Post-dissolution double-layer magnetite film.

Experimental conditions: room temperature; disk rotated at 16.7 Hz; $3x10^{-4}$ mol·dm^{-3} EDTA; $3x10^{-4}$ mol·dm^{-3} oxalate; $3x10^{-4}$ mol·dm^{-3} Na_2SO_4; pH = 3.10 ± 0.10; residual upper-layer crystals physically removed.

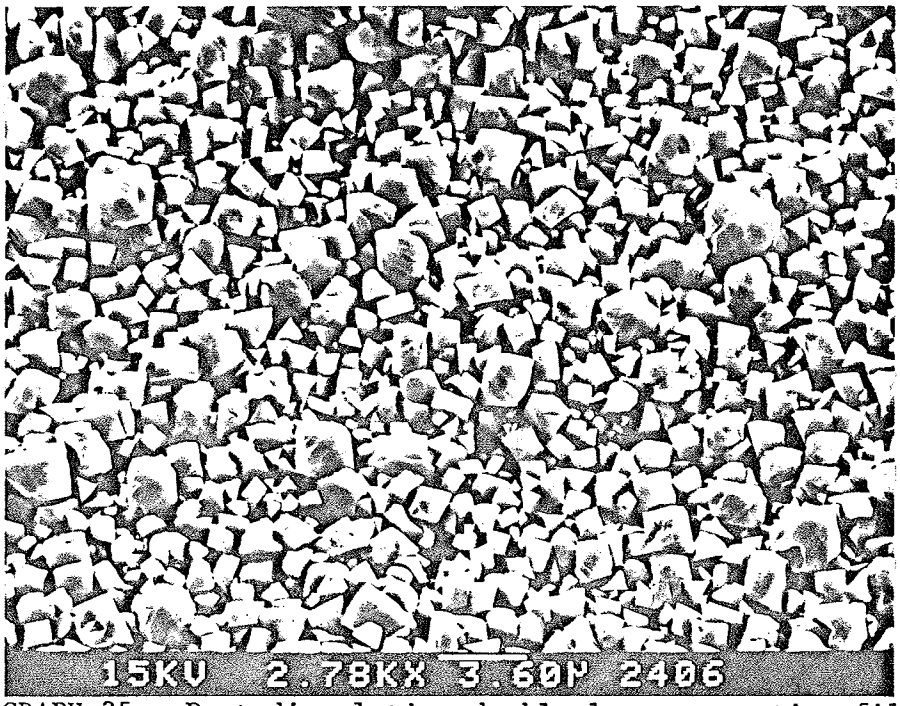

MICROGRAPH 35: Post-dissolution double-layer magnetite film.

Experimental conditions: room temperature; disk rotated at 16.7 Hz; $1x10^{-3}$ $mol \cdot dm^{-3}$ Na_2SO_4; pH = 3.10 ± 0.10.

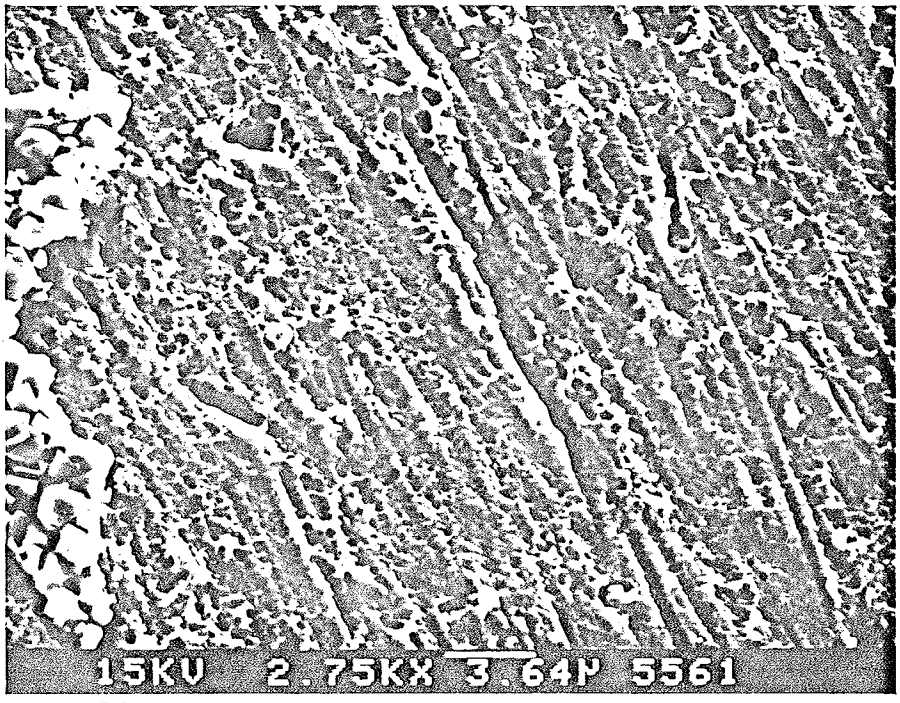

MICROGRAPH 36: Post-dissolution double-layer magnetite film.

Experimental conditions: room temperature; disk rotated at 16.7 Hz; $1x10^{-4}$ $mol \cdot dm^{-3}$ Na_2SO_4; pH = 3.10 ± 0.10; residual upper-layer crystals physically removed.

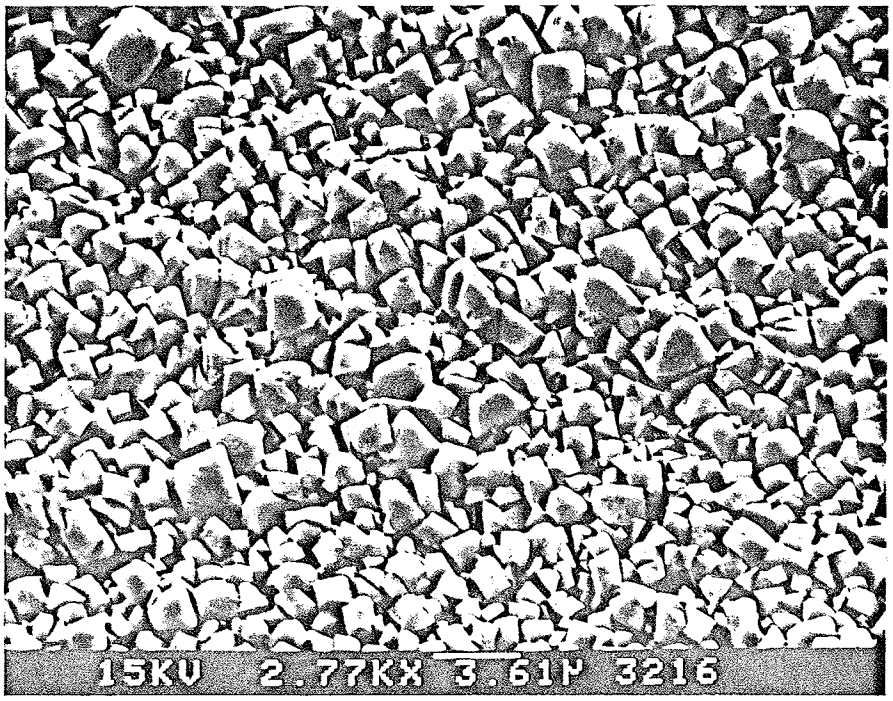

MICROGRAPH 37: Post-dissolution double-layer magnetite film.

Experimental conditions: room temperature; disk rotated at 16.7 Hz; 1×10^{-3} mol·dm^{-3} $NaClO_4$; pH = 3.10 ± 0.10.

APPENDIX A

SPECIATION OF Fe^{2+}-EDTA-OXALATE SOLUTIONS

Definition of equilibrium constants:

$$K_{1n} = \frac{[H_nL^{y-}]}{[H^+][H_{(n-1)}L^{(y+1)-}]}$$

The values of all equilibrium constants are taken from Reference 14

EDTA/H^+	K_1	$= 1.6\times10^{10}$
	K_{12}	$= 1.6\times10^{6}$
	K_{13}	$= 316$
	K_{14}	$= 100$
Oxalate/H^+	K_1	$= 1.38\times10^{4}$
	K_{12}	$= 17.8$

Thus, 1×10^{-3} mol·dm^{-3} solutions of oxalate and EDTA at pH=3.0 will have the following composition:

$[EDTA^{4-}]$	$= 3\times10^{-14}$ mol·dm^{-3}	$[C_2O_4^{2-}]$	$= 6.7\times10^{-5}$ mol·dm^{-3}
$[HEDTA^{3-}]$	$= 4.6\times10^{-7}$ mol·dm^{-3}	$[HC_2O_4^-]$	$= 9.17\times10^{-4}$ mol·dm^{-3}
$[H_2EDTA^{2-}]$	$= 7.42\times10^{-4}$ mol·dm^{-3}	$[H_2C_2O_4]$	$= 1.6\times10^{-5}$ mol·dm^{-3}
$[H_3EDTA^-]$	$= 2.34\times10^{-4}$ mol·dm^{-3}		
$[H_4EDTA]$	$= 2.34\times10^{-5}$ mol·dm^{-3}		

Consider a solution containing $1x10^{-3}$ mol•dm^{-3} EDTA and $1x10^{-2}$ mol•dm^{-3} oxalate to which ferrous ions are added.

The ligand complexations with Fe^{2+} are described by the following equilibrium constants:

$$K_n = \frac{[ML_n]}{[ML_{(n-1)}][L]}$$

$EDTA^{4-}/Fe^{2+}$	K_1	$= 2.14x10^{14}$
$HEDTA^{3-}/Fe^{2+}$	K_1	$= 7.24x10^{6}$
$C_2O_4^{2-}/Fe^{2+}$	K_1	$> 5x10^{5}$
	K_2	> 708
	K_3	~ 10

Assumptions and conditions:

(i) Equilibrium is established.

(ii) $[C_2O_4^{2-}] \gg [Fe^{2+}]$. Therefore, the concentrations of oxalate species remain unchanged by the addition of Fe^{2+}.

(iii) $[EDTA] \gg [Fe^{2+}]$. Therefore, the concentrations of EDTA species remain unchanged by the addition of Fe^{2+}.

(iv) That $H_2(CO_2)_2$, $H(CO_2)_2^-$, H_2EDTA^{2-}, H_3EDTA^- and H_4EDTA are non-complexing.

(v) Temperature ∿ 20°C.

(vi) The impact of the solution ionic strength on the stability constants is ignored.

The distribution of Fe^{2+} species in a $1x10^{-3}$ $mol \cdot dm^{-3}$ EDTA solution at pH=3 as a function of the concentration of added oxalate.

SPECIATION OF Fe(II)-EDTA-OXALATE SOLUTIONS

Oxalate Concentration ($mol \cdot dm^{-3}$)	$1x10^{-2}$	$1x10^{-3}$	$1x10^{-4}$	$1x10^{-5}$	0
COMPLEX	SPECIATION, EXPRESSED AS PERCENTAGES				
Fe^{II}_{aq}	0.2	2.2	7.2	9.1	9.4
$Fe^{II}(C_2O_4^{2-})$	66.3	73.3	24.0	3.1	
$Fe^{II}(C_2O_4^{2-})_2$	31.5	3.5	0.1	0.001	
$Fe^{II}(C_2O_4^{2-})_3$	0.2	0.002	0	0	
$Fe^{II}(EDTA^{4-})$	1.2	13.8	45.1	57.6	59.4
$Fe^{II}(HEDTA^{3-})$	0.6	7.2	23.6	30.1	31.1

These calculations reveal that at low oxalate concentrations the complexation between ferrous ions and oxalate is limited, the vast majority of Fe^{2+} being complexed with $EDTA^{4-}$ and $HEDTA^{3-}$. In solutions containing $1x10^{-2}$ $mol \cdot dm^{-3}$ oxalate and $1x10^{-3}$ $mol \cdot dm^{-3}$ EDTA, the ferrous ion oxalate complexes dominate. This demonstrates that under these conditions the presence of EDTA is not sufficient to prevent the precipitation of ferrous oxalate species.